Chemical and Structural Mapping of Cathodes for Li-Ion Batteries From the Nano- to the Electrode-Scale

BY

MARK F. WOLFMAN
B.S., Western Michigan University, June 2008

THESIS

Submitted as partial fulfillment of the requirements
for the degree of Doctor of Philosophy in Chemistry
in the Graduate College of the
University of Illinois at Chicago, 2019

Chicago, Illinois

Defense Committee:

Jordi Cabana	Chair and Advisor
Stephanie Cologna	
Ksenija Glusac	
Luke Hanley	
Volker Rose	Argonne National Laboratory

TABLE OF CONTENTS

TABLE OF CONTENTS (Continued)

CHAPTER **PAGE**

LIST OF TABLES

LIST OF FIGURES

LIST OF FIGURES (Continued)

FIGURE **PAGE**

LIST OF FIGURES (Continued)

FIGURE **PAGE**

LIST OF FIGURES (Continued)

LIST OF FIGURES (Continued)

LIST OF FIGURES (Continued)

LIST OF FIGURES (Continued)

FIGURE **PAGE**

LIST OF FIGURES (Continued)

FIGURE **PAGE**

LIST OF FIGURES (Continued)

FIGURE **PAGE**

LIST OF ABBREVIATIONS

AMPIX Argonne multi-purpose in-situ X-ray. 117

APS the advanced photo source. xi, 118

CNR contrast-to-noise ratio. 82

EELS electron energy-loss spectroscopy. 37

FF full-field. vi, 22, 32, 35, 81, 82

STXM scanning transmission X-ray microscopy. viii, xvii, 42, 43, 74, 76, 79

SX-STM synchrotron X-ray scanning tunneling microscopy. viii, xvii, 38, 44, 67, 69, 72, 77

TEM transmission electron microscopy. vi, 37, 38, 46, 160

TEY total electron yield. vi, 38, 40, 48, 50, 51, 53

TFY total fluorescence yield. vi, 38, 40, 50, 51

TXM transmission X-ray microscopy. vi, ix–xi, xvii, 22, 32, 35, 81–83, 85–89, 92, 93, 101–103, 105–107, 109, 112, 116–120

XANES X-ray absorption near-edge structure. ix, 30, 82, 83, 87, 92, 102, 106, 109, 112

XAS X-ray absorbance spectroscopy. iv, vi, xvii, 14, 23, 30, 32, 36, 37, 40, 42, 45, 50, 83, 88, 91, 96, 101, 112, 113, 117, 119–121, 160

XRD X-ray diffraction. iv, v, ix, xii, xvii, 16, 19, 23, 30, 82–84, 113, 117, 123, 124, 127, 130, 132, 133, 135–138, 144, 148, 155, 157, 158

μ-XRD micro-focused X-ray diffraction. vi, 35, 124

SUMMARY

The continuing ability of Li-ion batteries to meet ever increasing demands for reliable energy storage requires a more detailed understanding of the underlying chemical processes than is currently available. Cathodes used in Li-ion batteries exhibit a hierarchical structure, with reactions governed by distinct but overlapping phenomena spanning multiple length scales. In this work, X-ray imaging and mapping techniques are combined with spectroscopic and structural characterization to provide unique insights into the chemical behavior of select commercially relevant cathode materials at length scales ranging from a single atomic layer to the whole electrode.

Chapter 2 examines the distribution of Ni oxidation states within individual cathode particles at several states of charge. The results reveal incomplete oxidation unevenly distributed within the particles, and add insight into the role of undesirable secondary reaction pathways. Chapter 3 tracks oxidation and reduction of Ni in secondary particle agglomerates during charge and discharge. Discrepancies between ensemble-average and particle-level measurements are discussed in the context of local electrochemistry and particle micro-structure. Chapter 4 presents a novel structural mapping technique applied to high energy density electrodes. Heterogeneity within partially charged electrodes is used to elucidate the roles of chemical diffusion and migration in limiting reaction rates within the electrolyte and cathode solid matrix.

The electrochemical performance of a cathode at a given length scale depends on its behavior at smaller scales. The multi-length-scale approach presented here provides a more detailed view

of the underlying battery chemistry than is possible by conventional ensemble-averaged methods alone.

CONTRIBUTION OF AUTHORS

Brian M. May[1] synthesized morphologically controlled $LiNi_{0.8}Co_{0.15}Al_{0.05}O_2$ used for characterization of primary particles (Chapter 2), assisted with operando TXM of secondary particles (Chapter 3), and provided written contribution to the perspective reused in the introduction (Chapter 1). Sara Khawaja[1] assisted in XRD mapping of complete electrodes (Chapter 4). Vincent De Andrade[2], Kamila Wiaderek[2], and Karena W. Chapman[2,3] provided guidance and support for development of the Mantis in-situ electrochemical cell (Chapter 3). Nozomi Shirato[2,4] and Volker Rose[2,4] developed and provided guidance for SX-STM of $LiNi_{0.8}Co_{0.15}Al_{0.05}O_2$ primary particles (Chapter 2). Young-Sang Yu[5] performed STXM of commercial $LiNi_{0.8}Co_{0.15}Al_{0.05}O_2$ primary particles, and Young-Sang Yu[5] and David A. Shapiro[5] provided support and guidance for collection and interpretation of ptychography data from primary particles (Chapter 2). Zachary Lebens-Higgins[5,6], Shawn Sallis[5,6], and Louis F.J. Piper[6] measured ensemble XAS and performed Bayesian analysis of ptychography data of $LiNi_{0.8}Co_{0.15}Al_{0.05}O_2$ primary particles (Chapter 2). Nicholas Faenza[7], Nathalie

Pereira[7], and Glenn Amatucci[7] performed electrochemical cycling of morphologically controlled $LiNi_{0.8}Co_{0.15}Al_{0.05}O_2$ powder (Chapter 2).

---

[1]Department of Chemistry, University of Illinois Chicago

[2]Advanced Photon Source, Argonne National Laboratory

[3]Stony Brook University, New York

[4]Center for Nanoscale Materials, Argonne National Laboratory

[5]Advanced Light Source, Lawrence Berkeley National Laboratory

[6]Binghamton University, State University of New York

[7]Rutgers University

CHAPTER 1

INTRODUCTION

A portion of this chapter was previously published and is reused with permission[1] (Appendix A). The source article is available at https://pubs.acs.org/doi/abs/10.1021/acs.chemmater.6b05114. Further permissions related to the material should be directed to the American Chemical Society.

1.1 The Broader Impact of Chemical Energy Storage

Beyond the visible consumer electronics applications, energy storage plays a critical role in areas such as manufacturing, electric grid distribution, and transportation. By some estimates, US industries lose $80 billion each year due to power interruptions, while annual electric vehicle sales are seeing large and consistent increases.[2] If renewable sources are to become the primary method of energy production, new storage solutions are necessary that deal with the intermittent nature of wind and solar sources. Even when supplying the electric grid by burning fossil fuels, fluctuations in energy demand require that more responsive peaker-plants be brought online. These peaker plants are more expensive than base-load plants, and their use could be alleviated if energy produced by unused capacity from base-load plants can be stored when demand is low. Current low-cost grid storage methods, pumped-hydro and compressed-air, require specific geological topography, limiting their viability.[2] In transportation, electric vehicles require energy storage that is compact and light, while also maintaining high standards of safety

and reliability.[3] The performance of the vehicle is closely tied to the power capabilities of the energy storage system. Furthermore, the expected life-span of the battery does not currently match the life-span of the vehicle.[4]

Batteries are the preferred portable energy storage systems. Batteries contain two terminals (electrodes) where oxidation and reduction reactions (redox) take place.[5] The fundamental redox chemistry within batteries is non-trivial and governs the practical aspects that are relevant to the target application, such as capacity, cycle life, and power, among others.[6] Current battery technology leaves considerable room for improvement compared to both consumer expectations and theoretical limits in terms of both capacity and cyclability.[7,8] Therefore, advances in battery technology that yield cheaper, more reliable and better performing systems will result in large economic, environmental and geopolitical benefits. A key requirement for achieving this goal is a better understanding of the chemistry underlying these materials, to engineer gains that lead them to operate as close as possible to their theoretical limits.

1.2 Li-ion Battery Fundamentals

Batteries store energy by transferring charge between two electrodes across a difference in electric potential, E, determined by the associated redox couples. The instantaneous potential is often not constant for each charge carrier, dq, so the total energy stored (U) by transferring a total charge, Q, between the two electrodes is[9]

$$U = \int^{Q} E dq \tag{1.1}$$

A typical battery cell is constructed from two parallel electrodes separated by an ionically conductive and electronically insulating electrolyte and membrane (Figure 1). For electrochemical experiments, these components are most commonly assembled into a coin-cell battery (Figure 2), which provides reproducibility and ease of assembly. The electrode with the higher reduction potential is the positive electrode, and by convention is referred to as the cathode during both oxidation and reduction. When a load or potential difference is applied at the electrodes, redox reactions take place that result in charge flowing through the cell (Figure 3). During charge, oxidation occurs at the cathode. Since the electrolyte is electronically insulating, electronic current flows through the external circuit from anode to cathode. To compensate for the transfer of electrons and maintain charge neutrality, a charge-carrier must move between the electrodes. During charge, this ionic current moves through the electrolyte from cathode to anode. During discharge, the process is reversed, with reduction occurring at the cathode, and downhill, with electronic current performing work through an external load by flowing from the cathode to the anode. Li-ion batteries are so-named to reflect the use of Li^+ ions as the charge carrier between electrodes. While all components of a Li-ion battery warrant study, this work is primarily concerned with the chemical processes occurring at the cathode.

Several categories of Li-ion cathode have been developed. The most common is the intercalation cathode, where Li^+ enters and exits a host structure that does not change its underlying atomic framework. Within intercalation cathodes, transition-metal oxides have seen widespread

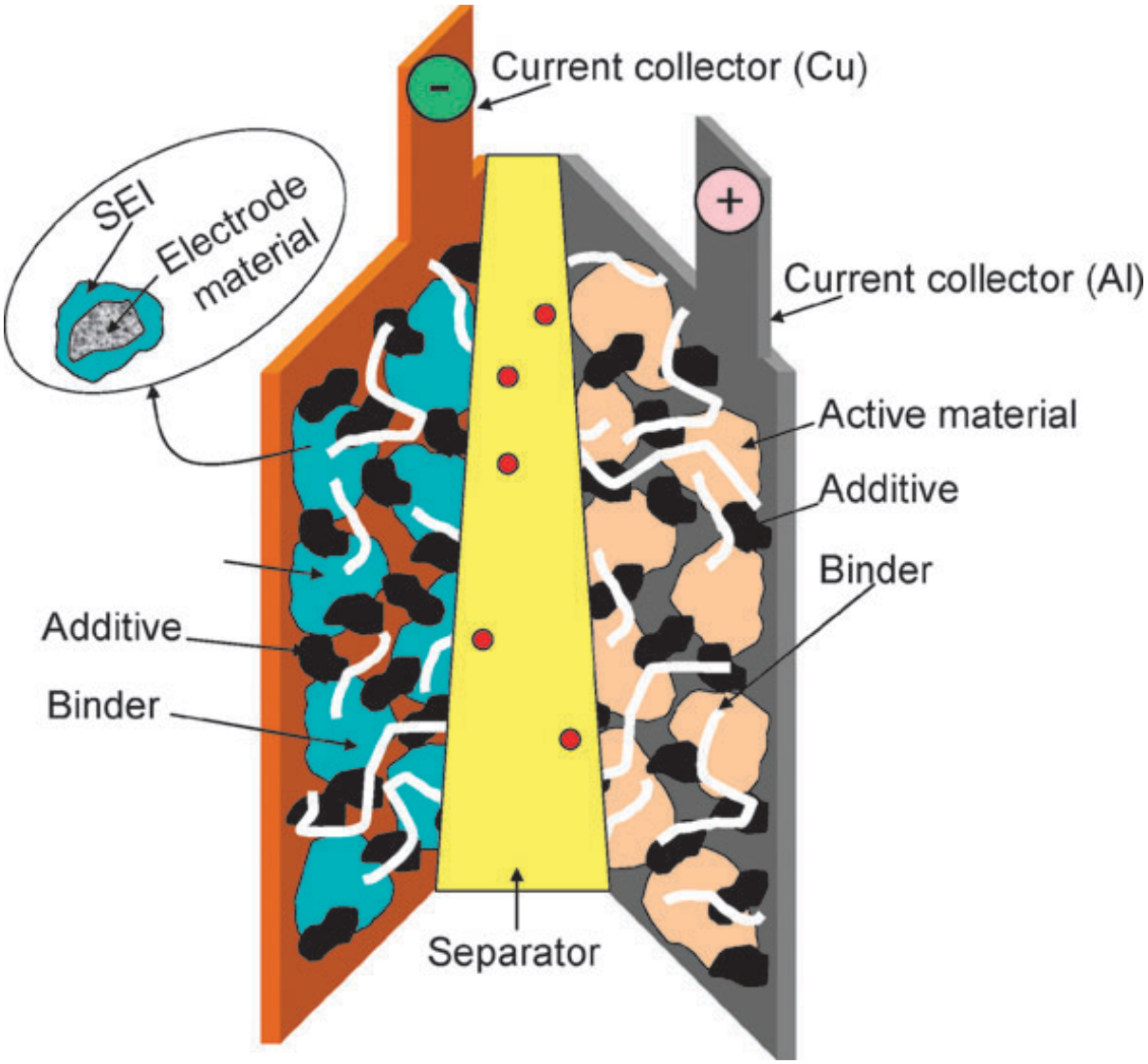

Figure 1: Schematic of a typical battery. The electrodes are made of multiple individual particles that participate in the electrochemical reaction (denoted as "active material"). Reproduced from Ref.[10] with permission from the Royal Society of Chemistry (Appendix A).

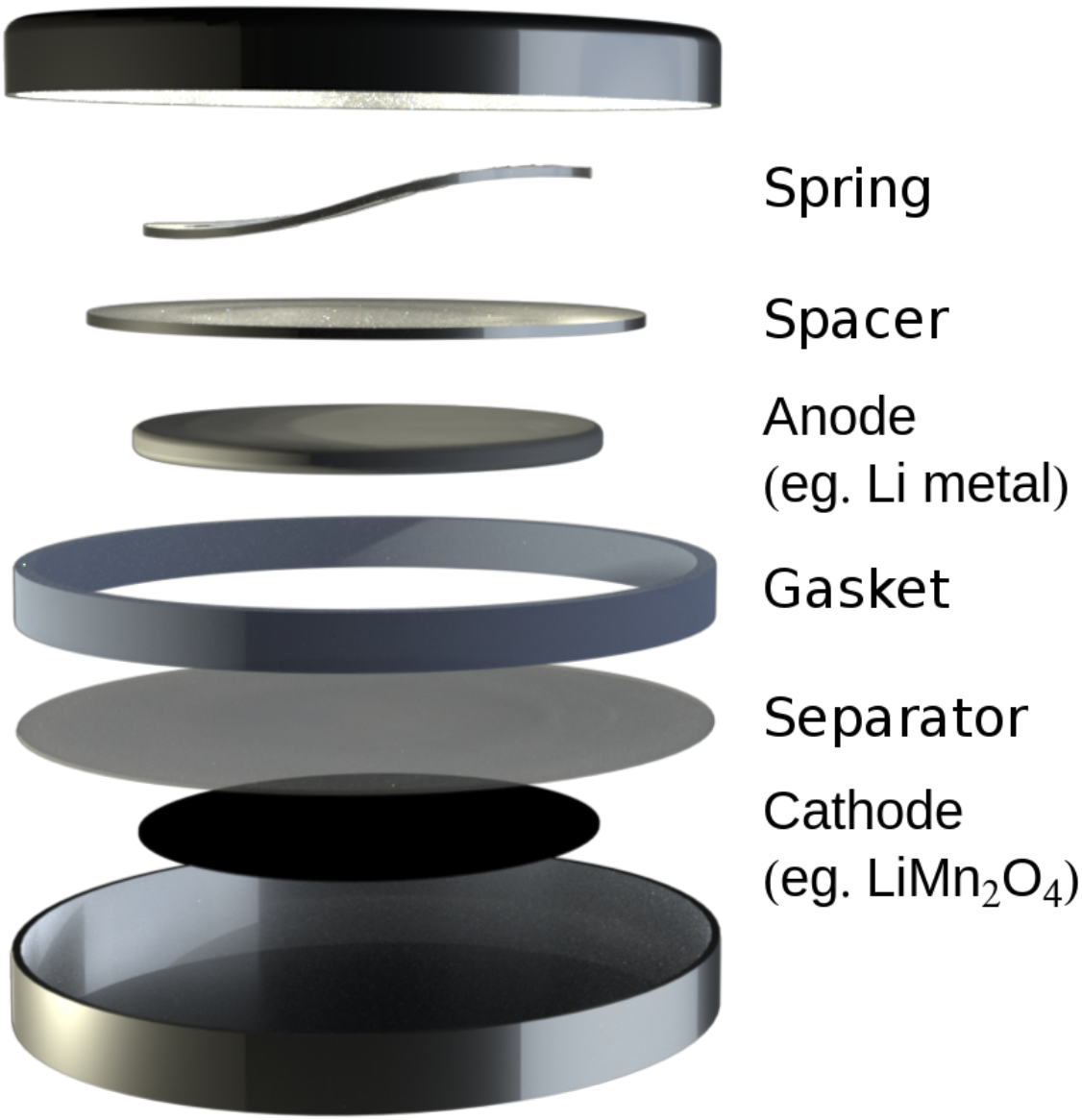

Figure 2: Diagram of a typical coin-cell battery. A stainless steel casing is sealed with a polypropylene gasket. Inside, a stainless steel wave spring and spacer apply force to a cathode and lithium metal anode separated by a polypropylene separator.

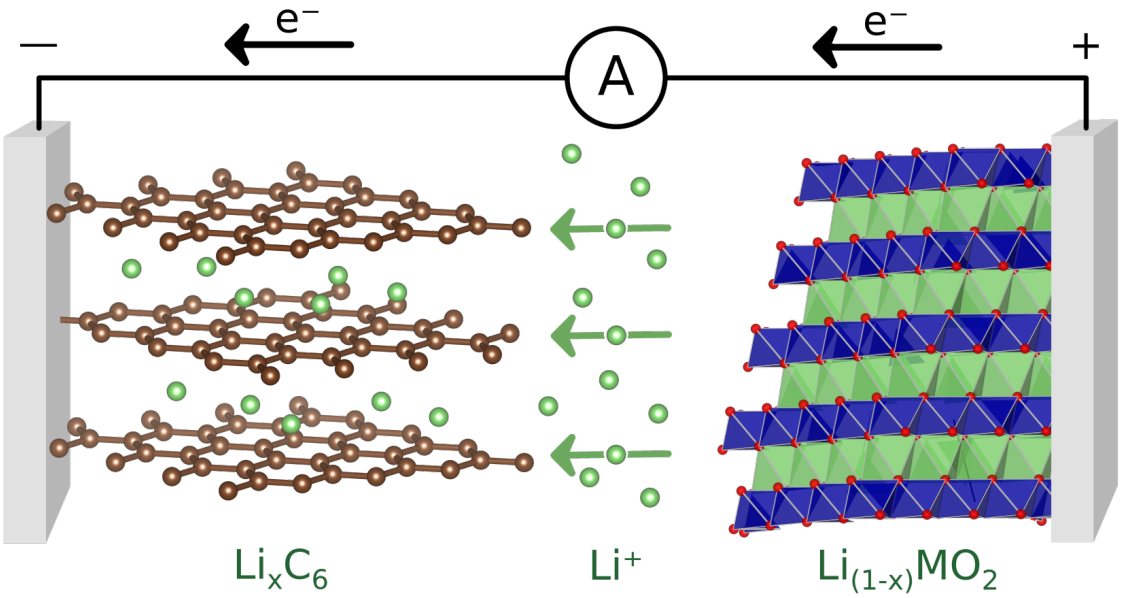

Figure 3: Schematic of charge flow in a Li-ion battery during charging. Current source, A, transports electrons from the $LiMO_2$ cathode to the graphite anode. Simultaneously, Li^+ leaves the MO_2 cathode host structure into the electrolyte, while Li^+ enters the graphite anode host structure from the electrolyte.

adoption in commercial batteries.[8,11] Figure 3 shows such a cathode paired with a graphite anode. The anode and cathodes half-reactions are

$$\mathrm{LiC_6} \rightleftharpoons \mathrm{Li^+ + C_6 + e^-} \qquad \Delta \mathrm{E^\circ} = -2.84\,\mathrm{V} \tag{1.2}$$

$$\mathrm{Li^+ + M^{IV}O_2 + e^-} \rightleftharpoons \mathrm{LiM^{III}O_2} \qquad \Delta \mathrm{E} \approx 0\,\mathrm{V\ to\ 2\,V} \tag{1.3}$$

where the potential for the cathode reaction depends on the choice of transition metal and degree of lithiation.[12,13] Although a graphite anode is used extensively in commercial cells to prevent dendrite formation,[14,15] lithium metal is often used as the anode in cathode research. Metallic lithium exhibits a stable potential over the full range of cathode delithiation, especially when used in large excess, allowing it to function as both a counter and reference electrode.

The electrochemical behavior of a cathode is evaluated by recording the cell potential as a function of the total charge accumulated (capacity) under an applied current. Reaction rates are often reported as the number of full charges per hour. For example, an experiment conducted at 2 C would undergo two full charge steps during one hour. The gravimetric capacity (defined in $\mathrm{mA\,h\,g^{-1}}$) is then converted to the extent of (de)lithiation (in moles of $\mathrm{Li^+}$ or $\mathrm{e^-}$ per mole of cathode active material) based on the reaction stoichiometry. The gravimetric capacity is applicable when engineering battery systems, while the extent of (de)lithiation is more pertinent to studying the redox chemistry. Figure 4 shows typical redox profiles for two common cathode compositions. The two horizontal axes represent equivalent gravimetric capacity, but differ in the extent of (de)lithiation due to the different molar masses of the two materials. Hysteresis

in potential and capacity between oxidation and reduction is the result of kinetic barriers and thermodynamic and chemical irreversibility.[16] This hysteresis becomes more severe at faster reaction rates (higher currents). Since both potential and capacity determine the total energy stored (Equation 1.1), any hysteresis in the oxidation-reduction profile translates to inefficiency in the operation of the battery.

Two intercalation cathode materials will be considered in this work: $LiMn_2O_4$ and $LiMO_2$ (M = transition metal). $LiMn_2O_4$ is a common cathode material for commercial cells, especially for electric vehicles, valued for its abundance and relatively low toxicity.[14,17,18] $LiMO_2$ is valued for its high gravimetric capacity, due to the 1:1 Li – TM ratio. The electrochemical behavior of $LiMO_2$ is determined by the metal composition. For example, addition of Mn^{4+} and/or Al^{3+} provides thermal stability, Co^{3+} increases rate capability, and $Ni^{2+/3+}$ provides higher usable capacity. The original $LiCoO_2$ cathode[19] has been partially supplanted by newer compositions such as $LiNi_{0.8}Co_{0.15}Al_{0.05}O_2$ and $LiNi_yMn_zCo_{1-y-z}O_2$,[11] which produce more reliable batteries using less toxic and more abundant metals.[14,18,20] Despite their popularity, $LiMO_2$ cathodes exhibit poor cyclability when used over their full capacity range (i.e. full delithiation), requiring artificial limits on the upper cut-off potential.[21–23] These artificial limits sacrifice energy storage capability for cyclability.

The mobility of Li^+ within a material is largely determined by its crystal structure (Figure 5). In both $LiMn_2O_4$ and $LiMO_2$, the TM atoms are octahedrally coordinated by O. In $LiMn_2O_4$, Li is tetrahedrally coordinated with O, producing Li^+ channels extending in all three crystallographic directions (Figure 5a). $LiMn_2O_4$ is similar in structure to the spinel

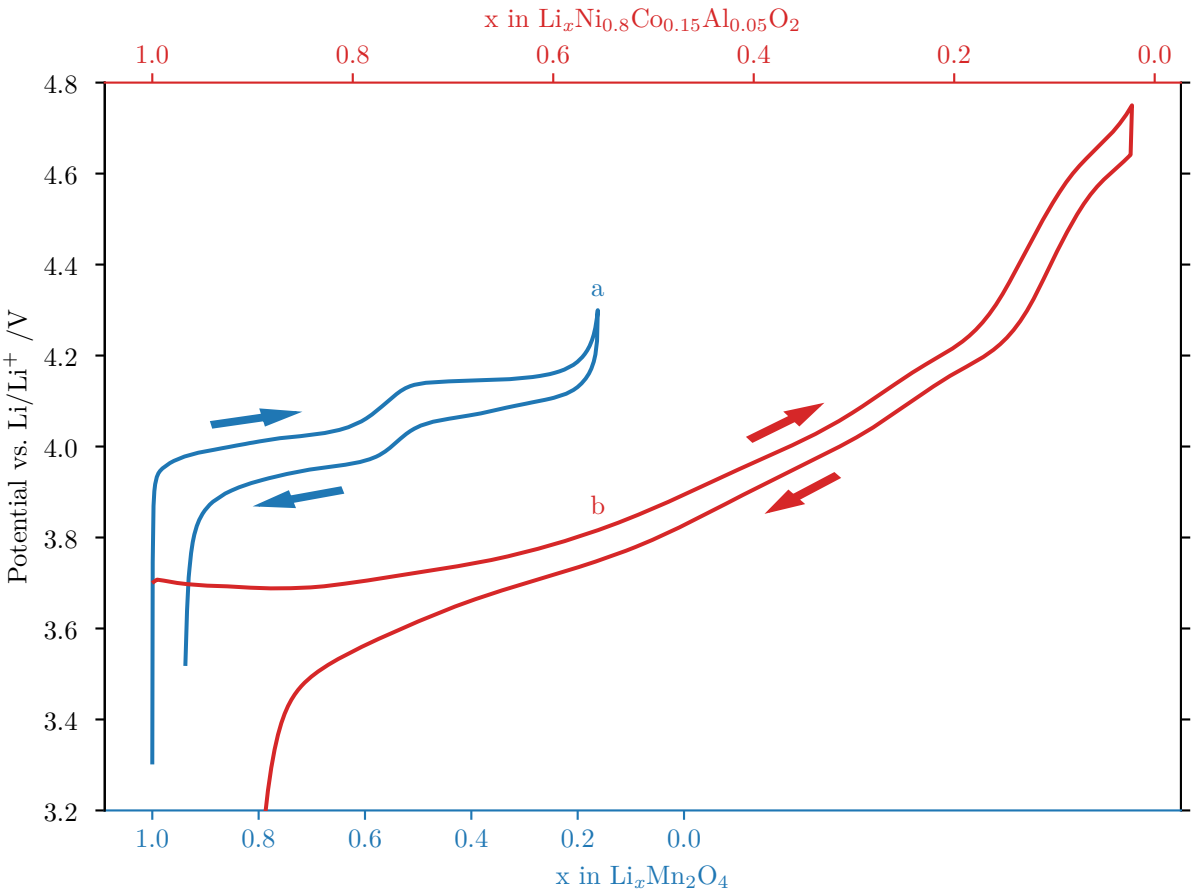

Figure 4: Electrochemical profiles of select lithium-ion battery cathodes. First galvanostatic charge-discharge cycle of (a) $LiMn_2O_4$ and (b) $LiNi_{0.8}Co_{0.15}Al_{0.05}O_2$. Arrows indicate reaction direction. Horizontal axes are normalized to show equivalent gravimetric capacity.

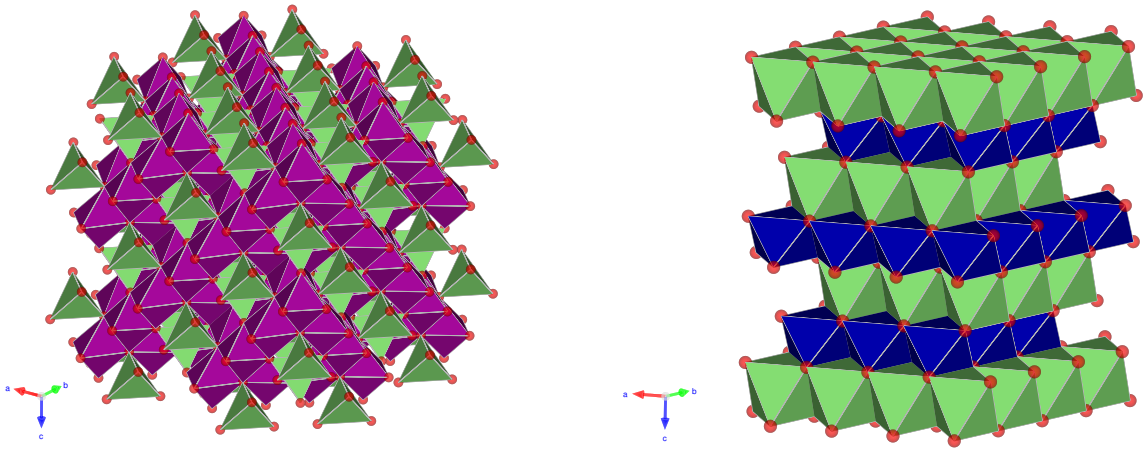

(a) $LiMn_2O_4$ (spinel) (b) $LiCoO_2$ (layered)

Figure 5: Crystal structures of target cathode materials. Structures are shown in fully lithiated state, with polyhedra showing octahedral or tetrahedral coordination of lithium (green), manganese (purple), and cobalt (blue) to oxygen (red). Simulated crystallographic information files obtained from the Materials Project[24] (mp-25015 and mp-24850) and visualized using VESTA.[25]

mineral and is often referred to as a spinel cathode. In contrast, $LiMO_2$ contains octahedrally coordinated Li with further ordering between Li and TM atoms. This ordering results in two-dimensional layers extending in the a and b crystallographic directions (Figure 5b). Li^+ mobility is high within a layer and low between layers. Cation mixing between the TM and Li layers will impede the movement of Li^+ through the Li layer due to reduced percolation.

The phase transformation between the lithiated and delithiated state can be either first order (two-phase) or second order (solid-solution or single-phase). Gibbs' phase rule connects the order of the transformation to the electrochemical potential of the cathode.[26] The number of degrees of freedom of intensive variables (F) for a mixture of C components in P distinct

phases is $F = C - P + 2$. Since the M−O host structure does not change over the course of the reaction, two chemical components are present: $LiMO_2$ and MO_2 (or $LiMn_2O_4$ and Mn_2O_4). As a result, in a cathode undergoing a first-order transformation, $P = 2$ and two degrees of freedom for intensive variables are available. Temperature and pressure are unconstrained in battery experiments and so account for these two degrees of freedom, resulting in a constant potential and flat voltage profile (see $x > 0.5$ in the upper portion of Figure 4a). For a cathode undergoing a second-order transformation, $P = 1$ and three degrees of freedom are available allowing temperature, pressure and potential to vary independently producing a sloped voltage profile (Figure 4b). The features specific to each electrochemical profile in Figure 4 will be addressed in subsequent chapters.

Two thermodynamic forces drive the movement of Li^+ within a battery. A chemical potential (μ) arises from the change in molar Gibbs free energy[23,27] $\mu_i = \frac{\partial G}{\partial n_i}$. Additionally, charged species are subject to an electrostatic force determined by their charge (z_i) and the electric potential (Φ), converted to a molar quantity by Faraday's constant (F). These two phenomena are combined in the electrochemical potential $\overline{\mu}_i = \mu_i + zF\Phi$. At a local level, delithiation and the associated metal reduction will proceed if $\overline{\mu}_{Li^+}$ in the electrode is greater than $\overline{\mu}_{Li^+}$ in the electrolyte ($\Delta\overline{\mu}$).[28] It is important to consider that Φ is the local electric potential, distinct from the electric potential applied to the whole cell. The local electrostatic potential is affected by multiple phenomena, such as the formation of electric double-layers, electric impedance in the solid, and ionic impedance in the electrolyte.

In order to function effectively as a means of energy storage, batteries must maintain a difference in electrochemical potential between the two electrodes, while simultaneously allowing only the chemically reversible (de)lithiation reaction. While their high operating potential makes Li-ion batteries valuable for energy storage, it also creates a strong driving force that makes them susceptible to secondary reaction pathways. At the cathode, these reactions often involve the irreversible oxidation of electrolyte and/or oxygen in the cathode host,[8] and so become more dramatic as the system is operated closer to its theoretical potential limits. Additionally, irreversible structure changes are known to occur at high states of charge.[23] These factors underlie the artificial limits often placed on battery performance, such as the restricted cut-off potential for commercial cells containing $LiMO_2$ cathodes.

Even if delithiation is thermodynamically favored, the net reaction will be slow when $\Delta\overline{\mu}$ is close to zero. In order to produce desirable reaction rates, an additional potential above the equilibrium potential must be applied to the cell, referred to as over-potential, which is a measure of the intrinsic kinetics of the electrochemical reaction. Reversing the reaction requires an over-potential below the equilibrium value. As a consequence, the required over-potentials contribute to the hysteresis in the voltage of the cell between charge and discharge (Figure 4).[16]

Several phenomena govern the kinetics of electrochemical reactions, with the two most notable being charge transfer and mass transport. Charge transfer describes the exchange of charged species directly involved in the redox reaction across the electrode-electrolyte interface. Charge-transfer kinetics can be modeled using the Butler-Volmer model, where the net current (i) increases exponentially with the applied over-potential (η):

$$i = i_0 \left[e^{\frac{-\alpha F \eta}{RT}} - e^{\frac{(1-\alpha) F \eta}{RT}} \right] \tag{1.4}$$

The transfer coefficient (α) accounts for asymmetry in the free energy barrier between the forward and reverse reactions (Equation 1.3).[29] Even with no applied potential ($\eta = 0$), background charge-transfer still occurs symmetrically across the cathode-electrolyte interface, with magnitude expressed as the exchange current (i_0). This value is analogous to, and partially derived from, the pre-exponential factor found in the Arrhenius equation. The exchange current is not necessarily uniform within an electrode, and depends on interface composition and morphology.

Mass transport encompasses both diffusion arising from concentration gradients and migration due to electric field gradients. These gradients occur in the electrolyte as well as the solid electrode matrix. The mass-transport behavior may also be non-uniform within an electrode, affected by properties such as local charge-carrier concentrations.[30] Additionally, local electric potentials may differ from the applied potential due to current-resistance (I–R) drops. Mass transport models will be discussed in more detail in Chapter 4.

A common theme in battery kinetics is that the phenomena underlying these models are localized, yet insight has been traditionally derived at the level of the ensemble average, for instance through the measurement of macroscopic electrochemical responses. Efficiency and reversibility may be lost for many reasons, including persistent irreversible reactions in the electrode bulk, consumption of electrolyte in the chemistry of the battery, excessive rate of charging, and overcharging the cell past its peak capacity or potential window.[5,6,10] Evaluating

the global electrochemistry is insufficient for a full understanding of the system because heterogeneity can affect kinetics and irreversibility. It is critical to consider local factors at multiple length scales to properly understand the underlying redox behavior.

1.3 X-ray Absorbance Spectroscopy

X-ray absorbance spectroscopy (XAS) measures the interaction of photons with the core electrons of a material. Once the incident photon energy exceeds that needed to excite a core electron, a sharp increase in absorptivity is seen, known as an "edge" (Figure 6). The energies associated with edges of different elements are well separated, allowing element-specific spectroscopy.[31] Each edge is named for its corresponding electronic ground state: "K-edge" for $n = 1$, "L-edge" for $n = 2$, etc. For the transition metals in $LiMn_2O_4$ and $LiMO_2$, the K-edge primarily results from dipole-allowed $1\,s \longrightarrow np$ transitions. While these metals' $4\,p$ orbitals are non-bonding, the K-edge transition energies depend of the effective nuclear charge which may be affected by changes in the degree of metal–ligand covalence.[32] Additionally, pre-edge peaks may be observed due to transitions involving valence $3\,d$ orbitals, either through quadrupole transitions or loss of centrosymmetry.[33] The metal's L-edges probe primarily $2\,s \longrightarrow 4\,p$ and $2\,p \longrightarrow 3\,d$ transitions. For the $2\,p \longrightarrow 3\,d$ transition, coupling between the spin angular momentum and orbital angular momentum of the resulting core-hole gives rise to both a singlet (L_2) and triplet (L_3) edge.[34] In addition to the edge jump, the $L_{3,2}$ edge spectra contain strong features from transitions to unoccupied $3\,d$ orbitals, making them sensitive to metal–ligand bonding. Features within L- and K-edge XAS spectra will be discussed in the context of cathode materials in chapters 2 and 3.

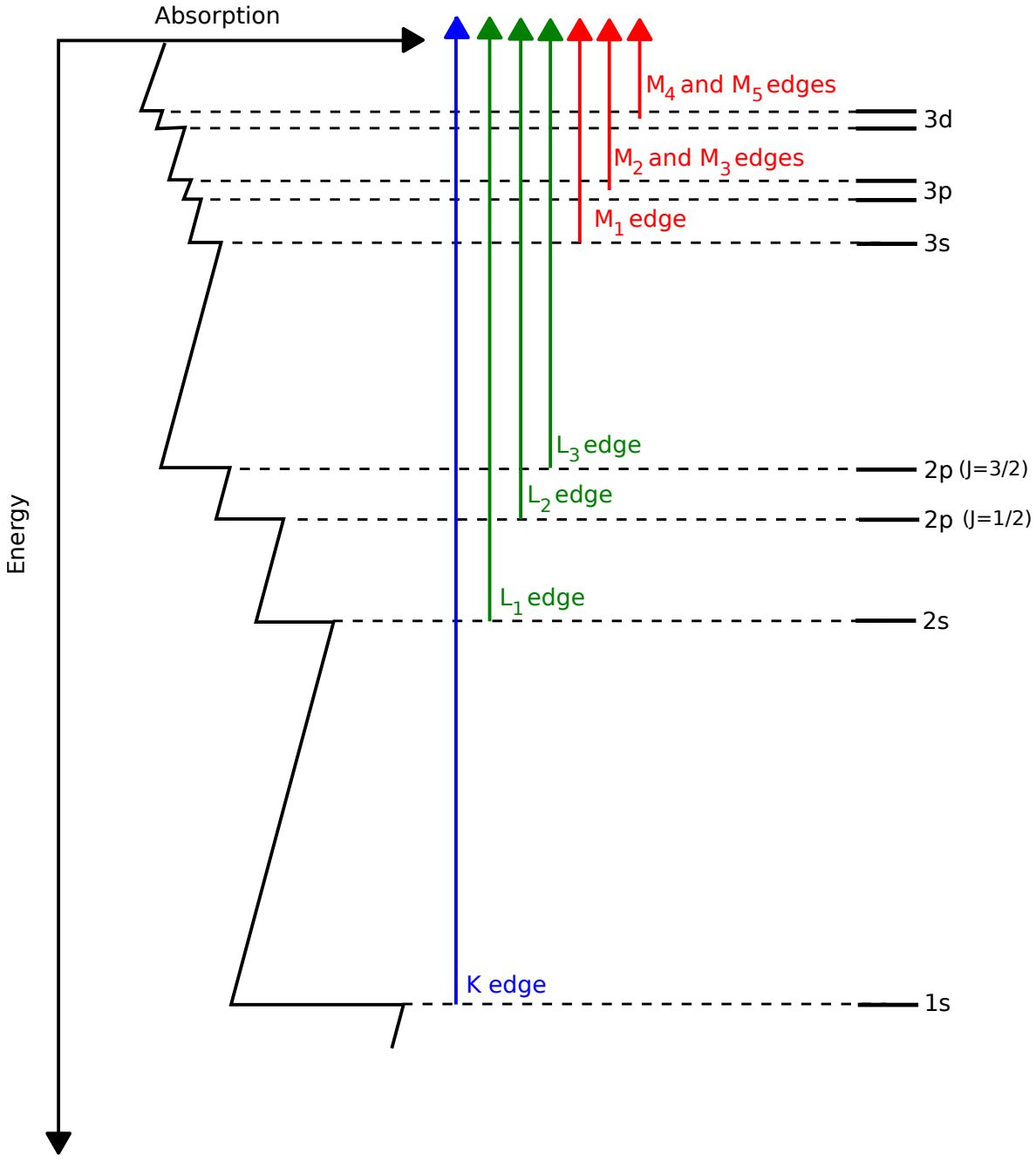

Figure 6: Diagram of electronic transitions contributing to X-ray absorption edges. From wikimedia commons user Atenderholt under Creative Commons BY-SA 3.0 license.[35]

1.4 X-ray Diffraction

X-ray diffraction (XRD) provides a probe of the structure of ordered materials. Photons scatter in all directions when interacting with an isolated atom. In an ordered material, each photon's relative path length depends on the incoming and scattering angles (θ). When the path length between neighboring atoms is equal to an integer multiple of the photon's wavelength ($n\lambda$), constructive interference is observed (Figure 7a). The angle at which this occurs depends on the distance between neighboring atoms (d), as described by Bragg's law

$$n\lambda = 2d\sin\theta \tag{1.5}$$

The atoms separated by distance d form a plane. Multiple planes typically exist within a crystal structure and are referred to by the reciprocal coordinates at which the plane intersects the unit-vectors of the unit-cell. For example, the (440) plane intersects the a and b axes at $\frac{a}{4}$ and $\frac{b}{4}$, and is parallel to the c axes (intersects at ∞). Figure 7b shows the (100), (110), and (111) planes for a cubic unit-cell. These planes are often called reflections since the diffracted photons appear as if they are reflecting from the sample when the diffraction condition is met. XRD experiments measure the diffracted intensity as a function of the combined source and detector angles (2θ). The experimentally measured diffraction angles depend on the wavelength (λ) of the X-ray source (Equation 1.5), complicating comparison between experiments with different X-ray wavelengths. Instead, diffractograms should be reported in relation to the length of the scattering vector, $|\vec{q}|$:

$$|\vec{q}| = \frac{4\pi \sin\theta}{\lambda} \tag{1.6}$$

This measure is preferred because $\vec{q}$ is independent of X-ray wavelength and so conveys a property of the sample rather than a property of the instrumentation.

Figure 7c shows a diffractogram for pristine $LiMn_2O_4$. In addition to instrumental effects, the features of the diffraction pattern arise from the properties of the specimen's crystal structure. The position of each peak depends on the d-spacing of the corresponding reflection plane, which in turn depends on the positions of the atoms within the unit-cell and the size of the unit-cell itself.[36] The intensity of each peak depends on the site occupancy within the unit-cell, the multiplicity of associated reflection planes, and any specimen-specific factors, such as preferred orientation.[36] The width of each peak depends on the lengths of the domains producing coherent diffraction, which can reflect grain size distribution within the specimen. Peak broadening also results from strain within grains producing deviations from the perfect crystalline array, as well as dynamic scattering.[36] As a result, analysis of diffraction experiments yields structural information for ordered materials. Continuous changes in the unit-cell parameters, such as in a solid-solution cathode, result in a gradual movement of peaks to new scattering lengths. The co-existence of multiple ordered phases, such as in a two-phase cathode, results in two distinct sets of diffraction peaks at different scattering lengths, with the ratio of peak intensities reflecting the ratio of phases present in the specimen. These types of crystallographic changes are directly related to the transformation of the electrode material during charge and

discharge of a battery, and provide a means to track the underlying redox chemistry. Local structural changes of battery cathodes will be discussed extensively in chapter 4.

1.5 Imaging and Mapping

Before exploring in detail the different techniques of interest, it is important to define a framework which guides the design of any imaging experiment. This framework is based on the fact that the objective of any chemical imaging experiment is to achieve the maximum resolution along three parameters: space, chemistry and time (as illustrated in Figure 8). Because advances in spatial resolution are desirable in order to achieve the ultimate objective of visualizing atomic structures, this parameter tends to be the focus of the attention of researchers developing these techniques. However, as will become apparent throughout this thesis, the deepest level of insight into the electrochemical reactions that determine battery function requires a thorough detection of different chemical states that may often present similar signals, all while operating under an electrochemical stimulus. The latter necessarily implies the importance of temporal resolution so as to acquire multiple data points along the reaction pathway, which may be as fast as seconds. Advances are still needed that push the three parameters forward at the same time. Instead, the current situation forces sacrifices in either of these scales of resolution.

X-ray generation is possible by two different means: laboratory sources and synchrotron facilities. The general concept of the lab source is based on tubes under vacuum, containing a cathode that is biased so as to generate and accelerate electrons. These electrons collide with the metallic anode, generating X-rays over a narrow range of wavelengths. The specific

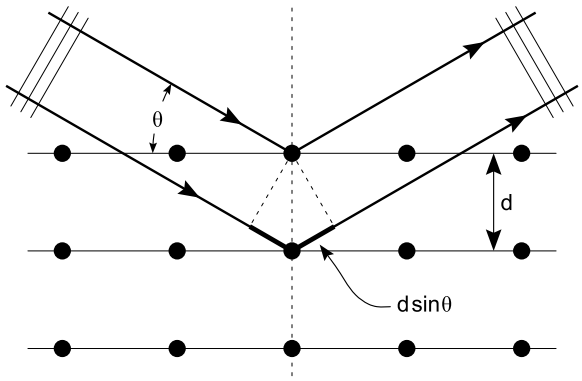

(a) Diagram of crystal diffraction mechanism showing photon path lengths differing by $2d\sin\theta$. From wikimedia commons user Hydrargyrum under Creative Commons BY-SA 3.0 license.[37]

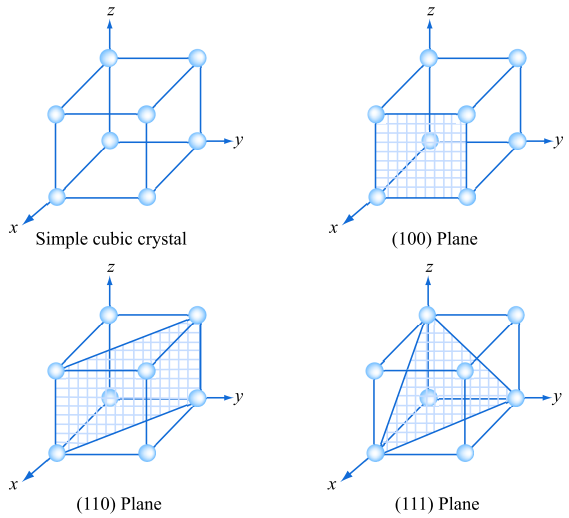

(b) Example crystallographic planes in a cubic unit-cell. From MIT OpenCourseware by Carol Livermore under Creative Commons BY-NC-SA 4.0 license.[38]

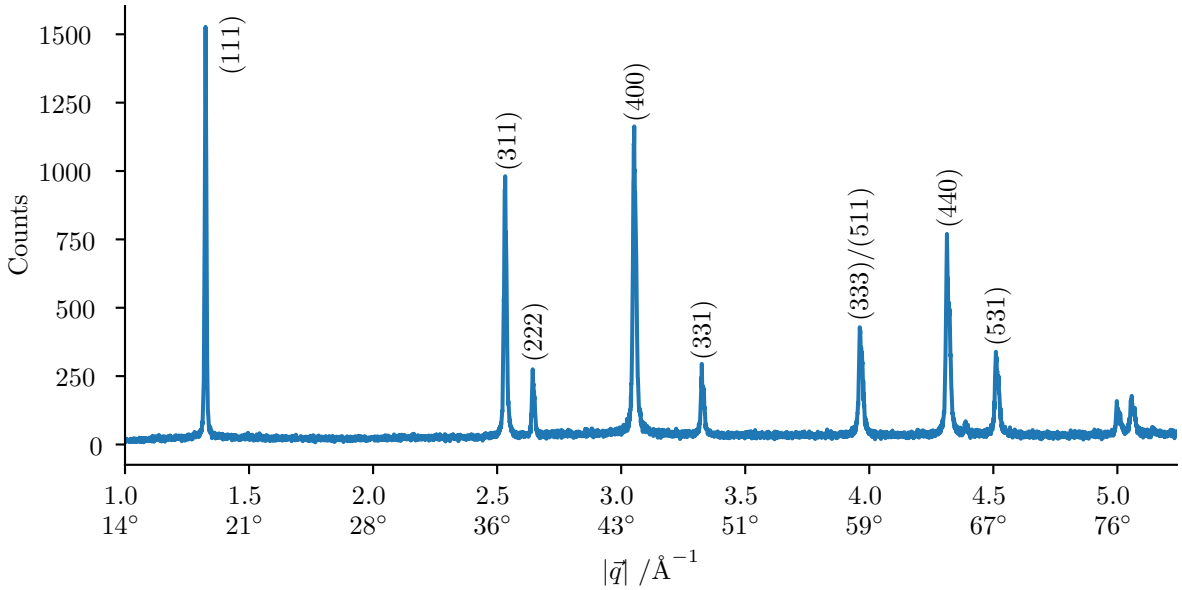

(c) Diffractogram of pristine $LiMn_2O_4$ electrode and associated (hkl) reflections. 2θ Bragg angles resulting from Cu K_α radiation are also shown for convenience.

Figure 7: Overview of XRD for structure analysis.

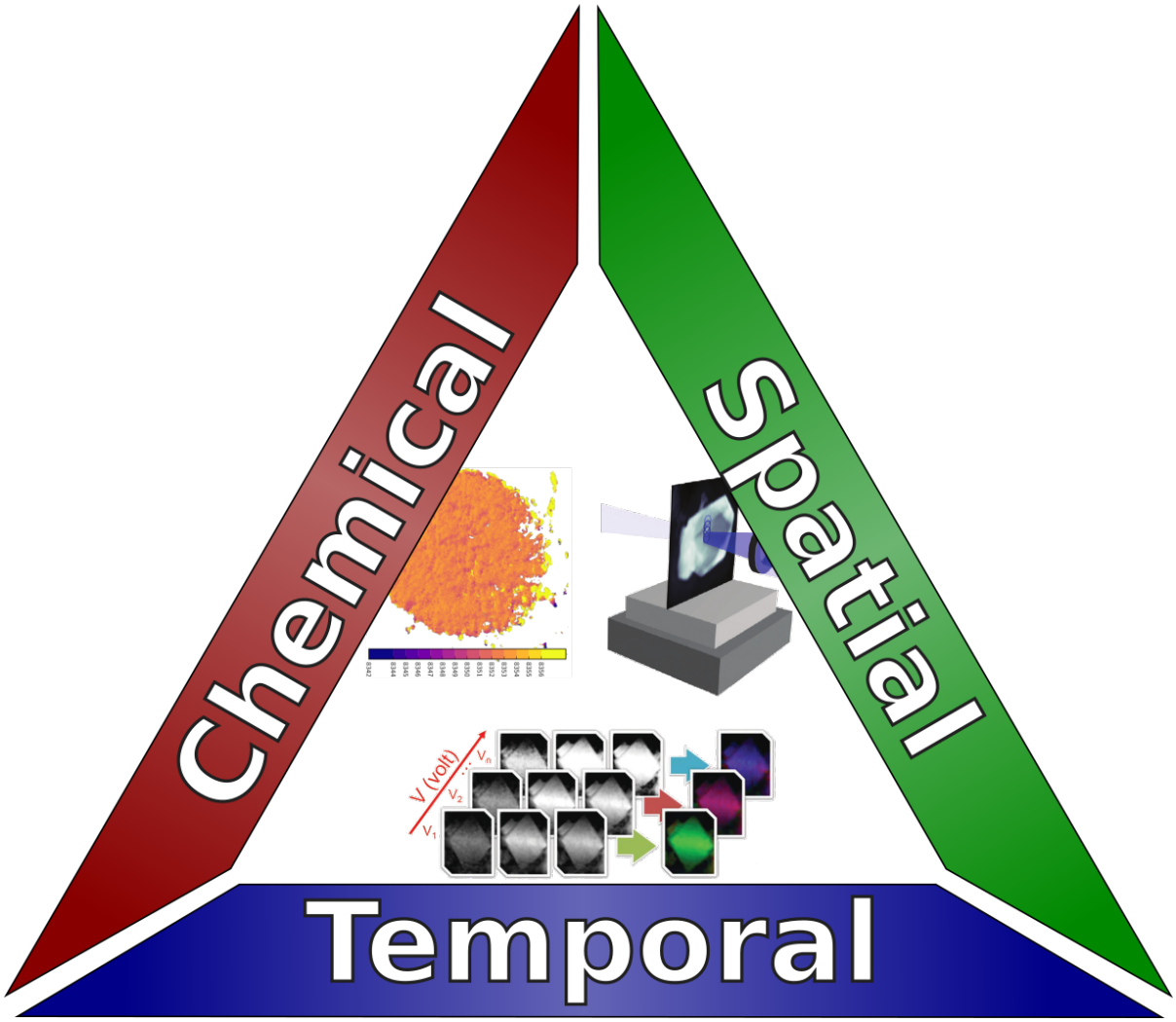

Figure 8: Resolution triangle, showing the trade-off between chemical, spatial and time resolution. Reprinted in part with permission from Yu et al. Nonequilibrium Pathways during Electrochemical Phase Transformations in Single Crystals Revealed by Dynamic Chemical Imaging at Nanoscale Resolution. *Advanced Energy Materials* **2015**, *5*. Copyright 2014 John Wiley and Sons. Reprinted in part from reference[39] (Appendix A).

wavelengths of the resultant X-rays are dependent on the metal used for the anode. Common laboratory X-ray sources include the sealed X-ray tube and rotating anode generator, which differ on the level of vacuum, seal and the arrangement of the metallic anode.[40]

Synchrotron radiation is also generated from accelerating charged particles, but provides higher intensity and better coherence than is currently possible with laboratory sources. Unlike laboratory sources, which are broadly available, synchrotrons require very large areal footprints and, thus, are part of central facilities that are open to users worldwide through a competitive proposal system. The particles, typically electrons, are first accelerated to relativistic speeds, at which point they enter the storage ring of the synchrotron. Beamlines are built tangential to the storage ring so as to utilize X-ray radiation generated when the particles are subjected to centripetal acceleration, either through bending magnets or insertion devices, such as wigglers and undulators. Bending magnets serve two purposes. First, they are placed in such a way that the charged particles in the storage ring are redirected to maintain a proper pathway. Second, each redirection generates X-rays, which are then used in experimental stations. Insertion devices are specialized for generating X-rays and differ from bending magnets in that they are straight sections of the ring that have alternating magnetic fields. Charged particles oscillate through the device, with each oscillation essentially equivalent to a single bending magnet. Therefore, the generated photons can reach higher energies than those generated by bending magnets.[41]

An important distinction between laboratory X-ray sources and synchrotron sources is the nature of the X-rays produced. Synchrotron light sources can generate X-rays at much higher

intensity than laboratory sources. Another major difference between laboratory sources and synchrotron sources is that the optics within a synchrotron create a tunable polychromatic X-ray beam, which can subsequently be set to a narrow energy range through the use of monochromators upstream from the end station. In contrast, laboratory sources only produce a limited range of X-ray energies, which is non-trivial to tune. While some techniques fully utilize the white beam,[42] it is more common to select a single desired wavelength and change it during the experiment. Different energy regimes are defined in the X-ray community. Typically, X-rays with energies below ∼2000 eV are termed "soft", whereas beamlines operating in the "hard" X-ray regime achieve values above ∼4000 eV. The intermediate regime between "soft" and "hard" is often termed "tender". The high intensity, brightness and tunability render synchrotrons as the preferred light sources for chemical imaging.

There are two general modes of X-ray microscopy: full-field (FF) and scanning (as illustrated in Figure 9). The operation of FF transmission X-ray microscopy (TXM) is similar to a conventional visible light microscope. In FF TXM, the X-ray beam is first focused down to a few microns. This microbeam illuminates the sample, generating a large field of view. The resulting photons are magnified by a second set of optics before reaching the detector. In this mode, the limit in spatial resolution is set by the detector pixel size and any aberrations in the optics. This method results in large images with fine resolution in a single shot. In contrast, a scanning microscope is based on focusing the beam prior to illuminating the sample. In order to collect frames of view that are larger than the illuminated spot, the beam is subsequently rastered over the region of interest in the sample. In this case, the spatial resolution is de-

termined by the combination of beam and scanning step size. Given the different methods of operation, it can easily be concluded that full-field imaging offers higher image throughput than scanning imaging at the highest possible setting. On the other hand, scanning techniques allow for higher versatility in contrast mechanisms than in full field mode, especially when combinations are desired.

X-ray microscopy utilizes a multitude of contrast mechanisms. Absorption contrast relies on the intensity of the X-rays that penetrate through the material, the same phenomenon underlying XAS. In spectromicroscopy, whether full-field or scanning, the same field-of-view is imaged repeatedly while the energy of the incident beam is changed over an absorption edge of the element(s) of interest. The resulting frame-stack provides a full absorbance and/or phase spectrum at each pixel. These spectra are then processed into a scientifically meaningful quantity to generate chemical maps of the field-of-view (Figure 10). In order for pixel-wise spectroscopic conclusions to be valid, it is critical that the images be properly aligned with one another, which is rarely the case for raw data-sets. The next step in the analysis involves normalization of the spectra relative to the background optical depth. As X-ray energy increases, the transmission of all materials increases as well. Correcting for this effect improves the reliability of analysis methods that involve decomposing the spectra into components of known materials.[43]

XRD microscopy provides spatially resolved structural information. Of particular interest in the context of this discussion is the ability to interpret the unit cell dimensions at a given chemical composition if prior knowledge of the system exists. The data generated in Bragg diffraction microscopy experiments can be treated very similarly to those collected during spec-

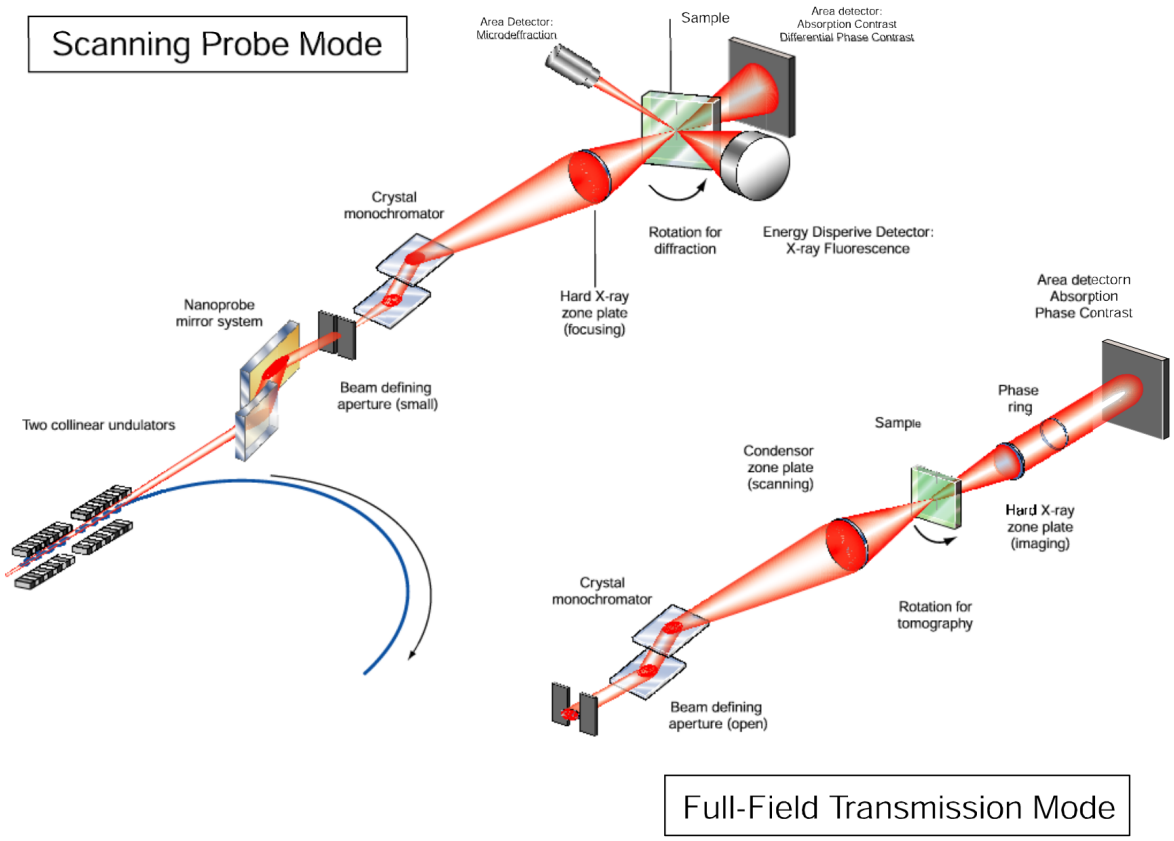

Figure 9: Illustration of experimental configurations for (a) scanning probe and (b) full-field imaging synchrotron hard X-ray microscopy methods. Reprinted with permission from Maser et al. Development of a Hard X-ray Nanoprobe Beamline at the Advanced Photon Source. *Microscopy and Microanalysis* **2005**, *11*, 680-681. Copyright 2005 Cambridge University Press (Appendix A).

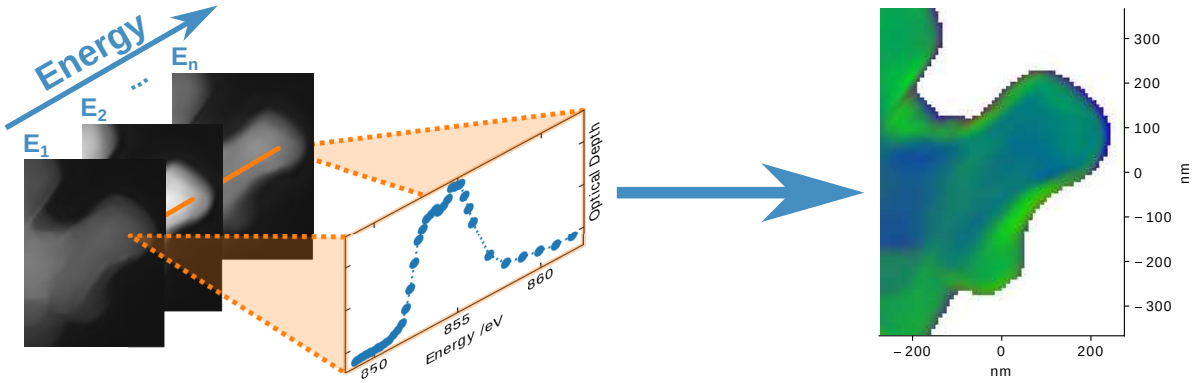

Figure 10: Diagram of map generation via spectromicroscopy. A series of micrographs are collected at energies across an absorption edge. Analysis of the resulting pixel-wise spectra produces a value at each pixel, which is then converted to a color and visualized.

tromicroscopy. Each mapping position is equivalent to a pixel in an X-ray micrograph and a series of frames are collected at different scattering vectors, $|\vec{q}|$. Generally, the spatial dimensions are the slowest-changing in diffraction mapping, whereas they are the fastest (or even simultaneous) in microscopy; this distinction does not change the structure of the data in a significant way. However, it does obviate the need to align each image. Rather than a full absorbance spectrum at each location, these experiments generate a diffractogram at each position. Theoretically, a researcher can analyze the two-dimensional diffraction pattern at each position; often, the 2D patterns are integrated to form the more traditional 1D diffractograms. From here, a refinement can retrieve crystallographic parameters, such as unit-cell dimensions, strain or phase ratios.

Ptychography is a lensless technique which relies on measuring a two-dimensional coherent scattering pattern. Small spots are collected in such a fashion that they spatially overlap on the sample. Ptychography then utilizes an iterative algorithm to reconstruct an image from the scattering patterns.[44,45] As a result, the ultimate spatial resolution is, to a large extent, independent from the size of the beam used to collect the overlapping patterns. Artifacts from the reconstruction process sometimes manifest as high frequency bands alongside sharp edges in the specimen. Since this technique is driven by an interference pattern, the best reconstructions are obtained from strongly scattering materials. As an added bonus, the reconstruction produces both the real and imaginary components of the object image. By comparison to an area with no material, the fully complex refractive index can be calculated. Exploiting the complex-valued nature of this technique is a relatively unexplored area.

Turning a large data-set into a two-dimensional image is a task of increasing difficulty as the number of dimensions increases. For applications with two spatial dimensions, images are generated by data-reduction depending on the contrast mechanism and goals of the experiment. The relationship between values and colors is known as a "colormap" or "lookup table". The choice of colormap can have subtle effects on how the data are interpreted. In general, human vision associates the brightness of a color with the value it represents, regardless of its hue. Therefore, an effective colormap translates high values to high-brightness colors and low values to low-brightness colors. Rainbow colormaps, such as *jet*, do not meet this criterion and should be avoided for representing sequential data.[46,47] Jet contains bands of high and low brightness that are perceived as sharp gradients in the data that do not actually exist. Perceptually

uniform colormaps, such as *viridis* for Matplotlib and *parula* for Matlab, are designed to avoid this problem. Additionally, viridis was tested against color blindness and ensures that data display properly to people in this category.[48]

1.5.1 Ex-Situ Versus Operando

To a large extent, electrochemistry is most interesting when away from equilibrium. As electrochemical devices, batteries are useful during operation, which is inherently under kinetic control. While the kinetic states are determined by the thermodynamics of the system, metastability is more prominent under electrochemical conditions than in other classical chemical environments, such as high temperatures. This prominence also implies that the probability of producing kinetic states that are only weakly metastable is high. In fact, the problem of self-discharge, common in certain batteries, is precisely the product of equilibration of a metastable charged state. As a consequence of the pervasive kinetic control, ex situ measurements, which rely on harvesting samples from a cell at a desired chemical state, introduce uncertainty when the goal is to describe relevant states under working conditions. Nonetheless, if caution is applied, and due to their simplicity, these measurements can still provide valuable guidance,[49] mainly because they do not critically suffer from constraints in measurement time and, thus, can result in the highest data quality. Ultimately, operando measurements of battery reactions are preferred because of the growing body of evidence showing that there are many cases where the state within an operating battery is different from what is observed once the cell is disassembled,[50,51] especially when high rates are employed. For this reason, researchers developing novel methods of imaging should have motivation to enter a path that results in means to

operando analysis. At this point, given certain confusion in the field, it is worth clarifying that we consider operando measurements to be a small subset of in situ science. The condition *sine qua non* for an operando experiment is that the cell is not stopped to collect data unless the goal is specifically to measure equilibration phenomena.

While operando measurements are preferred and should be pursued, they can present several challenges of varying degrees of difficulty. The setup must allow photons to pass through both the sample and apparatus with very little disturbance to the signal from the apparatus itself. First and foremost, X-ray absorbing materials have to be minimized in order to ensure sufficient signal reaches the detector. Ideally, supporting materials containing heavier elements should be removed, or made sufficiently thin so as to minimize their effects. Another challenge is avoiding X-ray induced damage to supporting materials, such as the polymer binder often used in the construction of cathodes. Maintaining adequate stack pressure may also be important, depending on the nature of the experiment.[52] Additionally, the possibility of deleterious effects of X-ray exposure on the behavior of cathode materials is not completely understood. One possibility is to use very high energy X-rays, which can penetrate the casing material[53] and are less damaging. This strategy is valid for some diffraction experiments, but cannot be applied to spectroscopic imaging since specific energies at which the X-ray beam is absorbed are required.

In situations where high-energy X-rays are not possible, a transparent window is necessary. Beryllium is a typical choice, but its use introduces stringent handling requirements due to its high toxicity, especially in the dispersible form that is generated, for instance, during machining. It also oxidizes relatively easily, making it unsuitable for high-voltage battery applications.

Silicon nitride is an appealing option since it can be purchased commercially in prefabricated windows down to tens of nanometers in thickness. At these thicknesses, it also does not have any noticeable morphological features, making it suitable for X-ray microscopy techniques. However, they are very fragile due to their thickness. Polyimide (Kapton) film has found widespread use in operando diffraction experiments, despite the fact that it also introduces an amorphous contribution to diffraction patterns. It has relatively high transmissivity, is easy to fabricate and is chemically inert. Unfortunately, it cannot ensure a complete seal and, like many other plastics, it often contains filler particles which are heavy enough to become visible in a microscopy experiment, interfering with observations and, thus, rendering it unsuitable. Amorphous carbon can also be used. A large advantage here is its electrical conductivity, which eliminates issues of electrochemical inactivity of the material behind the window. Since it is made entirely of carbon, it also interacts only very weakly with X-rays, so it induces minimal signal attenuation. However, it is difficult to fabricate, and can react under certain conditions, such as at very high potentials or against lithium metal. The AMPIX electrochemical cell, developed by Argonne National Laboratory, is an example of a cell with amorphous carbon windows that fits the requirements of an operando X-ray experiment. The cell design ensures good stack pressure as well as electrical conductivity, closely mirroring coin cell conditions.[52,54] Even more sophisticated cells are needed when using low energy, soft X-rays, where the sample volume must be small to avoid excessive absorption of the signal by the sample. In this case, designs that rely on microfabrication have recently been demonstrated.[51]

Operando measurements create the most severe challenges to an imaging experiment when considering the three scales of resolution above, namely spatial, chemical and temporal. Many battery reactions span several hours, but the need to build a reaction pathway means that it is desirable to collect at least 5 data points during the reaction. This goal imposes restrictions on the time available to complete an image containing the desired chemical information, at the desired level of spatial resolution. Unfortunately, all modes of chemical contrast require collecting multiple frames for the same reaction state to reconstruct a map of the species present in the field view. Using X-ray absorption near-edge structure (XANES) microscopy as an example, chemical resolution is achieved by collecting frames at a large number of energies, with the limit being set by the precision of the upstream optics. In the particular case of scanning techniques, spatial resolution requires the use of the smallest possible step size to raster the field of view, meaning that a similar trade-off emerges in that the acquisition time is directly affected by this parameter. Additionally, increasing the collection time for each frame will improve the signal-to-noise ratio and improve the accuracy of the data, again at the expense of longer acquisition times for a full frame-set. In practice, the most common choice is to minimize the number of points to obtain some level of chemical resolution in the individual frame-set, whether scanning energy (spectroscopy) or a beam-sample-detector angle (diffraction). This approach strongly relies on prior knowledge of the chemical species involved during the reaction, so that energies or angles are chosen at which signals between these species differ the most. Such prior knowledge is typically acquired through XAS or XRD measurements of the ensemble average, as opposed to spatially resolved regions. In the case

of the spectroscopy of transition metal species, a change of one unit in the formal oxidation state translates into a displacement of the signals of a few electron-volts, which renders the method viable. Challenges arise when the changes between species are small, for instance, when compounds exist at redox states intermediate between end members. The strategy also inherently lends itself to misinterpretation if previously unknown or unexpected states form in the measurement, especially if they are related to the known, expected species. The local character of an imaging measurement means that the limit of detection of minority species increases with respect to a data set gathered from the ensemble average, especially if they accumulated in specific regions of the image. All in all, it is important to be aware of the compromises made to avoid over-analyzing data. Since the field of X-ray imaging is vibrant and constantly pushing the boundaries in resolution, it is likely that these limitations will be alleviated with time, creating exciting opportunities for rich insight into battery operating conditions.

1.6 Motivation and Structure of this Thesis

Measuring chemical properties with spatial resolution provides a view of the underlying mechanisms that is often distinct from, though related to, the ensemble-average properties.[1,55–57] Electrodes generally adopt a hierarchical structure wherein single crystallites of a redox-active material combine to form agglomerate particles, which are then combined with conductive additives and flexible polymeric binders into a thick (ideally, above 100 µm), porous electrode architecture (Figure 1) where different distributions of components and particle sizes are likely to exist throughout the electrode, demonstrated in Figure 11. In addition, the thickness of the

electrode introduces asymmetries in the transport of ions (from the electrolyte) and electrons (from the current collector, Figure 11), which are both required in order for the redox reaction to proceed. As a result, a hierarchy of heterogeneities develops during the phase transformation, both within the electrode[58,59] and within individual particles. These heterogeneities are kinetic in origin, beyond the changes that would be inherent to the phase transformation within a particle, and, thus, prone to vary with the currents to which the battery is subjected. Probing all of these length-scales provides clues for helping meet the high demands placed on current and future technology.

This thesis describes three novel avenues of research that uncover and examine heterogeneities at the levels of primary particles, secondary particles, and a complete electrode (Figure 12). Chapter 2 uses ptychographic microscopy to overcome the diffraction limit of conventional X-ray optics. Spectropytchography was combined with advanced statistical analyses to probe the distributions of Ni oxidation states within $LiNi_{0.8}Co_{0.15}Al_{0.05}O_2$ primary particles at several states of charge. The resulting maps revealed surface and sub-surface irreversibility at the primary particle level, especially at high states of charge, limiting the efficient utilization of the material. Chapter 3 uses operando FF TXM to track Ni oxidation in $LiNi_yMn_zCo_{1-y-z}O_2$ and $LiNi_{0.8}Co_{0.15}Al_{0.05}O_2$ secondary particles during charge and discharge cycles. Individual secondary particles show a sharp transition in overall oxidation, which is distinct from the electrochemical profile of the cell and Ni oxidation by ensemble XAS. This discrepancy reveals a high degree of thermodynamic irreversibility, and highlights the importance of considering local electrochemical potentials when designing battery architectures. Chapter 4 presents diffraction

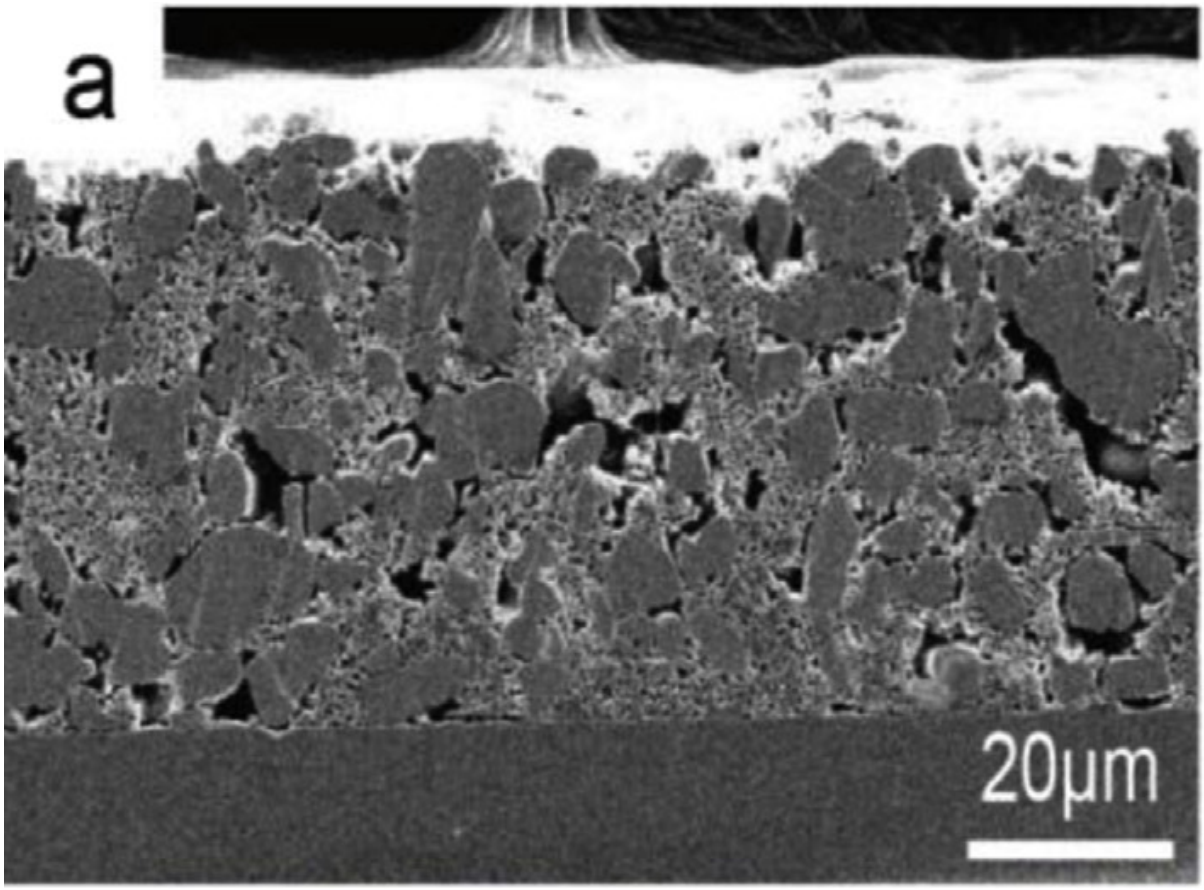

Figure 11: Scanning electron microscope image of the cross-section of a typical battery electrode. Multiple individual particles can be seen that participate in the electrochemical reaction. Reprinted from Journal of *Power Sources*, *252*, J. Choi et al., Improved high-temperature performance of lithium-ion batteries through use of a thermally stable co-polyimide-based cathode binder, 138-143, **2014**, with permission from Elsevier (Appendix A).

maps of entire $LiMn_2O_4$ cathodes. Electrode utilization is shown to be rate-dependent, with gradients in the extent of delithiation present into the thickness of the cathode due to limitations in the rate of lithium diffusion. The use of asymmetrically sized anodes produced further lateral heterogeneity across the electrode, allowing for an evaluation of diffusion versus migration kinetics revealing that lateral diffusion across the electrode is considerably slower than other modes of mass transport.

This multi-length-scale approach allows different sources of battery inefficiency to be untangled. Only by thoroughly understanding these inefficiencies at the appropriate length-scale will solutions be possible that allow batteries to approach their theoretical performance limits and satisfy future energy storage needs.

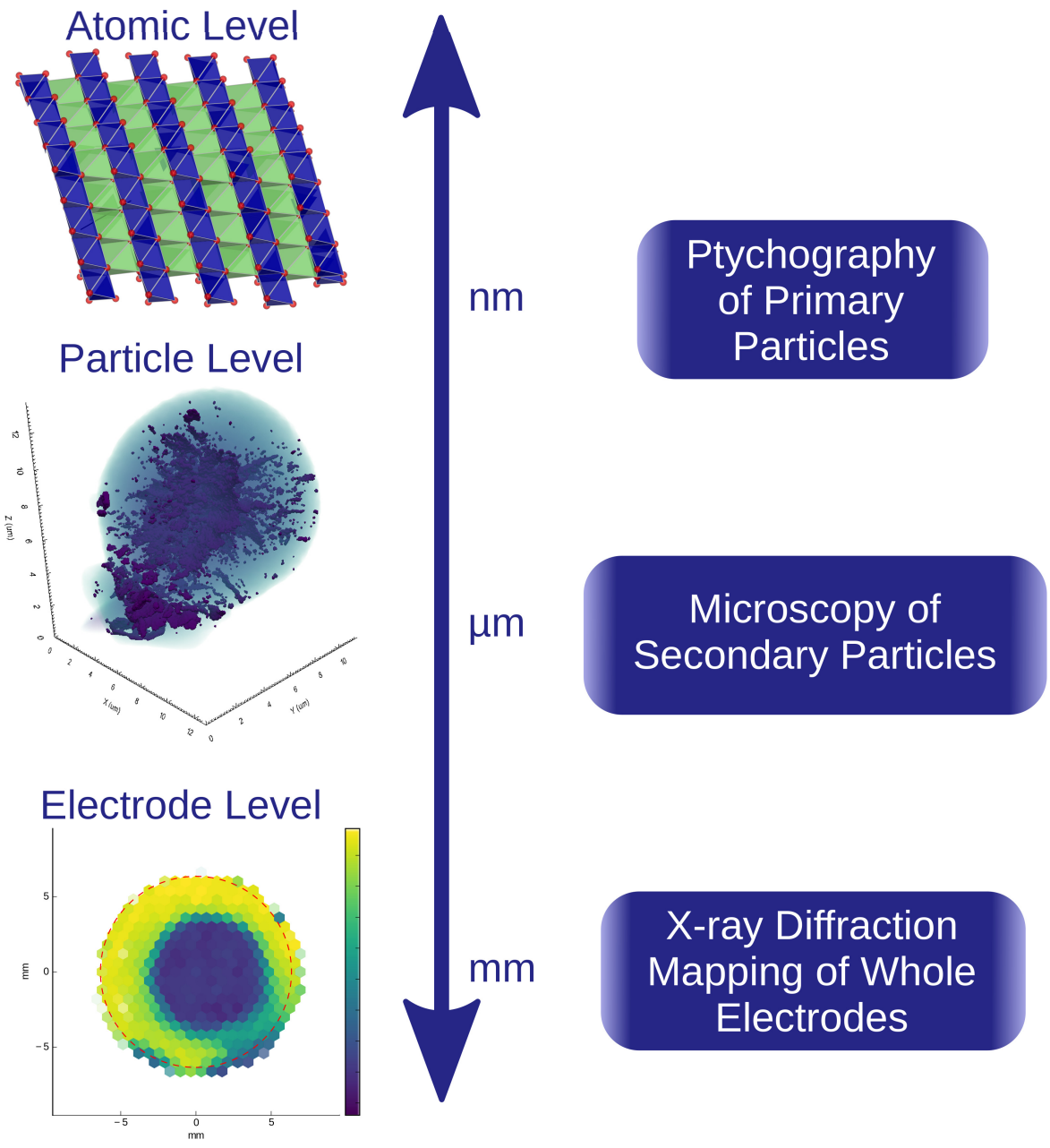

Figure 12: Overview of imaging projects and associated length-scales. Ptychography was used to image ≈100 nm primary particles, FF TXM was used to image ≈10 µm secondary particles, and micro-focused X-ray diffraction (µ-XRD) was used to image 12.7 mm cathodes.

CHAPTER 2

NANOSCALE CHEMICAL IMAGING OF PRIMARY PARTICLES OF $LiNi_{0.8}Co_{0.15}Al_{0.05}O_2$

2.1 Introduction

Theoretically, pristine $LiNi_{0.8}Co_{0.15}Al_{0.05}O_2$ operates through the Ni^{III}/Ni^{IV} formal redox couple, with full delithiation producing $Li_{0.05}Ni_{0.8}Co_{0.15}Al_{0.05}O_2$. In practice, the transformation is considerably more complicated. Prior research using XAS has shown that side-reactions produce a layer rich in reduced Ni on the surface of the electrode upon delithiation.[60–64] This behavior is exacerbated at high temperatures[65,66] and fast rates.[67] These layers show degraded carrier transport at the $LiNi_{0.8}Co_{0.15}Al_{0.05}O_2$-electrolyte interface[68] imposing an increased kinetic barrier that requires a higher over-potential for complete delithiation.[60] Since electrolyte stability imposes limits on the potential that can be applied, the result is a loss of capacity. These reactions can also result in O_2 evolution,[65,66,69] which has been implicated in catastrophic cell failure by thermal runaway, posing a serious safety risk.[69] Understanding the physical and chemical processes responsible for these losses will aid in reducing existing performance gaps, with the additional benefit of improved battery safety.

The extent of the heterogeneity resulting from surface reduction during charging has not been fully elucidated at the level of individual particles, especially considering that the exposed crystallographic facet partly determines the morphology of this surface layer.[56] XAS

provides a direct chemical probe of the material, but lacks spatial resolution since it is inherently an average over an ensemble of particles within the specimen. Transmission electron microscopy (TEM) provides high spatial resolution and has uncovered a simultaneous change from the nominal layered structure to a series of spinel and rock-salt structures.[60,65–68,70–73] Further measurements of electron energy-loss spectroscopy (EELS) in a TEM complemented these studies with spectroscopic information on the spatial distributions of reduced Ni species formed during charge in $LiNi_{0.8}Co_{0.15}Al_{0.05}O_2$ and similar layered cathodes.[22,65,70,73–76] However, TEM is limited by sample thickness (below 100 nm), typically locating measurements to a small section at the outside edge of a primary particle. Previous EELS analyses were carried out either on average spectra or microtome slices of particles, or were limited to spatial mapping at the edges of particles where the material is thinnest. EELS experiments are also limited in their energy resolution compared to XAS. None of the approaches described above are optimal for probing the spatial distribution of oxidation states within a single, whole $LiNi_{0.8}Co_{0.15}Al_{0.05}O_2$ particle, or for determining the prevalence of chemical oxidation states throughout the depth of the particle. Key areas that remain to be addressed within the present body of knowledge include: 1) determining which nickel oxidation states exist within a complete primary particle, 2) examining the distribution of irreversibly reduced nickel across the crystallographic facets, and 3) evaluating the penetration of irreversible nickel reduction from the surface to the interior of a particle. These chemical distributions determine the efficiency of the reaction and can translate directly into lost capacity as well as presenting possible kinetic barriers to lithium transport. Synchrotron X-ray microscopy methods provide both chemical and spatial

resolution suitable for bridging the gap between measurements of the ensemble average of an electrode and thin section of an individual particle.[1,77] We applied these tools to measure the Ni L_3-edge of $LiNi_{0.8}Co_{0.15}Al_{0.05}O_2$ particles in the pristine state and after charging to 4.0 V and 4.75 V. We confirmed the presence of reduced Ni associated with the surface reconstruction discussed above. Furthermore, we revealed regions of incomplete oxidation below the surface layers, which lowers both first-cycle capacity and cyclability.

2.2 Materials and Methods

The $LiNi_{0.8}Co_{0.15}Al_{0.05}O_2$ platelet particles analyzed by total electron yield (TEY)/total fluorescence yield (TFY) spectroscopy, ptychography, and synchrotron X-ray scanning tunneling microscopy (SX-STM) were synthesized via a hydrothermal method,[78] followed by calcination. $Ni(NO_3)_2 \cdot 6\,H_2O$, $Co(NO_3)_2 \cdot 6\,H_2O$, and $Al(NO_3)_3 \cdot 9\,H_2O$ were combined in a molar ratio equal to 80:15:5 in 70 mL of H_2O. NaOH was added to the mixture to achieve a 2:1 OH^-/TM ratio. The mixture was treated hydrothermally for 12 h at 160 °C. The product was washed with water, dried completely, and annealed for 4 h at 400 °C to remove the double layered hydroxide structure.[79] The resulting oxide was mixed with $LiOH \cdot H_2O$ such that $x = 1$ in $Li_xNi_{0.8}Co_{0.15}Al_{0.05}O_2$ and calcined at 800 °C for 1 h followed by 700 °C for 12 h. The material was structurally characterized by a Bruker D8 Advance X-ray Diffractometer using Cu–K_α radiation (Figure 52) and matched to prior literature for $LiNi_{0.8}Co_{0.15}Al_{0.05}O_2$.[80] TEM data were collected using a JEOL JEM-3010 transmission electron microscope with the accelerating voltage set to 300 kV.

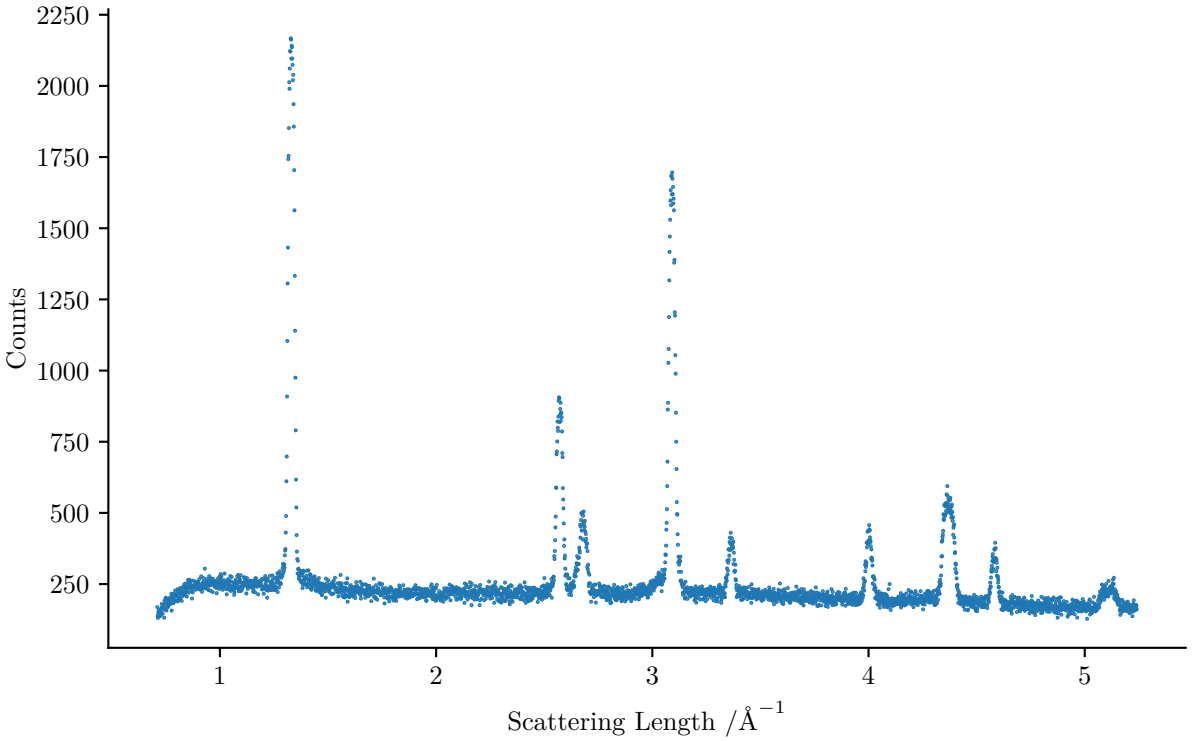

Figure 13: X-ray diffraction of pristine morphologically control $LiNi_{0.8}Co_{0.15}Al_{0.05}O_2$ primary particles.

For electrochemical preparation, dried $LiNi_{0.8}Co_{0.15}Al_{0.05}O_2$ powder was mixed in an argon-filled glove box with 2.5 wt% carbon black (SuperP, MMM) using a mortar and pestle. Powder cells (2032 Hohsen) were assembled using Li metal (FMC) negative electrodes with a combination of glass fiber (Whatman), polyolefin (Celgard) and PVDF-HFP depending on the test temperature, with 1 M $LiPF_6$ ethylene carbonate: dimethyl carbonate (EC:DMC) (1:1 volume ratio) electrolyte (BASF).

Ensemble soft XAS measurements were performed in TEY and TFY modes at beamline 6.3.1.2 ISAAC of the Advanced Light Source (ALS) at the Lawrence Berkeley National Laboratory (LBNL). For the O K-edge spectra, photon energies were normalized to a TiO_2 reference and scaled to the background. For the Co L_3-edge and Ni L_3-edge, photon energies were normalized to a Ni-metal reference. The Co L_3-edge and Ni L_3-edge spectra were scaled to the peaks at ≈780 eV and ≈855 eV respectively. Disassembled $LiNi_{0.8}Co_{0.15}Al_{0.05}O_2$ powder electrodes were mounted on conductive tape and transferred using vacuum suitcase set-ups between the glovebox and vacuum chamber to avoid air exposure. The $LiNi_{0.8}Co_{0.15}Al_{0.05}O_2$ powder electrodes were not washed prior to measurements to retain cathode-electrolyte interface species.

Ptychography was performed using the *Nanosurveyor* ptychographic microscope[45] on beamline 5.3.2.1 at the Advanced Light Source. After electrochemical treatment, samples were dispersed in dimethyl carbonate and drop-cast onto copper TEM grids coated with Formvar and lacey carbon support membrane. Specimens were prepared in an argon glovebox and transported under argon atmosphere. Scanning electron micrographs (eg. Figure 20) of candidate particles were collected using a JEOL 6320F field emission scanning electron microscope at

working distances of 9.0 mm to 12.0 mm and accelerating voltages of 3.0 kV to 3.6 kV. Specimen mounting prior to X-ray measurement was done in a nitrogen glovebox. The specimen stage was then transferred to the beamline vacuum chamber, limiting total air exposure to less than five minutes. Coherent X-rays were focused using a Fresnel zone plate with 60 nm outer zone width. The specimen was scanned in 50 nm steps. Scattering patterns were collected using a Princeton Instruments MTE-1300B in-vacuum CCD camera with a 300 ms dwell time per step. Reconstruction was done using the *SHARP* system.[44] The minimal spatial resolution was estimated to be below 10 nm (2 px) by inspection of line profiles over the clean edges of a TEM grid. Ptychography data analysis was done using the *xanespy* python library.[81] Image registration was performed via *scikit-image*[82] on the imaginary optical depth component using template matching followed by multiple passes of phase correlation. Peak positions were extracted by fitting a linear combination of functions to each real-value spectrum $OD_{obs}(E)$ using the scipy `leastsq` wrapper around MINPACK's *lmdif* routine. The function used for fitting was:

$$OD_{obs}(E) = G_1(E|h_1, c_1, w_1) + G_2(E|h_2, c_2, w_2) + G_3(E|h_3, c_3, w_3) + S(E|h_s, c_s, w_s) + b \quad (2.1)$$

where G_i is one of three Gaussian functions for each peak $G(E|h, c, w) = he^{\frac{-(E-c)^2}{2w^2}}$. S models the small jump in overall optical depth associated with the edge itself: $S(E|h, c, w) = h \operatorname{atan}\left(\frac{(E-c)w)}{\pi} + \frac{1}{2}\right)$.

For Bayesian source separation, the number of latent sources was determined via Principle Component Analysis (PCA) of a matrix of the data.[83] After the number of latent sources was determined, the sources themselves were estimated using a Bayesian-inference-based non-negative matrix factorization (NNMF) algorithm. The NNMF algorithm constrains the latent sources to be positive while simultaneously constraining the fractional abundances to be positive and sum to one as required by the physics of spectroscopy.[84] The algorithm uses a Gibbs sampler to simulate posterior distributions for the latent sources and the fractional abundances using prior distributions to enforce the aforementioned constraints. The constraints on the fractional abundances imply that the latent sources form a simplex around the data in an $N-1$ dimensional space where N is the number of latent sources. In order to keep the estimates of the latent sources from straying too far from the observations, additional constraints were added to the prior corresponding to the latent sources in order to minimize the volume of this simplex.[84] Separation of the sample pixels from background pixels was performed by calculating pixel-wise coefficients of determination (R^2), and selecting pixels with a coefficient greater than 0.92, capturing all particles and including minimal background pixels. Distance segmentation was performed using a Euclidean distance transform on the sample pixels, then segmenting pixels to the nearest 8 nm (1 pixel).

Evaluation of commercial $LiNi_{0.8}Co_{0.15}Al_{0.05}O_2$ was carried out by conventional scanning transmission X-ray microscopy (STXM) combined with XAS at the Advanced Light Source (ALS) at Lawrence Berkeley National Laboratory.[85] 80 wt% commercial $LiNi_{0.8}Co_{0.15}Al_{0.05}O_2$ powder (NAT-1050, Toda America, Inc., stored under ambient atmosphere) was mixed with

conductive carbon (10 wt%) and polyvinylidene fluoride binder (10 wt% as 6 wt% solution in N-methyl-2-pyrrolidone) and cast onto aluminum foil. 12.7 mm diameter cathodes were manually punched and assembled into 2032 coin-cells with metallic Li anodes under argon atmosphere. Coin-cells were galvanostatically charged, then disassembled under argon atmosphere. Recovered cathode powders were suspended in anhydrous ethanol by sonication for 20 min and drop-cast onto a lacey carbon grid (Ted Pella Inc.). Monochromatic X-rays were generated from a bending magnet beamline (Beamline 5.3.2.2) with resolving power $\frac{E}{\Delta E} \leq 5000$. X-rays were focused by a 25 nm outer zone width focusing optic and raster scanned on the sample with a square scan grid of 30 nm steps across the O K-edge (≈520 eV to ≈560 eV) and Ni $L_{3,2}$-edges (≈845 eV to ≈880 eV) with the finest energy step of 0.1 eV near the absorption resonance. Transmitted photons were recorded by a phosphor-photomultiplier tube (PMT) in pulse counting mode with 2 ms dwell time. To eliminate spectral distortions owing to the time gap between the incident and transmitted beams' intensities, the incident beam intensity was simultaneously measured through an open area of the sample.

The STXM image spectra were first roughly aligned to each preceding image by a phase correlation algorithm. The mean of the roughly-aligned image spectra was used as a reference image for second alignments. The second alignment was performed with intensity-based automatic image registration with non-reflective similarity transformations. The repeated procedures with updated reference image from the previous registration were performed until the aligned images were self-consistent. After image registration, the pixels with averaged optical depth bigger than 80 % of the highest averaged optical depth (i.e. the thickest part of the par-

ticle) were selected as the particle region. The particle regions were converted to binary images to compute the Euclidean distance transform. For each pixel in converted binary images, the distance transform assigns a number that is the distance between that pixel and the nearest nonzero pixel (i.e. surface of the particle). After segmenting pixels with respect to the distance map, averaged spectra of each pixel group were collected across O K-edge, Co L-edge, and Ni L-edge.

SX-STM measurements were carried out at beamline 4-ID-C of the Advanced Photon Source at Argonne National Laboratory.[86] This beamline provides photon energies of 500 eV to 2800 eV with a monochromatic photon flux of $1.8 \times 10^{12}\,\mathrm{s}^{-1}\,\mathrm{mm}^{-2}$ at 1350 eV. Prior to the SX-STM imaging, a specialized topographic filter was calibrated to control the feedback loop of the STM.[87] The X-ray beam was chopped at a frequency of ≈5 kHz to allow signal detection of X-ray induced currents using lock-in amplifiers. A nano-fabricated smart tip made of Au/Ti/SiO_2 coaxial films with a minimized conducting Pt–Ir apex was used as the probe.[88] The sharp Pt–Ir tip was coaxially coated by an insulating SiO_2 film and a conducting Au/Ti shell. The outermost conducting layer of the tip was grounded to avoid charging. The SX-STM measurements were performed under ultra-high vacuum (UHV) conditions at room temperature. A bias of typically −1.15 V was applied to the sample, with a current set-point of 0.7 nA. The synchrotron beam illuminated the sample under grazing incident conditions (≈5° with respect to the surface normal).

2.3 Results

$LiNi_{0.8}Co_{0.15}Al_{0.05}O_2$ platelets of less than 50 nm along the crystallographic c-axis were synthesized in order to probe whether effects due to specific surface facets existed (Figure 14). Two samples were then charged at $10\,mA\,g^{-1}$ to 4.0 V and 4.75 V, corresponding to $Li_{0.44}Ni_{0.8}Co_{0.15}Al_{0.05}O_2$ and $Li_{0.04}Ni_{0.8}Co_{0.15}Al_{0.05}O_2$, respectively. An additional sample was charged to and held at 4.75 V for 10 h, then discharged to 2.7 V, all at 60 °C. Electrochemical profiles for all samples are shown in Figure 15.

The resulting $LiNi_{0.8}Co_{0.15}Al_{0.05}O_2$ specimens were first analyzed by XAS to provide benchmarks for spectromicroscopy. Within the soft X-ray regime (<1000 eV), first-row transition metals undergo electronic transitions from the $n = 2$ state to unoccupied levels of higher energy; the resulting increase in optical density is known as the element's "L-edge". The transition metals in layered $LiNi_{0.8}Co_{0.15}Al_{0.05}O_2$ are nominally in an octahedral configuration bonded to neighboring O atoms, resulting in 3 d orbitals mixed with O 2 p orbitals close to the Fermi level, with the occupancy determined by the metal's oxidation state. Features in the TM $L_{3,2}$-edges correspond to transitions from the 2 p core states to TM-3 d/O-2 p valence states.[89] Changes in the peak position are primarily associated with changes in the energy of these valence states, or more specifically, changes in the electronics of the TM−O bonds. Changes in the ratio of peak intensities correspond to variation in occupancy and/or symmetry of those orbitals. At energies associated with the O K-edge, O will undergo transitions from the $n = 1$ state to higher unoccupied states, including orbitals overlapping with the TM's orbitals.

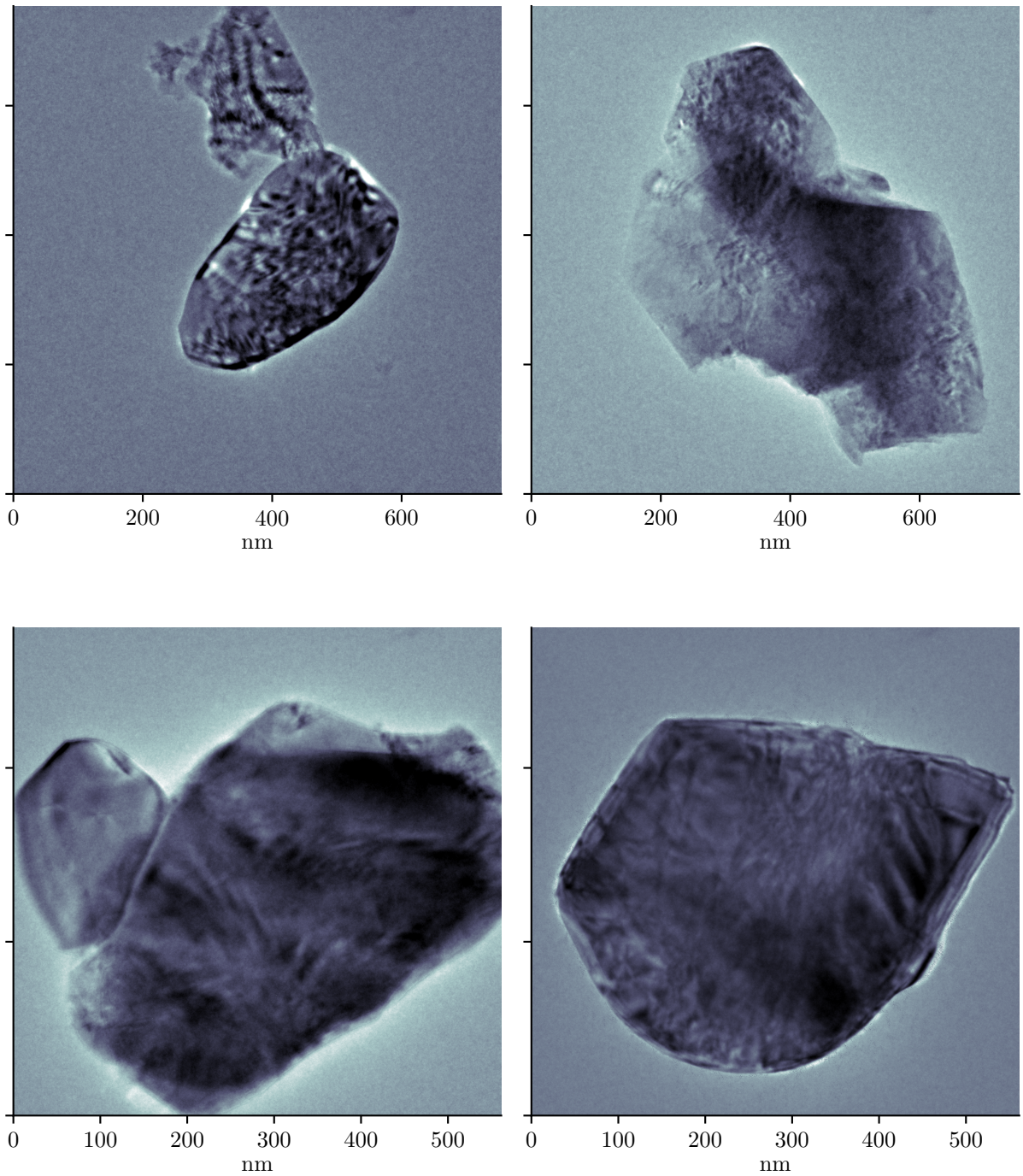

Figure 14: Representative TEM micrographs of pristine $LiNi_{0.8}Co_{0.15}Al_{0.05}O_2$ nano-platelets.

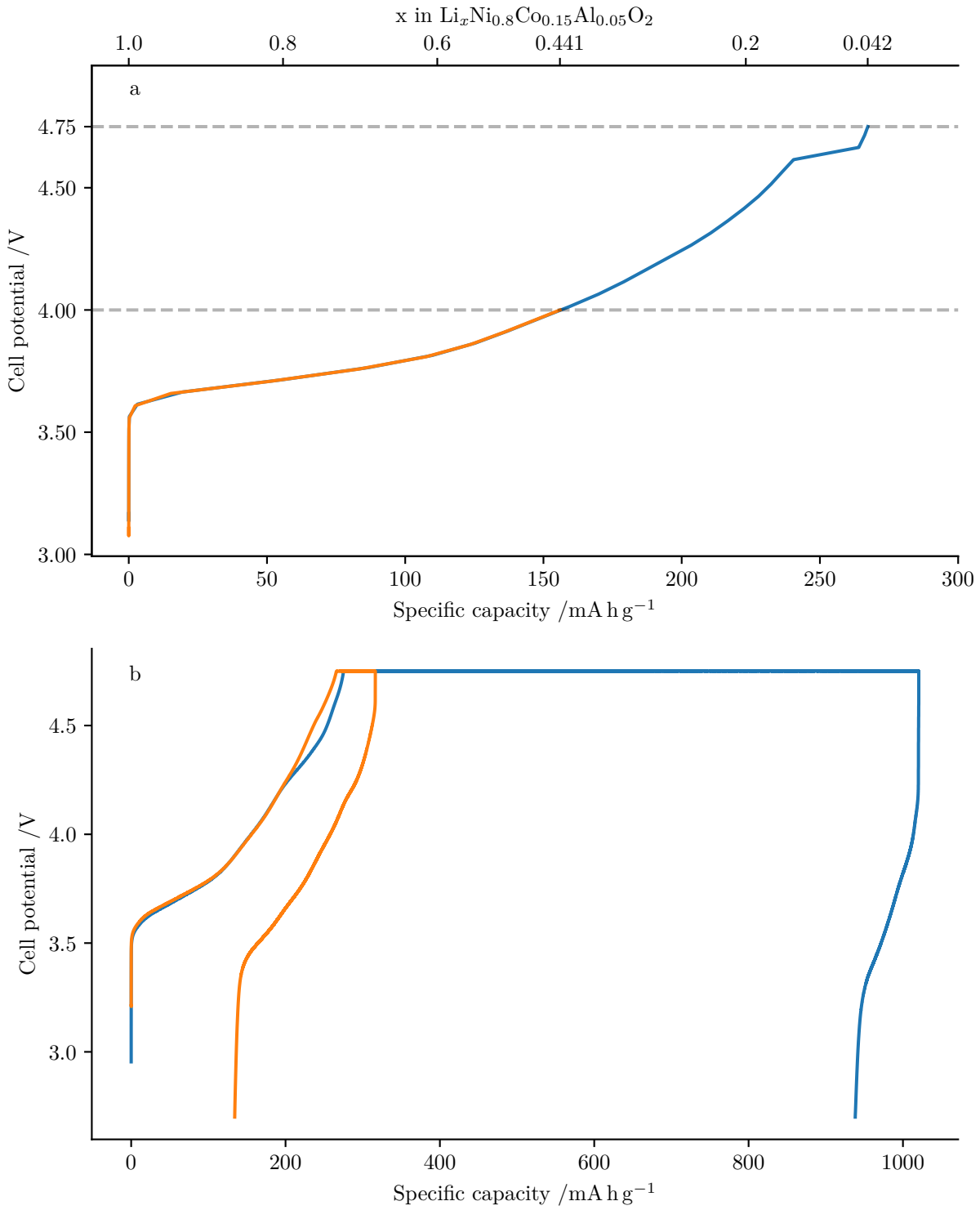

Figure 15: Galvanostatic charging curves for $LiNi_{0.8}Co_{0.15}Al_{0.05}O_2$ particles used during ptychography characterization. (a) Samples charged at 10 mA g^{-1} to 4.00 V and 4.75 V at room temperature. (b) Samples charged to 4.75 V at 340 µA, held for 10 h or 175 h, then discharged to 2.75 V at 68 µA all at 60 °C.

TEY spectra at the O K- and Ni $L_{3,2}$-edges are shown in Figure 16. These spectra reflect the average state over a several mm region on the electrode's surface to a depth of ≈10 nm. Peaks at 532 eV and 534 eV in the O K-edge are associated with NiO and Li_2CO_3 respectively.[13,60,90] Li_2CO_3 is formed by reaction of the as-made powder with CO_2, catalyzed by ambient H_2O, and is associated with reaction inefficiencies during first charge.[80,91] The small peaks at 534 eV in Figures 16b and c show that despite being protected from air exposure, some Li_2CO_3 was present in the pristine specimen and at low levels after charging to 4.0 V.[13,90] This Li_2CO_3 contamination decomposes at high potentials, and the accompanying 534 eV spectral feature is absent for the material collected after charging to 4.75 V (Figure 16d).

For the Ni $L_{3,2}$-edges, the relative intensities of the peaks close to 853 eV and 855 eV are directly related to the oxidation state of Ni.[92] In the pristine state ($Li_1Ni_{0.8}Co_{0.15}Al_{0.05}O_2$), these two peaks have roughly the same intensity (Figure 16b). Upon partial delithiation to 4.0 V (Figure 16c), the peak at 855 eV becomes more prominent as Ni^{III} is oxidized to Ni^{IV}.[62,93] This trend continues as the specimen is charged to 4.75 V (Figure 16d), where the majority of Ni exists in the Ni^{IV} state. In contrast, a spectrum dominated by the peak at 853 eV corresponds to Ni^{II},[63,94] as has been reported for pristine $LiNi_xMn_xCo_{1-2x}O_2$ materials[92,95,96] and other compounds,[97] and can be seen here in the spectrum of the NiO reference (Figure 16a). Some previously reported spectra of charged $Li_xNi_{0.8}Co_{0.15}Al_{0.05}O_2$ (Ni^{IV}) exhibited a small shift of the peak at 855 eV to higher energy at intermediate and high states of charge.[62,63] This was also observed in other Ni^{IV} compounds.[97,98] We therefore expected a Ni^{IV} signal with the ≈855 eV peak at slightly higher energies than in the Ni^{III} spectrum, though this was not observed in

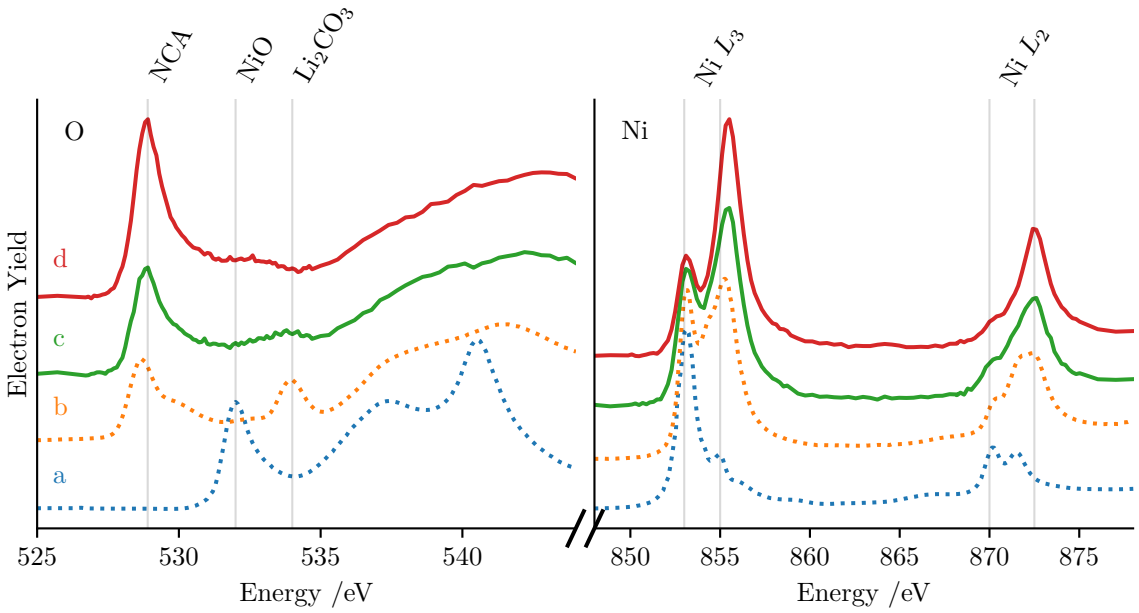

Figure 16: Normalized total electron yield at the O K and Ni $L_{3,2}$ edges. a) NiO reference and $LiNi_{0.8}Co_{0.15}Al_{0.05}O_2$ b) in the pristine state, c) charged to 4.0 V, d) charged to 4.75 V, e) charged to 4.75 V, held at 60 °C for 10 h, then discharged to 2.7 V. Vertical lines added at 528.9 ($LiNi_{0.8}Co_{0.15}Al_{0.05}O_2$ pre-edge); 532 (NiO); 534 eV (Li_2CO_3); 853 and 855 eV (Ni L_3 edge); 870 eV and 872.5 eV (Ni L_2 edge).

these bulk spectra (Figure 16b and d) . The Co L-edge spectrum (Figure 17) did not change noticeably between 4.0 V and 4.75 V. The low signal-to-noise ratios in the Co L-edge spectra compared to the Ni spectra (Figure 16) are due to the relative concentrations of these atoms in $LiNi_{0.8}Co_{0.15}Al_{0.05}O_2$.

Ptychography was used to obtain highly-localized X-ray spectra within primary particles. The resulting micrographs contain the complex-valued refractive index integrated over the thick-

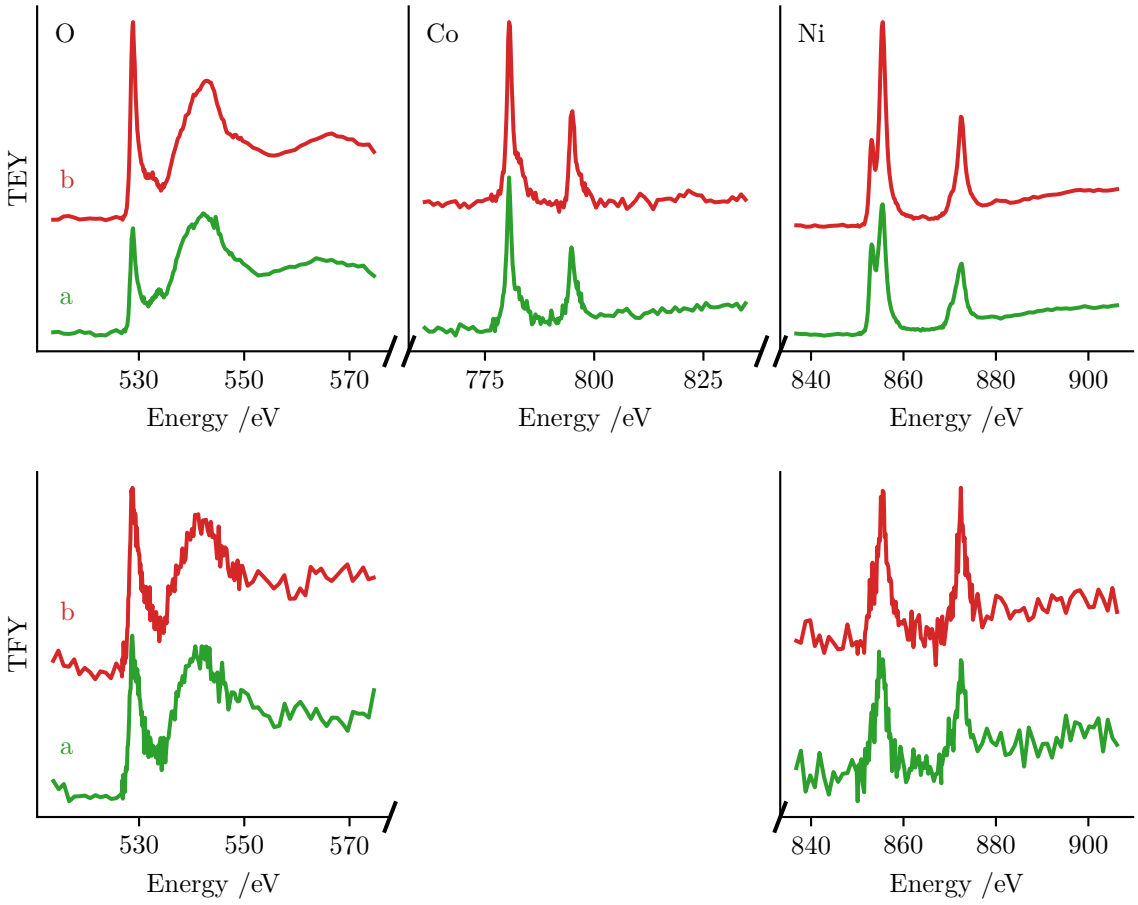

Figure 17: Ensemble XAS for $Li_xNi_{0.8}Co_{0.15}Al_{0.05}O_2$. O K-edge, Co L-edge, and Ni L-edge TEY and TFY spectra in a) charged to 4.0 V, and b) charged to 4.75 V.

ness of the specimen (relative to the surrounding space). While a complex analysis of these image-sets would be the most thorough,[99] this type of analysis is less developed than considering the optical depth alone, and does not allow comparison to other spectroscopy modes such as TEY and TFY, which only capture changes in X-ray intensity. Only the imaginary component will be considered here, which corresponds to optical depth obtained by conventional X-ray absorption techniques. The complex-valued spectra can be found in Figure 18. The cost of the improved spatial resolution is an increase in acquisition time and a tighter constraint on specimen thickness over conventional scanning microscopy: thick, highly-scattering specimens result in saturation of the area detector and the introduction of artifacts in the reconstructed images. The use of morphologically controlled particles that are constrained along the *c*-axis avoids this saturation problem, allowing maps of complete primary particles to be obtained. Due to the longer acquisition times needed for ptychography, only the Ni L_3-edge was scanned.

Collecting ptychography micrographs across the Ni L_3-edge generated a data-set containing ~5000 to 10 000 independent spectra. This level of data required automated analysis, which is often best achieved by comparison to known standards. For example, the spectrum of a partially oxidized $Li_{1-x}FePO_4$ cathode can be described as a linear combination of the spectra for the two thermodynamically stable phases: $FePO_4$ and Li_1FePO_4.[49] However, since there is no miscibility gap between $Li_1Ni_{0.8}Co_{0.15}Al_{0.05}O_2$ and $Li_{0.05}Ni_{0.8}Co_{0.15}Al_{0.05}O_2$, standards cannot be reliably isolated, making more sophisticated analyses necessary. The approach selected here builds up increasing levels of chemical and spatial detail. The different representations of the

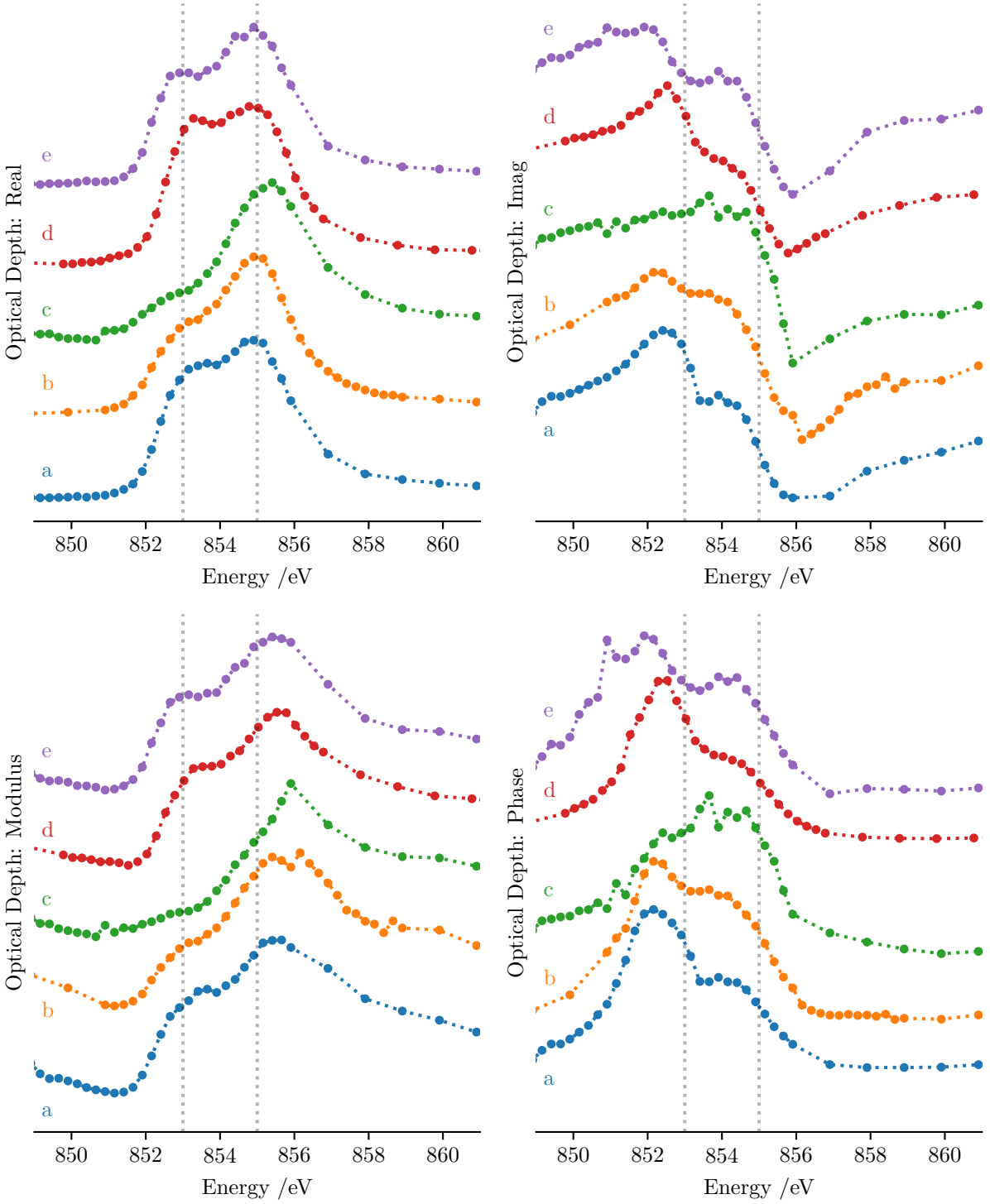

Figure 18: Complex components of mean optical depth spectra for $LiNi_{0.8}Co_{0.15}Al_{0.05}O_2$ particles in (a) pristine state; (b) charged to 4.0 V; (c) charged to 4.75 V; and charged to 4.75 V, held for (d) 10 h and (e) 175 h, then discharged to 2.7 V. Vertical lines inserted at 853 eV and 855 eV to aid the eye.

data will first be described briefly, and then considered together for particles at several states of charge.

Taking the mean optical depth across the full ensemble of pixels within a particle allows for comparison between particle-level and bulk spectra. Figure 19 shows these particle-level spectra, where the intensity at each energy is the mean optical depth of all pixels within the field-of-view with a detectable Ni signal. Micrographs of each field-of-view can be found in Figure 20. At low to intermediate states of charge (Figure 19a, b), there were two peaks present, at ≈853 and ≈855 eV. In the pristine state, their intensities were roughly equal, which we assign to Ni^{III}, whereas upon oxidation to 4.0 V, the ≈855 eV peak became dominant; neither peak significantly changed in position. This behavior mirrored the changes seen in the ensemble TEY spectra (Figure 16c). Upon oxidation to 4.75 V (Figure 19c), the high-energy peak dominated the spectrum, with its center blue-shifted by approximately 0.5 eV; the peak also became slightly wider compared to the pristine and 4.0 V specimens. The low-energy feature at ≈853 eV appeared to shift to a slightly lower energy compared to lower states of delithiation, though this was difficult to evaluate due to its low intensity. These changes in peak position were not visible in the ensemble-averaged TEY spectrum (Figure 16d). Upon returning to the discharged state (Figure 19d), the two peaks had equalized again, in line with previous reports.[13,100] However, the 853 eV peak remained subtly higher in intensity relative to the 855 eV peak than in the pristine sample (Figure 19a).

Going beyond these mean spectra toward nanoscale localization, different modalities of data visualization were employed. First, individual pixels were segmented based on distance from

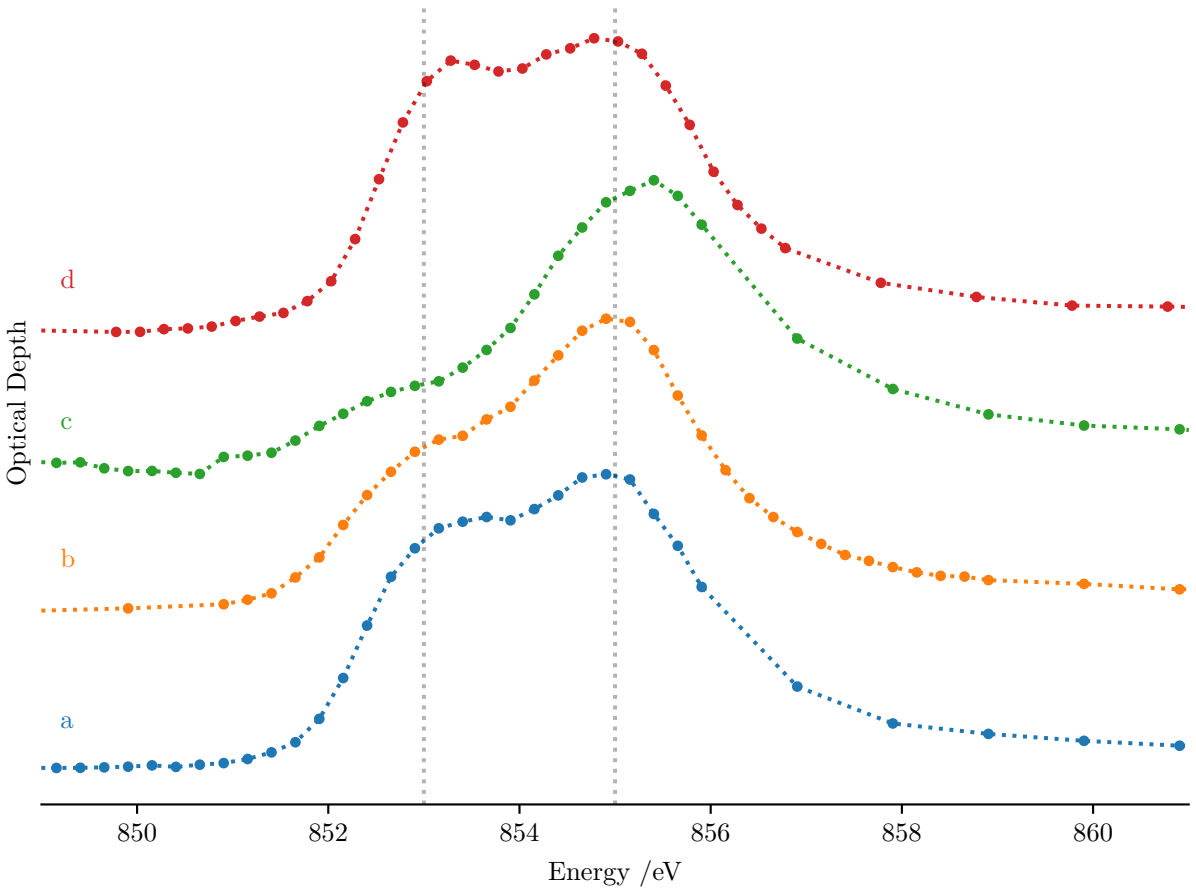

Figure 19: Mean optical depth spectra for $LiNi_{0.8}Co_{0.15}Al_{0.05}O_2$ particles in (a) pristine state; (b) charged to 4.0 V; (c) charged to 4.75 V; and d) charged to 4.75 V, held for 10 h at 60 °C and discharged to 2.7 V. Vertical lines inserted at 853 eV and 855 eV to aid the eye.

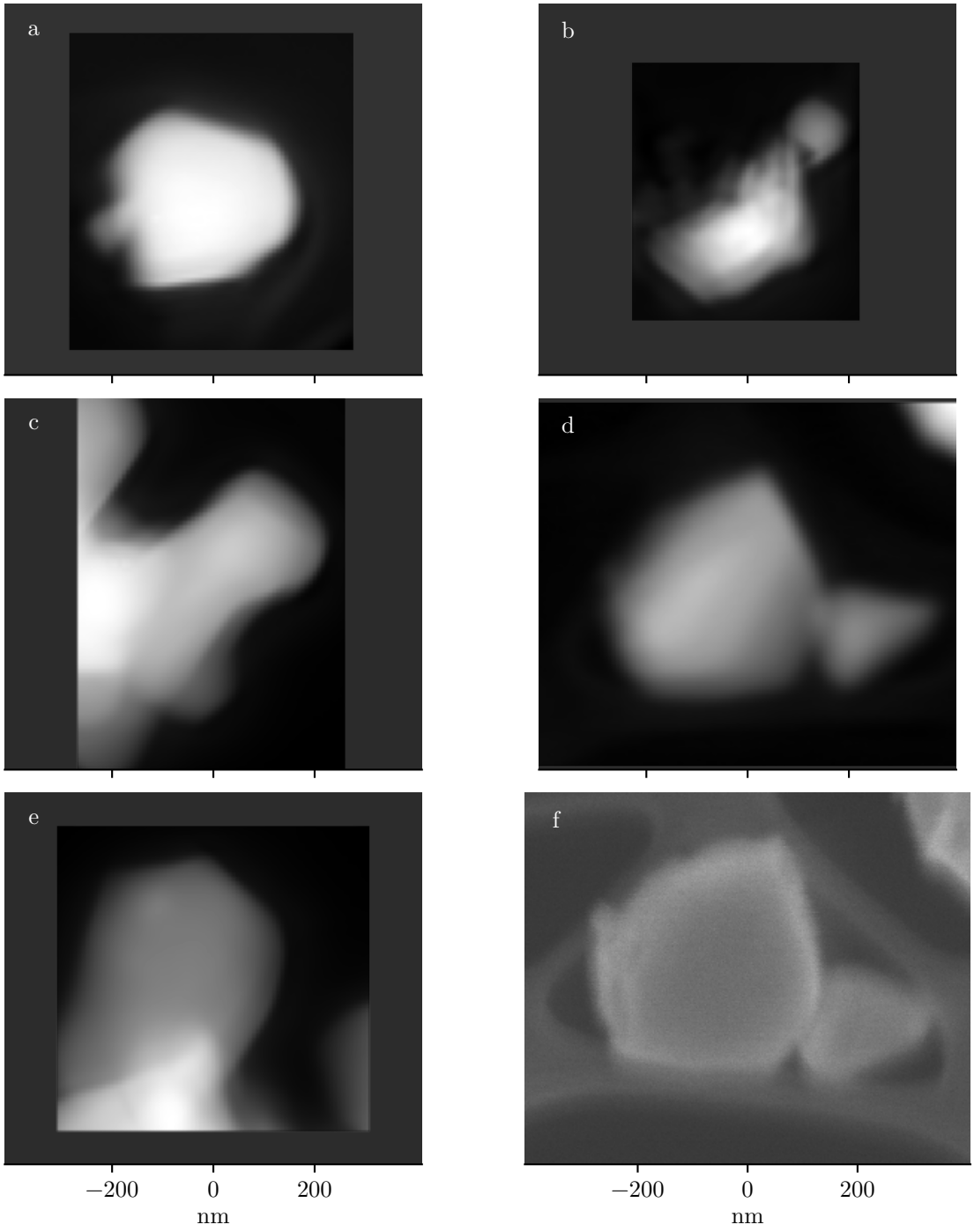

Figure 20: Mean optical depth maps for $LiNi_{0.8}Co_{0.15}Al_{0.05}O_2$ particles in (a) pristine state; charged at room temperature to (b) 4.0 V and (c) 4.75 V; or charged to 4.75 V at 60 °C and held for (d) 10 h or (e) 175 h. (f) Scanning electron micrograph of $LiNi_{0.8}Co_{0.15}Al_{0.05}O_2$ particle charged to 4.75 V at 60 °C and held for 10 h.

the edge of the particle and the spectra for each segment were averaged; the results are shown in Figure 21. The variability in the longest distance value between specimens is due to the different sizes of the particles. Uncharacteristic features in the spectrum closest to the particle edge are attributed to the inclusion of background pixels along with the material during segmentation. These discrepancies contribute to a 1-2 pixel (5 nm to 10 nm) error in segmentation. Since ptychography is a transmission-based imaging modality, all pixels contain some contribution from the surface material: even in the center of the particle in one of the two-dimensional images, photons must first pass through the surface before encountering the bulk of the material, and again upon leaving the particle. Pixels close to the edge, however, present a side-on view of the outermost regions of the particle so the signal is dominated by material close to the surface.

Second, to further explore the changes in peak position, the spectrum at each pixel was fit with a function approximating the features of the Ni L_3-edge, where the observed optical depths are given by three Gaussian functions and a step function, described mathematically in the methods sections (Equation 2.1). The positions and intensities of the peaks can then be analyzed quantitatively. Figures 22a-d show the correlation between the positions of the two main peaks at $\approx$853 eV and $\approx$855 eV. The third peak did not change position significantly so is not shown. The color of each point conveys the distance of the given pixel from the edge of the particle. A representative edge ("E") and center ("C") pixel were selected for each specimen and their spectra plotted in Figure 22e. A sample decomposition for the spectrum "(b)-C" in Figure 22e can be found in Figure 23. The peak centers in the pristine specimen (Figure 22a) provided a base-line of $\pm$200 meV for the amount of variability in peak center expected

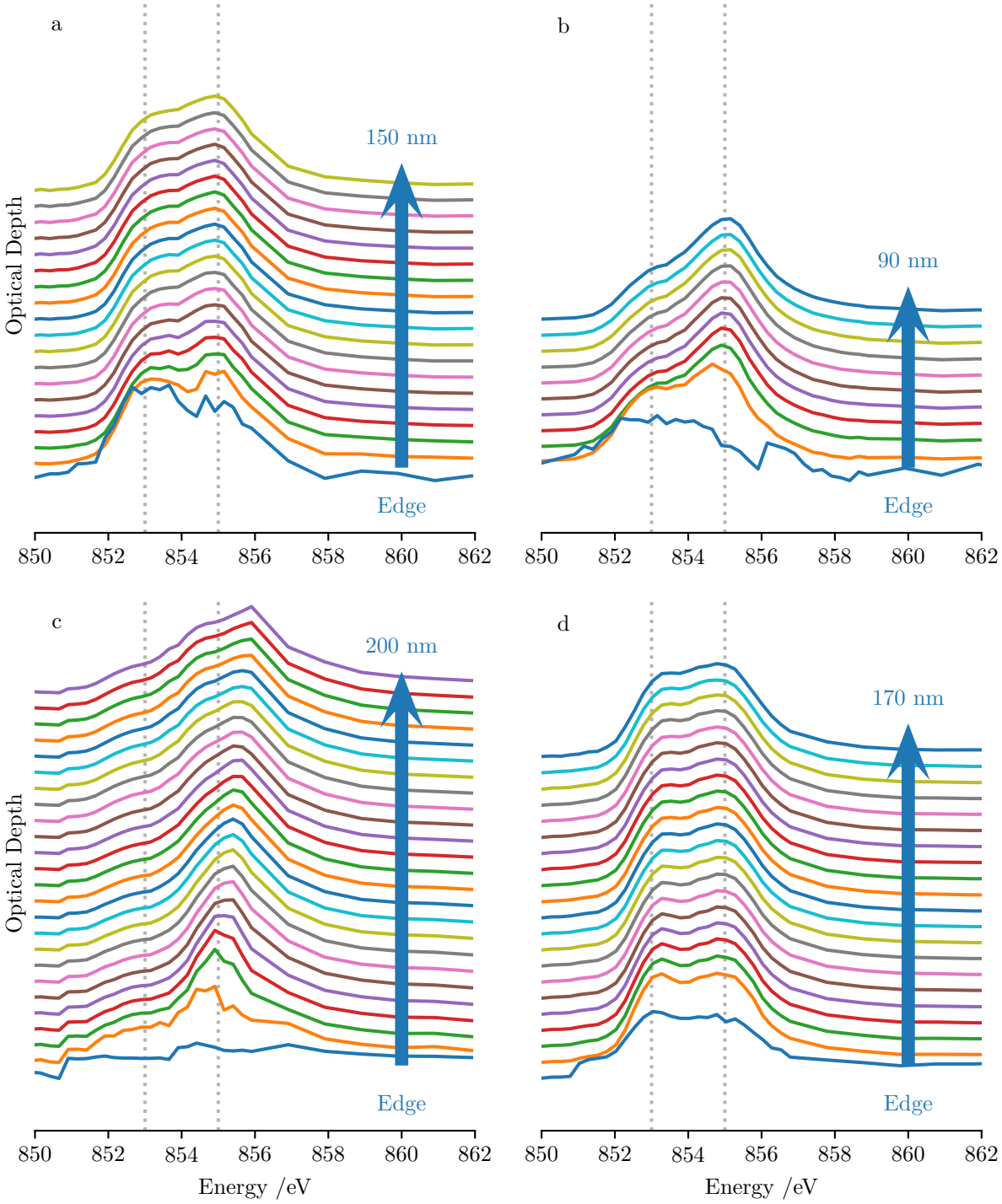

Figure 21: Mean optical depth spectra segmented by distance from edge of $LiNi_{0.8}Co_{0.15}Al_{0.05}O_2$ particle in a) pristine state, b) charged to 4.0 V, c) charged to 4.75 V, and d) charged to 4.75 V and discharged to 2.7 V.

as inherent to the measurement, indicated with a red ellipse. A small but persistent positive correlation exists between the two peak centers, and is consistent across all samples, except when charged to 4.75 V (Figure 22c), at which point variability increase notably.

The large distribution of energy values for the signals in the scatter plots (Figure 22) and the features seen in the particle ensemble spectra (Figure 19) suggest that several chemical states were present across the full range of delithiation. Therefore, a third layer of insight was provided by statistical analysis, which showed that three components ($\vec{c_i}$) best represented the optical depth frame-set (**OD**). The relationship can be described using an outer product ($\otimes$) such that $\mathbf{OD} = \vec{c_1} \otimes \mathbf{W_1} + \vec{c_2} \otimes \mathbf{W_2} + \vec{c_3} \otimes \mathbf{W_3}$, where $\mathbf{W_1}, \mathbf{W_2}, \mathbf{W_3}$ are two-dimensional matrices with the same shape as an individual frame, containing the contributions of the given component to each pixel; effectively these weight matrices quantify the intensities of each component. Extracting weights and components is an under-determined problem, so an analytical solution is not possible. Instead, a technique from the family of blind source separations must be used.[101] Among them, *Bayesian analysis* can incorporate additional information ("priors") to further constrain the model.[102] Figure 24 shows the sources $\vec{c_1},\ \vec{c_2},\ \vec{c_3}$ extracted in this way, and Figure 25 shows the component maps ($\mathbf{W}_i$). These maps combine the highest chemical and spatial resolution possible in the measurements. The components resulting from the analysis (Figure 24) are mathematical constructs, and so do not perfectly match the observed or calculated spectra of pure Ni species,[92,94,95,97] though they do resemble other statistically extracted sources.[98] Instead, these sources are treated as proxies for the extent of oxidation or reduction within the particles rather than pure chemical identities. An alternate representation of these

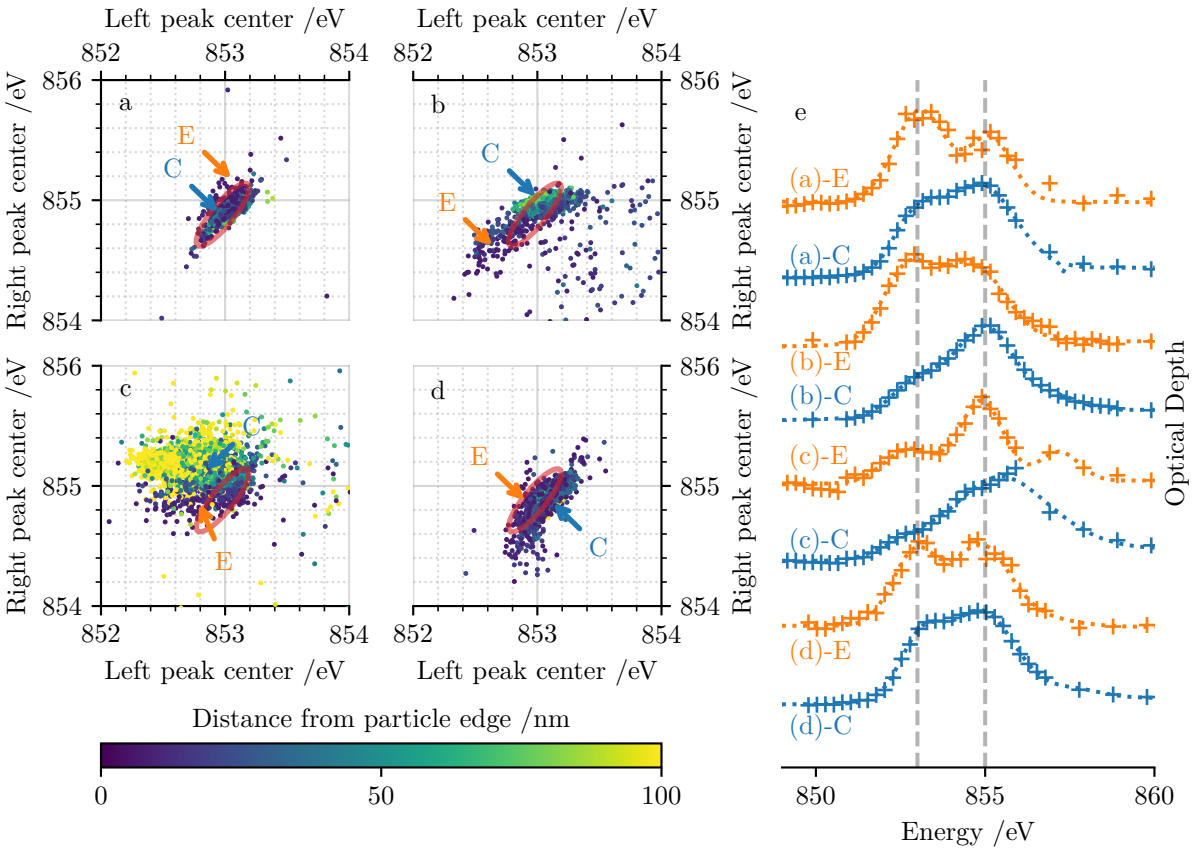

Figure 22: Scatter plot of pixels within primary $LiNi_{0.8}Co_{0.15}Al_{0.05}O_2$ particles showing positions of peaks within Ni L_3 edge in a) pristine state; charged to b) 4.0 V and c) 4.75 V; and d) charged to 4.75 V, held at 60 °C for 10 h, then discharged to 2.7 V. The color of each point represents that pixel's distance from the edge of the particle. The red ellipse highlights approximate positions of pristine data for comparison. e) Single-pixel spectra are selected from regions in either the edge (E) or the center (C) of the particle.

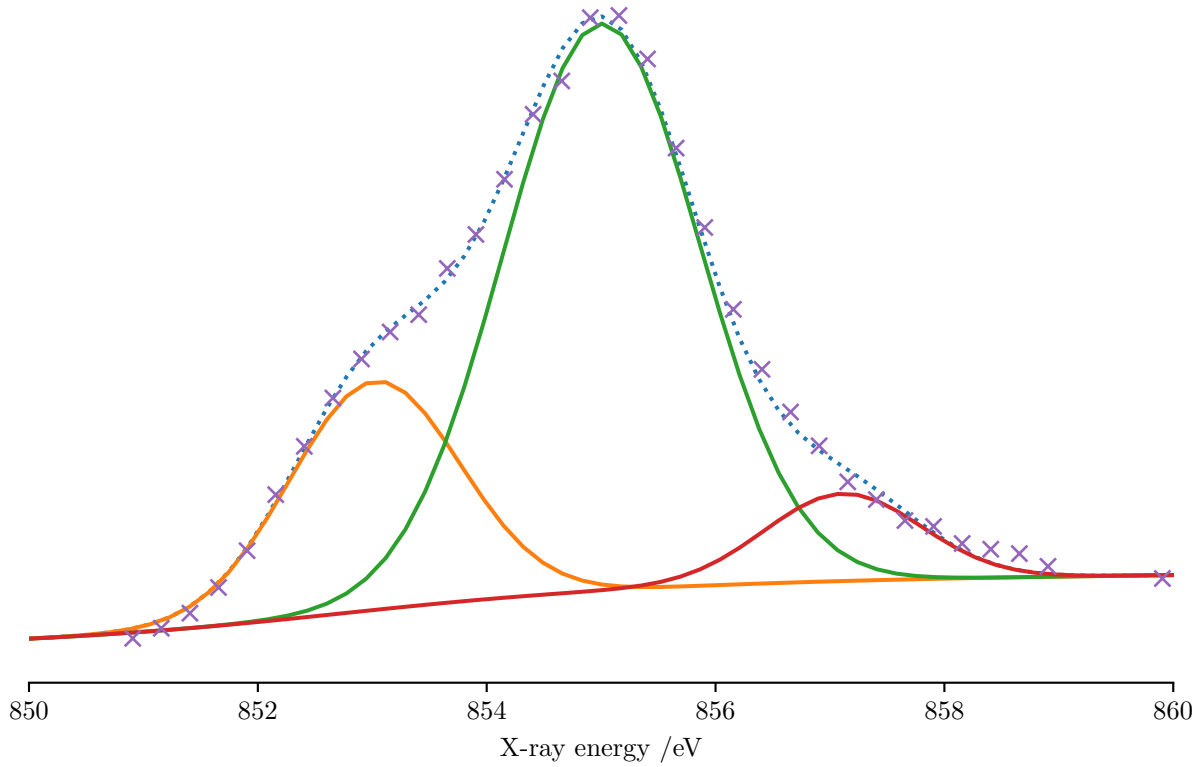

Figure 23: Sample decomposition of single-pixel ptychography spectrum to a linear combination of three Gaussian functions. Pixel is taken from center of $LiNi_{0.8}Co_{0.15}Al_{0.05}O_2$ particle charged to 4.0 V.

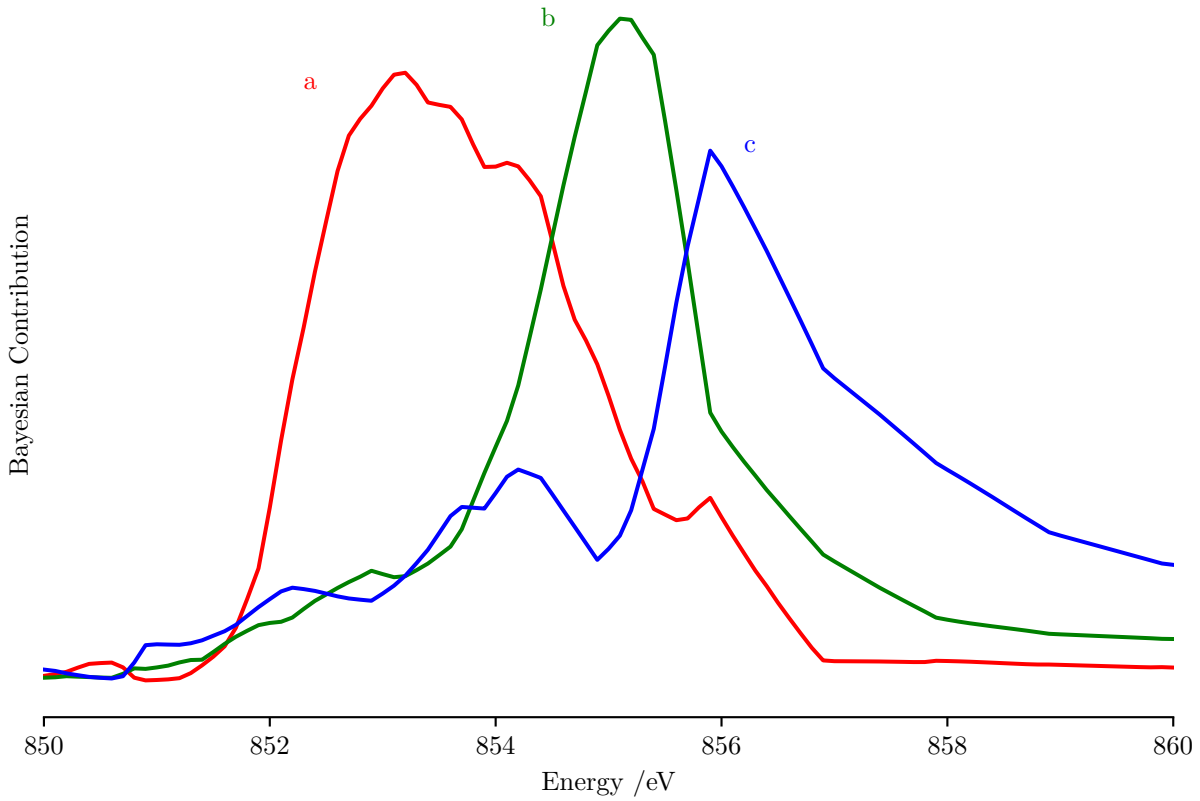

Figure 24: Component sources extracted through Bayesian analysis, identified as proxies for (a) reduced, (b) intermediate, and (c) oxidized Ni.

Bayesian maps is shown in Figure 26, where the sources' contributions are shown at a given distance from the edge of the particle. In this representation, the value at any given distance is the median of all pixels that are that distance away from the edge of the material. If the field-of-view contains multiple overlapping particles, the distance to the material edge may not be the same as the distance to the edge of a single particle.

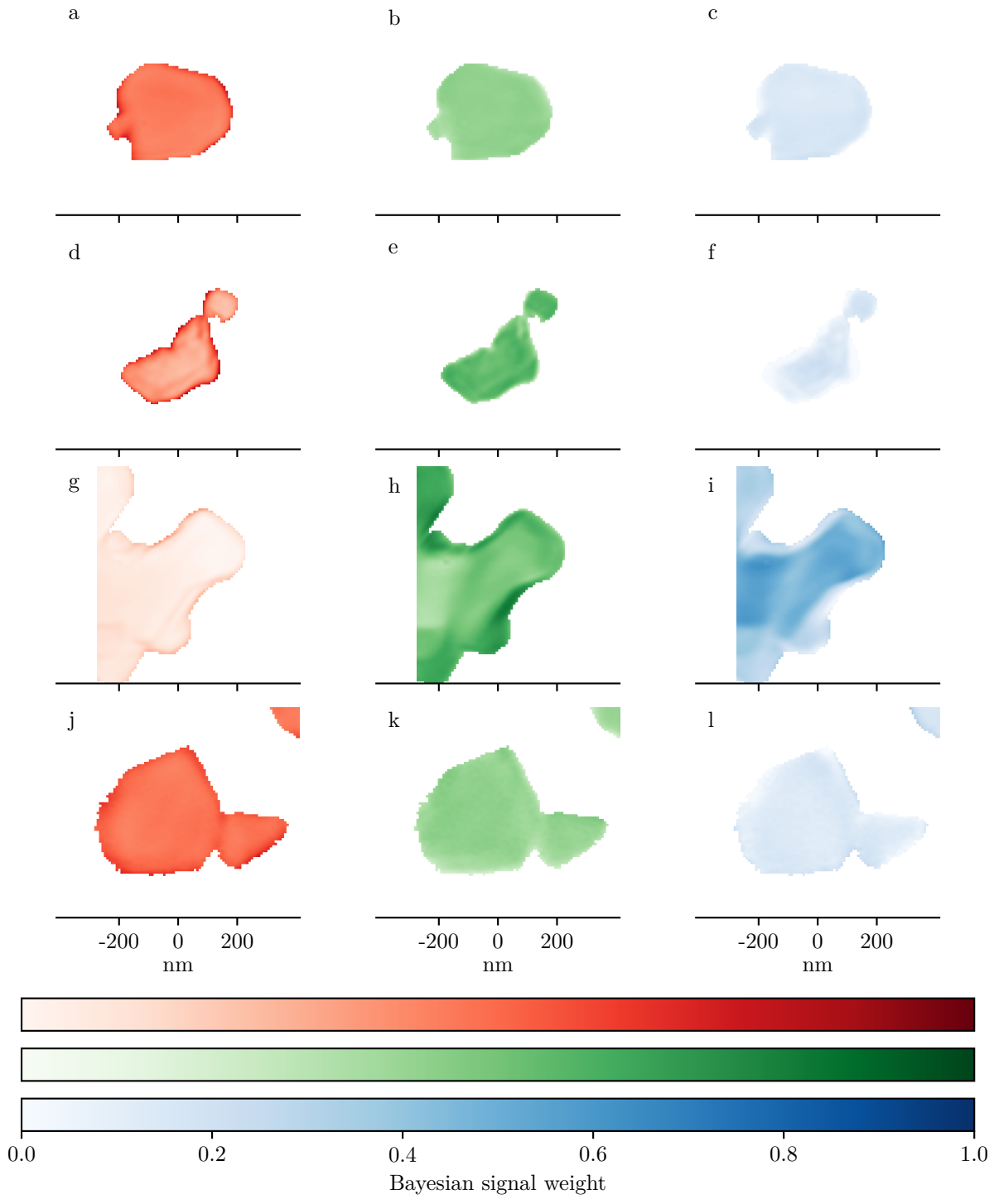

Figure 25: Maps of extracted Bayesian signals from Figure 24 for reduced (a,d,g,j), intermediate (b,e,h,k), and oxidized (c,f,i,l) Ni. $LiNi_{0.8}Co_{0.15}Al_{0.05}O_2$ primary particles in (a-c) pristine state; charged to (d-f) 4.0 V and (g-i) 4.75 V; and (j-l) charged to 4.75 V, held for 10 h and discharged to 2.7 V at 60 °C.

The pristine particle served as a baseline for the remaining analysis. Figure 22a shows the distribution of peak positions to have been tightly grouped around 853 and 855 eV, with no clear trend between pixels in the center and the edge. Representative spectra of pixels in an edge ("E") and center ("C") are shown in Figure 22e. The two pristine spectra shared common peak positions, but varied in the intensity ratio between these two peaks, which is a degree of freedom not captured in Figure 22a. The peak at 853 eV was dominant in pixels closest to the edge (Figure 21a and 22e), whereas material >10 nm from the edge exhibited peak ratios similar to the bulk and particle-average spectra (Figures 16b and 19a). All pristine spectra could be decomposed as varying mixtures of primarily sources *a* and *b* resulting from Bayesian analysis (Figure 24), emphasizing that they do not correspond to specific chemical species. The corresponding weight maps in Figure 25a-c further confirmed that the pristine particle had a slightly higher contribution at low energy towards the edges of the particle, while the center was fairly uniform. The spectra showing a higher intensity of the feature at 853 eV, and the associated Bayesian source *a*, denote the existence of Ni^{II} in the surface of the pristine particles, based on the spectrum of NiO in Figure 16a, and prior literature.[63,92,94–97] This phenomenon can be ascribed to the reconstruction of the surface into small domains of reduced Ni within a rock-salt structure during the synthesis of the material, as discussed in previous electron microscopy analysis of these same particles.[56] Source *c* represents a tail in the spectra toward energies higher than 856 eV. It is associated with Ni^{IV} by comparison to the fully-charged specimen and other Ni-containing oxides.[97,98] Given that this state is not stable in the conditions of synthesis of the oxide, the non-zero contribution of this source to spectra

in the pristine specimen map (Figure 25c) is considered to be within the error of the fitting process, and therefore to have no chemical relevance.

A map of mean optical depth (Figure 20) suggests that the unusual shape observed in the image of the specimen charged to 4.0 V results from the overlap of at least two particles. The spectral peak positions exhibited more variability than for the pristine, as shown by the spread outside the region of reference from the pristine state (marked by the ellipse in Figure 22b). A number of edge pixels showed a downward shift of the spectra, by as much as 0.75 eV in the case of low-energy features. The shift in peak position of the low-energy feature is manifested in the significantly larger width of source *a* in the Bayesian analysis (Figure 24a) than the other two (Figures 24b and c). The linear mixing model that underlies the Bayesian analysis cannot deal with peak movement directly but must use a broader peak that overlaps the full range of peak positions. The spectra at some pixels at the particle edge, such as "(b)-E" in Figure 22e and more generally in Figures 21b and 26, showed higher intensity of the low-energy peak compared to the average pristine spectrum (Figure 19a). This inversion of peak intensity ratios reveals the presence of an appreciable amount of Ni^{II} in the partially charged specimen. In contrast, the peak at ≈855 eV was clearly dominant in the center of the particle, as expected from Ni oxidation. The existence of reduced Ni at the edges of the particle, concurrent with the overall oxidation of the particles compared to the pristine state, was also reflected in a higher ratio of source *b* in the corresponding Bayesian weight maps (Figure 25d-f). There was also minor heterogeneity in oxidation state within the interior of the particles that was not present in the pristine particle. This heterogeneity is reflected in the gradient of Ni, from lower to higher

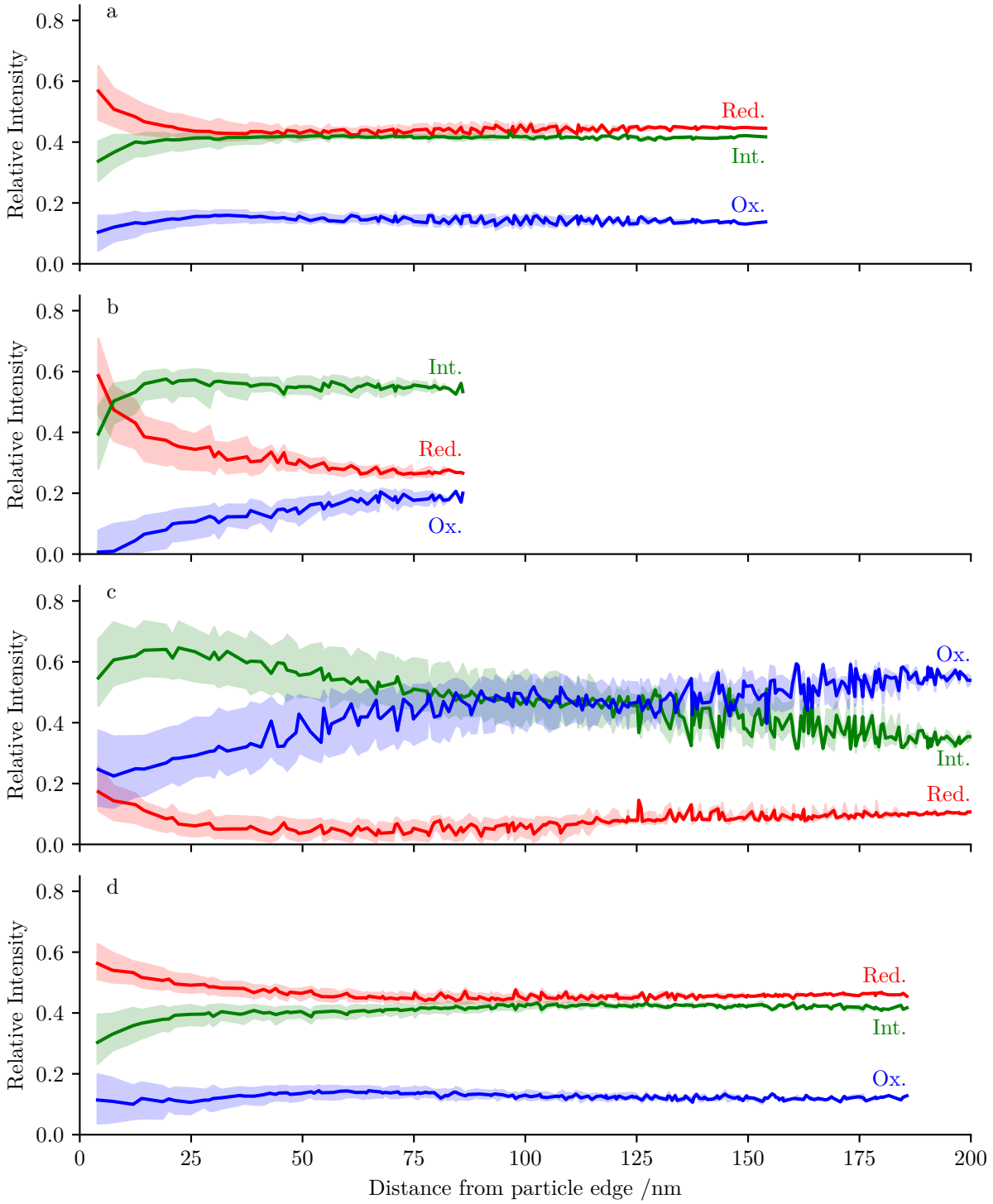

Figure 26: Median contribution of Bayesian sources as proxies for reduced, intermediate and oxidized nickel, segmented by distance from particle edge in $LiNi_{0.8}Co_{0.15}Al_{0.05}O_2$ particles: (a) pristine; (b) charged to 4.0 V and (c) 4.75 V; and (d) charged to 4.75 V, held for 10 h and discharged to 2.7 V at 60 °C. Filled regions cover one standard deviation above and below the mean.

oxidation states, observed up to 30 nm into the particle (Figure 26b). Nonetheless, there was a higher extent of oxidation at all distances from the edge than in equivalent regions of the pristine material (Figure 25a-c and 21b).

After charging to 4.75 V, there was a surge in the distribution of states within the particle, with the corresponding distribution of peak centers extending far outside the inherent variability denoted by the ellipse in Figure 22c. Furthermore, the peak centers were highly correlated with position within the specimen, with a stark contrast between the spectra at the edge and the center. Comparison of representative spectra (Figures 21c and 22e) shows that the edge had a considerable contribution at 853 eV, at a relative intensity which was, at most, comparable to the central, most oxidized regions of the 4.0 V specimen (Figure 26). In other words, no pixels matching reference spectra for pure Ni^{II} (Figure 16a) were found. There was a strong correlation between a pixel's distance to the specimen edge and its ratio of peak intensities (Figure 21c). The high-energy peak also gradually shifted from 855 eV to higher energy farther from the edge of the observed object. Pixels in the center tended to show almost no intensity at low energy indicating extensive oxidation of Ni. Additionally, a second peak appeared at 854 eV (Figure 21c and spectrum *(c)-C* in Figure 22e). The Bayesian source *c* (Figure 24c) contains peaks at 854 and 856 eV, indicating that their occurrence was at least partially correlated. The corresponding map (Figure 25g) and distance profiles (Figure 26c) show that source *a* (red), the component representing the most reduced states, is only present in the 10 nm to 30 nm closest to the particle edge. Changes in oxidation state are sharpest in this area (Figures 26c and 25g), which extends slightly further into the particle than the reduced regions seen in the pristine

and 4.0 V specimens (Figures 25a-f and 26c). These regions have a higher relative concentration of source *b*, which rapidly increases into the particle (Figure 26c), again reinforcing the notion that even the first 8 nm into the particle were already oxidized, on average, beyond the pristine state (Figure 21c and spectrum *(c)-E* in Figure 22e). Just below this surface region is a much larger region spanning 20 nm to 50 nm that is dominated by source *b*, with a progressive relative increase of source *c* toward the interior of the specimen, where spectra consistent with pure Ni^{IV} were found (*(c)-C* in Figure 22e). This region of intermediate source *b* appears artificially larger and more gradual in Figure 26c due to the effects of having multiple overlapping particles in the field of view.

Complementary analysis of surface states in $LiNi_{0.8}Co_{0.15}Al_{0.05}O_2$ charged to 4.75 V was achieved by SX-STM.[103,104] Figure 27a shows a schematic of the experimental setup. A monochromatic X-ray beam illuminates the junction between a conductive tip and the specimen. While the tip is located in the far-field position (10's of nanometers from the sample), it serves as a detector for photo-electrons,[105] with the probing depth determined by the mean free path for photo-electrons escaping the surface: $\approx$1.5 nm.[106] When the tip is in the near-field position (<1 nm), quantum electron tunneling occurs[107] and the topography of the sample surface can be recorded (Figure 27b). During X-ray exposure, the near-field signal is dominated by X-ray excited tunneling and not the photo-ejection of electrons, giving access to the electronic structure within the first atomic layer of the specimen.[88,108] Since the tip can be rastered over the sample while tunneling, such X-ray spectroscopy is highly localized in space.[88,108] As a result, it is possible to collect spectra of the Ni $L_{3,2}$-edges for an arbitrary point over an isolated

individual particle, confirmed by the absence of absorption peaks when the tip was placed over the silicon substrate (Figure 27b and e).

The spectrum obtained with a coated tip in the far-field (Figure 27c) exhibited X-ray absorption peaks at 853 eV, 855 eV, 870.4 eV and 871.8 eV. The greater intensity at 853 eV versus 855 eV again indicates a considerable contribution from Ni^{II} in the first ≈1.5 nm of the specimen. When the spectrum was collected with the tip in the near-field position, no distinct peaks were observed at 855 and 871.8 eV (Figure 27d). Instead, in addition to the main peaks at 853 and 870.4 eV, a shoulder was observed at 853.9 eV. The near-field spectrum closely resembles the spectra for NiO (Figure 16a) and other Ni^{II} layered cathode materials.[92,95] The absence of a clear feature at 855 eV is an indication that, while the outer regions of the particle are a mixture of Ni^{II} and $Ni^{III/IV}$, the outer atomic layer of the particle contains almost exclusively Ni^{II}.

An additional $LiNi_{0.8}Co_{0.15}Al_{0.05}O_2$ sample was charged to 4.75 V, held for 10 h, and then discharged to 2.7 V. Figure 22d shows that the resulting variability in the peak positions was very similar to that observed in the pristine material, indicating that all spectra contained features around 853 and 855 eV. A slight shift in the low-energy feature at 853 eV toward higher energies was observed in the overall distribution, seen as a displacement of the scatter plots in Figure 22d to the right relative to the red ellipse. The ratio of intensities at each energy region was again different between edge and center pixels (Figure 22e). Comparison of spectra segmented by distance from the edge (Figure 21d) showed a similar trend to the pristine and 4.0 V samples: the spectra closest to the center were comparable to the ensemble average

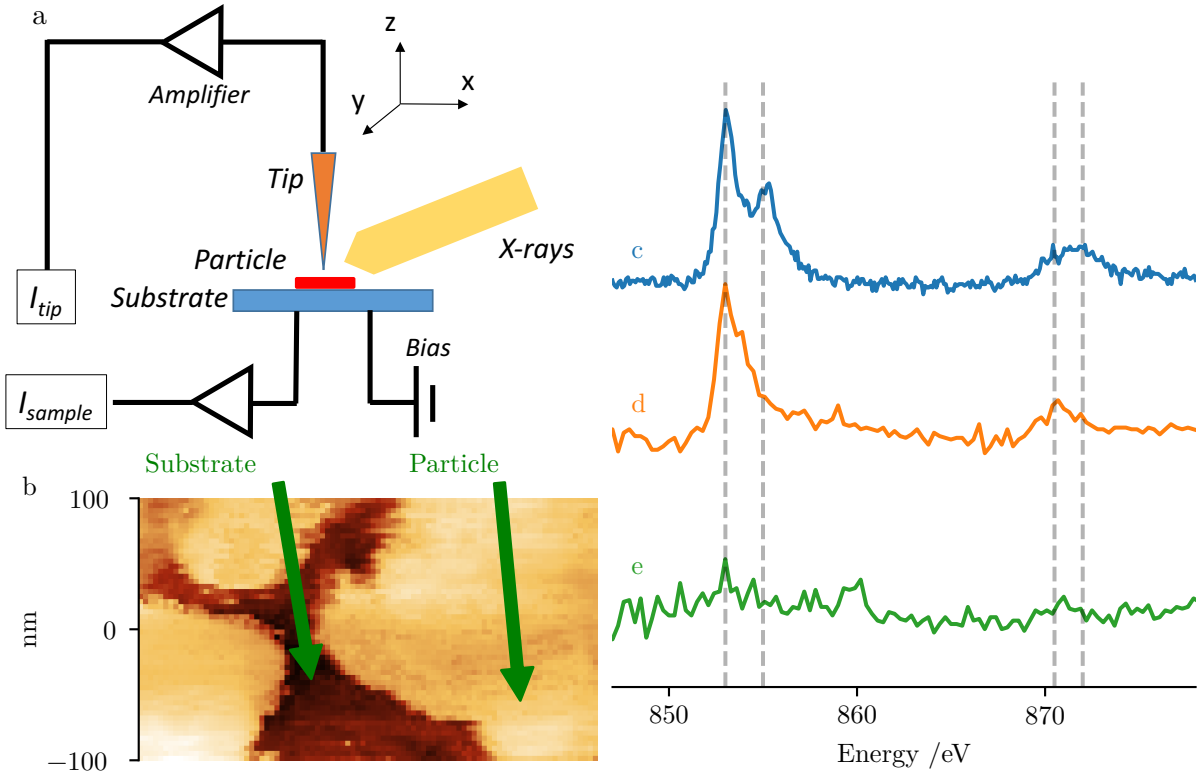

Figure 27: (a) Schematic of the experimental setup in SX-STM. A monochromatic X-ray beam illuminates the junction between a tip and the sample. The resulting X-ray excited sample and tip currents are measured simultaneously. A piezo scanner allows to scan or place the tip at any lateral X and Y position over the sample surface and adjust the tip/sample separation Z ranging from tunneling to far-field conditions. To enable electron tunneling a bias is applied to the sample. (b) Topography scan (200 nm × 350 nm) of $LiNi_{0.8}Co_{0.15}Al_{0.05}O_2$ particles charged to 4.75 V and transferred to a silicon substrate. (c-e) SX-STM spectra obtained with the tip (c) in the far-field (≈200 nm) and under tunneling conditions (near-field) (d) over a particle and (e) over the silicon substrate.

spectrum of the particle, whereas a greater intensity around 853 eV, indicative of the existence of Ni^{II}, was found closer to the edge (Figure 19d). Comparison of the distance profiles of the Bayesian sources shows that the gradient between these two end points extends farther in the discharged sample (Figure 26d) than in the pristine (Figure 26a), reaching up to 50 nm from the particle edge. These differences are subtle, and the Bayesian maps for the pristine (Figure 25a-c) and discharged (Figure 25j-l) samples look very similar. If the sample is instead held for 175 h, the heterogeneity in Ni oxidation state is aggravated, as seen in Figure 28. Several regions are visible with a higher contribution from the oxidized Ni signal than when held for 10 h (Figure 28e), signifying that these areas were not able to fully return to the reduced Ni^{III} state.

2.4 Discussion

Multiple calculated and experimental spectra have been reported for Ni^{III}, with variations in the positions of the two L_3-edge peaks that were found to be sensitive to phenomena such as crystal field splitting, spin-orbit coupling and Coulomb interactions.[63,94,109] Comparison of the observed spectra of pristine $LiNi_{0.8}Co_{0.15}Al_{0.05}O_2$ in Figures 16b and 19a with these literature reports[110,111] confirms that the pristine material contains predominantly Ni^{III}, consistent with the expectation from the chemical formula. Subsequent comparison of the pristine spectrum (Figure 19a) to the Bayesian component designated as intermediate Ni (Figure 24b) demonstrates that the Bayesian component does not represent pure Ni^{III}. This observation indicates that while these components are proxies for the degree of oxidation/reduction of Ni, they are best described as statistically independent spectral signals that likely depend on the underlying

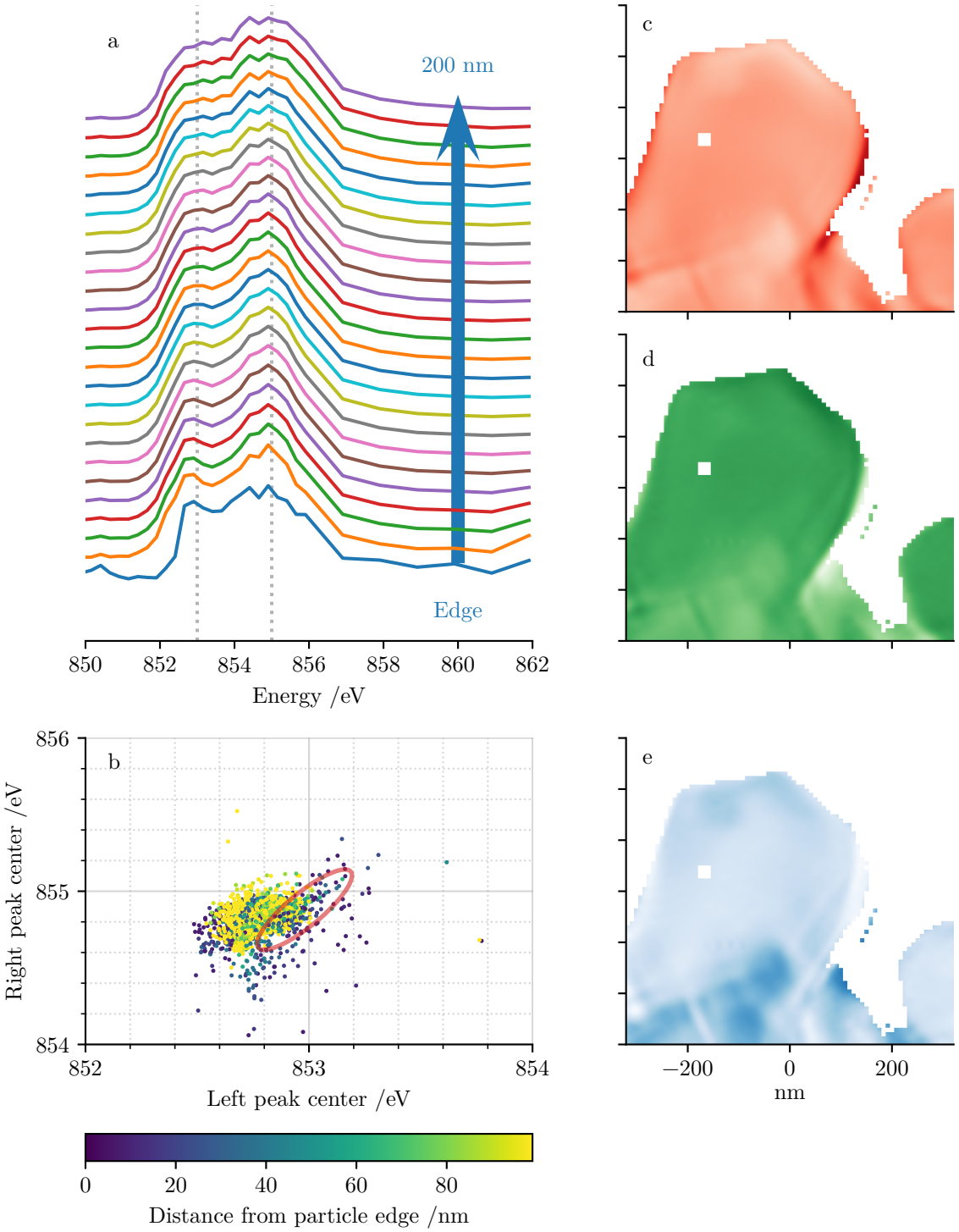

Figure 28: $LiNi_{0.8}Co_{0.15}Al_{0.05}O_2$ particle charged to 4.75 V, held for 175 h, and discharged to 2.7 V, all at 60 °C. (a) Ni L_3 spectra segmented by distance from particle edge. (b) Scatter plot of Ni L_3 peak positions with color indicating distance from particle edge. (c-d) Maps of weights for Bayesian components as proxies for (c) reduced, (d) intermediate, and (e) oxidized nickel.

Ni electronic states. For example, source *c* (Figure 24c) does not represent Ni^{IV} per se; instead it captures electronic changes occurring at high levels of delithiation.

The Bayesian maps show an enhanced contribution from the reduced source *a* (Figure 24a) distributed around the edges of the particles at all states of charge (Figure 25a,d,g,j). Comparison to the NiO reference spectrum (Figure 16a) reveals that this outer reduced layer is rich in Ni^{II}. Even at 4.75 V (Figure 25g), the reduced edges are still present, demonstrating that this region does not significantly oxidize even at high potentials. All of the maps of the reduced component (Figure 25a,d,g,j) show this reduced layer present on all sides of the particle, though not with uniform thickness (eg. right side of Figure 25g). This observation suggests that it forms on all crystallographic facets parallel to the *c*-axis, with some facets being more susceptible. The reduced layer becomes thicker at higher states of charge, from ≈15 nm in the pristine specimen to ≈40 nm at higher states of charge (Figure 26a-c). The reduced layer that results from discharging from 4.75 V is also thicker than in the pristine particle (Figure 25j). Since this reduced layer exhibits poor lithium transport, the increase in its thickness will inhibit complete delithiation. As this trend continues over multiple cycles,[112] it will contribute to the poor cyclability seen in $LiNi_{0.8}Co_{0.15}Al_{0.05}O_2$ when charged to high potentials. The reduced outer layer thickness did not increase noticeably when charged to 4.0 V, leading to the higher cyclability of $LiNi_{0.8}Co_{0.15}Al_{0.05}O_2$ when lower cut-off potentials are used.

SX-STM reveals that only Ni^{II} is present in the first atomic layer, with higher oxidation states starting to emerge in the immediate subsurface (Figure 27). These observations are consistent with the fact that no domains of pure Ni^{II} could be isolated by ptychography, where

spatial resolution is ≈10 nm from the surface. Therefore, the rock-salt structure observed within the first 2 nm to 5 nm of the surface by TEM[60,67,70–73] only contains pure Ni^{II} in the outermost atomic layer, with different mixtures of Ni^{II} and Ni^{III} present immediately below.

In the pristine, 4.0 V, and discharged states this thin reduced outer layer is the dominant heterogeneity in the particle. However, at 4.75 V, a new region is seen in a layer below the surface showing a high contribution from the intermediate component (Figure 25h). This larger intermediate layer is seen up to 100 nm deep, which represents a significant fraction of the particle's width, especially when considering some particles were less than 200 nm wide (Figure 20b,d). This intermediate layer is therefore seen as distinct from the surface reduction in the pristine and 4.0 V specimens, and is better described as layered $LiNi_{0.8}Co_{0.15}Al_{0.05}O_2$ that is prevented from reaching the fully oxidized state seen closer to the center of the particle (Figure 25i). In order to maintain charge neutrality, the lower nickel oxidation state in this layer must be compensated by other charged species. Oxygen loss has been shown to play a role in the surface reconstruction previous discussed,[66,70,72,113–117] as well as electrolyte decomposition at high states of charge.[118–120] Additionally, energy dispersive spectroscopy (TEM-EDS) has shown areas of oxygen deficiency within a particle's interior after repeated cycling.[115] However, the associated structural transformation requires Ni back-diffusion from the surface, which quickly becomes kinetically hindered and has an average diffusion length below 1 nm.[117] An alternative explanation for the intermediate Ni layer comes from the poor lithium conductivity of the surface rock-salt,[121] creating a high diffusion barrier. Slow lithium transport at the

surface could result in a build-up of lithium concentration underneath the rock-salt surface that accounts for the intermediate Ni oxidation layer (Figure 25h).

2.4.1 Relevance of High Resolution Observations to Commercial Materials

Commercial $LiNi_{0.8}Co_{0.15}Al_{0.05}O_2$ electrodes are typically composed of primary particles of roughly spherical shape with diameters well over 100 nm,[122] and aggregated into spherical secondary objects with diameters over 5 µm. These objects are too thick for the constraints of ptychography, and their strong aggregation makes it difficult to isolate individual primary particles that are intact. Furthermore, their shape makes it impossible to isolate effects in different crystallographic facets. For ptychography, synthesis conditions were controlled to limit growth in the *c* crystallographic axis, to produce well-defined plates that were thin enough to image. To compare the relevance of the observations from these nano-plates with respect to commercial particles, complementary experiments were conducted with conventional STXM. STXM gives a lower spatial resolution (≈30 nm) than ptychography, but is less constrained by sample thickness. The faster data collection provided by STXM also enables spectroscopy at both the Ni L and O K-edges. Figures 31a,d and g show micrographs of these $Li_{1-x}Ni_{0.8}Co_{0.15}Al_{0.05}O_2$ specimens at several states of charge. The objects in these fields of view have convex and irregular shapes and are >1 µm size, suggesting that they are small agglomerates composed of several primary particles, however the lower spatial resolution provided by STXM is insufficient to see individual particle outlines. As with spectro-ptychography, the transmissive nature of this technique means that the "center" spectra also contain contributions from the surface. The presence of a Ni mirror in the beamline's upstream optics caused energy-dependent artifacts

that overlap with features in the Ni $L_{3,2}$-edges. As a result, the intensities and line-shapes of a given spectrum cannot be reliably compared to external spectra. However, relative changes between spectra within the same particle frame-set are likely real if accompanied by corresponding changes in the O K-edge, which is not subject to artifacts from the mirror. We therefore consider these spectra to establish qualitative trends.

Figure 31 shows optical depth maps and optical depth spectra segmented by distance from the particle edge, as in Figure 21, for commercial $LiNi_{0.8}Co_{0.15}Al_{0.05}O_2$ primary particles at several states during first charge. In the pristine specimen (Figure 31a-c), edge spectra showed a greater relative spectral intensity at 853 eV compared to 855 eV. This gradient in the Ni edge was accompanied by a concurrent variation in intensity of a small shoulder at 532 eV in the O K-edge. Both features are associated with the presence of Ni^{II}, mirroring what was observed in the model nano-plate objects. At higher states of charge (Figure 31c,d), the gradient in peak intensities at 532 eV and 853 eV extended farther into the particle. If overcharged to 5.0 V (Figure 29a-c) this gradient extended through the entire particle. No changes were seen in the position of the high-energy peak at ≈855 eV.

The low energy peak at 853 eV appeared to move to lower energies close to the particle edge, though this may be an artifact of the relative peak intensities (modeled in Figure 30). Edge spectra also showed a change in the O main edge with increased intensity coming from a feature at 538 eV. This is attributed to the formation of P–O–F species formed by reaction with the $LiPF_6$ electrolyte.[123] Similar to trends of surface Ni^{II}, the P–O–F feature at 538 eV

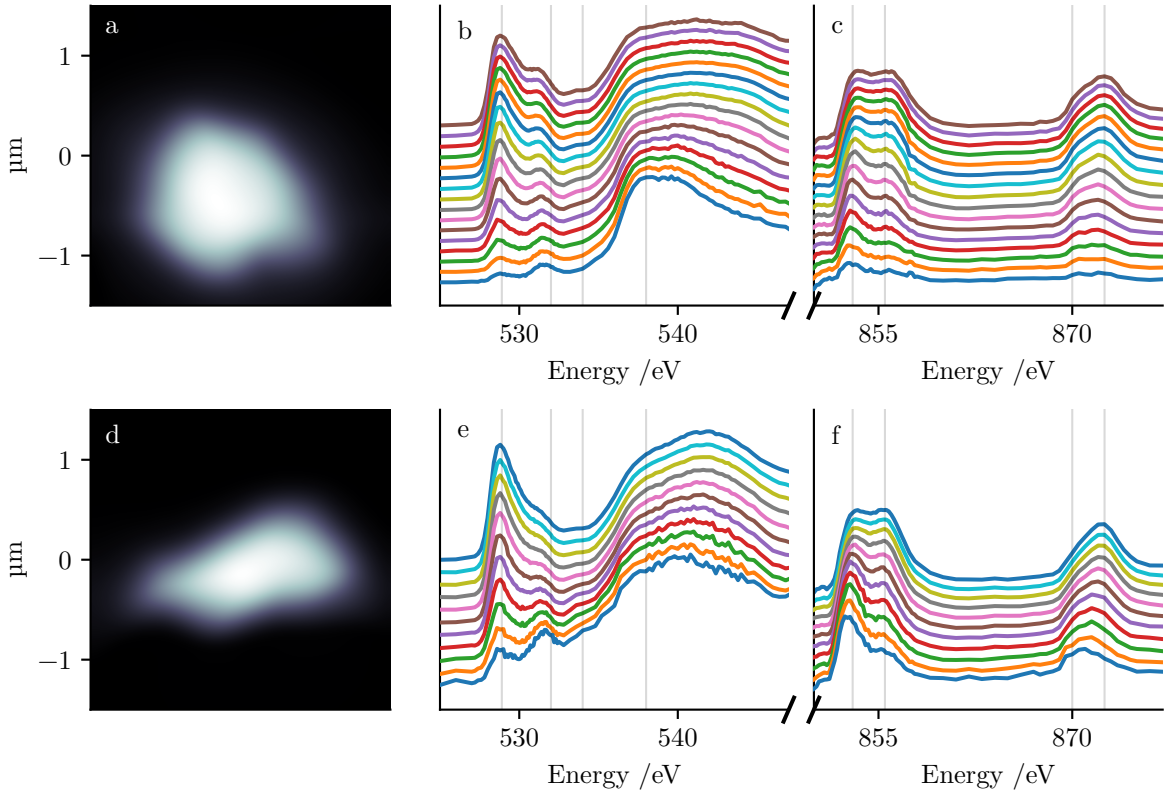

Figure 29: STXM maps with spectra at O K-edge and Ni $L_{3,2}$-edges segmented by distance from particle edge in 30 nm increments for $LiNi_{0.8}Co_{0.15}Al_{0.05}O_2$ particles (a-c) charged to 5.0 V and (d-f) after 200 cycles. Vertical lines added at 528.9 eV ($LiNi_{0.8}Co_{0.15}Al_{0.05}O_2$), 532 eV (NiO), 534 eV ($LiCO_3$), 538 eV (P−O−F), 853.5 eV, 855.5 eV (L_3-edge), 870 eV and 872.5 eV (L_2-edge).

was limited to the particle edge in the pristine specimen (Figure 31b) and extended closer to the center of the particles at higher states of charge (Figures 31e,h).

2.5 Conclusion

$LiNi_{0.8}Co_{0.15}Al_{0.05}O_2$ cathodes are unable to reach their theoretical performance limits. To better understand the underlying processes, we used X-ray spectromicroscopy to measure localized Ni $L_{3,2}$-edges spectra with sub 10 nm resolution for $LiNi_{0.8}Co_{0.15}Al_{0.05}O_2$ primary particles in the pristine state and after charging to 4.0 V and 4.75 V. Multiple modes of advanced statistical analyses provided complementary views of the spectral changes taking place. These analyses, combined with SX-STM, revealed multiple chemical inhomogeneities. An outer region was observed at all potentials, containing Ni primarily in the Ni^{II} state. Comparison to prior TEM results suggests that this outer region was a rock-salt/spinel phase exhibiting poor lithium transport. The reduced outer layer became thicker at higher states of charge: the pristine specimen had an outer region of approximately 15 nm, compared to the 40 nm thickness seen at (4.75 V). This increase was preserved upon subsequent discharge, where the reduced layer extended farther below the edge than in the pristine specimen. Since the reduced layer has poor lithium conductivity, the increase in its thickness during the charge-discharge process is a likely contributor to the poor of cyclability of $LiNi_{0.8}Co_{0.15}Al_{0.05}O_2$ at high potentials.

Below the reduced outer layer, oxidation at low potentials (4.0 V) was mostly uniform. However, at high potentials (4.75 V), a larger region of Ni at an intermediate oxidation state was observed. This intermediate region extended deeper into the particle than the reported rock-salt/spinel phases, so was likely still in a layered structure but was unable to reach the

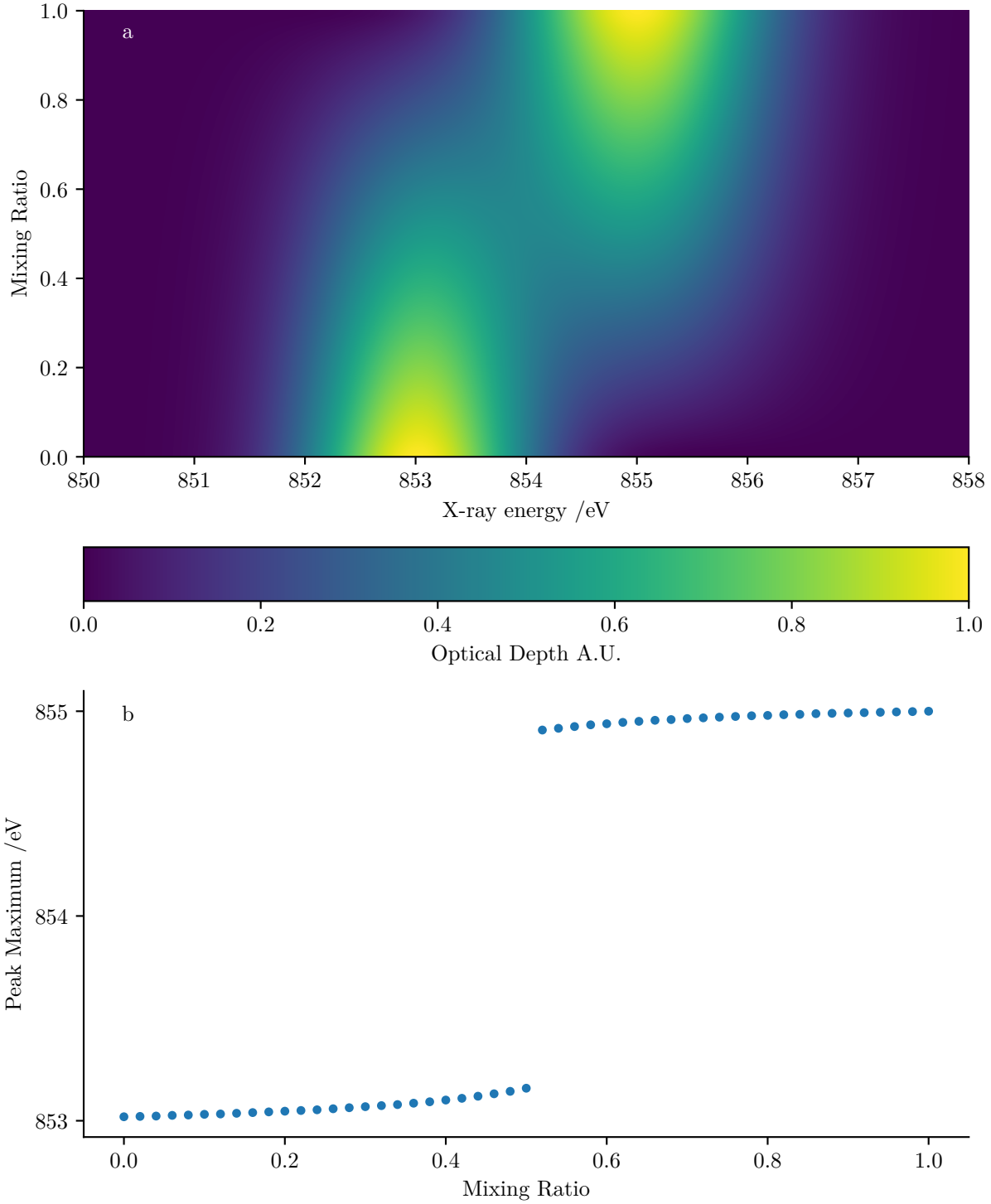

Figure 30: Relationship between mixing ratio of Gaussian peaks and effective overall peak position. (a) Optical depth spectra resulting from linear combinations of normalized peaks at 853 eV and 855 eV in Figure 23 with mixing ratios between 0 and 1. (b) Effective peak maximum of linear combinations of two Gaussian peaks with varying mixing ratios.

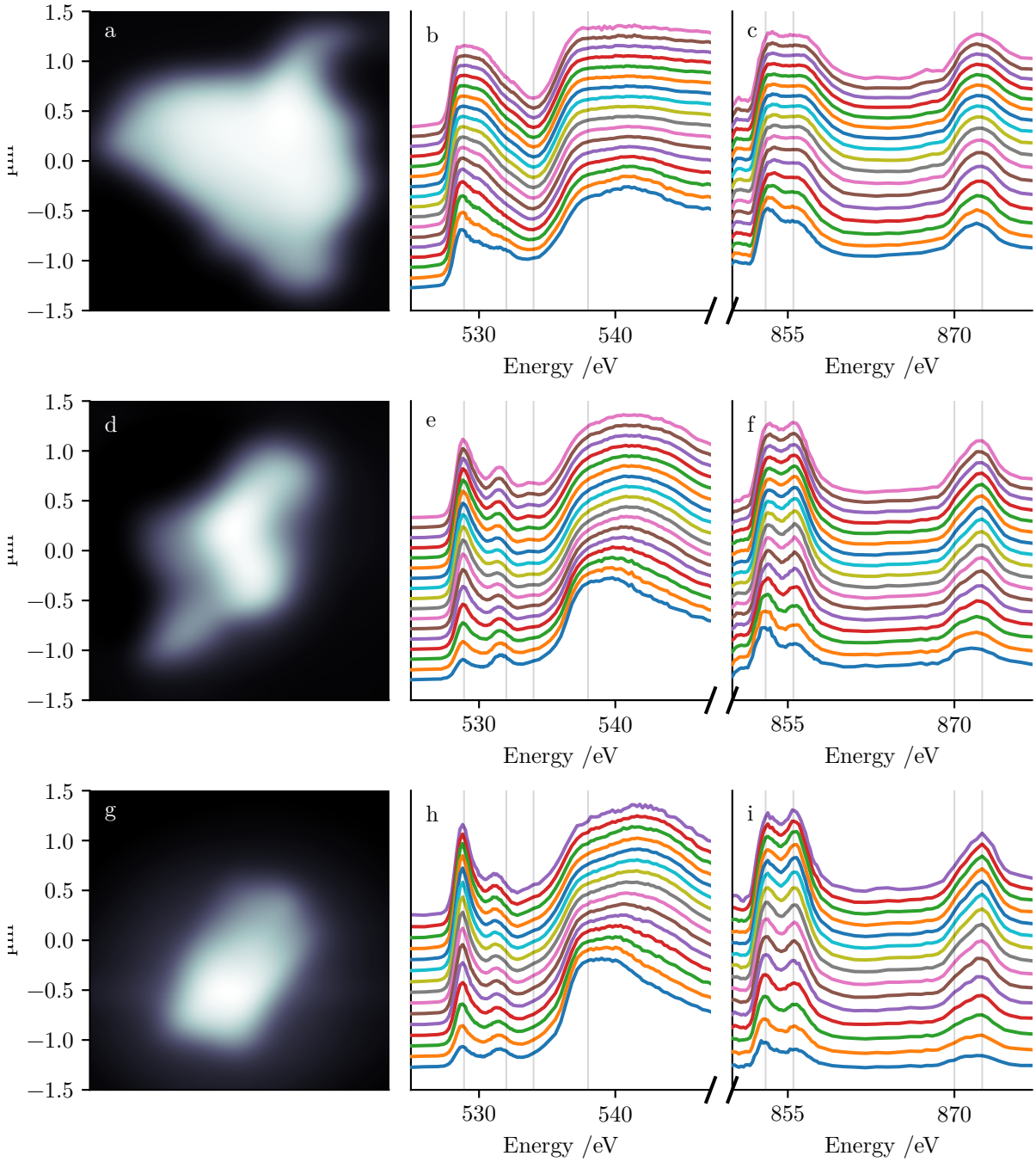

Figure 31: STXM maps with O K-edge and Ni $L_{3,2}$-edges spectra segmented by distance from particle edge in 30 nm increments for $LiNi_{0.8}Co_{0.15}Al_{0.05}O_2$ particles in (a-c) pristine state, and charged to (d-f) 4.2 V ($Li_{0.33}Ni_{0.8}Co_{0.15}Al_{0.05}O_2$) and (g-i) 4.8 V ($Li_{0.1}Ni_{0.8}Co_{0.15}Al_{0.05}O_2$). Vertical lines added at 528.9 eV ($LiNi_{0.8}Co_{0.15}Al_{0.05}O_2$), 532 eV (NiO), 534 eV ($LiCO_3$), 538 eV (P−O−F), 853.5 eV, 855.5 eV (L_3-edge), 870 eV and 872.5 eV (L_2-edge).

fully oxidized state. Oxygen loss may be responsible for the lower oxidation state, while poor nickel back-diffusion inhibits the associated structure transformation. Alternately, poor lithium diffusion through the surface rock-salt phase may prevent complete delithiation. While the outer rock-salt and spinel layers have been the target of extensive characterization, this work uniquely describes their relationship to the underlying layered $LiNi_{0.8}Co_{0.15}Al_{0.05}O_2$, which is a key requirement in overcoming current performance limitations towards future battery systems.

CHAPTER 3

OPERANDO CHEMICAL IMAGING OF SECONDARY PARTICLES OF LAYERED OXIDES

3.1 Introduction

FF TXM provides a means to evaluate heterogeneity within secondary particles of layered cathode materials. This technique produces projection micrographs showing the optical depth of the object with ≈30 nm resolution, depending on the instrument configuration. The tunable nature of synchrotron X-ray sources allows micrographs of the same field of view to be captured at several energies. To produce chemical maps, images are collected at a range of energies spanning an X-ray absorption edge, producing a separate spectrum for each pixel in the field of view and, after data reduction, a chemical map (Figure 10). Since the individual optical depth frames are projections through the specimen, the resulting map shows the average state through the optical axis (perpendicular to the image plane).

The high transmission provided by hard X-rays is conducive to making measurements inside an assembled cell (is-situ) and, ideally, while the cell is actively cycling (operando). In addition to avoiding relaxation effects (Section 1.5.1), in-situ measurement allows the same object to be measured repeatedly at different states of charge. Tracking the same object during a (dis)charge cycle allows for a direct comparison between different states of charge and provides a clearer picture of how heterogeneity evolves. Since FF TXM captures the entire field of view at once,

spatial resolution cannot be tuned by changing the scanning step-size. However, operando FF TXM still requires a balance of spatial, temporal and chemical resolutions, as described in Section 1.5. The instrument's true resolution is partly determined by the contrast-to-noise ratio (CNR) of the resulting image, which depends on exposure time. Increasing the exposure time produces a higher CNR and allows smaller features to be resolved, but also allows fewer images to be captured during an operando experiment resulting in lower temporal resolution. The objective of a given operando TXM XANES experiment determines the optimal balance of these three aspects of resolution.

Ensemble XRD has shown a mixture of phases in $LiNi_{0.8}Co_{0.15}Al_{0.05}O_2$ electrodes during the first charge when stored in ambient conditions, in contrast with the solid-solution, single-phase transformation seen during subsequent charge cycles.[124] A possible origin is the presence of a lithium diffusion barrier arising from surface Li_2CO_3 formation upon exposure to CO_2 and H_2O (Figure 32). When pristine $LiNi_{0.8}Co_{0.15}Al_{0.05}O_2$ was protected from ambient air exposure, a single-phase solid-solution reaction was observed during first charge. This observation led to the conclusion that the secondary particles contained an uneven coating of Li_2CO_3, which must be broken electrochemically before the reaction can proceed. The need to break this coating would produce different timelines for reaction initiation in different particles, resulting in a bimodal distribution of oxidation states and the appearance of non-equilibrium heterogeneity by XRD.[80] The oxidation states of individual secondary particles were measured by operando TXM XANES and, indeed, particles were observed to be either in a pristine or partially oxidized state with more particles becoming oxidized at higher states of charge.[125]

While Li_2CO_3 clearly plays a role in the ability of lithium to penetrate into the secondary particle, it was also demonstrated that the presence of two phases by XRD is suppressed by stronger compaction of the electrode during laminate preparation.[126] A related layered cathode material, $LiNi_{1/3}Mn_{1/3}Co_{1/3}O_2$, is less prone to Li_2CO_3 formation, even showing lower levels of Li_2CO_3 after one month of air exposure than those found in pristine $LiNi_{0.8}Co_{0.15}Al_{0.05}O_2$.[127] In-situ XRD studies of $LiNi_{1/3}Mn_{1/3}Co_{1/3}O_2$ during first charge show a largely single-phase (solid-solution) transformation,[128–130] though some studies reveal two crystallographic phases with a small difference in a and c unit-cell parameters and coexisting over a narrow range of delithiation compared to $LiNi_{0.8}Co_{0.15}Al_{0.05}O_2$.[131,132] The oxidation dynamics of these layered cathode materials warrant further study to clarify the nature of the chemical transformation, especially in view of locating the onset and progression of heterogeneity, within and between the secondary particles that typically compose a cathode. It is important to elucidate how general this behavior is among the general class of layered oxides that are leading candidates as battery materials.

This work further examined the heterogeneities present in secondary particles of established layered cathode materials, namely $LiNi_{1/3}Mn_{1/3}Co_{1/3}O_2$, $LiNi_{0.8}Co_{0.15}Al_{0.05}O_2$, and $LiNi_{0.5}Mn_{0.3}Co_{0.2}O_2$. A series of operando TXM XANES experiments probed both the inter- and intra-particle heterogeneity within particles. While the cell potential and prior reports of ensemble XAS indicated a smooth transition to higher oxidation state upon delithiation,[74,133] individual particles exhibited a sharp and stochastic transition from an initial, latent state to one containing highly oxidized Ni. Optimizations for temporal and spatial resolution revealed

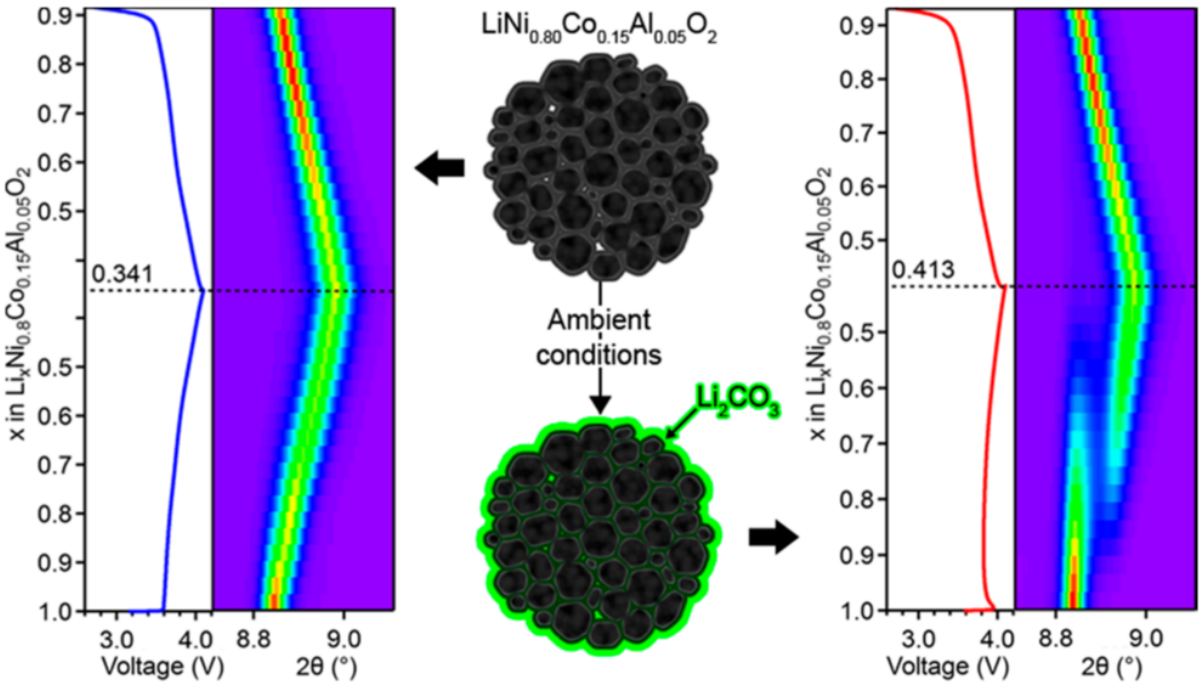

Figure 32: Effect of Li_2CO_3 surface layer on distribution of reaction states in $LiNi_{0.8}Co_{0.15}Al_{0.05}O_2$ during first charge. Operando XRD shows a single phase in pristine $LiNi_{0.8}Co_{0.15}Al_{0.05}O_2$ during charge (left), whereas storage under ambient atmosphere (right) leads to a bimodal distribution of reaction states. Reprinted with permission from Grenier, A. *et al.* Reaction heterogeneity in $LiNi_{0.8}Co_{0.15}Al_{0.05}O_2$ induced by surface layer. *Chem. Mater.* **29,** 7345–7352 (2017). Copyright 2017 American Chemical Society (Appendix A)

internal heterogeneity within secondary particles during charge, and comparison of chemical maps and particle morphology show correlations between internal micro-structure and Ni reduction.

3.2 Materials and Methods

$LiNi_{0.8}Co_{0.15}Al_{0.05}O_2$ (NAT-1050), $LiNi_{1/3}Mn_{1/3}Co_{1/3}O_2$ (NM-3100) and $LiNi_{0.5}Mn_{0.3}Co_{0.2}O_2$ (NCM-045T) were purchased from TODA America, Inc. and either stored under ambient atmosphere (Figures 36, 44, 45, 42, 46, 47, 34a-d) or in a dry room followed by an argon-filled glovebox (Figures 33, 40, 34e,f, 43, 38). $LiNi_{0.8}Co_{0.15}Al_{0.05}O_2$ or $LiNi_yMn_zCo_{1-y-z}O_2$ powder (20 %, TODA) and acetylene black (60 %) were ground in a mortar and pestle, then mixed with polyvinylidene fluoride (Solvay, 2 % in N-methyl-2-pyrrolidone) to equal 20 % of dry composite. The resulting slurry was spread onto battery grade aluminum foil using a cylindrical applicator set to 102 µm coating thickness. Electrode laminate was dried in ambient atmosphere under infrared lamp for ≈15 min and placed in vacuum oven at 110 °C overnight.

Cells for operando TXM were prepared by drilling holes of 800 µm (bottom, cathode-side), 1500 µm (top), or 3000 µm (spacer, anode-side) diameter in the centers of the corresponding coin-cell parts (2032, 316L stainless steel, Hohsen Corp.). 12.7 mm diameters cathodes were assembled in these modified coin-cell parts with 1 M $LiPF_6$ in 1:1 EC/DMC electrolyte and 12.7 mm diameter Li metal anode inside an argon-filled glovebox. Once crimped, holes in coin-cell were covered with 1 µm thick Si_3N_4 windows (Norcada NX5200F) using Torr-Seal vacuum-rated epoxy. Assembled and sealed cells were removed from the glovebox and mounted in the X-ray microscope.

TXM was performed at either the Stanford Synchrotron Radiation Lightsource beamline 6-2c (Figures 43, 44 and 45) or the Advanced Photon Source beamline 8-BM-B (Figures 33, 40, 41, 42, 46, and 47), both equipped with an XRadia transmission microscope. Beamline 6-2c utilizes a 56-pole, 0.9-Tesla Wiggler with 1.2 mrad acceptance focused and $\approx 1 \times 10^{-4}$ energy resolution ($\frac{\Delta E}{E}$). A 60 nm outer-zone-width objective zone-plate was used to render a magnified image on a 2048×2048 charge-coupled device with binning factor 2, producing 1024×1024 intensity images. Beamline 8-BM-B utilizes a bending magnet source. The remaining optical setup is similar to beamline 6-2c.

Operando data acquisition was performed by collecting frames at each energy of both the specimen and a reference frame with no cell or sample in the field of view. Image processing was performed using the xanespy package.[81] Optical depth (OD) images were calculated from the object frame (I) and reference frame (I_0) as

$$OD = \log\left(\frac{I_0}{I}\right)$$

All images within a full operando experiment were aligned using multiple passes (as needed) of the `register_translation` function provided by scikit-image[82] using the mean optical-depth frame as the target image. Image normalization was performed on each frame by subtracting the median optical depth of all background pixels (determined by thresholding using Otsu's method[134]) of that frame.[43] Pixels not containing an appreciable level of Ni spectral signal were masked by calculating the ratio of the edge jump (difference between the post-edge and

pre-edge optical depths) to the standard deviation of the optical depth spectrum. This ratio was calculated for the whole frame-set, then a threshold for the mask was determined using Otsu's method[134] through scikit-image.[82] Spectra for pixels passing this edge filter were then fit with a linear combination of a background line, Gaussian peak and arctangent function:

$$OD(E) = t + s\left[\frac{1}{\pi}\arctan(\sigma(E - E_0)) + \frac{1}{2} + a\mathrm{e}^{\frac{-(E-E_0-b)^2}{2c^2}} + m(E - E_0)\right] \tag{3.1}$$

with fitting parameters σ to control the width of the arctangent edge jump; a, b, c to control the height, position and width of the Gaussian whiteline peak; m to control the slope of the background; E_0 to represent the absolute energy of the edge; and s, t to control the overall scale and vertical offset of the spectrum. Fitting was performed with the `scipy.optimize.leastsq` wrapper around the MINPACK `lmdif` routine.[135] Whiteline positions were extracted by re-sampling the above parametric function with 200 energies and selecting the energy of maximum optical depth. Plotting was performed using matplotlib.[136]

3.3 Results

3.3.1 $LiNi_{1/3}Mn_{1/3}Co_{1/3}O_2$ Inter-particle Dynamics

Dilute (20%) $LiNi_{1/3}Mn_{1/3}Co_{1/3}O_2$ electrodes were assembled in modified coin-cells, and operando TXM XANES frame-sets were collected during the first galvanostatic charge/discharge cycle (Figure 33a,b). After an initial resting phase, the potential increased once a constant current was applied. As the potential reached ≈4.0 V, a peak was observed in the rate of change of the cell potential (Figure 34a,b). This rate of change is the inverse of the more

common $\frac{dQ}{dV}$, where the applied current provides the proportionality constant between dt and dQ. This increase in rate of change of cell potential was consistent with previous reports for $LiNi_{1/3}Mn_{1/3}Co_{1/3}O_2$.[131,137–145] A sharp feature in the potential was observed at the start of charging (t=4 h in Figure 33b). This initial peak is more commonly observed in high-Ni layered cathodes[131,146,147] where it has been associated with low diffusivity surface layers,[80] but has also been reported for $LiNi_{1/3}Mn_{1/3}Co_{1/3}O_2$.[141] Limited formation of surface Li_2CO_3 was expected due to the cathode material being stored and manipulated in a dry room or argon-filled glovebox, thereby limiting exposure to CO_2 and H_2O. The profile at the start of oxidation in layered TM-oxide cathodes is further influenced by the synthesis conditions of the active material,[140,145] and is at least partly rate-dependent.[91,148]

Localized XAS K-edge spectra were produced from operando TXM frame-sets and then averaged over either individual particles or an entire field-of-view to maximize spectral resolution. Example TXM frames showing several particles in a field of view are shown in Figure 35. Upon delithiation, a progressive increase was seen in the energy of the absorption edge and the associated whiteline (Figures 36 and 37). Comparison of the Ni near-edge structure at increasing degrees of delithiation revealed an isobestic point at 8351 eV (Figure 36a), often associated with the co-existence of two spectroscopic signals with varying contributions to the observed spectrum. Ideally, chemically pure reference samples are prepared for the two constituents and the observed spectra analyzed by linear combination fitting of the two reference spectra, as is done for $LiFePO_4$.[94] However, the absence of a miscibility gap for layered cathodes prevents the preparation of chemically pure reference samples. Instead, a more direct approach is used.

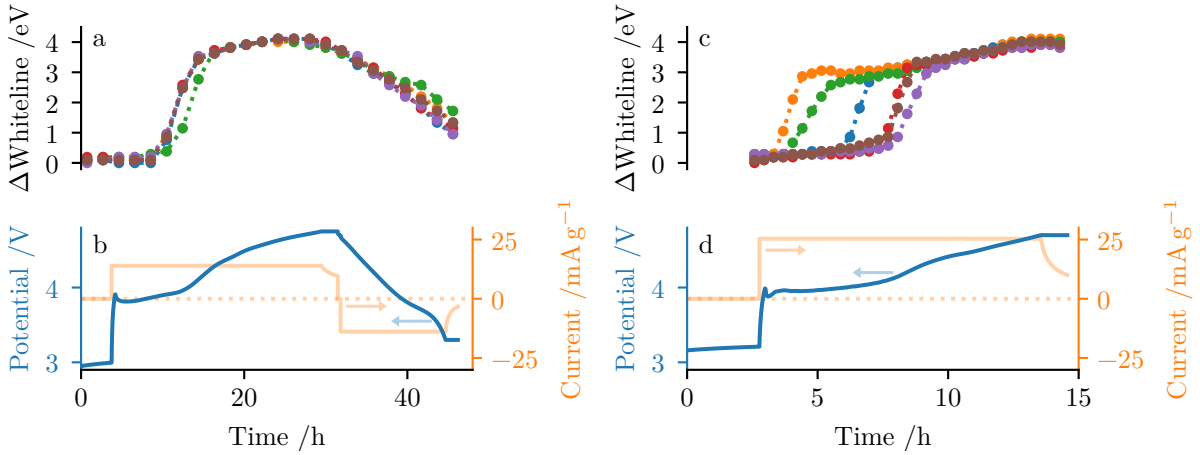

Figure 33: Particle-level oxidation during first charge and discharge of $LiNi_{1/3}Mn_{1/3}Co_{1/3}O_2$. (a) Changes in mean whiteline energies relative to 8351.69 eV for secondary particles during first charge and discharge. (c) Changes in mean whiteline energies relative to 8351.22 eV for secondary particles with higher temporal resolution. (b,d) Operando potential (—) and current (—) for galvanostatic cycling with 4.75 V potentiostatic step for $LiNi_{1/3}Mn_{1/3}Co_{1/3}O_2$ samples in modified coin-cells.

Figure 36b shows spectral mixing of the two extremes from Figure 36a in ratios ranging from 0 to 1. Since the whiteline peak is broad relative to the energy difference between the two components, the maximum of the linear combinations changes smoothly over the full range of spectral mixing (Figure 36c). This allows the whiteline position to be used directly as an approximation of Ni oxidation. Instead of simply selecting the energy with maximum optical depth for a given pixel, the full spectrum at each TXM pixel was fit with a combination of a background line, arctangent function, and Gaussian peak (Equation 3.1 and Figure 38), after which the whiteline energy was extracted from the fit parameters. In addition to providing a

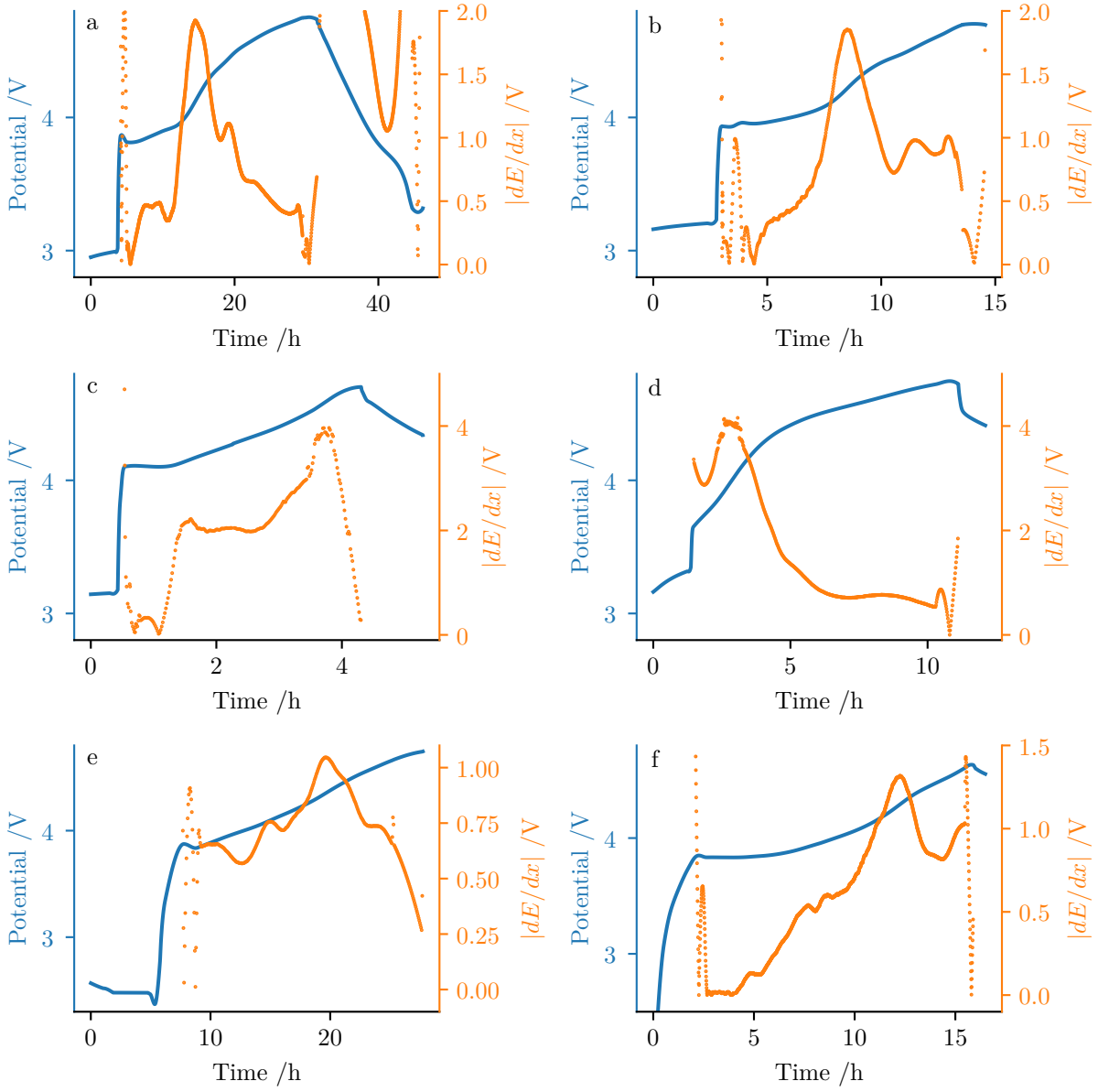

Figure 34: Cell potential (—) and derivative of potential with respect to x in Li_xMO_2 (···) during galvanostatic charge/discharge. (a,b) $LiNi_{1/3}Mn_{1/3}Co_{1/3}O_2$ cathode in modified coin-cell during first charge, (c) $LiNi_{0.8}Co_{0.15}Al_{0.05}O_2$ cathode in pouch-cell during first charge, (d) $LiNi_{0.8}Co_{0.15}Al_{0.05}O_2$ cathode in pouch-cell during second charge, (e) $LiNi_{0.8}Co_{0.15}Al_{0.05}O_2$ cathode charged in modified coin-cell, and (f) $LiNi_{0.5}Mn_{0.3}Co_{0.2}O_2$ cathode charged in modified coin-cell. All galvanostatic profiles treated with third-order Sovitzky-Golay filter with 101-point window prior to calculating derivative.

precision beyond the energy resolution of the instrument, this approach was more tolerant of noise in individual micrographs since the fitting routine relied on the entire spectrum as input.

Fields of view containing multiple secondary particles were selected from within the coin-cell window (Figure 35), allowing comparison of the dynamics between separate particles. Since different layered materials have different starting Ni oxidation states and therefore different whiteline positions (Table I and Figure 39), whiteline energies were compared to the lowest value observed for any particle in the field of view during the operando experiment, reported here as Δwhiteline. The mean energies for several $LiNi_{1/3}Mn_{1/3}Co_{1/3}O_2$ secondary particles are shown in Figure 33a. Initially, the whiteline energies were constant, indicating no Ni oxidation. After $\approx$10 h, the whiteline energy increased rapidly by $\approx$3.75 eV over a period of 5 h. Five out of the six particles underwent this rapid oxidation simultaneously, while the remaining particle transitioned within the next 2 h. Over the remaining 15 h of the charge cycle, the particle whiteline positions increased gradually by an additional 0.6 eV. This particle-level behavior is in contrast with the that seen by in-situ ensemble-average XAS,[133] which shows a gradual increase in whiteline position over the full range of delithiation (Table I and Figure 39a). The total change in whiteline energy for all observed secondary particles was $>$4 eV (Figure 33a). While ensemble XAS studies[74,133] did not reach the 4.7 V cell cut-off potential needed for full lithium extraction and hence full Ni oxidation, extrapolation of the trend in Table I and Figure 39a predicts a change in whiteline energy upon full delithiation of $\approx$3 eV. This discrepancy between particle-level and ensemble average Ni oxidation suggests that an appreciable portion of the particles in the specimens measured by ensemble XAS had not

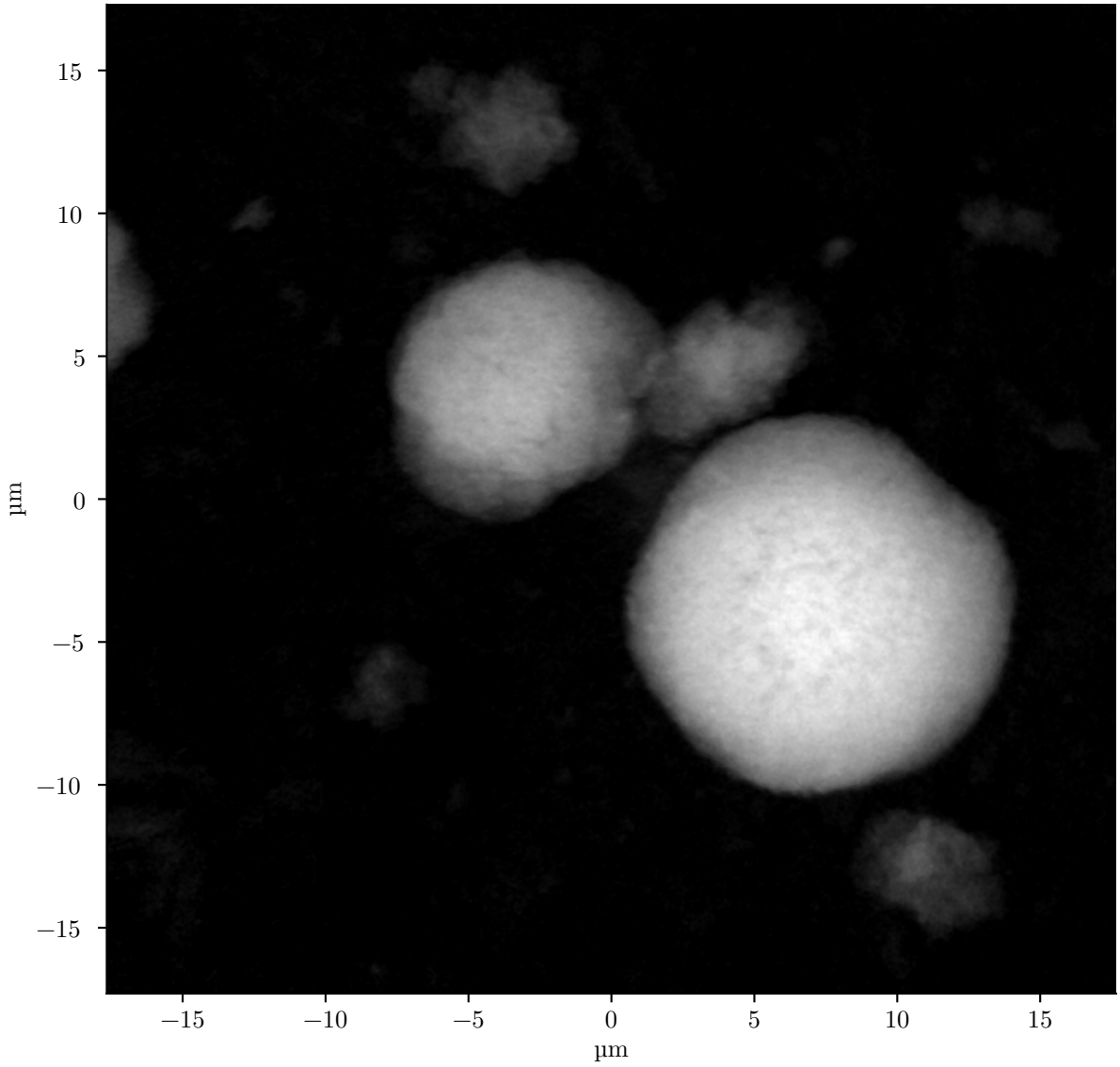

Figure 35: Select single-energy frames used for operando TXM XANES. Optical depth of secondary particles of (a) $LiNi_{1/3}Mn_{1/3}Co_{1/3}O_2$ at 8640 eV, (b) $LiNi_{0.5}Mn_{0.3}Co_{0.2}O_2$ at 8490 eV, and (c) $LiNi_{0.8}Co_{0.15}Al_{0.05}O_2$ at 8640 eV.

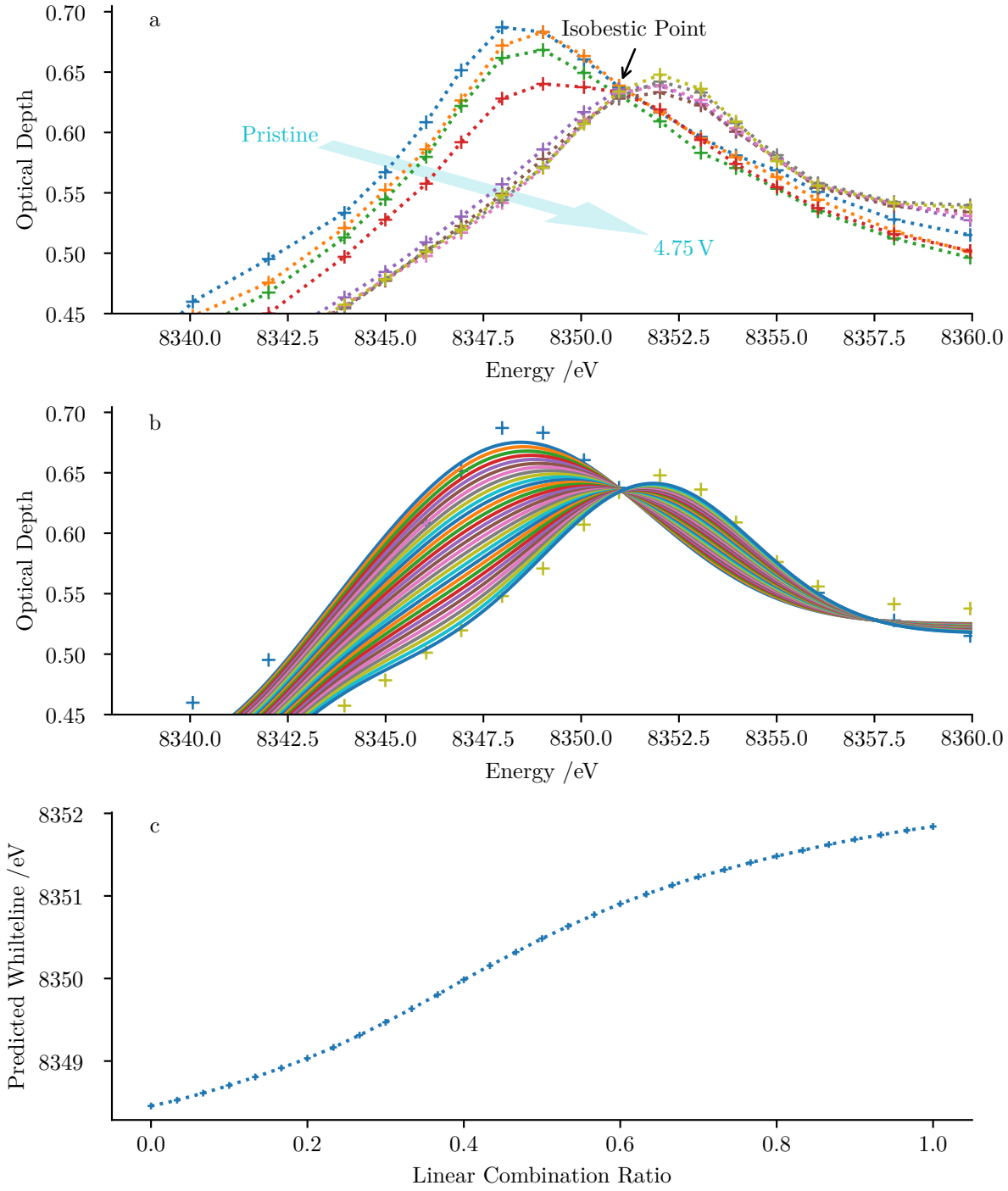

Figure 36: Demonstration of isobestic point for $LiNi_{1/3}Mn_{1/3}Co_{1/3}O_2$ Ni K-edge. (a) Observed mean optical depth spectra for TXM frames during operando oxidation, with dashed lines added as visual guides. (b) Results of mathematical linear combinations of fit spectra (—) for observed spectral end-members for the most reduced (+) and oxidized (+) points in the $LiNi_{1/3}Mn_{1/3}Co_{1/3}O_2$ frames in (a). (c) Effect of linear combination ratio of spectral end-members in *b* on resultant whiteline energy.

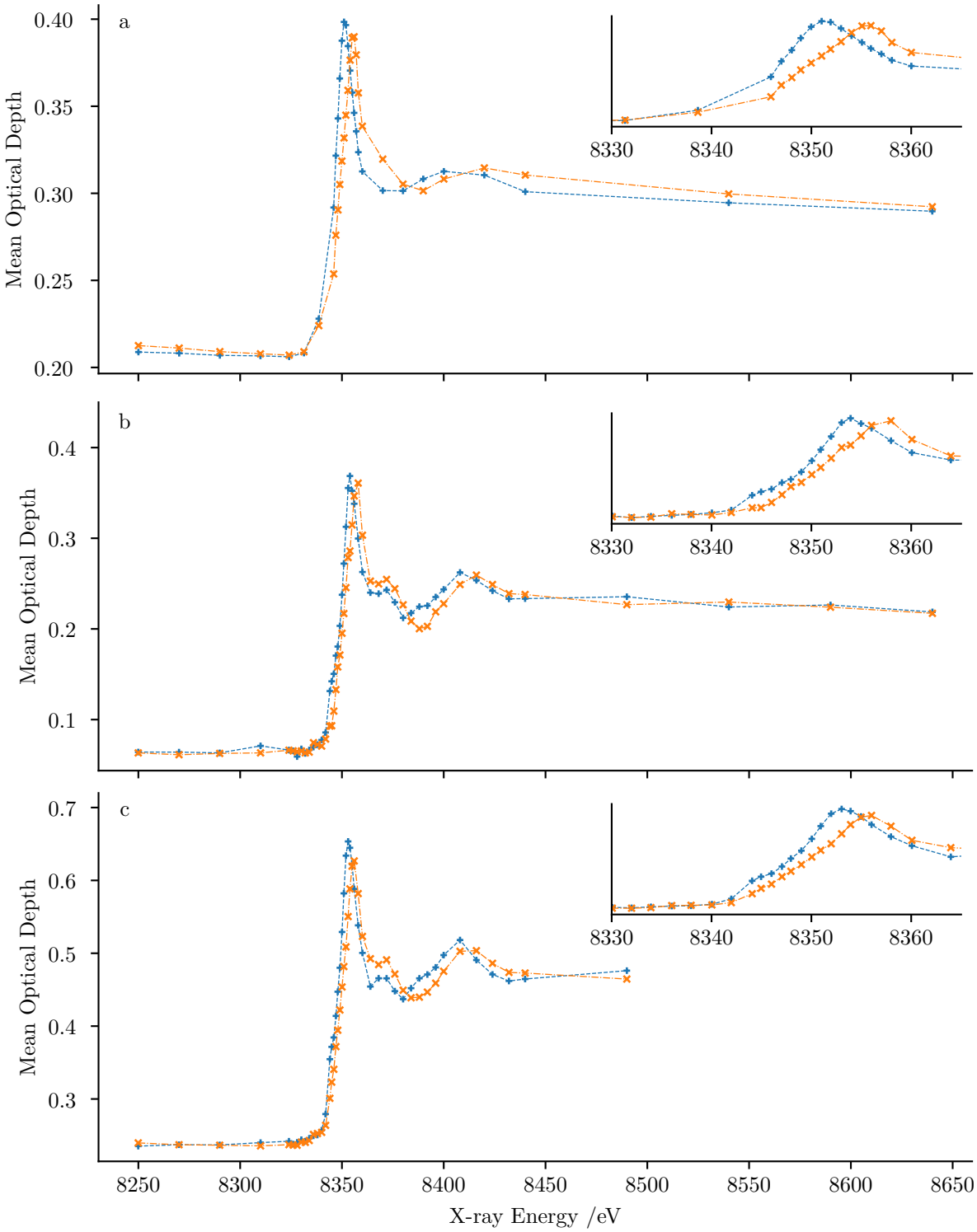

Figure 37: Ni K-edge absorption spectra for TXM fields of view. Mean optical depth of pixels after edge filter for (-+-) most reduced and (·×·) most oxidized time-steps for (a) $LiNi_{1/3}Mn_{1/3}Co_{1/3}O_2$, (b) $LiNi_{0.8}Co_{0.15}Al_{0.05}O_2$, and (c) $LiNi_{0.5}Mn_{0.3}Co_{0.2}O_2$.

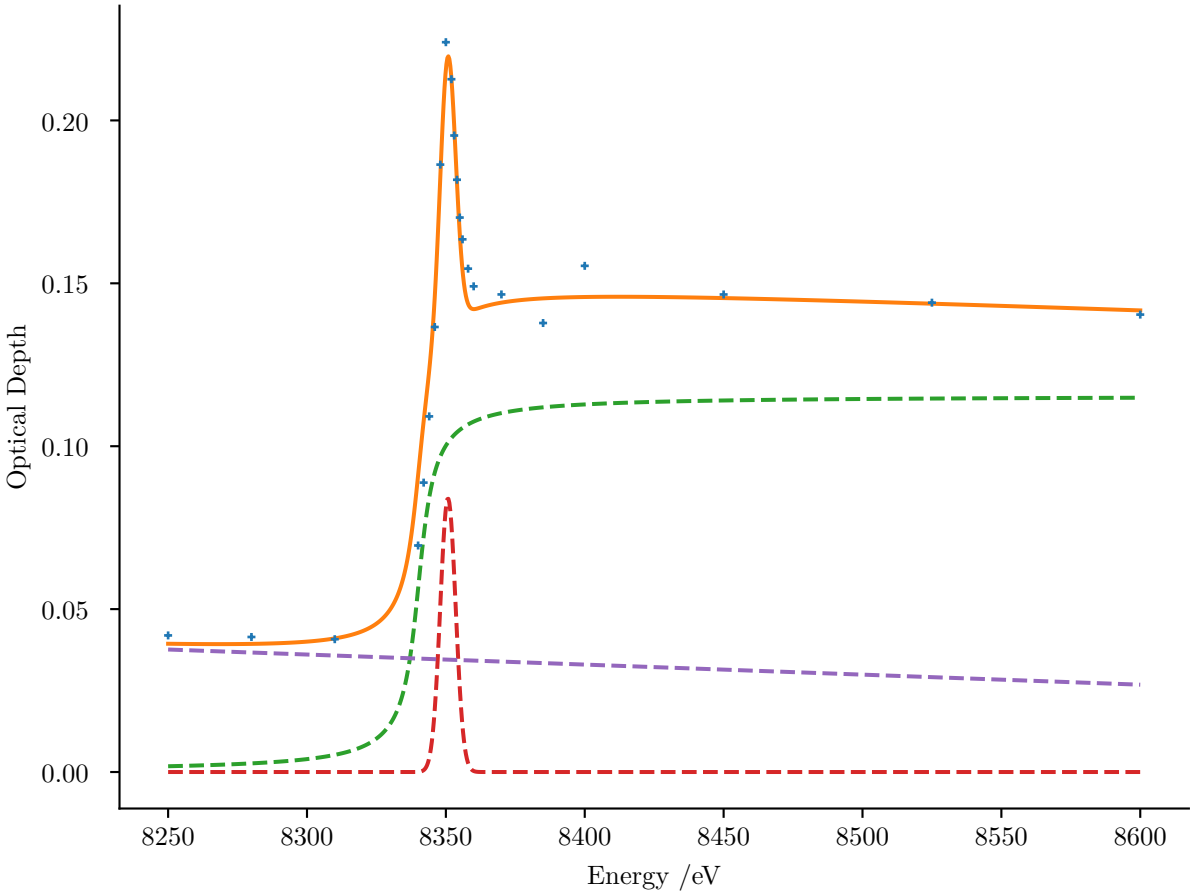

Figure 38: Sample decomposition of Ni K-edge fitting. Spectrum of mean optical depth of a frame of $LiNi_{0.8}Co_{0.15}Al_{0.05}O_2$ particles as (+) observed optical depth; (—) overall least squares fit; and (- -) arctangent, (- -) Gaussian and (- -) background components of least squares fit.

$Li_xNi_{1/3}Mn_{1/3}Co_{1/3}O_2$			$Li_xNi_{0.8}Co_{0.15}Al_{0.05}O_2$		
x	Whiteline /eV	Δ /eV	x	Whiteline /eV	Δ /eV
0.945	8353.98	0.21	1.00	8348.84	0.00
0.751	8354.72	0.94	0.80	8349.61	0.78
0.570	8355.45	1.68	0.60	8350.14	1.30
0.386	8356.12	2.35	0.25	8350.78	1.95
0.257	8356.43	2.66	0.00	8351.16	2.32

TABLE I: Reported energies of Ni K-edge whiteline. In-situ XAS of $LiNi_{1/3}Mn_{1/3}Co_{1/3}O_2$ (Ref.[133]) and ex-situ XAS $LiNi_{0.8}Co_{0.15}Al_{0.05}O_2$ (Ref.[74]). Data extracted from published figures using WebPlotDigitizer.[149] Relative shifts in whiteline energy (Δ) calculated as difference from fully lithiated state (x=1).

reached their fully oxidized states. During discharge (Figure 33a), the particles' whitelines gradually moved to lower energies, indicating gradual reduction of Ni. The whiteline energy did not return to the pristine starting point, demonstrating that the particles did not reach fully reduced Ni when discharged to 3.3 V.

A second experiment was conducted during the first charge cycle, but optimized for time resolution (Figure 33c,d). The same initial latent phase and subsequent rapid oxidation were seen, however individual particles underwent the rapid oxidation asynchronously over the 5 h window (Figure 33c). Once rapid oxidation had occurred, the subsequent gradual increase to 4.1 eV was again observed. In both experiments, the peak in the rate of change of the potential ($\frac{\mathrm{d}E}{\mathrm{d}t}$, Figure 34a,b) occurred once all particles had undergone that rapid transition in oxidation state (Figure 33a,c).

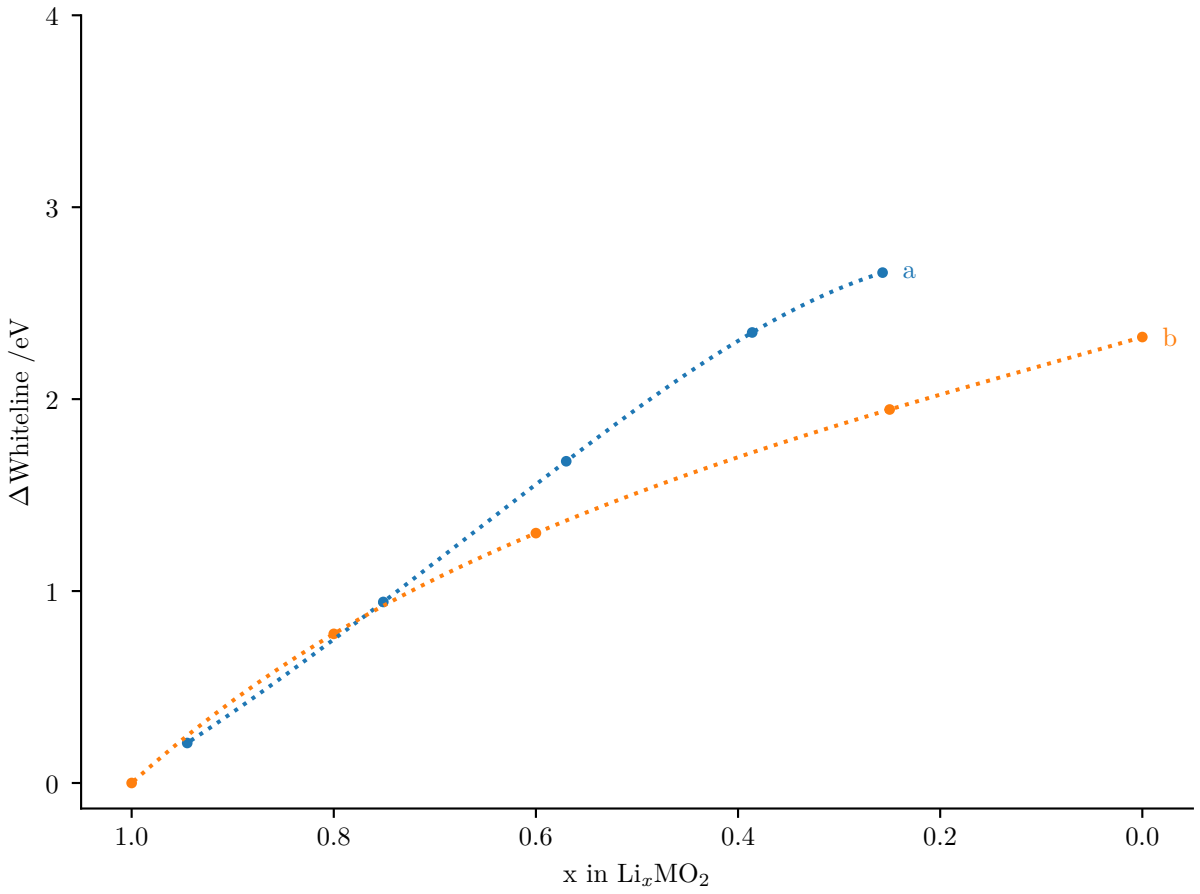

Figure 39: Reported changes of Ni K-edge whiteline energy. (a) In-situ XAS of $Li_xNi_{1/3}Mn_{1/3}Co_{1/3}O_2$ and (b) ex-situ XAS of $Li_xNi_{0.8}Co_{0.15}Al_{0.05}O_2$. Data extracted from published figures as described in Table I.

3.3.2 $LiNi_{1/3}Mn_{1/3}Co_{1/3}O_2$ Intra-particle Dynamics

An additional benefit of optimization for high temporal resolution was that two particles were measured during the rapid transition to higher whiteline energies (Figure 40). Both objects showed boundaries between regions with different whiteline positions and hence between regions of reduced and oxidized Ni (Figure 40c-e,g-i). These boundaries did not appear to significantly move within the particle during the transition in whiteline energy. While it is tempting to interpret these boundaries as occurring within secondary particles, the projection nature of transmission microscopy makes it difficult to determine if objects such as those in Figure 40 are isolated particles or multiple particles separated along the optical axis. One object showed a correlation between the boundaries in whiteline energy (Figure 40c-e) and several sharp boundaries in optical depth (Figure 40b). This suggests that the observed boundary in the whiteline maps was due to different extents of oxidation of separated agglomerates. This conclusion is supported by the observation that the object also showed a more gradual transition in whiteline energy (Figure 40a) since the measured changes in whiteline energy are the average of at least two distinct particles. The other object did not contain noticeable boundaries in optical depth, though it did exhibit extensive fracturing (Figure 40f)). This implies, though does not demonstrate conclusively, that the object is a single agglomerate. This object also exhibited a transition to higher whiteline energies with a speed consistent with the other particles in the field of view (see slope in Figure 40a).

During discharge, the rapid transition in whiteline energy was not observed (Figure 41a) and no distinct boundaries were seen in oxidation state maps (Figure 41c-e,g-i). Instead, lines

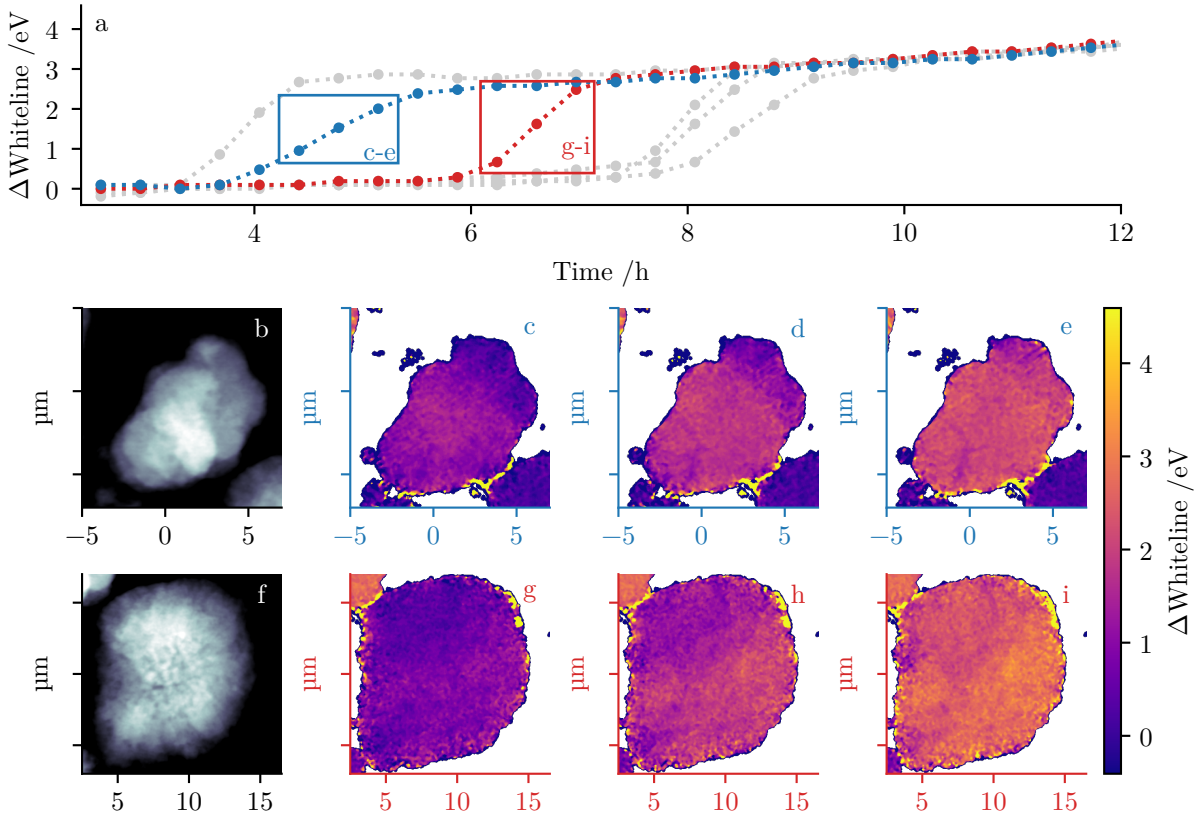

Figure 40: Chemical heterogeneity within $LiNi_{1/3}Mn_{1/3}Co_{1/3}O_2$ particles during first charge. (a) Changes in mean whiteline energies relative to 8351.41 eV for $LiNi_{1/3}Mn_{1/3}Co_{1/3}O_2$ particles. (b,f) Mean optical depth of select particles across all energies and time-steps. (c,d,e,g,h,i) Maps of changes in whiteline energies relative to 8351.41 eV during transitions indicated on (a).

of lower whiteline energy (reduced Ni) within the whiteline maps were observed (arrows in Figure 41d,h). These regions did not correspond to noticeable features in the optical depth maps (Figure 41b,f).

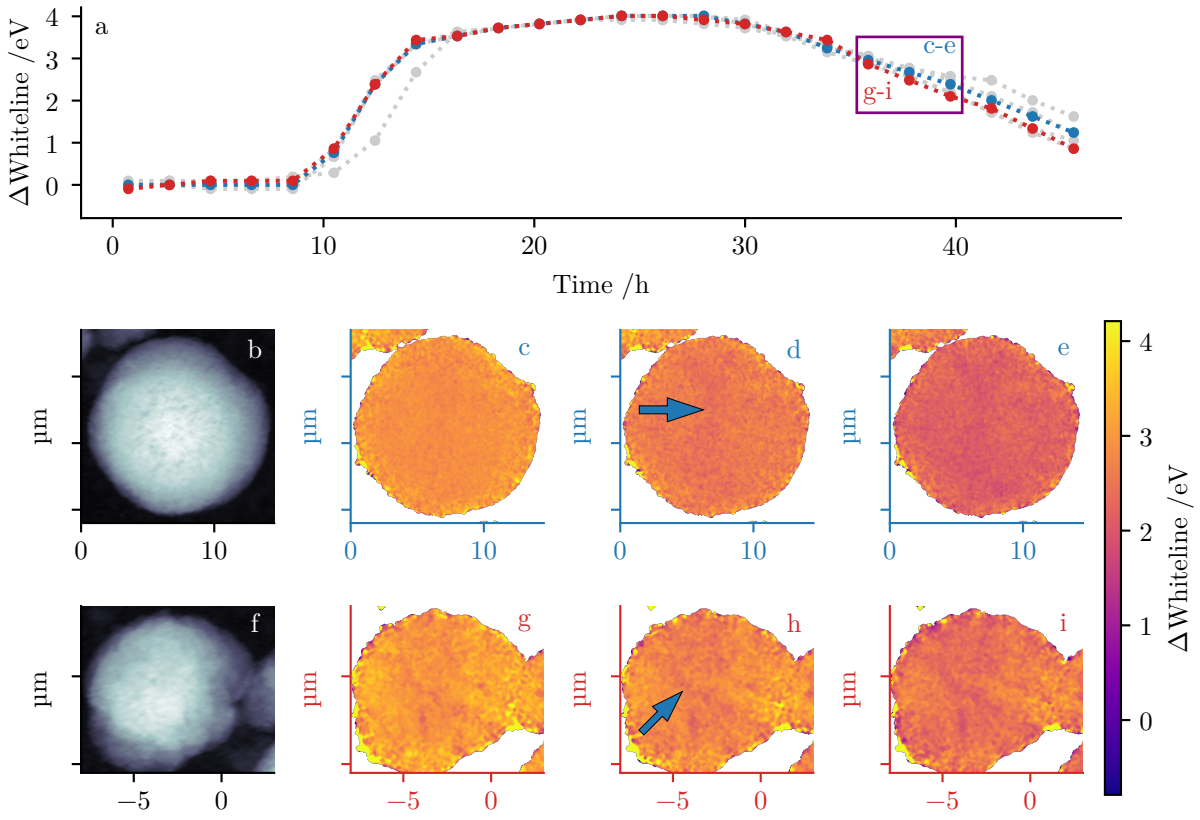

Figure 41: Chemical heterogeneity within $LiNi_{1/3}Mn_{1/3}Co_{1/3}O_2$ particles during first charge and discharge. (a) Changes in mean whiteline energies relative to 8351.79 eV for $LiNi_{1/3}Mn_{1/3}Co_{1/3}O_2$ particles. (b,f) Mean optical depth of select particles across all energies and time-steps. (c,d,e,g,h,i) Maps of changes in whiteline energies relative to 8351.79 eV during transitions indicated on (a). Arrows indicate features discussed in the text.

3.3.3 $\underline{\mathbf{LiNi_{0.8}Co_{0.15}Al_{0.05}O_2}}$

A dilute (20 %) $LiNi_{0.8}Co_{0.15}Al_{0.05}O_2$ cathode was prepared and charged in an operando TXM experiment (Figure 42) similar to those using $LiNi_{1/3}Mn_{1/3}Co_{1/3}O_2$ discussed above. Galvanostatic electrochemistry exhibited a gradual increase in cell potential (Figure 42c), with a slight increase in the rate of potential increase after 20 h (Figure 34e). A small initial peak in cell potential was observed at 7 h, and was less pronounced than the peak observed when charging an $LiNi_{1/3}Mn_{1/3}Co_{1/3}O_2$ cathode (Figure 33b,d). The whiteline energies of individual particles exhibited an initial latent stage followed by rapid increase after 9 h, then a gradual increase until reaching the fully charged state (Figure 42a). This behavior is similar to that observed in $LiNi_{1/3}Mn_{1/3}Co_{1/3}O_2$, except with a smaller overall change in whiteline energy. This difference in whiteline energy range is also observed in ensemble XAS (Table I and Figure 39) and reflects the smaller change in formal nickel oxidation state: $Ni^{III} \longrightarrow Ni^{IV}$ for $LiNi_{0.8}Co_{0.15}Al_{0.05}O_2$ compared to$Ni^{II} \longrightarrow Ni^{IV}$ for $LiNi_{1/3}Mn_{1/3}Co_{1/3}O_2$.[23]

The possibility of the rapid oxidation dynamics being the result of using modified coin-cells was investigated by operando TXM of a dilute (20 %) $LiNi_{0.8}Co_{0.15}Al_{0.05}O_2$ electrode using pouch-cells in a mount fitted with beryllium windows. These rigid windows ensured even application of pressure to the battery stack, including the region being imaged.[150] The galvanostatic charging profile exhibited an initiation peak once current was applied (Figure 43b), despite the cathode material being stored and manipulated in a dry room or argon-filled glovebox, thereby limiting the formation of Li_2CO_3. Changes in whiteline energy were tracked for a secondary particle during first charge, and again underwent an initial latent

stage following by a rapid increase in whiteline energy (Figure 43a). However, in contrast to previous experiments, the rapid transition occurred during open-circuit conditions after the cell had reached the upper cut-off potential (Figure 43b), indicating a large over-potential for this transformation to complete.

To investigate inter-particle dynamics during the second cycle, a cell was prepared with a dilute (20 %) cathode and put through an initial galvanostatic charge/discharge cycle between 4.75 V to 3.0 V outside the instrument before operando TXM XANES during the second cycle (Figure 43c,d). The rate of change of the potential was initially high, decreasing after 5 h (Figure 34d). This change in electrochemical profile suggests a notable increase in over-potential in the experiment, likely due to degradation of the dilute electrode. The particles exhibited a gradual increase in whiteline energy (Figure 43c) compared to the behavior observed during the previous experiments during the first-cycle. However, an initial period of slow oxidation was still observed, followed by a more rapid transition after 5 h. The difference between these rates of oxidation during the second charge were less dramatic than those observed during the first charge (Figures 43a and 42a). During the second discharge, a small, gradual decrease in oxidation state, without returning to the original state, was again observed in all particles (Figure 43c).

Heterogeneity within individual $LiNi_{0.8}Co_{0.15}Al_{0.05}O_2$ particles was investigated by operando TXM XANES during first discharge by using increased X-ray flux, providing a higher contrast-to-noise ratio and better resolution of particle features. However, the increased X-ray dose has the ability to cause particle disintegration at high potentials during the first charge. To avoid

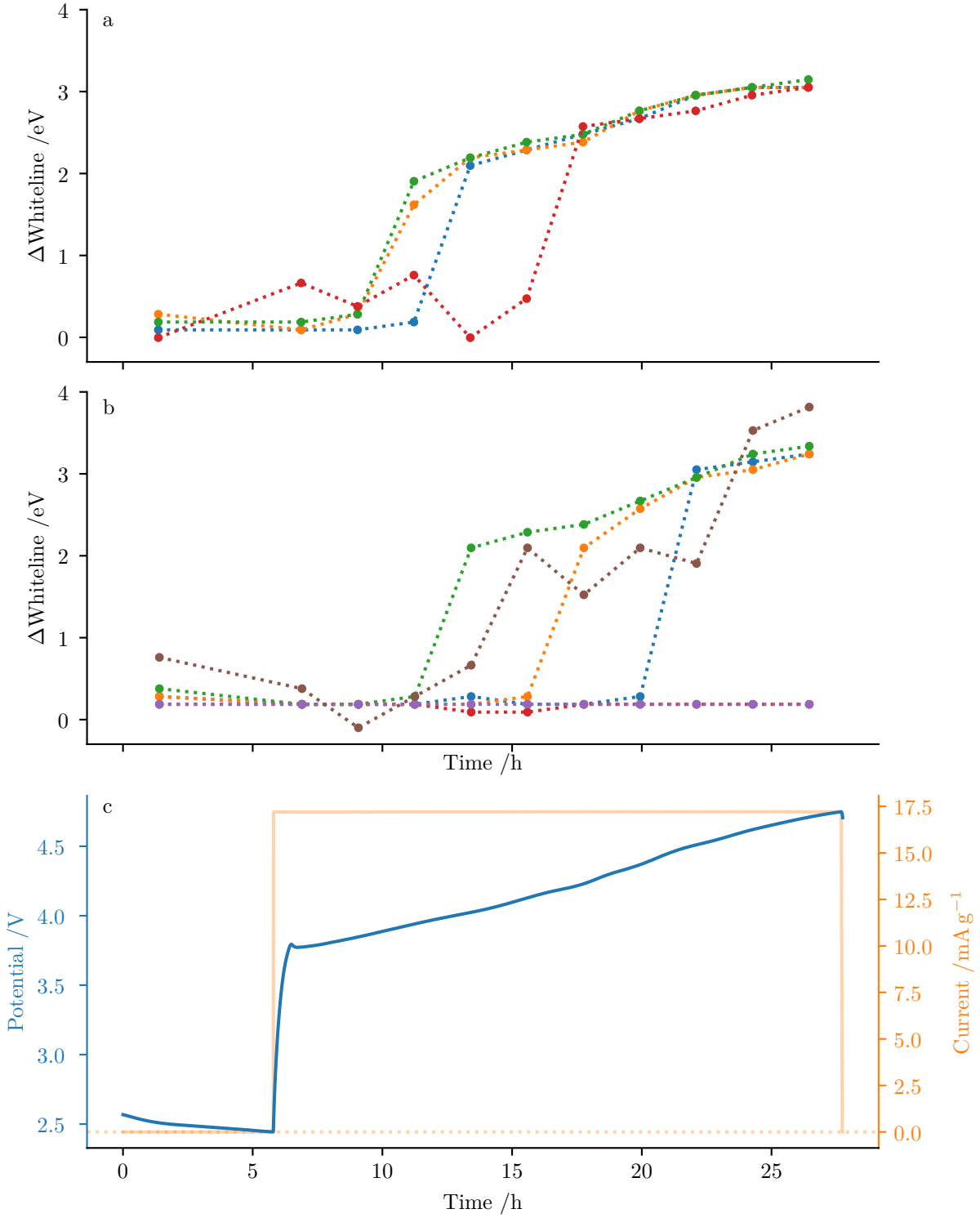

Figure 42: Operando TXM of secondary $LiNi_{0.8}Co_{0.15}Al_{0.05}O_2$ particles during first charge. Mean changes in whiteline energies relative to 8354.18 eV for secondary particles (a) without static X-ray exposure, and (b) with a 3 h static X-ray exposure prior to operando imaging. (c) Galvanostatic charging profile for modified coin-cell with $LiNi_{0.8}Co_{0.15}Al_{0.05}O_2$ cathode.

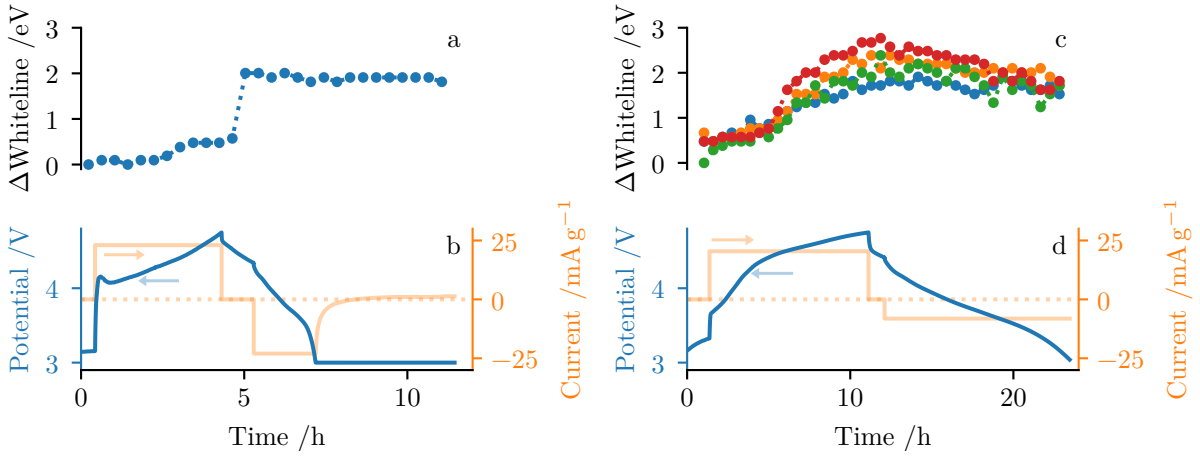

Figure 43: Particle-level oxidation during first and second discharge of $LiNi_{0.8}Co_{0.15}Al_{0.05}O_2$ samples in pouch cells. (a) Changes in mean whiteline energies relative to 8350.92 eV for secondary particle during first charge/discharge cycle. (c) Changes in mean whiteline energies relative to 8350.45 eV for secondary particles during second charge and discharge cycle. (b) Operando potential (—) and current (—) for galvanostatic oxidation, open-circuit potential, galvanostatic reduction, and potentiostatic reduction during first cycle. (d) Operando potential (—) and current (—) for galvanostatic oxidation, potentiostatic oxidation, and galvanostatic reduction during second cycle.

this disintegration, the cell was first partially charged to 4.1 V with no X-ray exposure, then imaged by operando TXM during the subsequent remaining charge to 4.3 V and first discharge to 2.7 V (Figure 44a). The same field of view was measured at the start and end of the first discharge cycle (Figure 44b-e). Comparison of optical depth maps from before (Figure 44b) and after discharge (Figure 44d) showed the development of visible fractures during discharge, a continuation of fracturing previously shown to occur within $LiNi_{0.8}Co_{0.15}Al_{0.05}O_2$ secondary particles during first charge.[151,152] Whiteline maps at the start of the discharge cycle revealed some particles with exterior regions of lower whiteline energy and thus reduced nickel (Figure 44c), observations which are similar to previous reports.[125] Upon completion of the first discharge, these exterior regions continued to exhibit lower whiteline energies compared to the rest of the particle, even as the average whiteline energy of the particle decreased (Figure 44e). Comparison of spectra from select pixels of an $LiNi_{0.8}Co_{0.15}Al_{0.05}O_2$ particle before and after discharge (Figure 44f-i) show that the difference in whiteline energy between the more reduced exterior region and the more oxidized interior region decreased from 1.43 eV prior to discharge (Figure 44f,g) to 1.24 eV after discharge (Figure 44h,i). This difference indicates that the more oxidized regions in Figure 44c underwent a slightly larger change in their extent of Ni reduction during discharge than the reduced outer regions. More generally, the degree of heterogeneity observed during discharge of $LiNi_{0.8}Co_{0.15}Al_{0.05}O_2$ particles was higher than that observed in $LiNi_{1/3}Mn_{1/3}Co_{1/3}O_2$ (Figure 41).

In addition to the reduced outer regions, evidence of internal heterogeneity, similar to $LiNi_{1/3}Mn_{1/3}Co_{1/3}O_2$ in Figure 41i, was also observed in other particles of this field of view

after discharge (Figures 44c,e and 45). These features are spatially correlated with the fractures found in the optical depth images (Figure 44d). Profiles over the same line path (horizontal line in Figure 45e) before and after discharge showed the formation or expansion of local minima in the optical depth of the particle (Figure 45c,d), indicating the formation and/or enlargement of fracture lines. In some cases, these fractures correlated with the emergence of valleys in the whiteline energy profile (4.25 µm, 4.88 µm, 6.05 µm and 6.78 µm in Figure 45a,b), indicating the formation of reduced Ni along particle cracks during discharge. Previous reports have shown a corresponding correlation of oxidized Ni to crack formation after extensive cycling and particle degradation.[153] These observations suggest that the presence of fractures in the particle micro-structure promotes (de)lithiation at the newly exposed surfaces. Furthermore, these regions of reduced nickel resembled more pronounced versions of the line of lower whiteline energy (reduced Ni) seen in $LiNi_{1/3}Mn_{1/3}Co_{1/3}O_2$ particles during discharge (arrows in Figures 41d,h). $LiNi_{1/3}Mn_{1/3}Co_{1/3}O_2$ exhibits less extensive fracturing than $LiNi_{0.8}Co_{0.15}Al_{0.05}O_2$,[151] which may explain both the increased heterogeneity in $LiNi_{0.8}Co_{0.15}Al_{0.05}O_2$ particles, and the anecdotally observed particle disintegration when $LiNi_{0.8}Co_{0.15}Al_{0.05}O_2$ particles were exposed to X-rays at high potentials. Other $LiNi_{0.8}Co_{0.15}Al_{0.05}O_2$ fractures had no associated change in whiteline energy (7.1 µm in Figure 45b,d).

3.3.4 $\mathbf{LiNi_{0.5}Mn_{0.3}Co_{0.2}O_2}$

Operando TXM XANES was also performed using a dilute (20 %) $LiNi_{0.5}Mn_{0.3}Co_{0.2}O_2$ cathode in a modified coin-cell. The galvanostatic charge profile (Figure 46) showed the expected initial slow change in potential, followed by a slight increase in the rate of change of potential

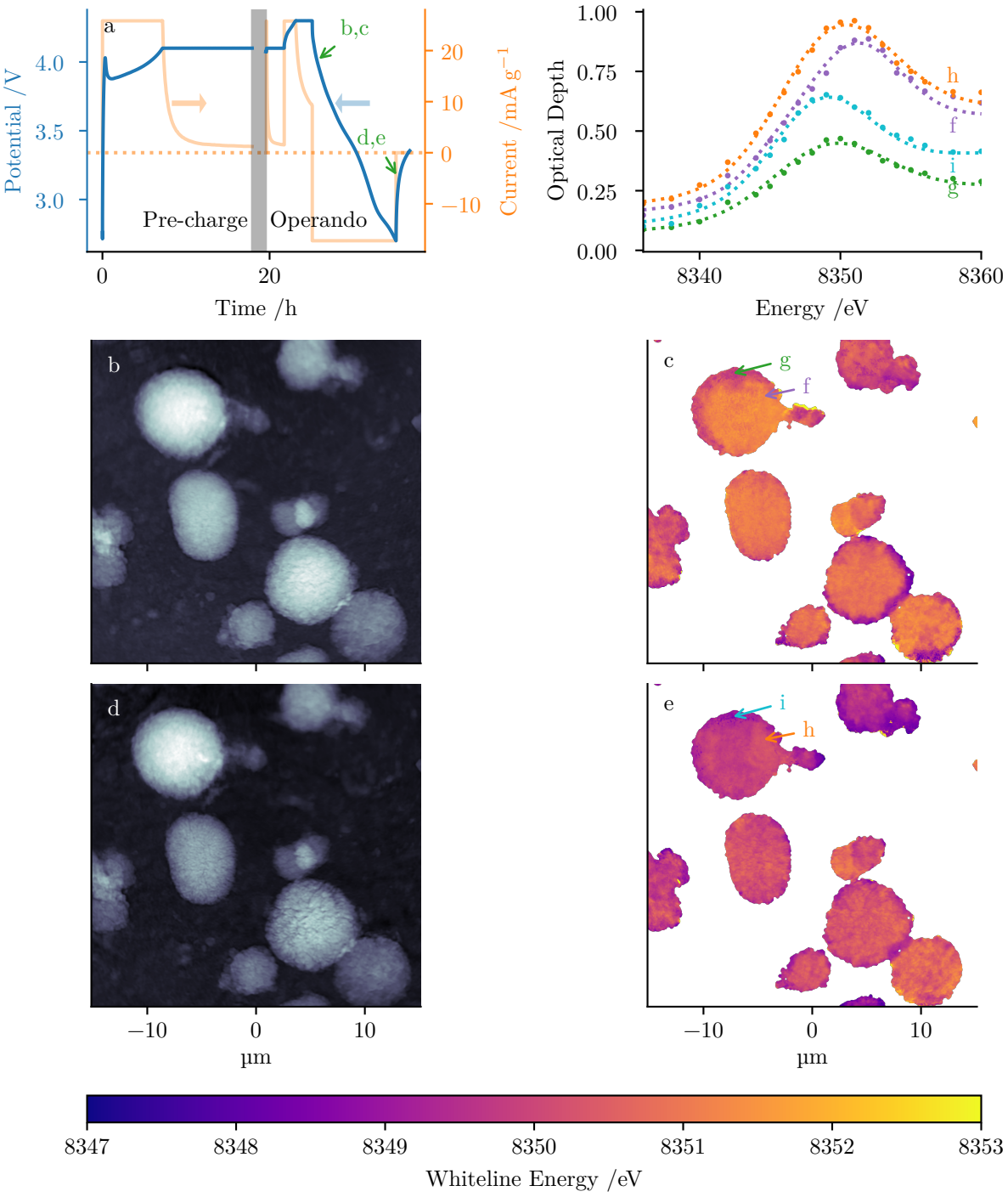

Figure 44: Operando TXM of $LiNi_{0.8}Co_{0.15}Al_{0.05}O_2$ secondary particles during discharge. (a) Potential (—) and current (—) during oxidation to 4.1 V without exposure to X-rays, and subsequent further operando oxidation to 4.3 V followed by reduction to 2.7 V. (b,d) Mean optical depth micrograph across Ni K-edge at (b) start of reduction and (d) end of reduction. (c,e) Maps of Ni K-edge whiteline energy at (c) start of reduction and (e) end of reduction. (f-i) Ni K-edge optical depth spectra for select single pixels from whiteline maps.

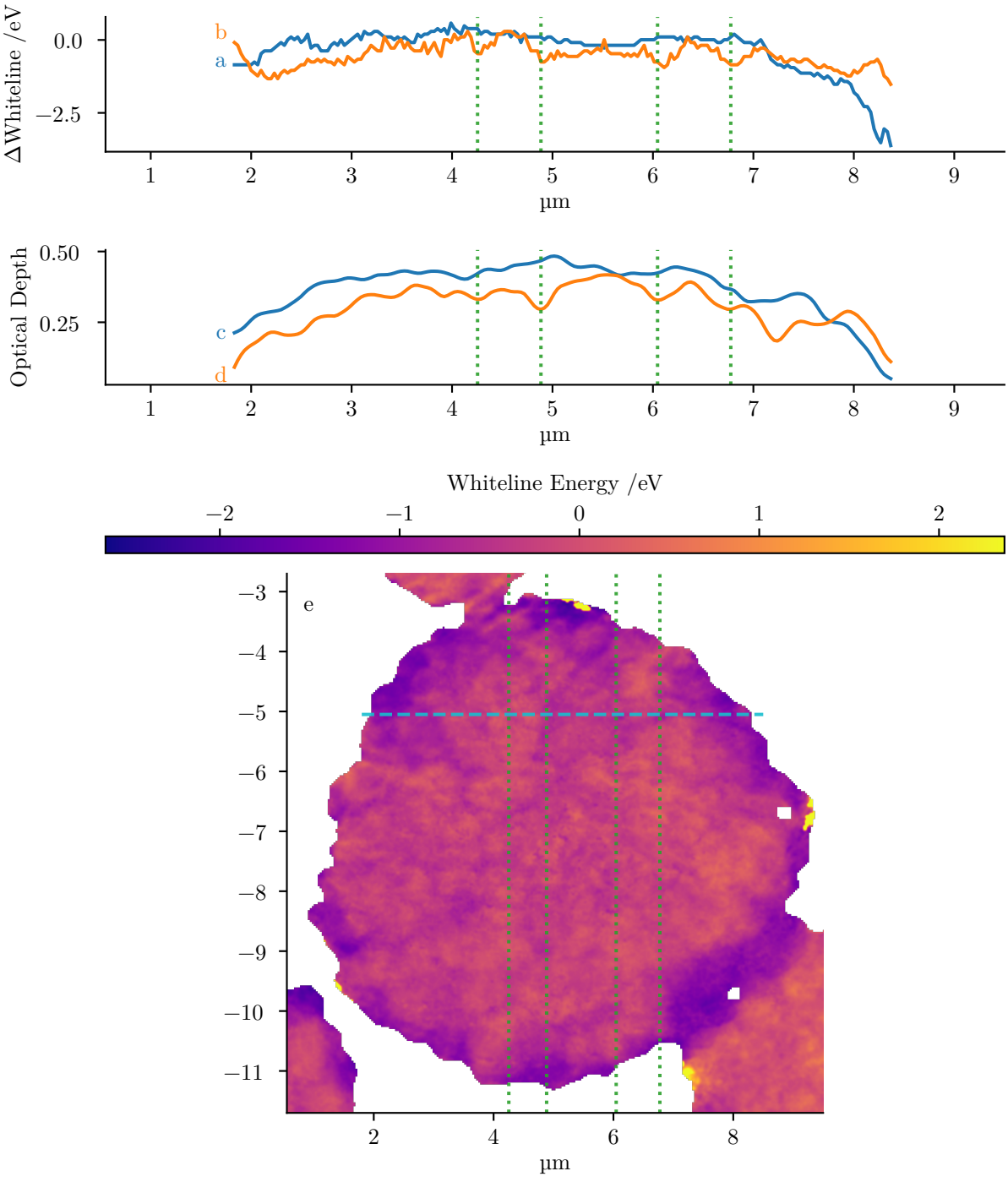

Figure 45: Comparison of Ni oxidation and morphology within $LiNi_{0.8}Co_{0.15}Al_{0.05}O_2$ secondary particle. Line scans of (a,b) deviation of Ni K-edge whiteline energy from mean particle whiteline energy, and (c,d) mean Ni K-edge optical depth. Sample was discharged from (a,c) 4.0 V to (b,d) 2.7 V. (e) Map of whiteline energy at 2.7 V, showing horizontal line-scan position (- - -). Vertical lines (···) added at the same position to *a-e* for comparison.

after 12 h, similar to $LiNi_{1/3}Mn_{1/3}Co_{1/3}O_2$ (Figure 33b,d) and $LiNi_{0.8}Co_{0.15}Al_{0.05}O_2$ (Figures 42 and 43). However, the $LiNi_{0.5}Mn_{0.3}Co_{0.2}O_2$ cathode showed almost no initial peak in cell potential at 2 h, as was observed for $LiNi_{0.8}Co_{0.15}Al_{0.05}O_2$ and $LiNi_{1/3}Mn_{1/3}Co_{1/3}O_2$ cathodes. During the first half of the charge cycle, particles again exhibited an initial latent phase followed by rapid increase in whiteline energy (Figure 46a), consistent with the particle-level dynamics observed in $LiNi_{1/3}Mn_{1/3}Co_{1/3}O_2$ (Figure 33) and $LiNi_{0.8}Co_{0.15}Al_{0.05}O_2$ cathodes (Figure 43). X-ray micrographs were not collected beyond 10.5 h due to scheduled facility maintenance. All but one particle had entered this rapid transition before the last operando TXM frame-set was collected and the increase in the rate of change of potential at 12 h (Figure 34f). Some particles showed heterogeneity in whiteline energy during the rapid transition (Figure 47d,h) with no corresponding features in the optical depth micrographs.

3.3.5 Effects of X-ray Exposure

To evaluate the effects of extended X-ray exposure on the oxidation dynamics of particles, two fields of view were selected for operando TXM XANES within the same coin-cell containing a dilute (20 %) $LiNi_{0.8}Co_{0.15}Al_{0.05}O_2$ cathode (Figure 42). One field of view was subjected to a 2 h continuous exposure of X-rays prior to the application of current. In both fields of view, particles showed an initial latent stage, following by a rapid increase in whiteline energy, indicating Ni oxidation. Overall, particles exposed to the initial static X-ray dose (Figure 42b) underwent this rapid whiteline transition later than those that did not receive the initial X-ray exposure (Figure 42a). Two particles that received the additional X-ray does showed no appreciable Ni oxidation over the course of the experiment. The previously discussed peak in

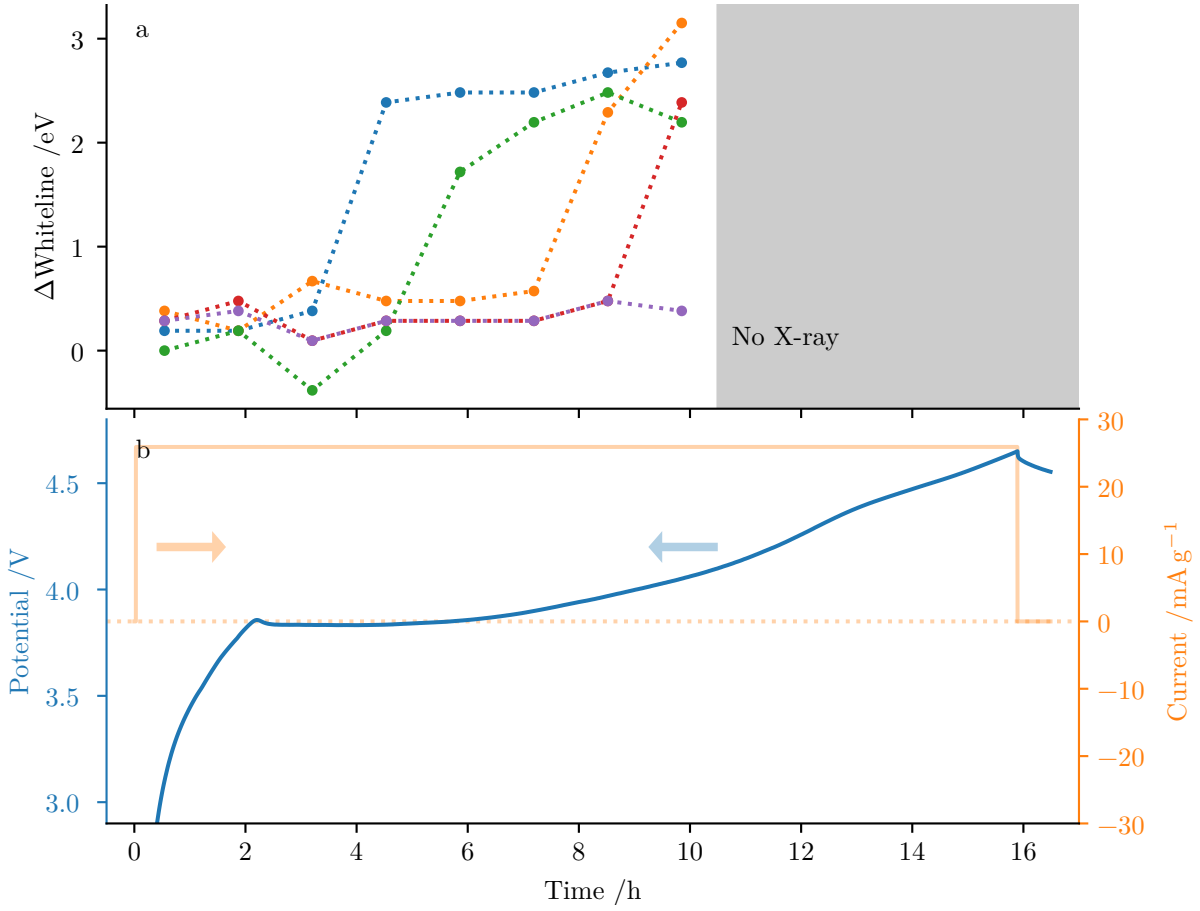

Figure 46: Particle-level oxidation during first charge and discharge of $LiNi_{0.5}Mn_{0.3}Co_{0.2}O_2$. (a) Mean whiteline energies of secondary particles during charge discharge. (b) Operando potential (—) and current (—) for galvanostatic cycling for $LiNi_{0.5}Mn_{0.3}Co_{0.2}O_2$ samples in modified coin-cells. X-ray shutter disabled after 10 h for storage ring maintenance.

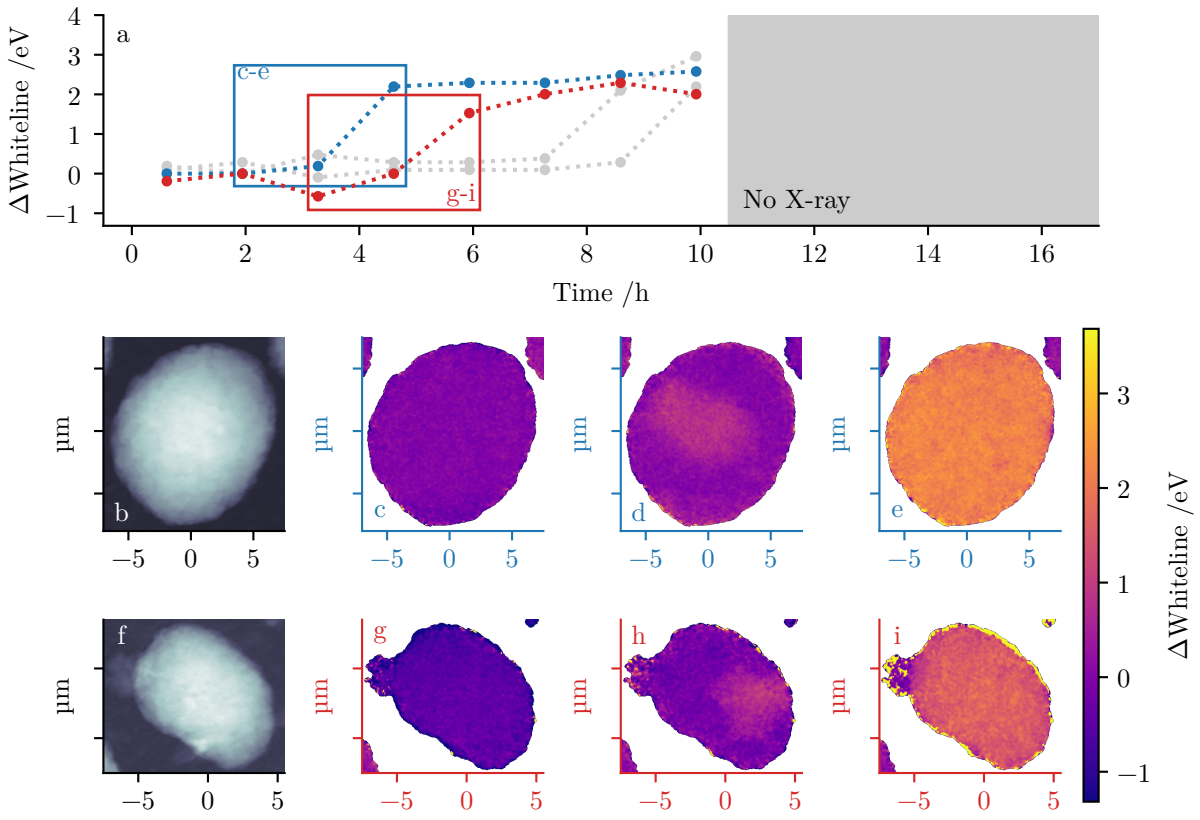

Figure 47: Chemical heterogeneity within $LiNi_{0.5}Mn_{0.3}Co_{0.2}O_2$ particles during first charge. (a) Changes in mean whiteline energies relative to 8353.31 eV for $LiNi_{1/3}Mn_{1/3}Co_{1/3}O_2$ particles. (b,f) Mean optical depth of select particles across all energies and time-steps. (c,d,e,g,h,i) Maps of changes in whiteline energies relative to 8353.31 eV during transitions indicated on (a).

the rate of change of cell potential (Figures 42c and 34e) occurred after particles in both fields of view had undergone the rapid transition in whiteline energy.

3.4 Discussion

For all three cathode materials, a more or less noticeable initiation peak was observed at the beginning of the first galvanostatic charge during operando TXM XANES (Figures 33, 42, 43, 44, and 46). This initiation peaks has been attributed to increased electrode polarization due to diffusion limiting surface layers.[80,147,154] One such surface layer is formed during exposure to CO_2 and H_2O, producing Li_2CO_3.[80,154,155] However, the initiation peak was still present with cathodes containing $LiNi_{1/3}Mn_{1/3}Co_{1/3}O_2$, which is significantly less prone to form Li_2CO_3 due to its low Ni content,[127] and consequently, less sensitive to exposure to air. Furthermore, the initiation peak was still prominent during the first charge of cathodes made from $LiNi_{0.8}Co_{0.15}Al_{0.05}O_2$ and $LiNi_{1/3}Mn_{1/3}Co_{1/3}O_2$ that was protected from Li_2CO_3 formation by being stored in a dry room and argon-glovebox (Figures 33 and 43). An increase in electrode over-potential over time has previously been reported for $LiNi_{0.8}Co_{0.15}Al_{0.05}O_2$ protected from atmospheric CO_2 and H_2O by storage under argon atmosphere,[154] demonstrating that Li_2CO_3 is not the only factor in electrode polarization. Independent of its source, the absence of this initiation peak during the second charge (Figure 43d) indicates removal of the diffusion barrier during the first charge/discharge cycle.

The gradual increase in cell potential observed during charge (Figures 33, 42, 43, 44 and 46) reflects a gradual increase in the average Ni oxidation state. This is confirmed by previous reports of ensemble average XAS, showing a smooth increase in the energy of the whiteline

in the Ni K-edge spectrum (Table I and Figure 39). The difference between the end-points of particle-level and ensemble average Ni oxidation suggests that an appreciable portion of the particles in the specimens measured by ensemble XAS had not reached their fully oxidized state. This difference between the redox dynamics observed at the ensemble and secondary-particle levels underscores the importance of considering the redox chemistry of battery materials at multiple length scales.

It has been previously demonstrated by operando ensemble XRD that $LiNi_{0.8}Co_{0.15}Al_{0.05}O_2$ exhibits a bimodal distribution of cell parameters during the first charge.[124] This behavior has been attributed to a layer of Li_2CO_3 with poor lithium diffusion, producing at least two populations of particles at different oxidation states.[80] This model is consistent with the observations presented here that individual secondary particles oxidized rapidly and stochastically. However, the rapid particle-level oxidation dynamics are observed even when no initiation peak is observed in the galvanostatic profile (Figure 43), when using $LiNi_{1/3}Mn_{1/3}Co_{1/3}O_2$ which exhibits low levels of Li_2CO_3 formation (Figure 33),[127] or when the cathode powder is stored under low-moisture atmosphere (Figures 33 and 43). Kinetic barriers in addition to surface Li_2CO_3 must also contribute to this rapid oxidation behavior. One such candidate is the formation of a surface disordered rock-salt, which may also pose a transport barrier.[121] However this surface rock-salt reconstruction is known to persist after the first charge/discharge cycle,[13,73] and so is incompatible with the observed return to a gradual oxidation behavior at the secondary-particle level during the second charge (Figure 43d).

In every instance presented here, the observed peak in the rate of change of cell potential (Figure 34) occurred at, or shortly after, the time when all particles had undergone the rapid transition in whiteline energy. Variation of the rate of change of the cell potential can occur with changes in the nature of the underlying chemical processes. As an example, a sharp spike in the rate of change of potential is expected when changing from one phase boundary to another in a thermodynamically two-phase material.[156] However, layered materials are not predicted to exhibit a miscibility gap over the full range of (de)lithiation. Instead, this peak in the rate of change of potential may signal the transition from rapid, stochastic oxidation to the more gradual oxidation seen at high states of charge. During the second charge of $LiNi_{0.8}Co_{0.15}Al_{0.05}O_2$, the stochastic oxidation of particles is subdued, though not eliminated entirely (Figure 43c). A slight increase in rate of change of whiteline energy is seen (5.5 h in Figure 43c), but does not show a corresponding increase in the rate of change of the cell potential (Figure 34d). These observations suggest that manipulation of the mechanism of phase propagation at the nanoscale could be used to subsequently manipulate the shape of the electrochemical profile.

The observed correlation between Ni whiteline energy (Figure 45a,b) and fractures in the particle (Figure 45c,d) indicate that additional Ni reduction is taking place along fractures during discharge of $LiNi_{0.8}Co_{0.15}Al_{0.05}O_2$. Electrolyte penetration into particle fractures provides a more direct Li^+ diffusion pathway through the solid, and so promotes delithiation at the newly formed surface.[157] Under this model, the material exposed to electrolyte via fracture formation undergoes redox more readily than the surround material. A secondary contribution may come

from the formation of a reduced Ni layer known to occur by electrolyte interaction accompanied by oxygen loss[13,73] as discussed in chapter 2, which has also been shown to occur within particle fractures.[22,153] Not all local minima in optical depth (Figure 45d) had a corresponding minimum in whiteline energy (Figure 45b), and so not all fractures exhibited this additional Ni reduction. Since crack initiation originates in the interior of the particle,[151,153,158] these inert fractures have likely not propagated to the exterior of the particle and do therefore not allow electrolyte penetration.

During the observed rapid transitions in Ni oxidation state, two instances of spatial heterogeneity were found within $LiNi_{1/3}Mn_{1/3}Co_{1/3}O_2$ (Figure 40c-e,g-i). In both cases, the particle exhibited a boundary between more reduced and more oxidized Ni. As the reaction proceeded, the boundary did not change position. For comparison, $LiFePO_4$ is a material that exhibits a miscibility gap between two phases.[159,160] $LiFePO_4$ transforms by nucleation followed by propagation of the new phase across the particle.[51,156,161] This is in contrast to the boundary seen here in $LiNi_{1/3}Mn_{1/3}Co_{1/3}O_2$, which maintains the same position while the two regions on either side of the boundary increase in Ni oxidation state. Instead, the spatial heterogeneity is better thought of as kinetic in origin. One of the observed spatial heterogeneities coincided with sharp gradients in optical depth (Figure 40b-e), suggesting two or more separate secondary particles overlapping in the field of view. These particles are not necessarily in physical contact and may be separated along the optical axis. Therefore, the observed heterogeneity is likely the result of variations between the particles in either e^- transport through the conductive carbon matrix, or Li^+ transport through the electrode pores. Differences in transport within a secondary

particle, for instance, due to differences in packing density of the individual particles, are likely convoluted in this outcome, as well. The other instance of spatial heterogeneity in whiteline energy has no sharp gradients in the corresponding optical depth map (Figure 40f-i). Instead, the many small features in the optical depth map indicate a complex micro-structure, possibly due to extensive fracturing. In this case, e^- and/or Li^+ transport are again rate-limiting, with the difference that the variations in transport kinetics occur between isolated grains within a secondary particle rather than between particles.

3.5 Development of the Mantis Operando Cell

An ever-present concern with in-situ characterization is the effect of measurement technique on the phenomena under study. Operando studies provide a more representative view of the cathode electrochemistry by avoiding relaxation within the material. At the same time, consideration must be given to the modification of the electrochemical cell needed to enable X-ray transmission along with the impact these modifications have on the electrochemical reactions being observed. At the X-rays energies required for K-edge spectroscopy of first-row transition metals, the steel coin-cell casing does not permit measurable transmission, requiring the addition of X-ray transparent windows into the cell. The current state of the art for operando TXM studies uses either Si_3N_4, such as described previously in this chapter, or polyimide film. However, it has been shown that the lower battery stack pressure as well as the lack of electrical conductivity of the window alters the extent of oxidation in the cathode during operando X-ray characterization.[52] Additionally, modified coin-cells provide an X-ray transmission path

only when oriented near 90° to the optical axis, whereas tomographic reconstruction relies on projection images at angles ranging from 0° to 180°.

The problems arising from window conductivity and rigidity have largely been solved for in-situ XRD thanks to the development of the Argonne multi-purpose in-situ X-ray (AMPIX) cell.[54] The AMPIX cell uses amorphous carbon windows, which provide both a rigid surface for applying battery stack pressure and high electric conductivity as a cathode current collector. However, the AMPIX cell is too large for TXM setups, which have short working distances due to constraints of the X-ray optics. Furthermore, the angular rotation range for the AMPIX cell is not sufficient for tomography. Therefore, a new cell was designed to apply the AMPIX cell approach to TXM. The resulting Mantis electrochemical cell also uses amorphous carbon windows, providing the same rigid, electronically conductive surface for the cathode as the AMPIX cell. A wide, tapered aperture and low-profile electric connectors allow for >150° rotation while maintaining a clear path for X-ray transmission (Figure 48a).

The Mantis cell provides high transmission through the cell at the energies needed for first-row transition metal XAS over a 150° rotation range. The measured optical depth is dependent on the rotation angle due to the larger path length through the battery stack when away from 90°. This angular dependence at a given angle ($\mu(\theta)$) is described by

$$\mu(\theta) = \frac{\mu(\frac{\pi}{2})}{\cos\theta}$$

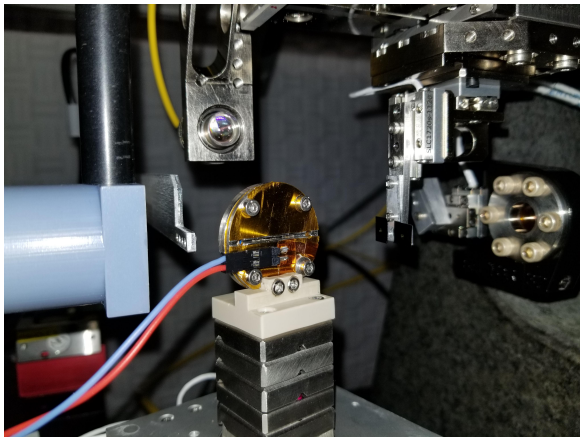

(a) Mantis electrochemical cell in operation.

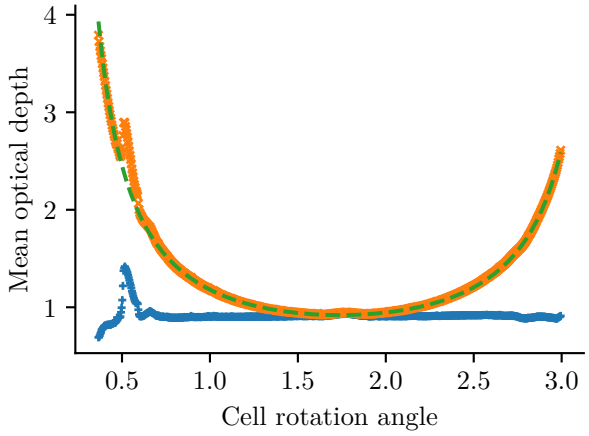

(b) Angular correction for in-situ tomography, showing mean optical depth (×), fit angular correction (--), and corrected mean optical depth (+).

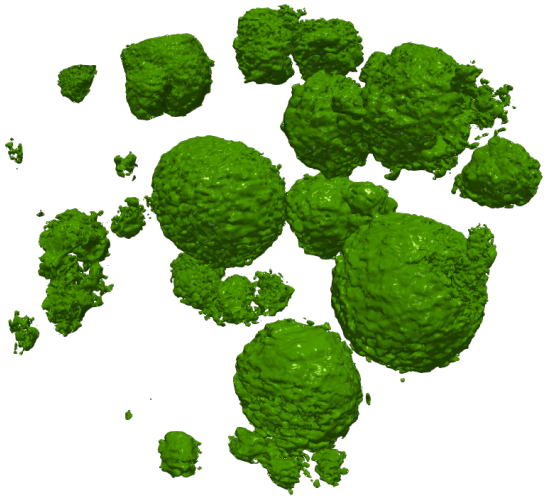

(c) 3D rendered in-situ $LiNi_{0.8}Co_{0.15}Al_{0.05}O_2$ secondary particles.

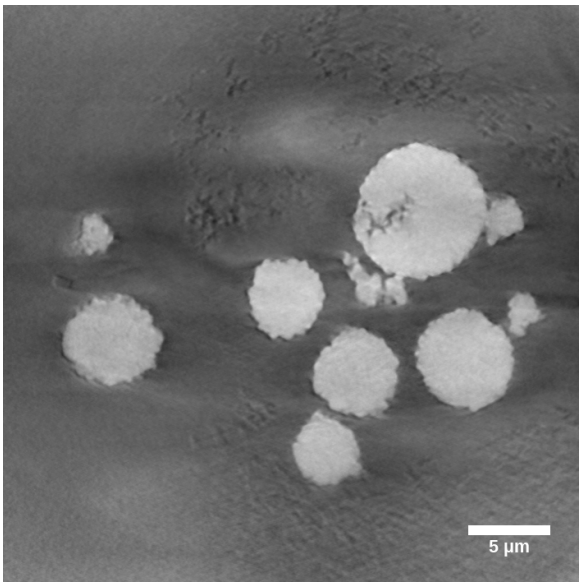

(d) Reconstructed slice of in-situ $LiNi_{0.8}Co_{0.15}Al_{0.05}O_2$ secondary particles.

Figure 48: Tomography capabilities of Mantis electrochemical cell at the advanced photo source (APS) 32-ID-C TXM.

and can be largely corrected (Figure 48b). With this angular correction, the 150° rotation range was sufficient to allow tomographic reconstructions, producing three-dimensional volumes in-situ of $LiNi_{0.8}Co_{0.15}Al_{0.05}O_2$ secondary particles (Figures 48c and 48d). XAS enabled tomography would allow for three-dimensional maps of Ni whiteline energy, clarifying the relationship between Ni oxidation state and secondary particle micro-structure.

The electrochemical behavior of working electrodes in the Mantis cell is similar to that observed with conventional coin-cells. An 80 % $LiNi_{0.8}Co_{0.15}Al_{0.05}O_2$ cathode was charged and discharged for 4 cycles in the Mantis cell with a Li metal counter electrode, and the non-aqueous electrolytes described in section 3.2 (Figure 49b). Compared to a 2032 coin-cell reference (Figure 49a), the Mantis cell shows similar specific capacities across all cycles, and minimal hysteresis between potential during charge/discharge. There was a small loss of capacity between each charge and subsequent discharge cycle. The onset of oxidation in the Mantis cell did not exhibit the initiation peak observed during first charge in the coin-cell and in the operando TXM studies described earlier in this chapter. The Mantis cell will now allow more representative and sophisticated operando TXM experiments, providing a new level of insight into the dynamic redox chemistry of Li-ion batteries.

3.6 Conclusion

The redox dynamics of secondary particles were measured in layered Li-ion battery cathodes by operando X-ray spectromicroscopy. During first charge, individual secondary particles exhibited an initial latent period followed by rapid Ni oxidation, consistent across particles within layered cathode materials of different transition metal compositions, and was not observed dur-

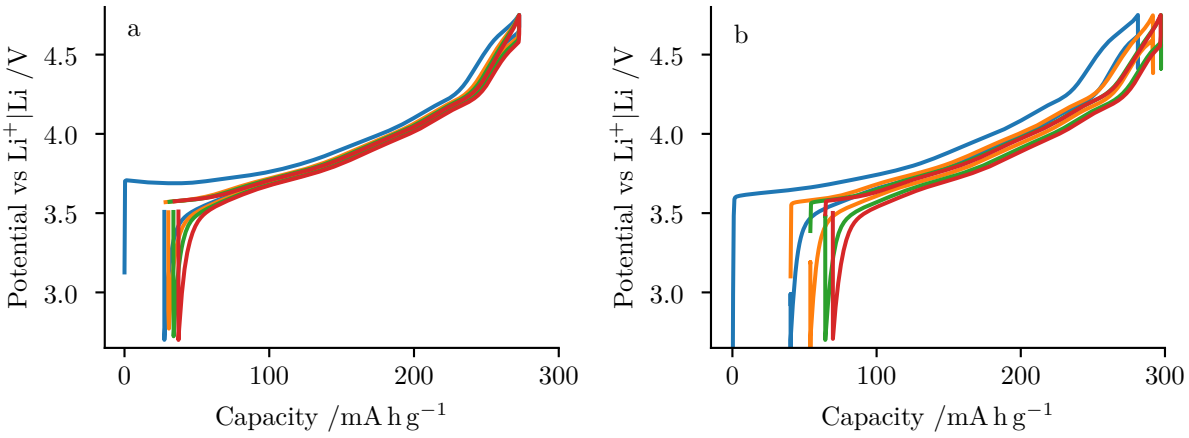

Figure 49: Galvanostatic (dis)charge profile of Mantis cell with comparison to coin-cell reference. 80 % $LiNi_{0.8}Co_{0.15}Al_{0.05}O_2$ cathode charged for 4 cycles at 0.1 C from 2.7 V to 4.75 V with Li metal anode. (a) 2032 coin-cell reference. (b) Mantis operando TXM cell.

ing subsequent discharge or during the second cycle. This behavior stands in contrast to the gradual oxidation of Ni observed when measuring the ensemble-average by conventional XAS. These rapid transition dynamics are currently ascribed to local gradients arising from barriers in either Li^+ or e^- transport, though the particle dynamics could not be attributable to a single indisputable phenomenon. Further work is needed to elucidate the fundamentals of this behavior, which is possible now that the experiments demonstrated in this chapter are viable.

Intra-particle heterogeneity in Ni oxidation state was also observed. Areas of reduced Ni were partially correlated with regions of lower density in the particles' micro-structures. The correspondence between this anomalous Ni reduction and visible internal fractures suggests electrolyte penetration promoting Ni reduction at the newly exposed surfaces. Variations in e^- and/or Li^+ transport result in further heterogeneity, both between particles and across

fractures within individual particles. The observed disparities between the local oxidation states of secondary cathode particles and the dynamics measured by ensemble-average XAS highlight the value of spectro-microscopy in probing oxidation as influenced by local phenomena, and of performing these measurements inside functional cells during active redox. The successful development of a novel electrochemical cell with the capability to perform 3D chemical imaging will now enable experiments that further elucidate the relationship between secondary particle micro-structure and electrochemistry.

CHAPTER 4

DIFFRACTION MAPPING OF HETEROGENEITY IN $LiMn_2O_4$ CATHODES

4.1 Introduction

The existence of heterogeneity implies a kinetic limitation in the material. Because the active material is initially homogeneous at large scales, a system operating without kinetic limitation (i.e. at thermodynamic equilibrium) would also transform homogeneously. Conversely, a region of an electrode subject to increased kinetic hindrance will not reach the same state of charge as a region operating close to optimal conditions, resulting in heterogeneities and, potentially, the creation of inactive areas that induce a loss of capacity within the cell. These inefficiencies can be overcome by applying higher over-potentials to increase the reaction rate of kinetically hindered material, at the cost of lower energy density and possible overcharging elsewhere in the electrode. Since the electrochemical reaction is nominally the same throughout the electrode, the existence of localized gradients in kinetics reflects limitations in the rate of transfer of charge carriers, whether electrons from the current collector or ions from the electrolyte.

A common strategy with Li-ion batteries is to create thick, dense electrodes, thereby increasing the mass of active material relative to inert support materials, and improving the volumetric and specific energy density. However, increasing the electrode's density allows less electrolyte penetration, hindering electrolyte-mediated Li^+ transport, relying instead of diffu-

sion through the solid matrix. Evaluation of capacity retention in dilute cathodes has shown a rate-dependence in the balance between ion-transport at the cathode surface versus through the cathode matrix as the rate-limiting step.[162] Furthermore, increasing the electrode's thickness increases the maximum diffusion length. Diffraction tomography has revealed faster reaction rates towards the electrolyte and current collector boundaries in $LiFePO_4$ cathodes, driven by both Li^+ and e^- transport through the composite matrix.[163] These issues are aggravated in practice, due to the inevitably uneven distribution of conductive additives during fabrication, and pore structure tortuosity. Local particle shuffling and mechanical strain during cycling can add to these inhomogeneities.[153] These considerations combine to produce higher kinetic transport barriers, explaining why these thick electrodes present lower power density and rates of full utilization, with the possibility of creating reaction inefficiencies and accompanying heterogeneity into the depth of the electrode.

At the level of the electrode, heterogeneity can develop at the micron to millimeter scale, calling for tools to map states of charge at different electrode conditions. XRD is a common technique to analyze solid-state compounds, providing crucial information on the structure of a material. Conventional bulk XRD has the benefit of being relatively straightforward to perform, but employs probes that are many millimeters in size, thereby averaging signals over large portions of the electrode. As a result, this approach obfuscates spatial heterogeneities that hold the desired insight into the underlying transformations of the material. This barrier can be overcome through the use of X-ray micro-diffraction.

Synchrotron radiation is the de facto choice for location-specific XRD experiments, where minor research progress has been made using micro-scale XRD to produce full chemical maps of an electrode,[52,164,165] or else obtaining localized XRD patterns to complement mapping with other modalities, such as X-ray fluorescence.[166] However, access to synchrotron user facilities is limited and highly competitive. Use of a laboratory X-ray diffractometer provides the ability to run continuously and can significantly increase sample throughput compared to synchrotron experiments. The lower flux of laboratory X-ray sources is not a problem for ex-situ analysis since longer acquisition times are acceptable, while the lower X-ray dose may help avoid radiation induced damage to the material.[52]

Thanks to the presence of both a first-order (two-phase) and second-order (single-phase) transition in $LiMn_2O_4$ cathodes during (de)lithiation, structural changes are easily followed by XRD.[167–170] Thick $LiMn_2O_4$ electrodes were subject to a variety of cycling conditions, and the ensuing heterogeneities were probed by µ-XRD mapping. Lateral gradients in transport were further introduced by cycling these electrodes against a much smaller Li metal anode, thereby uncovering the possibility of forming metastable gradients far from equilibrium. The experiments point at the extent of transport limitations in high-energy electrodes, generating valuable insight for the design of better architectures than can surpass the metrics today.

4.2 Materials and Methods

4.2.1 Electrochemical Preparation

The composite cathode laminate used throughout these experiments was provided by the *Cell Analysis, Modeling, and Prototyping (CAMP)* Facility at Argonne National Laboratory.

A 76 µm coating of TODA $LiMn_2O_4$ (90 %), Timcal C45 carbon black (5 %) and Solvay 5130 PVDF binder (5 %) was cast and pressed atop 20 µm thick aluminum foil. The final coating loading and density were 18.86 g cm^{-2} and 2.48 g cm^{-3} respectively. 2032 coin cells were prepared in an argon-filled glove box with 12.7 mm diameter cathodes, a 25 µm thick micro-porous polypropylene separator (Celgard 2400), 1.2 M $LiPF_6$ in 3:7 EC:EMC electrolyte, and a lithium metal anode. Anodes were either 12.7 mm or 6.35 mm diameter, as indicated in Table II. Galvanostatic cycling was performed with a Bio-Logic VMP3 or BCS-50 cycler. Cathodes were removed from coin cells in an argon-filled glove box within 24 h of the end of electrochemical cycling, rinsed with dimethyl carbonate, and allowed to dry before further analysis.

4.2.2 Ensemble X-Ray Diffraction

Conventional powder X-ray diffractograms were collected in 0.02° intervals with 500 ms exposure using a Bruker D8 Advance DaVinci diffractometer with copper Kα radiation (λ= 0.154 18 nm), equipped with 2.5° Soller slits on both primary and secondary sides, an 18 mm anti-scatter slit, and 0.02 mm Ni foil fluorescence filter. Divergence slits on the primary optic were fixed at 0.6 mm (Figure 52e,g,h,i,j) or 1.0 mm (Figure 52f), or set to constant volume illumination at 1.0 mm (Figure 52a,b,c,d). Specimens were fixed to an acrylic disk with double-sided cellophane tape and rotated at 30 rev/ min. Unit-cell parameters were extracted by Pawley refinement using GSAS-II.[171]

4.2.3 X-Ray Diffraction Mapping

Local powder diffraction maps were collected using a Bruker D8 Discover Series 2 using copper Kα radiation (λ= 1.5418 Å). A 0.8 mm collimator was used to limit the beam size. The

source and detector were kept at fixed angles during acquisition of mapping data. To reduce beam-spreading on the specimen, the source angle was set to 50°. A single, two-dimensional diffraction frame was collected at each mapping position (locus) using a Våntec-500 area detector at a sample-to-detector distance of 193 mm with an exposure time of 400 s and a sample-detector angle of 15°, corresponding to a 2θ range of 50° to 70°. The probe size was measured using X-ray responsive paper and was determined to be 1.0 mm perpendicular to the diffraction plane and 1.2 mm in the diffraction plane, with the latter being dependent on the source angle. Data acquisition was performed via Bruker's GADDS application controlled by scripts created with a custom-built open-source python package, scimap.[172]

Each two-dimensional diffraction frame was integrated over the azimuthal angle using GADDS. The resulting one-dimensional diffractograms were then imported into scimap and the background was fit with either uni-variate splines or Chebyshev polynomials. The (333)/(511), (440), (531) peaks were fit with Gaussian peaks to extract peak positions, heights and widths. Phase intensities were calculated by summing the areas after background subtraction for peaks associated with each phase. Phase ratios were calculated by dividing phase intensities for each phase by the total of all phase intensities. Cell parameters were calculated by minimizing the sum-of-squares difference between observed and calculated peak positions using

$$2\theta = 2 \arcsin\left(\frac{\lambda}{2d}\right)$$

where, for cubic unit cells, d is calculated as

$$d = \sqrt{\frac{a^2}{h^2 + k^2 + l^2}}$$

4.3 Results and Discussion

4.3.1 Electrode Kinetics

Deliberate control of the experimental conditions of the electrochemical cell produced maps that explored distinct properties of the cathode's chemistry. Three such mapping experiments will be presented and discussed in detail below. First, however, a general overview of the electrochemical and structural behaviors of $LiMn_2O_4$ will be provided as well as a summary of the mapping process.

The galvanostatic profile can be used to qualitatively describe the nature of the chemical transformation, which is necessary for a reliable analysis of the XRD data. At 0.1 C (Figures 50a,e, 51), the electrochemistry shows an initial regime of increasing potential between the nominal compositions $Li_1Mn_2O_4$ and $Li_{0.6}Mn_2O_4$, indicative of a second-order, solid-solution transformation. Between $Li_{0.6}Mn_2O_4$ and the fully delithiated state, the potential is roughly constant over the composition range, indicating a first-order, two-phase transformation.[167] At higher rates (Figure 50b-d,g), the over-potential increases, and the distinction between the two regimes becomes less pronounced.

These two modes of the phase transformation can also be discerned by XRD. During delithiation from $Li_1Mn_2O_4$ to $Li_{0.6}Mn_2O_4$ (the solid-solution regime), a single set of peaks was

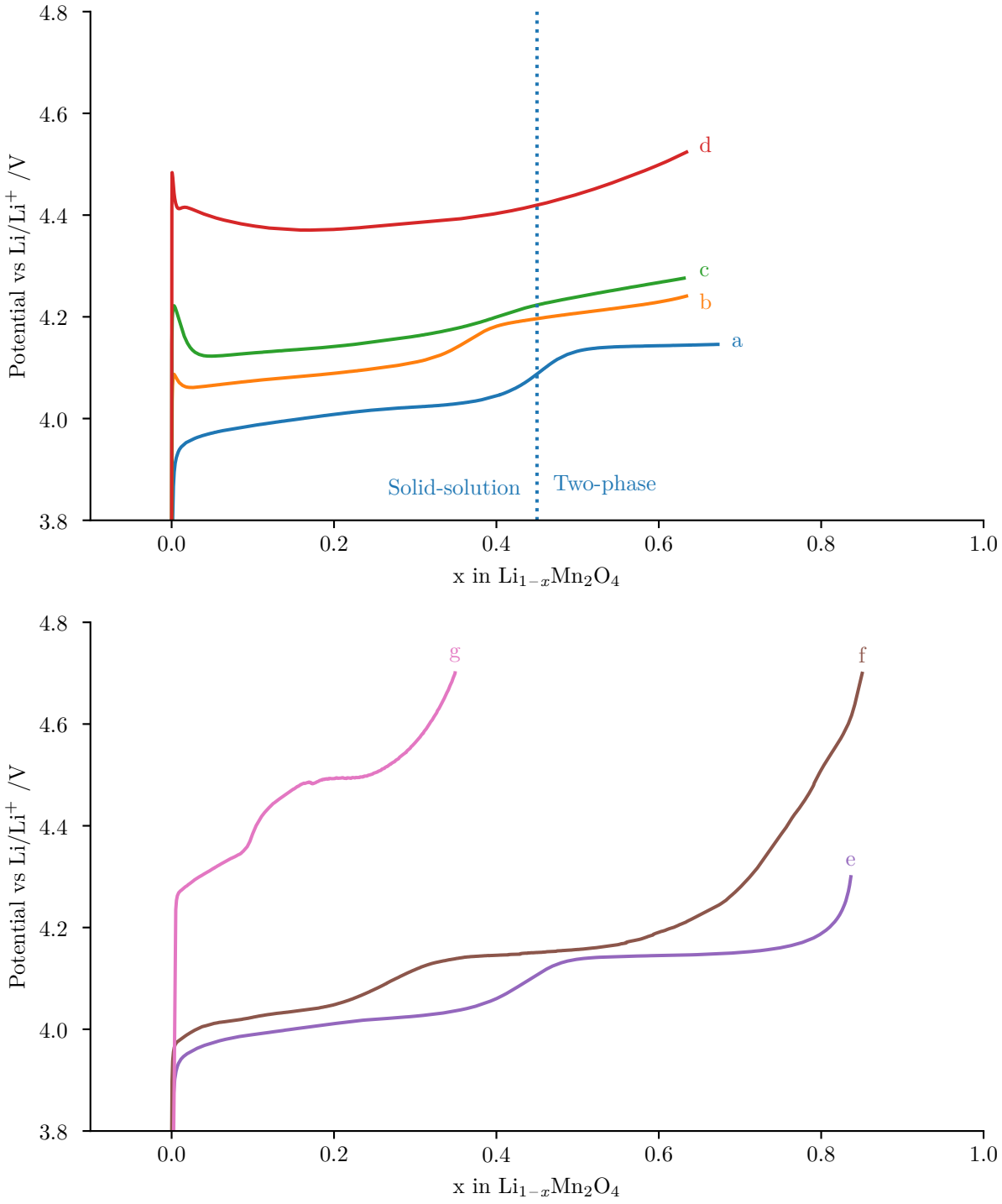

Figure 50: Galvanostatic cycling of $LiMn_2O_4$. (a) Charged to $Li_{0.29}Mn_2O_4$ at 0.1 C, (b) charged to $Li_{0.36}Mn_2O_4$ at 1 C, (c) charged to $Li_{0.36}Mn_2O_4$ at 2 C, (d) charged to $Li_{0.36}Mn_2O_4$ at 5 C, (e) charged to 4.3 V at 0.1 C, (f, g) charged to 4.7 V with half-sized lithium metal anode at (f) 0.1 C and (g) 2 C. Vertical line indicates expected boundary between solid-solution and two-phase mechanisms.

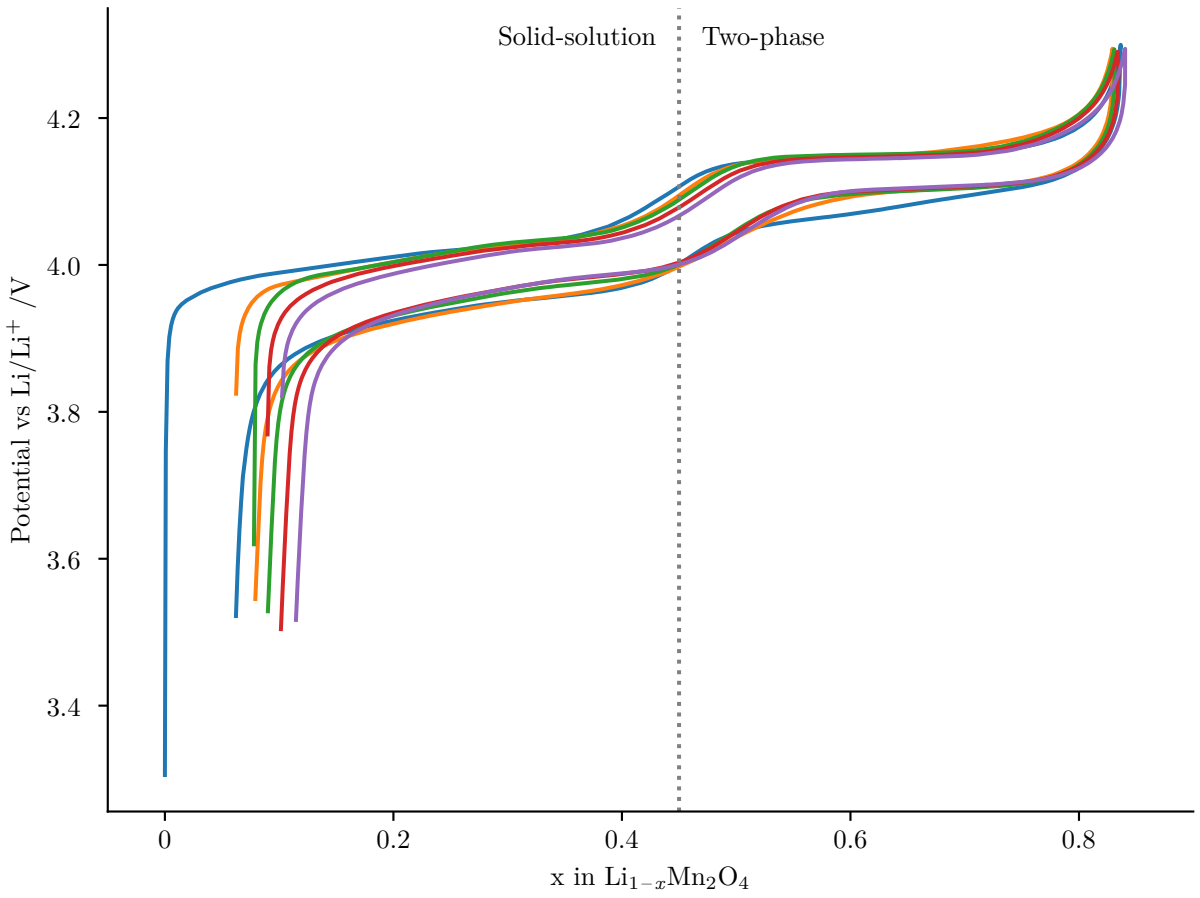

Figure 51: First five cycles of a coin cell with $LiMn_2O_4$ cathode and lithium metal anode at 0.1 C.

present (Figure 52a). As the lithium concentration decreased, these peaks shifted to higher scattering lengths, indicating a contraction of the unit-cell. During further delithiation beyond $Li_{0.6}Mn_2O_4$ (the two-phase regime), two sets of peaks were present corresponding to the partially-lithiated and fully-delithiated phases (Figure 52b), with the fully-delithiated phase having higher scattering angles reflecting a smaller unit-cell. As more material was converted to the delithiated phase, the relative intensity of the peaks at higher scattering lengths increased. There is no definitive answer regarding the compositions of the phases present in the two-phase regime,[167,170,173–176] and even within the two-phase regime the cell parameters change by ≈0.04 Å.[168,169,177] Therefore, $Li_{◒}Mn_2O_4$ and $Li_{○}Mn_2O_4$ will be used to refer to the partially-lithiated and fully-delithiated phases respectively. Some of the effects discussed below occur as metastable heterogeneities within the solid-solution regime, so $Li_{●}Mn_2O_4$ will be used to represent the fully lithiated phase ($\approx Li_1Mn_2O_4$) where necessary. It is important to note that there is no miscibility gap between $Li_{●}Mn_2O_4$ and $Li_{◒}Mn_2O_4$ and therefore the coexistence of $Li_{●}Mn_2O_4$ and $Li_{◒}Mn_2O_4$ does not represent a true two-phase transformation, but rather heterogeneity imposed by kinetics. When possible, cell parameters refined from XRD patterns will be used to estimate the extent of (de)lithiation by comparison to previous reports of $LiMn_2O_4$ structure evolution,[167,169,173] and will be presented as $Li_{\approx x}Mn_2O_4$.

The presence of both solid-solution and two-phase behavior during oxidation of $LiMn_2O_4$ provides several options for analysis. While in the solid-solution regime at the beginning of the charging process, cell parameters can be extracted based on peak position. The extracted cell parameters serve as an indicator of the extent of delithiation.[167] During the two-phase process,

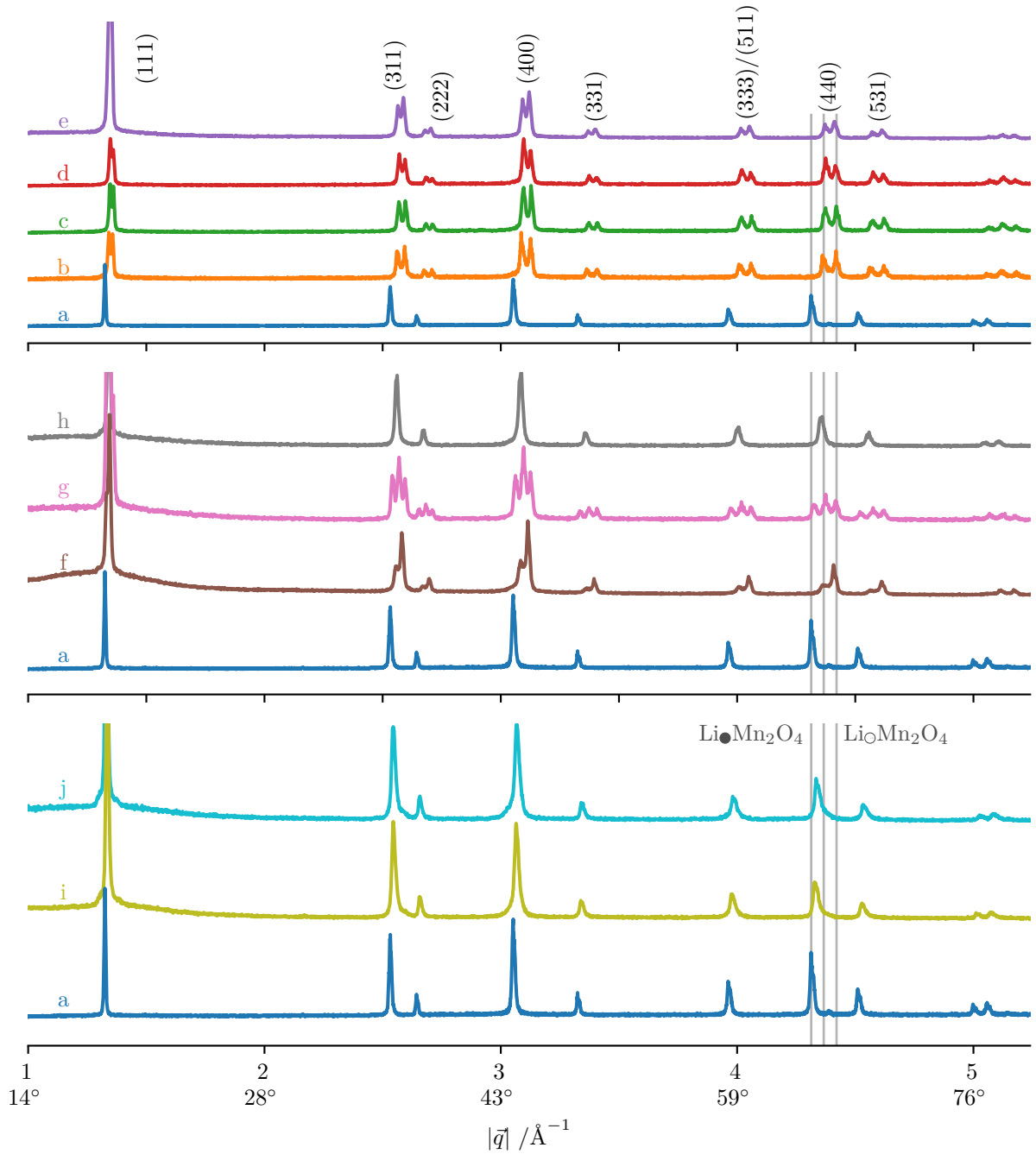

Figure 52: Powder X-ray diffractograms of $LiMn_2O_4$ cathodes. (a) Pristine; (b) after charging to $Li_{0.29}Mn_2O_4$ at 0.1 C; (c-e) after charging to $Li_{0.36}Mn_2O_4$ at (c) 1 C, (d) 2 C and (e) 5 C; (f-h) charging to 4.7 V with under-sized anode at (f) 0.1 C, (g) 2 C, and (h) 2 C followed by soaking in electrolyte for 6 days; (i, j) cycled from 3.5 V to 4.7 V for (i) 33 cycles ending on discharge, and (j) 40 cycles ending on charge. Vertical lines indicate the expected positions of the $Li_{\bullet}Mn_2O_4$ (4.31 Å^{-1}), $Li_{\textcircled{-}}Mn_2O_4$ (4.37 Å^{-1}), and $Li_{\bigcirc}Mn_2O_4$ (4.42 Å^{-1}) phases.[167] 2θ Bragg angles resulting from Cu K_α radiation are shown for convenience.

the relative intensities of the peaks depend on the prevalence of each phase in the material. Since $LiMn_2O_4$ maintains its space-group during this transformation, and the interaction of lithium with X-rays is negligible, the lithiated and delithiated phases are not expected to differ significantly in their structure functions. As a result, the peak area ratio gives a good measure of the ratio between the $Li_{◒}Mn_2O_4$ and $Li_{○}Mn_2O_4$ phases and therefore the extent of delithiation.

Several $LiMn_2O_4$ cathodes were charged at different rates to similar capacities within the two-phase regime (Figure 50a-d). Bulk XRD (Figure 52b-e) shows two sets of peaks corresponding to lithiated $Li_{◒}Mn_2O_4$ at lower angles, and delithiated $Li_{○}Mn_2O_4$ at higher angles. The four specimens have different ratios of these two sets of peaks and therefore have different abundances of the two phases, despite all samples having similar nominal compositions. Samples charged at 0.1 C and 1 C (Figures 52b,c) were prepared by punching from the slurry-side of the electrode, leading to delamination of the active material composite from the current collector (Figure 53b), which will have artificially altered the bulk diffractograms if the delaminated cathode material is unable to react. Consequently, these two samples were not analyzed further. The remaining samples, charged at 2 C and 5 C, were prepared by punching from the foil-side of the electrode laminate resulting in no delamination. The sample charged at 5 C (Figure 52d) showed a stronger intensity of the high-angle peaks associated with the $Li_{○}Mn_2O_4$ phase compared to the sample charged at 2 C. This implies a greater extent of lithiation at faster rates, despite both samples being charged to the same overall capacity ($Li_{0.36}Mn_2O_4$). In fact, the 5 C sample (Figure 52d) had a stronger intensity for the $Li_{○}Mn_2O_4$ phase than even the 0.1 C sample (Figure 52b), despite the latter reaching a slightly higher state of charge ($Li_{0.36}Mn_2O_4$

End-Point	Figure	Rate	Cycles	Anode Size	Unit-Cell Parameter /Å		
Pristine	Reference				8.24–8.248		
$Li_{◒}Mn_2O_4$	Reference					8.14–8.156	
$Li_{○}Mn_2O_4$	Reference						8.04–8.048
Pristine	52a, 56a				8.239		
$Li_{0.29}Mn_2O_4$	52b, 57a, 54a	0.1 C	1	12.7 mm		8.145	8.051
$Li_{0.36}Mn_2O_4$	52c, 54b	1 C	1	12.7 mm		8.137	8.051
$Li_{0.36}Mn_2O_4$	52d, 57c, 54c	2 C	1	12.7 mm		8.132	8.057
$Li_{0.36}Mn_2O_4$	52e, 57e, 54d	5 C	1	12.7 mm		8.130	8.060
4.7V	52f, 61c, 55a	0.1 C	1	6.35 mm		8.125	8.050
4.7V	52g, 59a, 55b	2 C	1	6.35 mm	8.227	8.138	8.058
4.7V, equilibrated	52h, 59d, 55c	2 C	1	6.35 mm		8.169	
ending on discharge	52i, 56b	2 C	33	12.7 mm	8.213		
ending on charge	52j, 63, 56c	2 C	40	12.7 mm	8.194		

TABLE II: Summary of cell parameters for $LiMn_2O_4$ after various electro-chemical preparations. Values were extracted by Pawley refinement from powder XRD of entire electrode. Reference values included for pristine $Li_{●}Mn_2O_4$ and the two phases present ($Li_{◒}Mn_2O_4$ and $Li_{○}Mn_2O_4$) upon reaching the upper cut-off potential.[167–170]

vs. $Li_{0.29}Mn_2O_4$). Additionally, the refined unit-cell parameters varied with charge-rate (Table II and Figures 54, 55 and 56). At faster rates, the $Li_{◒}Mn_2O_4$ phase had a smaller unit-cell parameter (8.130 Å at 5 C versus 8.145 Å at 0.1 C) and the $Li_{○}Mn_2O_4$ phase had a larger unit-cell parameter (8.060 Å at 5 C versus 8.051 Å at 0.1 C).

This rate-dependent behavior was investigated further by diffraction mapping. When using a conventional θ-2θ coupled scan, the X-ray beam smears out considerably at low angles over the area of the sample in the diffraction plane, resulting in a probe with significantly lower spatial resolution. In order to minimize this beam spreading, a high source angle was preferred. Additionally, acquisition time can be minimized by selecting an angular range covered by one

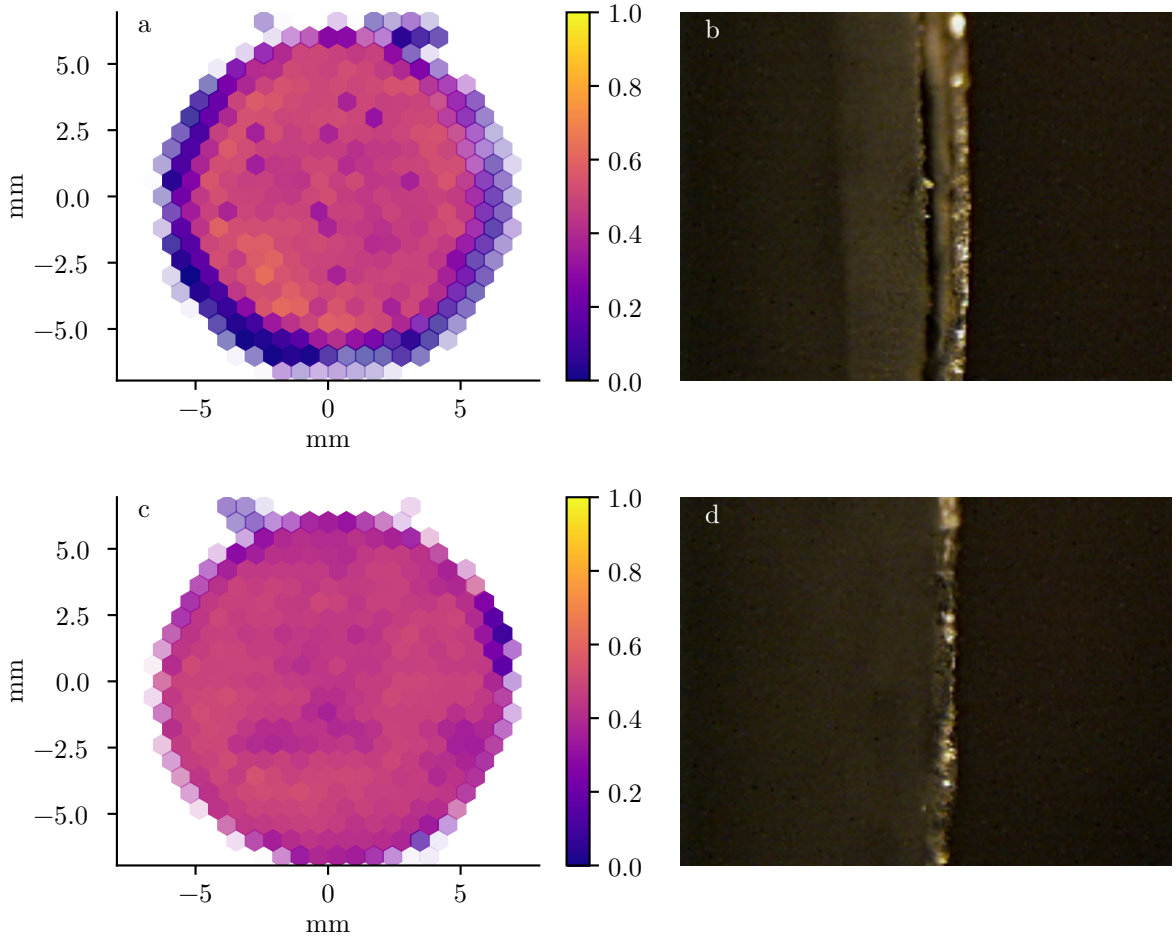

Figure 53: Side view of electrode edge and maps of relative fraction of $Li_{0.27}Mn_2O_4$ phase for electrodes charged at 2 C to $Li_{0.36}Mn_2O_4$, punched from (a and b) foil side and (c and d) material side.

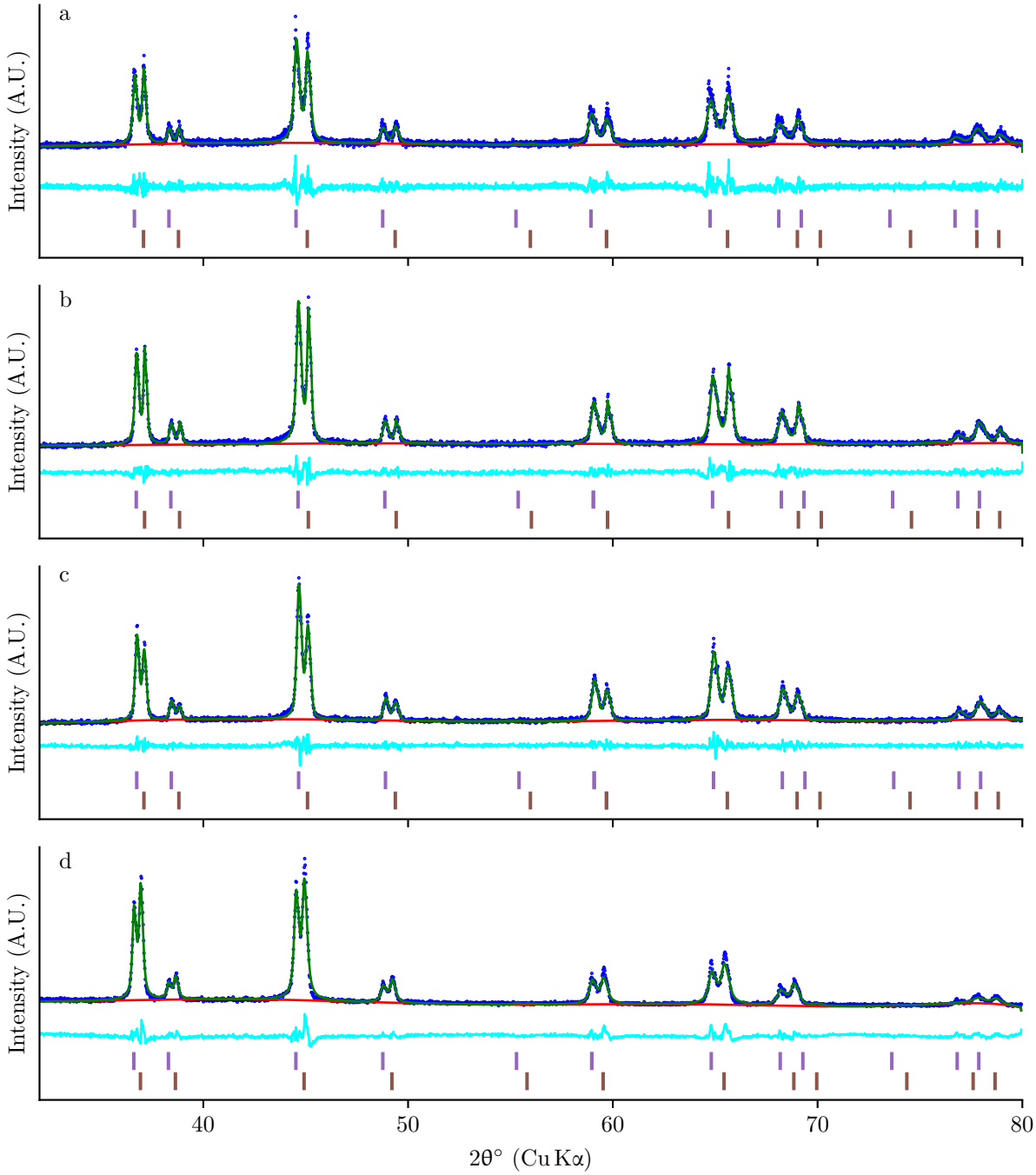

Figure 54: Pawley refinement of powder XRD patterns. Observations (···), calculated diffraction (—), background (—), and observations minus calculated (—). Vertical ticks indicate positions of predicted reflections. (a) after charging to $Li_{0.29}Mn_2O_4$ at 0.1 C; (b-d) after charging to $Li_{0.36}Mn_2O_4$ at (c) 1 C, (d) 2 C and (e) 5 C.

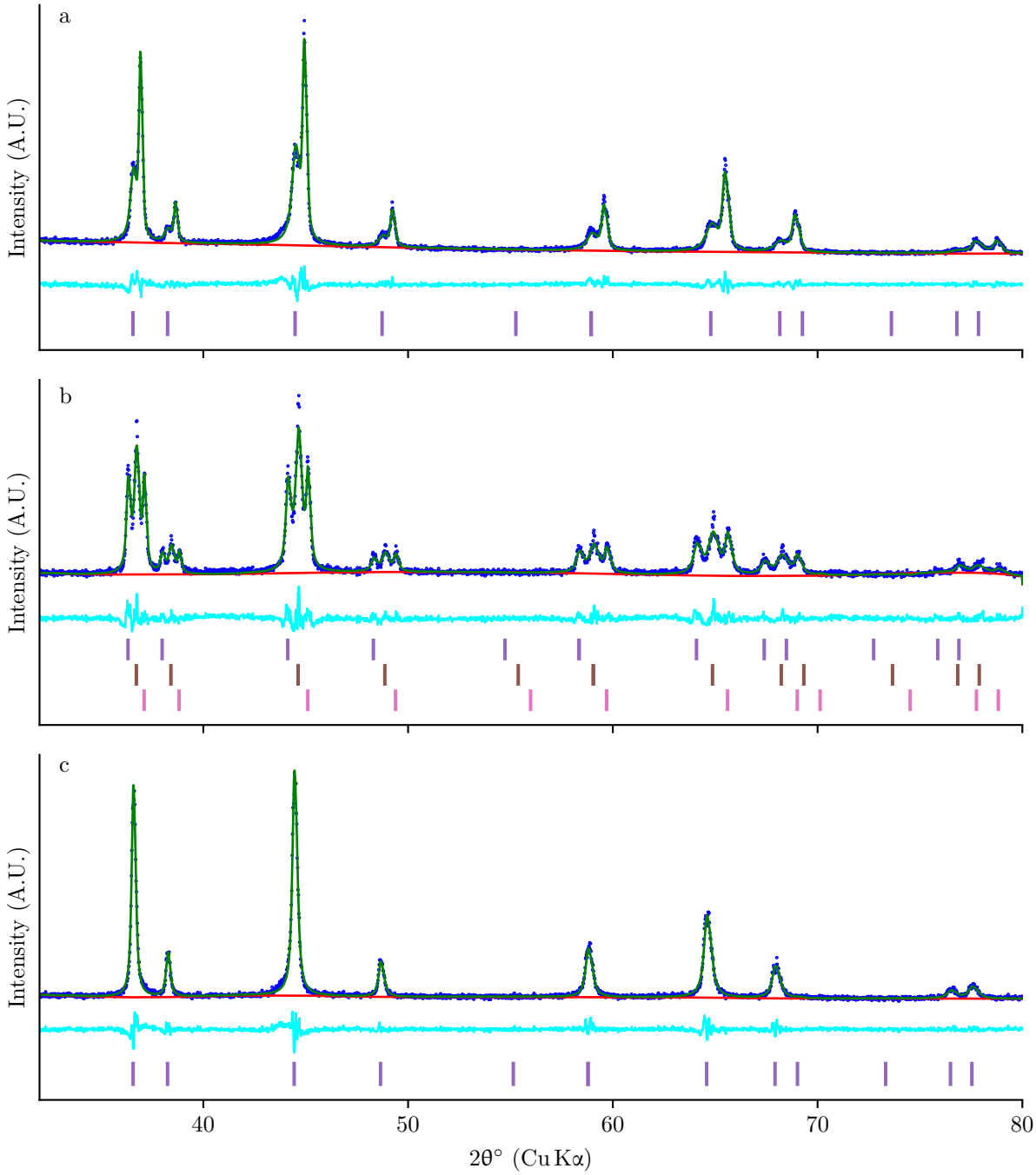

Figure 55: Pawley refinement of powder XRD patterns. Observations (···), calculated diffraction (—), background (—), and observations minus calculated (—). Vertical ticks indicate positions of predicted reflections. $LiMn_2O_4$ cathodes charged to 4.7 V with under-sized anode at (a) 0.1 C, (b) 2 C, and (c) 2 C followed by soaking in electrolyte for 6 days.

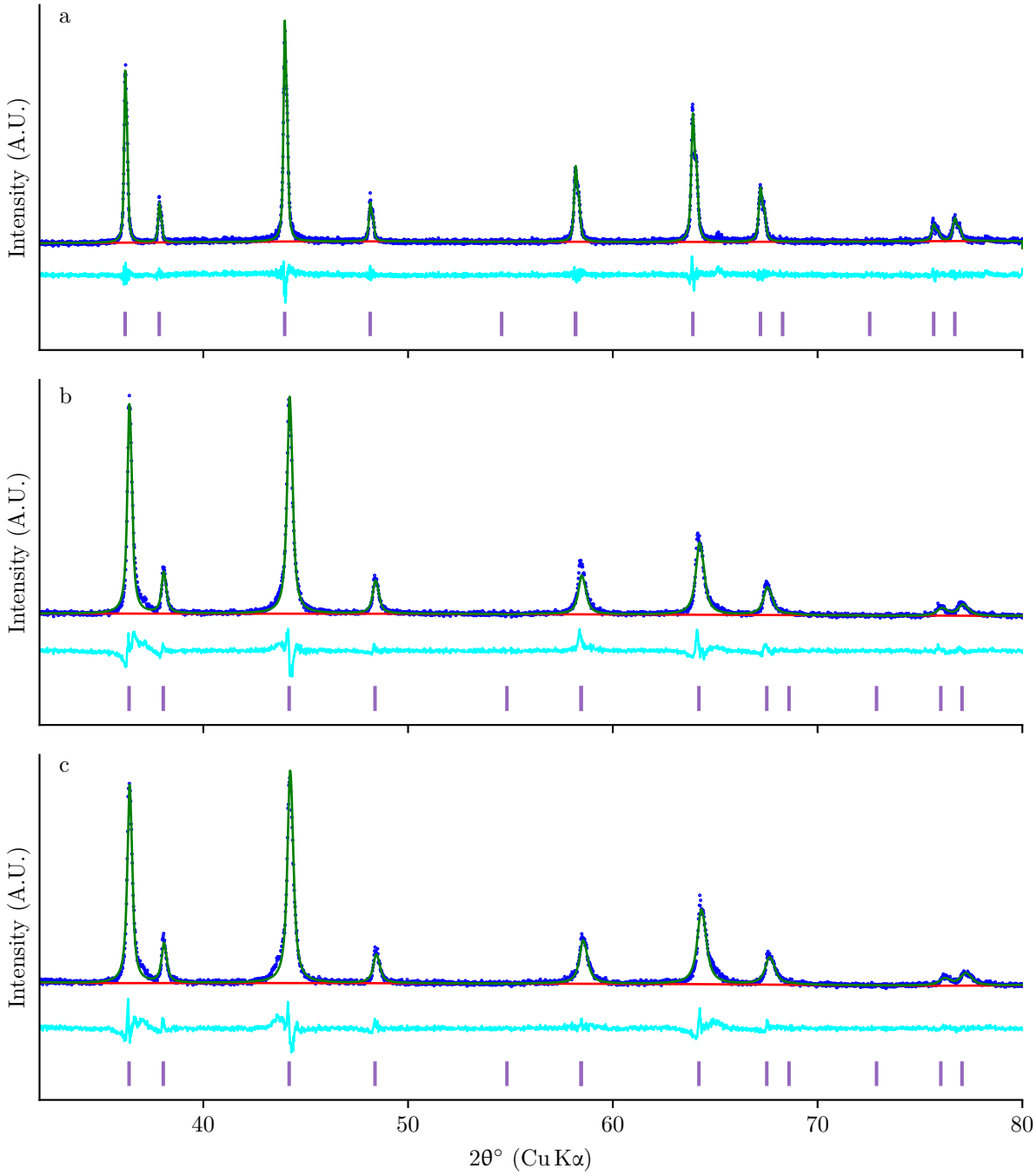

Figure 56: Pawley refinement of powder XRD patterns. Observations (···), calculated diffraction (—), background (—), and observations minus calculated (—). Vertical ticks indicate positions of predicted reflections. (a) Pristine $LiMn_2O_4$; and cycled from 3.5 V to 4.7 V for (b) 33 cycles ending on discharge, and (c) 40 cycles ending on charge.

frame of the area detector. The region of the diffractogram from 3.8 $Å^{-1}$ to 5.0 $Å^{-1}$ (55° to 75°) was used for mapping since it optimizes both the high source angle and single detector frame conditions while capturing the (333)/(511), (440) and (531) reflections, making it rich in diffraction signal. Due to the weak interaction between Li^+ and X-rays, the phase distribution can be measured by comparing the integrated peak areas for the $Li_{◒}Mn_2O_4$ and $Li_{○}Mn_2O_4$ phases. Figure 57 shows the abundance of the $Li_{○}Mn_2O_4$ phase relative to the sum of the $Li_{○}Mn_2O_4$ and $Li_{◒}Mn_2O_4$ phases (the "phase fraction") for electrodes charged at 0.1 C (Figure 57a,b), 2 C (Figure 57c,d), and 5 C (Figure 57e,f). All maps showed heterogeneous phase fractions across the electrode, with portions of the electrode having a lower contribution from the delithiated $Li_{○}Mn_2O_4$ phase compared to the surrounding electrode material, seen as darker regions in Figures 57a, c and e. In all three samples, these less delithiated "lagging" regions had similar phase fractions. However, the histograms for the 0.1 C and 5 C specimens (Figures 57b,f) showed more occurrences towards higher phase fractions than the 2 C specimen (Figure 57d), consistent with the bulk XRD above. This observation indicates that the overall extent of delithiation for the volume probed in the samples charged at 5 C is higher than in the sample charged at 2 C (Figure 57b). It results in a larger difference between the inhomogeneous, lithiated regions and the remainder of the electrode. The higher extent of oxidation for the 0.1 C specimen is at least partly due to its higher state-of-charge compared to the other specimens: $Li_{0.29}Mn_2O_4$ vs. $Li_{0.36}Mn_2O_4$. In a separate experiment with electrodes punched from the slurry-side, the above-mentioned delamination of the specimen induced an inactive ring around the outside of the electrode at 2 C, but had a less dramatic impact at 0.1 C (Figure 53).

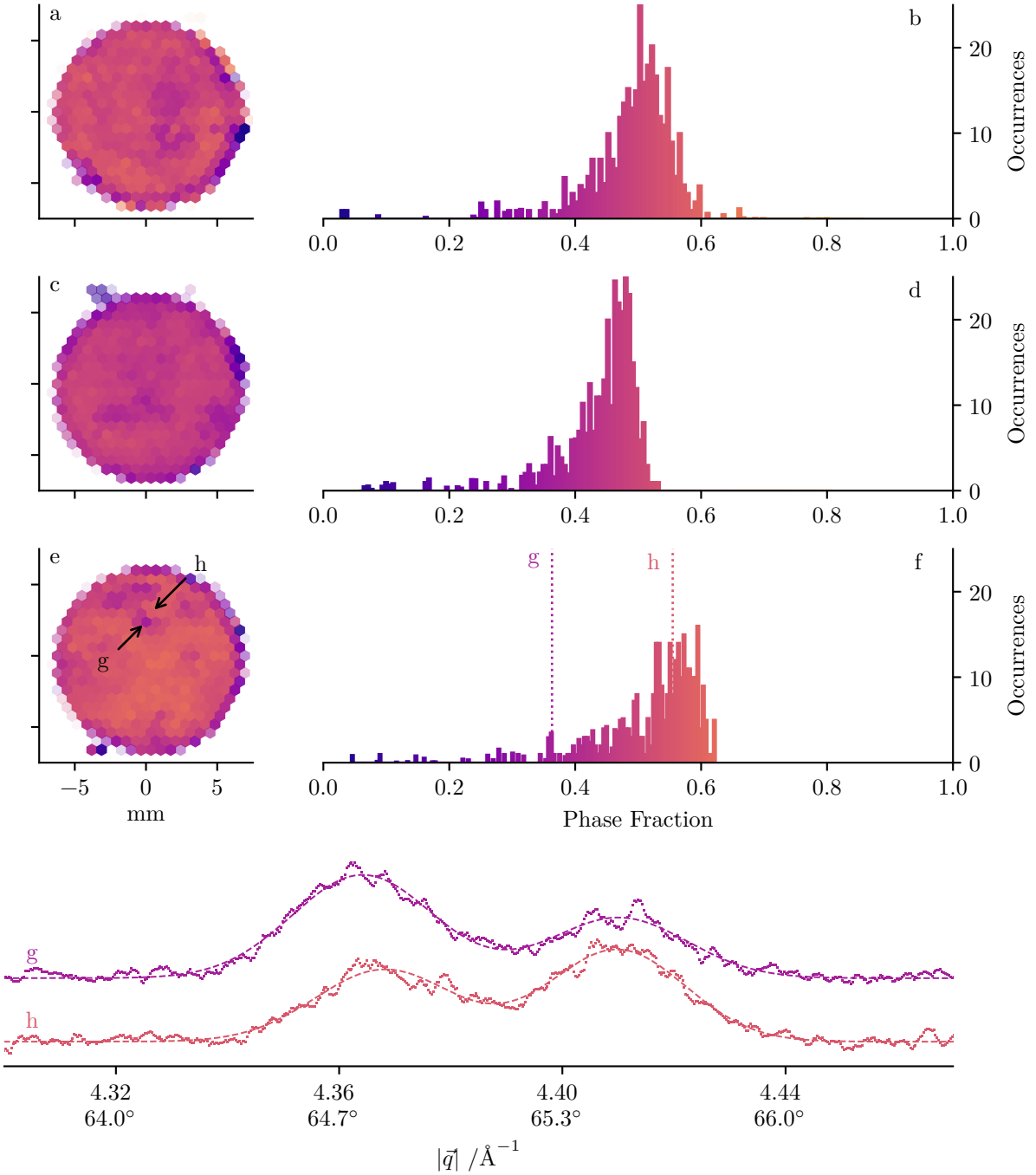

Figure 57: Maps and histograms showing fraction of oxidized $Li_{\bigcirc}Mn_2O_4$ phase as estimated by integral of (333), (440) and (531) peaks. Cathodes were charged to a nominal state of (a, b) $Li_{0.29}Mn_2O_4$ at 0.1 C, or to a nominal state of $Li_{0.36}Mn_2O_4$ at (c, d) 2 C and (e, f) 5 C. Color ranges are consistent between all four plots. (g, h) X-ray diffractograms of (440) peak for select loci in *e* with phase fractions of (g) 0.36 and (h) 0.56. Dashed lines show least-squares fit of Gaussian peaks. 2θ Bragg angles resulting from Cu K_α radiation are shown for convenience.

The difference in overall phase fraction between the 2C and 5C samples is unexpected, since the mean phase-fraction is an indirect measure of the state-of-charge of the electrode, and both electrodes were charged to the same overall state of $Li_{0.36}Mn_2O_4$ (Figure 50c,d). The simplest explanation is a gradient of chemical states through the thickness of the electrode, which is not probed in its entirety by the X-ray beam. The X-ray transmission through the cathode (T) is described by

$$T = \frac{I}{I_0} = \mathrm{e}^{-A\rho x}$$

where x is the linear distance traveled by a given photon.[36] This linear distance depends on the electrode's thickness and the angles of the X-ray source and detector (θ_1 and θ_2).

$$x = x_{in} + x_{out} = z(\csc\theta_1 + \csc\theta_2)$$

These two equations can be combined and rearranged to give transmission as a function of penetration depth.

$$T = \frac{I}{I_0} = \mathrm{e}^{-Az(\csc\theta_1 + \csc\theta_2)}$$

An estimate for the linear attenuation coefficient, A, of $376.27\,\mathrm{cm}^{-1}$ was obtained from each component's photo-absorption cross section[31] combined with its specific concentration and the overall coating density reported by the *CAMP* facility. The resulting transmission function is shown in Figure 58 as a function of electrode depth over the range of scattering

angles used for mapping, with cumulative transmission being calculated as the cumulative sum of the transmission function normalized to the total integrated transmission. The cumulative transmission function predicts that 95 % of the transmitted intensity comes from the top 9 µm to 19 µm of the cathode, depending on the exact scattering angle. This conclusion is further supported by the absence of aluminum peaks at 2.68 $Å^{-1}$, 3.10 $Å^{-1}$ and 4.39 $Å^{-1}$ in Figure 52, confirming that the X-ray probe did not reach the aluminum current collector.[178] Consequently, the material closer to the top of the electrode dominated the resulting X-ray diffractograms. The observed increase in the signal associated with the delithiated $Li_{\bigcirc}Mn_2O_4$ phase when charged at 5C implies that oxidation occurs closer to the anode (top of the electrode in the coin cell configuration) when the material is charged faster, leaving reduced material primarily closer to the current collector. Similar behavior has been reported in $LiFePO_4$ when only one edge of the cathode is exposed to electrolyte.[164] X-ray depth profiling of layered cathode materials also shows depth-dependent inhomogeneities at high discharge rates.[179] As discussed in the introduction, heterogeneities at these length scales are caused by the inability of the electrolyte to deliver lithium ions through the micro-structure of the electrode, or by the inability of the active-material/carbon matrix to deliver electrons from the current collector. The observation that delithiation occurs closer to the electrolyte, rather than the current-collector, at high rates demonstrates that Li^+ transport is the limiting factor.

The lateral inhomogeneities were explored by comparison of local diffraction patterns of two adjacent regions. Figures 57g,h shows example diffractograms of the (440) peaks for these two regions. In the more delithiated region (Figure 57h), the higher intensity of the $Li_{\bigcirc}Mn_2O_4$ peak

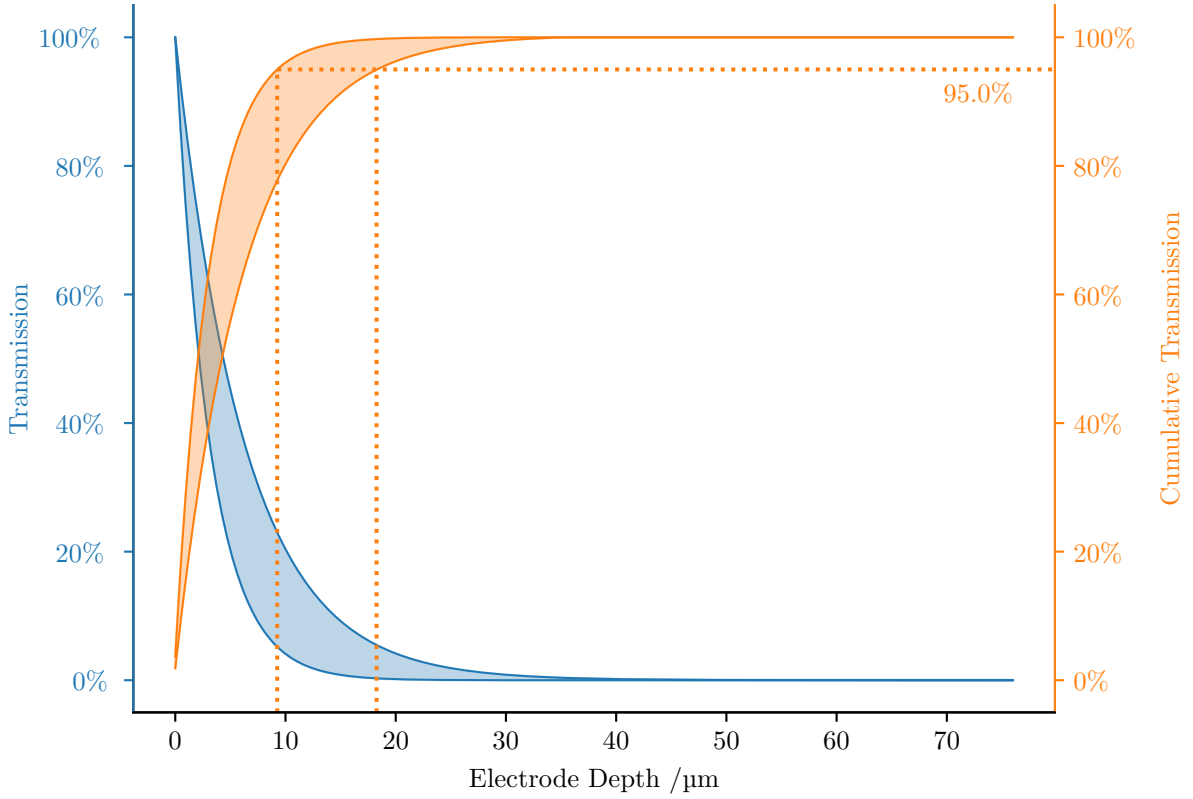

Figure 58: Calculated transmission and cumulative transmission of X-rays based on depth into an electrode of 90 % $LiMn_2O_4$, 5 % carbon, and 5 % polyvinylidene fluoride binder. Cu-Kα (λ = 1.5418 Å) X-ray source was position at $\theta_1 = 50°$ and detector spanning $\theta_2 = 8°$ to 20°. Dashed lines show the range for 95 % cumulative transmission.

at ≈4.41 $Å^{-1}$ is responsible for the higher calculated phase fraction for this locus. Additionally, the $Li_{◒}Mn_2O_4$ peak at ≈4.37 $Å^{-1}$ is at higher angles compared for the lagging locus (Figure 57g). Cell parameters of 8.135 Å | 8.059 Å were refined for the phases in the delithiated locus (Figure 57g), and 8.145 Å | 8.060 Å in the lagging locus (Figure 57h). The larger cell parameter for the $Li_{◒}Mn_2O_4$ phase in the lagging locus (8.145 Å) indicates that this region did not fully complete the solid-solution transformation before entering the two-phase regime. The total contraction from 8.24 Å to 8.14 Å covers a range from $LiMn_2O_4$ to $Li_{0.6}Mn_2O_4$,[167] so, according to Vegard's law, the 0.01 Å difference in cell parameters between the delithiated and lagging loci corresponds to a difference in lithium content of roughly $Li_{0.02}$. Analogously, the range of phase fractions from 0 to 1 in the two-phase region represents a reported difference of between $Li_{0.33}$ and $Li_{0.5}$ in composition,[167,168,170,173–176] so the difference in phase ratio between the delithiated and lagging loci (0.56 versus 0.36) corresponds to an additional difference in lithium content of up to $Li_{0.096}$. The combined effect is that, at 5 C, these lagging regions may be up to $Li_{0.12}$ behind the rest of the cathode. At slower rates, the differences in phase fraction across these laterally heterogeneities was less dramatic (Figure 57a-d).

Inhomogeneities can also be artificially induced laterally across the electrode by using a Li-metal anode with a smaller diameter than the cathode. The electrochemical response of the 12.7 mm diameter $LiMn_2O_4$ cathodes charged to 4.7 V at 0.1 C and 2 C against 6.35 mm diameter Li anodes showed comparably higher over-potentials than when electrodes had equal diameters, with lower reachable capacities at typical potentials for $LiMn_2O_4$ (Figures 50e-g). Cells could not be charged at 5 C in this configuration. At 0.1 C, two phases were found

in the ensemble XRD (Figure 52f), with unit-cell parameters of 8.050 Å and 8.125 Å. These parameters are similar to those for $Li_{◒}Mn_2O_4$ (8.14 Å) and $Li_{○}Mn_2O_4$ (8.04 Å).[167] However, both values are slightly inside the two-phase regime, where no miscibility gap is expected. At 2 C (Figure 52g), three phases were present with unit-cell parameters of 8.227 Å, 8.130 Å and 8.058 Å. The latter two phases correspond to $Li_{◒}Mn_2O_4$ and $Li_{○}Mn_2O_4$ within the two-phase regime. The first phase had a cell parameter consistent with the lithiated $Li_{●}Mn_2O_4$ phase seen in the solid-solution regime,[167] though its cell parameter was slightly smaller than the 8.239 Å in the pristine $LiMn_2O_4$ electrode (Table II). At any rate it is striking that $Li_{●}Mn_2O_4$ and $Li_{◒}Mn_2O_4$ can coexist in a sample measured ex situ, under no bias, since their existence along a solid solution path should provide a strong driving force for equilibration through remixing.

The diffraction map of the cathode charged at 2 C revealed a large degree of heterogeneity for the cathode charged with a small anode (Figure 59a,b). Since the cathode contained phases within the solid-solution regime, the unit-cell parameter of the most lithiated phase was initially used as a proxy for the state of charge of a local area (Figure 59). After charging to 4.7 V, there was a ≈6 mm diameter central region containing a phase with a cell parameter of 8.14 Å (Figure 59a), drastically different from the surrounding ring containing a phase with a cell parameter of 8.24 Å, similar to pristine $LiMn_2O_4$. Figure 59c shows a two-dimensional plot of the diffractograms segmented by distance from the center of this heterogeneity, which presumably marks the anode's position within the assembled coin-cell. Within 3.45 mm from the center, two phases were present (Figure 59c). The cell parameters of these two phases were similar to the $Li_{◒}Mn_2O_4$ and $Li_{○}Mn_2O_4$ phases (Table II), with the most oxidized phase having

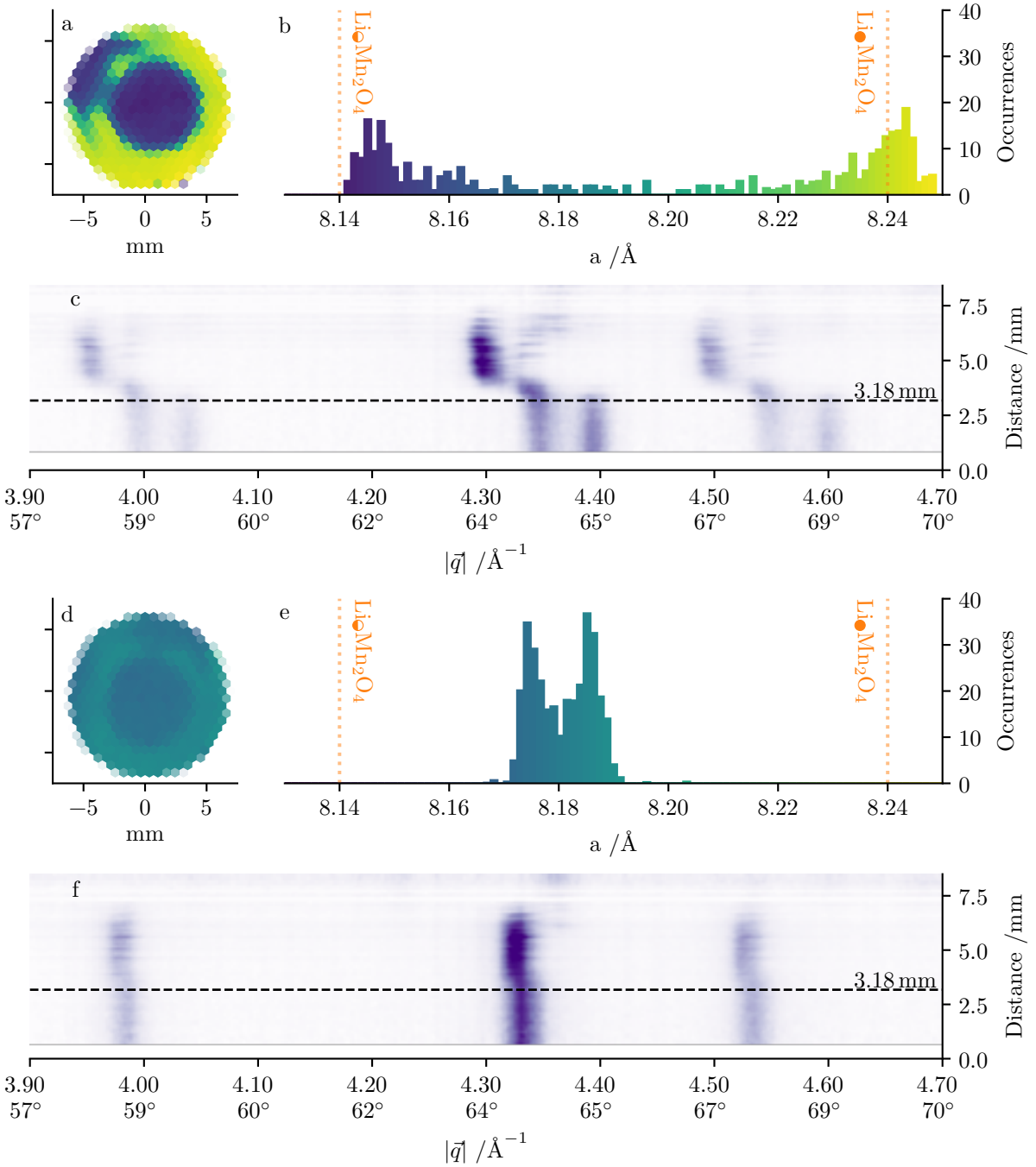

Figure 59: Maps and histograms of unit-cell parameter a in a $LiMn_2O_4$ cathode charged to 4.7 V at 2 C with a 6.35 mm diameter lithium anode. The same cathode was mapped before (a, b) and after (d, e) being left in electrolyte solution for five days. (c, f) Diffractograms for $LiMn_2O_4$ cathode segmented by distance from center of lithium anode (c) before and (f) after equilibration in electrolyte. In loci where two phases are present, the larger cell parameter is selected. Dashed line indicates nominal radius of lithium metal anode. 2θ Bragg angles resulting from Cu K_α radiation are shown for convenience.

a slightly larger cell parameter (8.058 Å) than reported for fully delithiated $LiMn_2O_4$ (8.04 Å to 8.048 Å), indicating incomplete delithiation.[168,169,177] Between 3.45 mm and 4.12 mm from the center, two phases were again present, though now with the range of cell parameters associated with the solid-solution region of the phase diagram. Inspection of selected individual diffractograms (Figure 60) showed that these two phases indeed existed within single ≈1 mm loci. Furthermore, within this region there was a gradient in the peak positions between these two phases, favoring the smaller cell parameter closer to the center of the electrode (Figure 59c). Peaks at 4.37 $Å^{-1}$ also seen at high radial distances are associated with the aluminum current collector, since they did not coincide with the (333) or (531) peaks of the $LiMn_2O_4$ phases. At these distances, the X-ray probe appeared to illuminate areas with less active material. The nominal radius of the lithium metal anode was 3.18 mm, and within this radius only phases with cell parameters similar to $Li_{◒}Mn_2O_4$ and $Li_{○}Mn_2O_4$ phases were present. Beyond 4.12 mm (yellow region in Figure 59a), the patterns were dominated by a single, highly lithiated phase (Figures 59c and 60). There was also a portion of the outer edge that showed a similar state to the center region (top left of Figure 59a), despite no lithium metal being present in this region. Instrumental artifacts due to X-ray shadowing were ruled out by rotating the specimen on the instrument stage, resulting in a corresponding movement of this delithiated edge region. This edge feature resulted in the periodic presence of a second peak at 4.34 $Å^{-1}$ in diffractograms far from the center of the electrode in Figure 59c because the segmentation procedure averaged along a perimeter of the electrode.

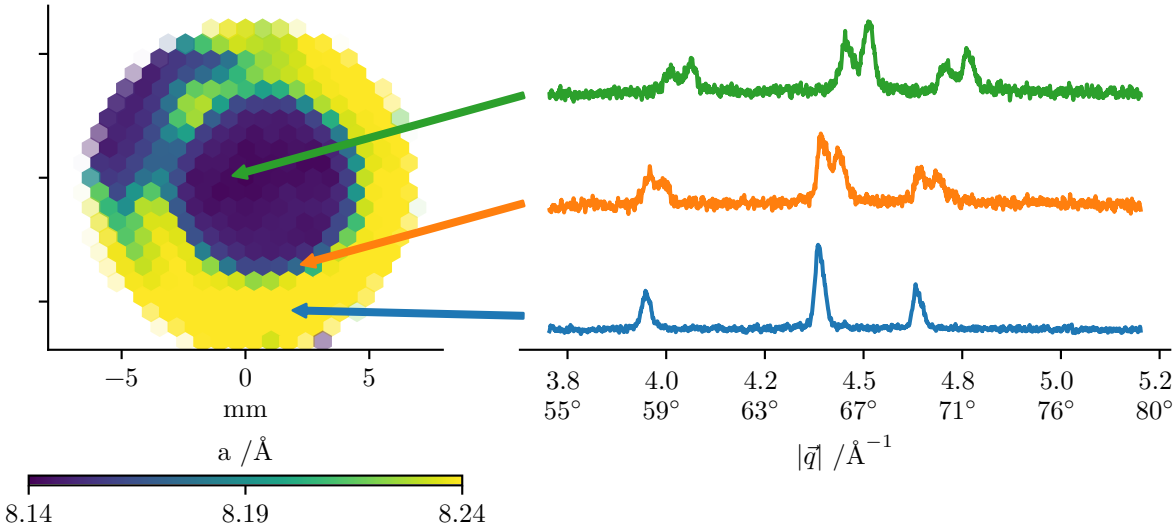

Figure 60: Map of the unit-cell parameter a in a single $LiMn_2O_4$ cathode charged to 4.7 V at 2 C with a 6.35 mm lithium anode, and corresponding diffractograms for select loci. 2θ Bragg angles resulting from Cu K_α radiation are shown for convenience.

Since the center region in Figure 59a entered the two-phase regime, it is worth considering the relative phase fractions to gauge the extent of delithiation. Despite being charged all the way to 4.7 V, the phase fractions within this center region (Figure 61a,b) were at or below those from electrodes charged to $Li_{0.36}Mn_2O_4$ at the same 2 C rate with full-sized lithium metal anodes (Figure 57c). However, when a cell containing a small anode was charged more slowly, at 0.1 C, the distribution of phase fractions exhibited a higher extent of delithiation and the phase fractions were more uniformly distributed across the entire electrode, independent of the position of the 6.35 mm diameter lithium anode (Figure 61c,d). Despite its apparent uniformity,

this electrode still exhibited a lower fraction of oxidized material compared to an electrode with a full-sized lithium anode charged to 4.7 V at 2 C (Figure 61e,f).

Within the solid-solution regime, different compositions have different chemical potentials.[156] Therefore, the co-existence of two such phases inside the domain of miscibility within the same electrode would produce a driving force towards equilibration by exchange of Li^+ and e^- through the solid matrix. The distribution of domains in Figure 59a was re-analyzed periodically; the striking heterogeneity remained essentially unchanged over a period of several weeks. In the absence of electrolyte, equilibration would require exchange of Li^+ ions and electrons through the solid phase; the former was expected to be slow. As a result, to further test the possibility of equilibration, the cathode was placed in electrolyte solution under argon head-space for five days and analyzed again. The resulting ensemble XRD pattern (Figure 52h) contained peaks from a single phase with a cell parameter part way through the solid-solution regime, suggesting a high degree of equilibration. However, the associated map still contained two distinct regions, with a smaller cell parameter where the lithium metal anode had been present (Figure 59d). The cell parameters in the two regions were now much closer, approximately midway through the solid-solution transition: 8.175 Å and 8.185 Å (Figure 59e). The presence of two distinct cell parameters was not detectable by ensemble XRD (Figure 52h). Furthermore, no peaks associated with the fully delithiated $Li_{\bigcirc}Mn_2O_4$ phase were visible at 4.4 $Å^{-1}$ (Figure 59f). The two phases differ in unit cell parameter by ≈0.1 Å, which corresponds to a lithium content difference of $Li_{0.02}$. This difference in lithium content can be used to estimate the potential difference between the regions. When charging at 0.1 C within the solid-solution

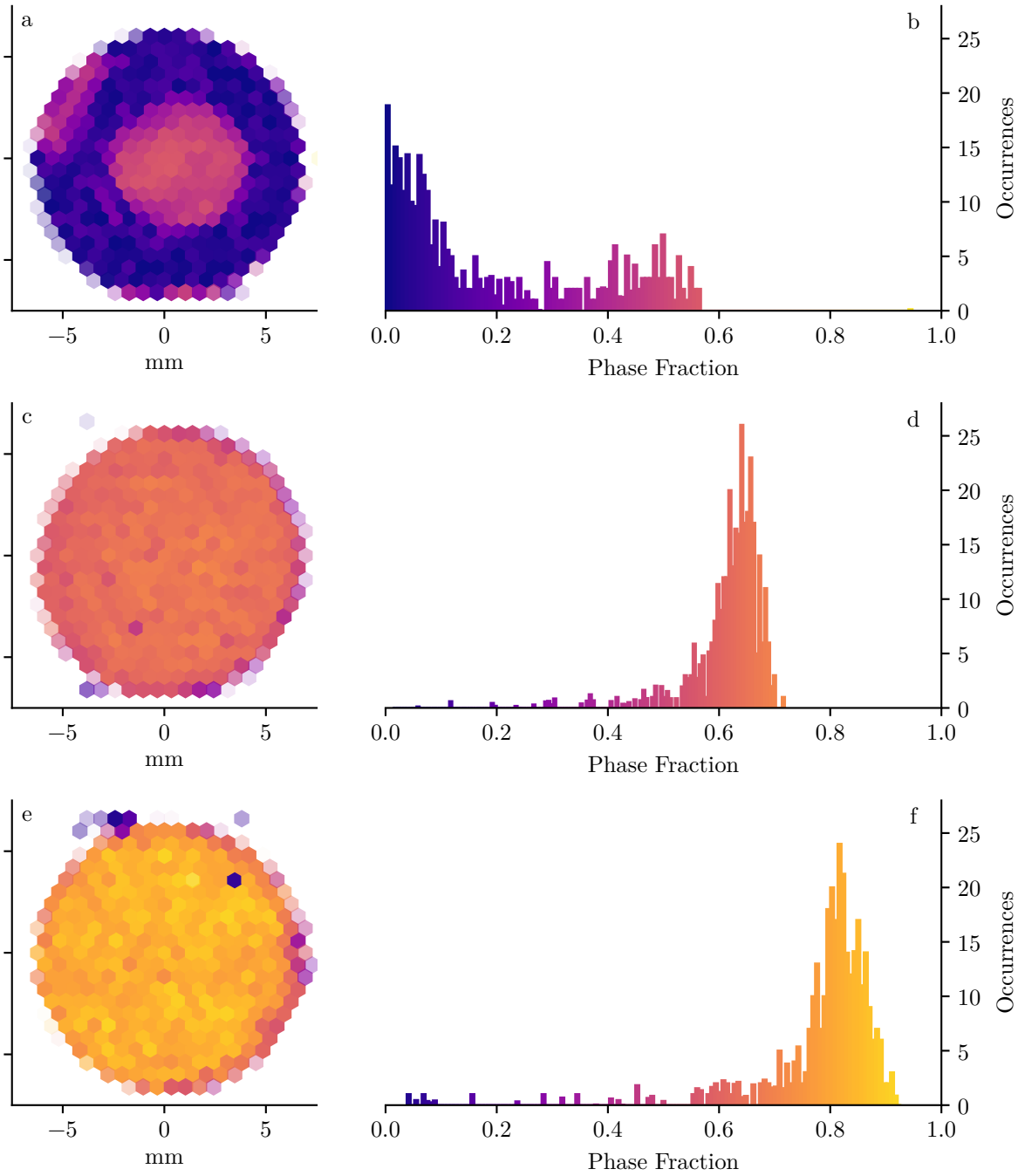

Figure 61: Maps and corresponding histograms of relative fractions of $Li_{0.27}Mn_2O_4$ phase in cathodes charged to 4.7 V with 6.35 mm lithium metal anode at (a,b) 2 C and (c,d) 0.1 C; and (e,f) charged to 4.7 V with 12.7 mm lithium metal anode at 2 C.

regime (Figure 50a,e), the slope of the galvanostatic curve ($\frac{dE}{dx}$) is ≈0.2 V. Combining this slope with the $Li_{0.02}$ composition difference provides an estimate for the potential difference between the two phases of 4 mV. While this potential difference is not the true thermodynamic potential since the slope was obtained under an applied current, it nevertheless provides an estimate of the over-potential needed to overcome the kinetic limitations of this $LiMn_2O_4$ electrode.

The heterogeneous region seen on the outer rim at the top left of Figure 59a had equilibrated to the same extent as the central region (top of Figure 59d). The faint feature seen above 5 mm radial distance at 4.37 $Å^{-1}$ is again attributed to the aluminum current collector. This relaxation demonstrates that the solid-solution phase segregation (Figure 59a) is a meta-stable phenomenon, with a high kinetic barrier preventing equilibration when no electrolyte is present. However, the incomplete relaxation shows that this kinetic barrier is not completely removed in the presence of electrolyte. At slow rates (0.1 C), the phase fraction is independent of the position of the anode (Figure 61c), showing the system is able to overcome the kinetic barrier when more time is available for mass and charge transport.

The mm-scale lateral distances between the lithium anode and the unreacted outer material has implications for lithium-ion transport since these distances are considerably larger than the 25 µm separation between the two electrodes. Movement of lithium ions is driven by the gradient of electrochemical potential between the two electrodes.[180] Assuming no convection within the electrolyte, the flux of lithium ions $\mathbf{J}_{Li^+}$ can be described using the Nernst-Planck equation:

$$\mathbf{J} = -\Big[D\nabla c + \frac{De}{k_B T} c(\nabla \phi)\Big]$$

where D is the diffusivity of Li^+, c is the concentration of the ionic species, e is the elementary charge, k_B is the Boltzmann constant, T is the absolute temperature, and ϕ is the electrostatic potential. The Nernst-Planck equation can be divided into two parts: $D\nabla c$ describes the diffusion of ions due to a concentration gradient ∇c, and $\frac{De}{k_B T} c(\nabla \phi)$ describes the migration of ions due to an electrostatic potential gradient $\nabla \phi$. Traditionally, this equation has been considered only in the direction between the two electrodes, however for this system the flux and gradients must be considered in two directions: normal to the electrode face ($\mathbf{J}_\perp$), and parallel to the electrode face ($\mathbf{J}_\parallel$). Since the equation is linear with regards to each spatial dimension, the full equation can be broken down into these two components:

$$\mathbf{J} = \mathbf{J}_\perp + \mathbf{J}_\parallel = -D\Big[\nabla_\perp c + \frac{e}{k_B T} c(\nabla_\perp \phi) + \nabla_\parallel c + \frac{e}{k_B T} c(\nabla_\parallel \phi)\Big]$$

The lithium anode is attached to a steel spacer that is parallel to the electrode faces, is larger than both the anode and cathode, and is at the same potential as the anode (Figure 2). This means that in the region where lithium metal is present and in regions far away from the lithium metal, the system resembles one composed of two parallel conducting plates. In these cases, only electric potential gradients normal to the electrode face ($\nabla_\perp \phi$) are non-zero, while $\nabla_\parallel \phi = 0$. The concentration gradient during charge is created by the adsorption of Li^+ at the anode and desorption of Li^+ at the cathode. At the mm scale, both the anode and cathode faces

are relatively uniform and so the rate of ion adsorption/desorption will be considered uniform across both faces. This means that in areas of the cathode where lithium metal is present, the concentration gradient parallel to the electrode face ($\nabla_{\parallel} c$) is zero. The over-potential required to deposit lithium on bare stainless steel is on the order of tens of millivolts,[181] suggesting that the rate of lithium plating on stainless steel is slow relative to the rate on lithium metal. If so, for regions of the cell far from the lithium metal anode, negligible Li^+ reduction would occur on the steel spacer. Under this assumption, once a potential difference is applied between the two electrodes, electric double-layers form at both the cathode and steel spacer, separately. These double-layers oppose further electric migration in the perpendicular direction, by establishing both an opposing electric potential and an opposing concentration gradient. Therefore, the perpendicular component of the electric field gradient ($\nabla_{\perp} \phi$) and concentration gradient ($\nabla_{\perp} c$) will both be close to zero. A high level of lithium plating on the stainless steel spacer would generate Li^+ flux from electric migration and would be expected to result in appreciable levels of delithiation at all areas of the cathode. The low extent of delithiation seen in regions of the cathode not near the lithium metal anode (Figure 59a,b) is consistent with the initial assumption of slow lithium plating on the stainless steel spacer.

The end result is two different equations governing the Li^+ flux for the two cathode regions:

$$\mathbf{J}_{center} = -D\left[\frac{e}{k_B T} c(\nabla_{\perp} \phi) + \nabla_{\perp} c\right]$$

$$\mathbf{J}_{rim} = -D\nabla_{\parallel} c$$

Where lithium metal is present ($\mathbf{J}_{center}$), the Nernst-Planck equation follows the conventional 1-dimensional transport dynamics. Where no lithium metal is present ($\mathbf{J}_{rim}$), transport is governed by the parallel component ($\mathbf{J}_{\parallel}$)). The physical interpretation is that because there is no sustained adsorption of Li^+ to the anode in these areas, diffusion is only occurring laterally. Li^+ diffusion is dependent on local concentration gradients, $-D\nabla_{\parallel}c$, and these gradients will be smaller when the full difference in concentration spans a larger distance, as is the case for cathode regions not near the anode. We therefore conclude that Li^+ diffusion is limiting in the edge region, where no sink of Li^+ ions is available at the lithium metal anode. A more complete model can be built by solving the partial differential equations resulting from the *Poisson-Nernst-Planck* equations,[182–185] however prior efforts have generally been limited to 1-dimensional transport between the electrodes; the situation discussed here would require a two-dimensional simulation for this unique cell geometry.

Electron-transfer kinetics may be affected by the absence of proper stack pressure where the anode is not present. This would increase the electronic resistance between the current collector and the cathode material, or between the $LiMn_2O_4$ agglomerates and the surrounding conductive carbon matrix. Poor composite/current-collector conductivity can be artificially produced by inducing delamination through the choice of punching direction. The effect of delamination is still dramatic even when sufficient stack pressure is applied (Figure 53). It is note-worthy that the effects of delamination in Figure 53 occur at similar rates to the effects of the under-sized lithium-metal anode. The small delithiated region on the outer edges in Figure 59, opposite to which there is no anode material, could indicated a “see-saw” effect, where

one side of the steel spacer is always pressed down onto the cathode by the internal spring. Ultimately, both Li^+ and e^- transport can be rate-limiting and their relationship depends on the specifics of cathode construction.[186]

4.3.2 Long-Term Capacity Loss

As a cell repeatedly cycles, there is inevitably a measurable loss of capacity. Diffraction mapping can be used to probe the nature of this capacity loss because it indicates domains with extremely disparate rates of the reaction. A standard coin cell was charged and discharged thirty-three times at 2C, targeting ≈50 % capacity loss from the first cycle. The experiment was repeated with a second cell with the addition of a final charge before disassembly. The capacity losses between the first and last discharge for the two cells were 43 % and 66 % (Figure 62b,c). Bulk X-ray diffractograms (Figure 52i,j) contained a single set of peaks within the solid-solution regime. The unit-cell parameters when ending on discharge (43 % loss) and charge (66 % loss) were 8.213 Å and 8.194 Å (Table II), corresponding to $Li_{\approx 0.85}Mn_2O_4$ and $Li_{\approx 0.77}Mn_2O_4$.[167,169,170] These cell parameters were well within the solid-solution regime. The bulk diffractograms (Figures 52i,j) exhibited shoulders towards higher scattering lengths on all peaks, corresponding to smaller cell parameters. To explore the distribution of states, the electrode with a final charging step was mapped (Figure 63). A region with smaller cell parameters was visible on the right side of the cathode (Figure 63a). The accompanying histogram showed that the majority of the cathode had a cell parameter of 8.20 Å ($Li_{\approx 0.79}Mn_2O_4$), with the smaller region having a cell parameter just above 8.18 Å ($Li_{\approx 0.71}Mn_2O_4$). This distribution

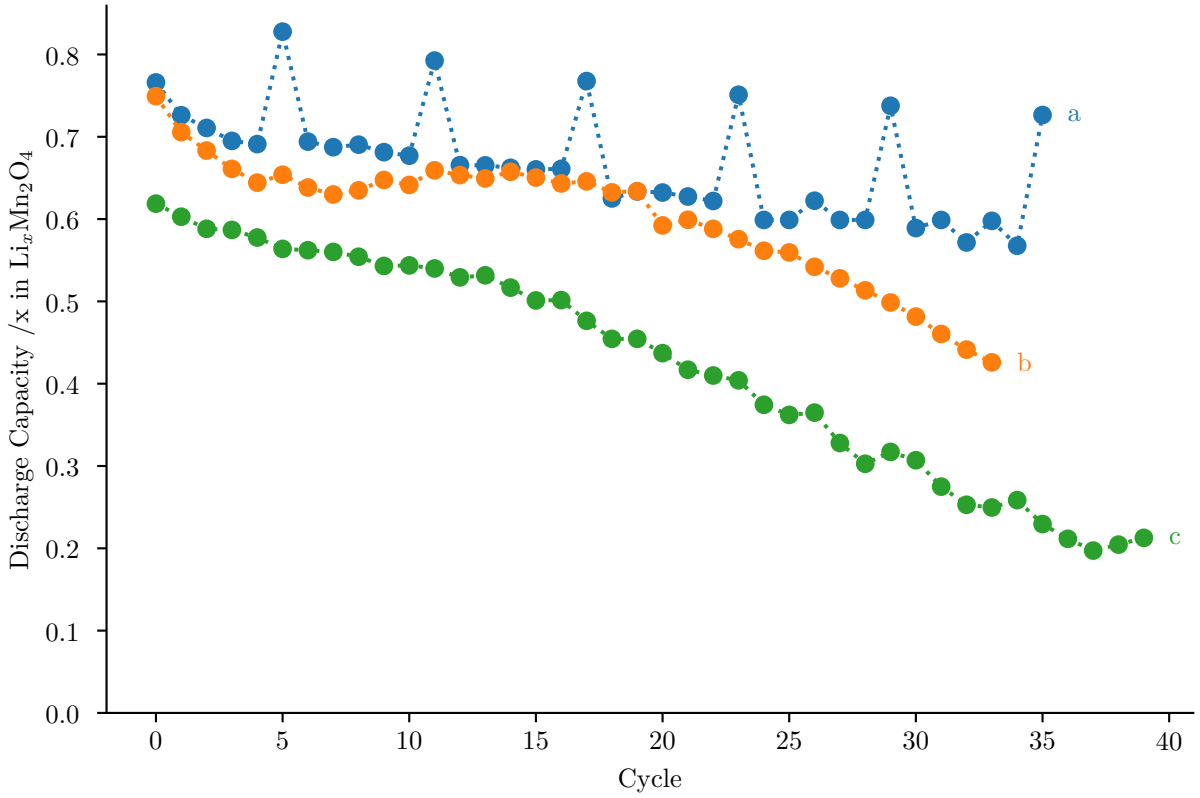

Figure 62: Discharge capacities of coin cell with $LiMn_2O_4$ cathode and lithium metal anode at 2 C a) with intermediate cycles at 0.1 C, b) ending on discharge, and c) ending on charge.

of cell parameters (Figures 63 and 64) was consistent with the ensemble XRD pattern (Figure 52j).

The cell parameters for both samples charged for multiple cycles were within the range of the $Li_●Mn_2O_4$ and $Li_◒Mn_2O_4$ end-members of the solid-solution regime (Table II). This indicates that both full re-lithiation to $Li_●Mn_2O_4$ and appreciable de-lithiation to $Li_◒Mn_2O_4$ were hindered. For the sample ending on discharge (43 % capacity loss), the capacity during the final

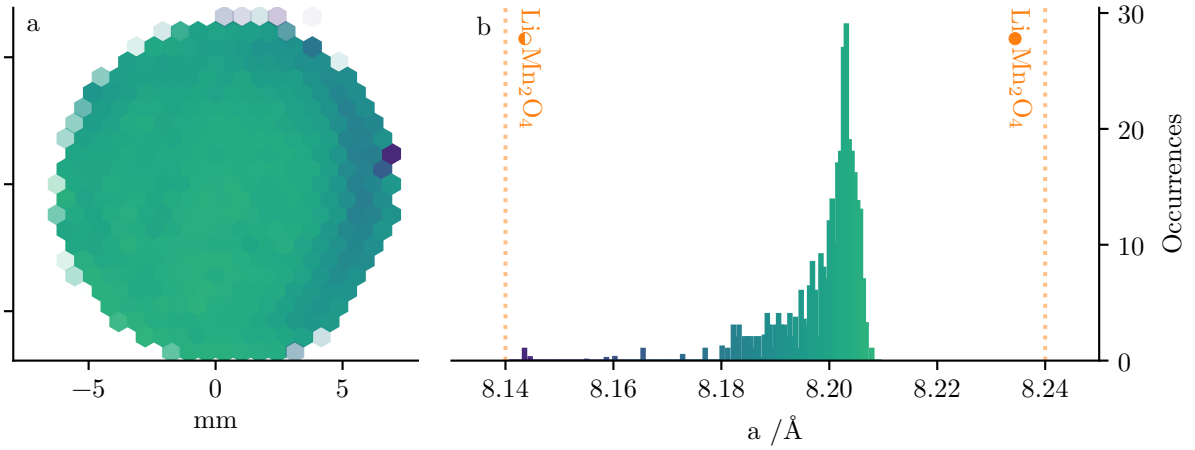

Figure 63: (a) Unit-cell parameter map and (b) histogram of an $LiMn_2O_4$ cathode after forty charge-discharge cycles at 2 C between 3.5 V and 4.7 V, followed by final charge to 4.7 V.

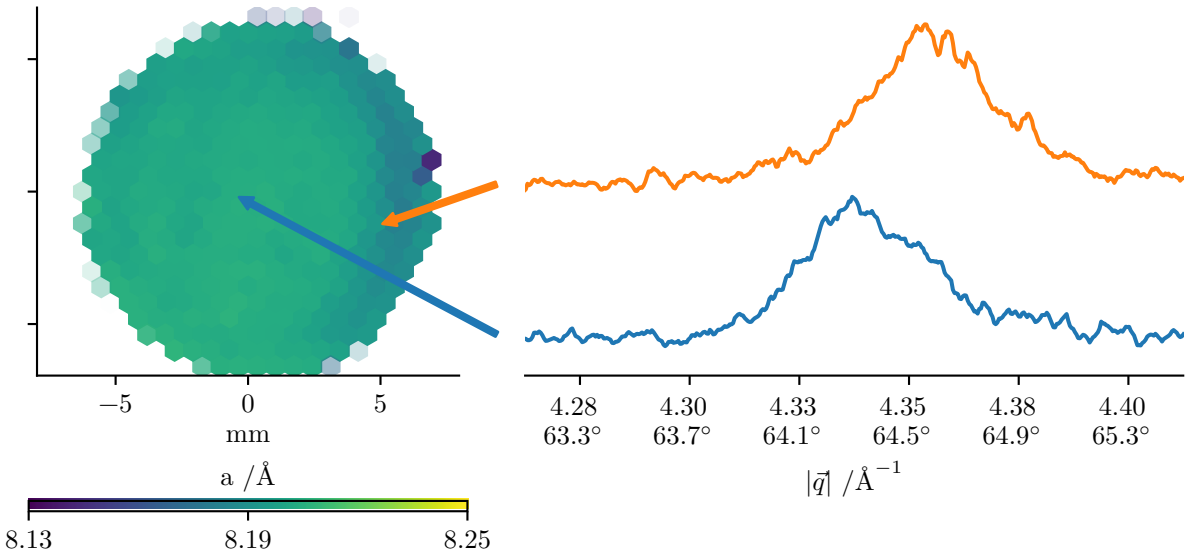

Figure 64: Map of the unit-cell parameter a in a single $LiMn_2O_4$ cathode charged to 4.7 V at 2 C for 40 cycles, ending on charge. Corresponding diffractograms for select loci. 2θ Bragg angles resulting from Cu K_α radiation are shown for convenience.

discharge cycle was equivalent to $Li_{\Delta 0.42}Mn_2O_4$ (Figure 62b). Combining this capacity with the extent of delithiation, estimated above from ensemble XRD, provides a range of delithiation during the final cycle of $Li_{0.85-0.43}Mn_2O_4$. For the sample ending on charge (66 % capacity loss), the capacity during the final charge cycle was $Li_{\Delta 0.20}Mn_2O_4$, producing an estimated range of delithiation during the final cycle of $Li_{0.97-0.77}Mn_2O_4$. The sample ending on charge had a lower final capacity, and also a lower overall level of delithiation during the final cycle. The sample with a higher final capacity (Figure 62b) was delithiated beyond $Li_{0.5}Mn_2O_4$, which marks the start of the two-phase regime.[167,169] The sample exhibiting a lower final capacity (Figure 62c) cycled only within the solid-solution regime. These results suggest that the loss of cyclability is driven by ever increasing barriers to delithiation. However, this limitation against delithiation is not uniform. The small region on the right of Figure 63a is more active and able to reach smaller cell parameters. There is a similarity between the radius of the cathode and the shape of the more oxidized region on the right side of Figure 63a. One possibility is that the cathode and anode were misaligned within the coin cell. The suggestion that misaligned electrodes could produce higher oxidation states is initially counter-intuitive, since the small-anode experiments demonstrated that area without adjacent lithium metal did not reach appreciable levels of delithiation (Figure 59a-c). However, inspection of the relationship between lateral distance from the anode and the position of diffraction peaks (Figure 59c) shows that a $\approx$1 mm region outside the expected radius of the metal anode exhibited larger unit-cells than the material directly opposite the lithium metal anode, and hence experienced a smaller degree of delithiation.

4.4 Conclusion

XRD mapping was performed with 1 mm resolution on $LiMn_2O_4$ cathodes after electrochemical cycling. Samples were mapped after being partially charged at rates from 0.1 C to 5 C, and also after being charged to 4.7 V with a lithium metal anode of half the diameter of the $LiMn_2O_4$ cathode. At all rates, electrodes exhibited regions where delithiation was inhibited, and when charged at high rates, samples showed higher degrees of delithiation towards the surface of the electrode demonstrating a gradient of delithiation into the depth of the electrode. The use of an anode smaller than the cathode dimensions produced appreciable delithiation at 2 C only where the cathode was present, with mass transport being insufficient to enable delithiation of more distant regions.

Some degree of heterogeneity appeared at intermediate states of charge, regardless of the experimental conditions. When charged to capacities part-way through the two-phase regime, $LiMn_2O_4$ cathodes contain heterogeneous regions that are behind the overall state-of-charge of the rest of the electrode. This behavior is independent of rate and is aggravated by mismatched electrode geometries. However, when the electrode is taken to its full capacity (or 4.7 V cut-off), the difference in extent of delithiation between the loci within the electrode is smaller. Diffraction mapping shows that differences in local over-potential exist at the mm scale during the first charge. Even if the full state-of-charge is reached, the higher over-potential needed in these areas translates to a lower energy-density for the electrode.

Furthermore, these inhomogeneities were detected to occur either normal or parallel to the electrode face. Inhomogeneities normal to the electrode face (i.e. into the depth of the electrode)

result from limited diffusion of Li^+ through the porous cathode matrix. Inhomogeneities parallel to the electrode face result from more complex effects, likely involving limited Li^+ diffusion through the electrode and electrolyte. When the anode and cathode do not overlap fully, a sharp loss of reactivity away from the electrode overlap reveals a reduced mass transport capability over these long distances. However, this is only true at high rates (2 C); at low rates (0.1 C), mass transport is sufficient to allow delithiation several mm from the anode. The observation that this solid-solution phase segregation does not reach equilibrium even in the presence of electrolyte highlights the slow transport within these dense electrode, providing a possible explanation for the decay in power density observed upon increasing electrode thickness.

CHAPTER 5

CONCLUSION

Details of the electrochemical mechanisms underlying commercially relevant cathode materials were explored using X-ray imaging and mapping techniques optimized for detecting chemical and structural heterogeneity at the levels of primary particles, secondary particle agglomerates, and complete electrodes. Spatially resolved XAS of primary particles showed an outer layer of reduced Ni on all measurable crystallographic facets, even at high states of charge. Additionally, a sub-surface layer of Ni at an intermediate oxidation state extended farther into the particle than expected from TEM characterization. The presence of these irreversible reaction products will hinder both lithium diffusion and full electrode utilization.

Spectromicroscopy of secondary particles showed rapid and stochastic oxidation, in contrast to the gradual oxidation observed by ensemble XAS. This discrepancy highlights the importance of the local electrochemical environment on redox chemistry, and the value of performing operando studies using chemically sensitive imaging techniques. Further correlation was found between internal particle micro-structure and anomalous Ni reduction, showing the importance of particle micro-structure in controlling electrochemical reactions.

At the level of a complete electrode, long-range transport properties were evaluated in thick, high-density electrodes, such as those preferred for commercial cells. Structural mapping of such cathodes charged at different rates demonstrated that delithiation was restricted by poor Li^+ transport into the electrode solid matrix. Additionally, asymmetric placement of the cathode

and anode resulted in limited delithiation laterally across the electrode, showing that diffusion through the electrolyte was insufficient over long distances. This lateral heterogeneity across the electrode was found to be meta-stable, resisting equilibration even when a diffusion pathway was made available by the addition of fresh electrolyte.

Armed with a more sophisticated understanding of the underlying chemical phenomena, improvements to cathode performance can be engineered that target the relevant length-scale. These solutions will lead to more efficient, more reliable, and safer electrochemical energy storage systems.

CITED LITERATURE

1. Wolf, M., May, B. M. & Cabana, J. Visualization of Electrochemical Reactions in Battery Materials with X-ray Microscopy and Mapping. *Chem. Mater.* **29,** 3347–3362 (2017).
2. Whittingham, M. S. History, Evolution, and Future Status of Energy Storage. *Proc. IEEE* **100,** 1518–1534 (May 2012).
3. Andre, D. *et al.* Future generations of cathode materials: an automotive industry perspective. *J. Mater. Chem. A* **3,** 6709–6732 (2015).
4. Hawkins, T. R., Gausen, O. M. & Strømman, A. H. Environmental impacts of hybrid and electric vehicles—a review. *The International Journal of Life Cycle Assessment* **17,** 997–1014 (May 2012).
5. M. Armand, J. T. Building Better Batteries. *Nature* **451,** 652–657 (2008).
6. Winter, M. & Brodd, R. J. What are batteries, fuel cells, and supercapacitors? *Chem. Rev.* **104,** 4245–4269 (2004).
7. Whittingham, M. S. Ultimate Limits to Intercalation Reactions for Lithium Batteries. *Chem. Rev.* **114,** 11414–11443 (2014).
8. Etacheri, V., Marom, R., Elazari, R., Salitra, G. & Aurbach, D. Challenges in the development of advanced Li-ion batteries: a review. *Energy Environ. Sci.* **4,** 3243–3262 (9 2011).
9. Huggins, R. A. in *Advanced Batteries* 1–24 (Springer Science+Business Media, LLC, 233 Spring Street, New York, NY 10013, USA, 2009).
10. Palacin, M. R. Recent Advances in Rechargeable Battery Materials: A Chemist's Perspective. *Chem. Soc. Rev.* **38,** 2565–2575 (9 2009).
11. Pillot, C. *The Rechargeable Battery Market and Main Trends 2016–2015* `http://cii-resource.com/cet/FBC-TUT8/Presentations/Pillot_Christophe.pdf`. Presented at the 33rd International Battery Seminar and Exhibit. Mar. 2017.
12. Vanỳsek, P. *Electrochemical Series in Handbook of Chemistry and Physics* 2011.
13. Faenza, N. V. *et al.* Electrolyte-Induced Surface Transformation and Transition-Metal Dissolution of Fully Delithiated $LiNi_{0.8}Co_{0.15}Al_{0.05}O_2$. *Langmuir* **33,** 9333–9353 (2017).
14. Nitta, N., Wu, F., Lee, J. T. & Yushin, G. Li-ion Battery Materials: Present and Future. *Mater. Today* **18,** 252–264 (2015).
15. Xu, W. *et al.* Lithium metal anodes for rechargeable batteries. *Energy Environ. Sci.* **7,** 513–537 (2014).
16. Liu, C., Neale, Z. G. & Cao, G. Understanding electrochemical potentials of cathode materials in rechargeable batteries. *Mater. Today* **19,** 109–123. ISSN: 1369-7021 (2016).
17. Whittingham, M. S. Lithium Batteries and Cathode Materials. *Chem. Rev.* **104,** 4271–4302 (2004).
18. Li, M., Lu, J., Chen, Z. & Amine, K. 30 Years of Lithium-Ion Batteries. *Adv. Mater.* **30,** 1800561.

19. Mizushima, K., Jones, P., Wiseman, P. & Goodenough, J. Li_xCoO_2 ($0 < x < -1$): A new cathode material for batteries of high energy density. *Mater. Res. Bull.* **15,** 783–789 (June 1980).
20. Wang, L. *et al.* Recent advances in layered $LiNi_xCo_yMn_{1-x-y}O_2$ cathode materials for lithium ion batteries. *J. Solid State Electrochem.* **13,** 1157–1164 (Sept. 2008).
21. Yin, S.-C., Rho, Y.-H., Swainson, I. & Nazar, L. F. X-ray/Neutron Diffraction and Electrochemical Studies of Lithium De/Re-Intercalation in $Li_{1-x}Co_{1/3}Ni_{1/3}Mn_{1/3}O_2$ (x = 0 → 1). *Chem. Mater.* **18,** 1901–1910 (2006).
22. Watanabe, S., Kinoshita, M., Hosokawa, T., Morigaki, K. & Nakura, K. Capacity fade of $LiAl_yNi_{1-x-y}Co_xO_2$ cathode for lithium-ion batteries during accelerated calendar and cycle life tests (surface analysis of $LiAl_yNi_{1-x-y}Co_xO_2$ cathode after cycle tests in restricted depth of discharge ranges). *J. Power Sources* **258,** 210–217 (2014).
23. Radin, M. D. *et al.* Narrowing the Gap between Theoretical and Practical Capacities in Li-Ion Layered Oxide Cathode Materials. *Adv. Energy Mater.* ISSN: 1614-6840. doi:10.1002/aenm.201602888.
24. Jain, A. *et al.* The Materials Project: A materials genome approach to accelerating materials innovation. *APL Mater.* **1,** 011002 (2013).
25. Momma, K. & Izumi, F. *VESTA3* for three-dimensional visualization of crystal, volumetric and morphology data. *J. Appl. Crystallogr.* **44,** 1272–1276 (Dec. 2011).
26. Atkins, P. & de Paula, J. in *Physical Chemistry* 9th ed., 137–140 (W.H. Freeman and Company, New york, NY, 2010).
27. Atkins, P. & de Paula, J. in *Physical Chemistry* 9th ed., 156–161 (W.H. Freeman and Company, New york, NY, 2010).
28. Bard, A. J. & Faulkner, L. R. in *Electrochemical Methods* 60–62 (John Wiley & Sons, Inc., New York, NY, 2001).
29. Bard, A. J. & Faulkner, L. R. in *Electrochemical Methods* 87–107 (John Wiley & Sons, Inc., New York, NY, 2001).
30. Bard, A. J. & Faulkner, L. R. in *Electrochemical Methods* 137–155 (John Wiley & Sons, Inc., New York, NY, 2001).
31. Henke, B., Gullikson, E. & Davis, J. X-Ray Interactions: Photoabsorption, Scattering, Transmission, and Reflection at E = 50-30,000 eV, Z = 1-92. *Atomic Data and Nuclear Data Tables* **54,** 181–342 (1993).
32. Niewa, R., Hu, Z. & Kniep, R. Mn and Fe K-edge XAS Spectra of Manganese and Iron Nitrido Compounds. *European Journal of Inorganic Chemistry* **2003,** 1632–1634 (Apr. 2003).
33. De Groot, F. & Kotani, A. in *Core Level Spectroscopy of Solids* 255–260 (CRC Press, Boca Raton, FL, 2008).
34. De Groot, F. & Kotani, A. in *Core Level Spectroscopy of Solids* 14–15 (CRC Press, Boca Raton, FL, 2008).
35. https://commons.wikimedia.org/wiki/File:XASEdges.svg. Accessed: 2019-05-06.
36. Pecharsky, V. K. & Zavalij, P. Y. in *Fundamentals of Powder Diffraction and Structural Characterization of Materials* 2nd ed., 159–202 (Springer Science+Business Media, LLC, 233 Spring Street, New York, NY 10013, USA, 2009).

37. https://commons.wikimedia.org/wiki/File:Bragg_diffraction_2.svg. Accessed: 2019-05-06.
38. Livermore, C. *Course materials for 6.777J / 2.372J Design and Fabrication of Microelectromechanical Devices* MIT OpenCourseWare (http://ocw.mit.edu/), Massachusetts Institute of Technology. Accessed: 2019-05-06. 2007.
39. Shapiro, D. A. *et al.* Chemical Composition Mapping with Nanometre Resolution by Soft X-ray Microscopy. *Nat. Photonics* **8,** 765–769 (Oct. 2014).
40. Guinebretière, R. *X-ray Diffraction by Polycrystalline Materials* 39–48. ISBN: 978-1-905209-21-7 (ISTE Ltd, 2007).
41. Mobilio, S., Boscherini, F. & Meneghini, C. *Synchrotron Radiation. Basics, Methods and Applications* ISBN: 978-3-642-55314-1. doi:10.1007/978-3-642-55315-8 (Springer-Verlag Berlin Heidelberg, 2015).
42. Ice, G. E. & Pang, J. W. Tutorial on X-ray microLaue diffraction. *Mater. Charact.* **60,** 1191–1201 (2009).
43. Li, L. *et al.* Visualization of Electrochemically Driven Solid-State Phase Transformations Using Operando Hard X-ray Spectro-imaging. *Nat. Commun.* **6,** 6883 (Apr. 2015).
44. Marchesini, S. *et al. SHARP*: a distributed GPU-based ptychographic solver. *J. Appl. Crystallogr.* **49,** 1245–1252 (Aug. 2016).
45. Shapiro, D. A. *et al.* Ptychographic Imaging of Nano-Materials at the Advanced Light Source with the Nanosurveyor Instrument. *J. Phys.: Conf. Ser.* **849,** 012028 (2017).
46. Borland, D. & Ii, R. M. T. Rainbow Color Map (Still) Considered Harmful. *IEEE Computer Graphics and Applications* **27,** 14–17 (Mar. 2007).
47. Borkin, M. *et al.* Evaluation of Artery Visualizations for Heart Disease Diagnosis. *IEEE Transactions on Visualization and Computer Graphics* **17,** 2479–2488 (Dec. 2011).
48. Van der Walt, S. & Smith, N. *A Better Default Colormap for Matplotlib* http://bids.github.io/colormap/. Accessed: 2019-06-15.
49. Yu, Y.-S. *et al.* Dependence on Crystal Size of the Nanoscale Chemical Phase Distribution and Fracture in Li_xFePO_4. *Nano Lett.* **15,** 4282–4288 (2015).
50. Liu, H. *et al.* Capturing Metastable Structures During High-Rate Cycling of $LiFePO_4$ Nanoparticle Electrodes. *Science* **344,** 1252817 (2014).
51. Lim, J. *et al.* Origin and hysteresis of lithium compositional spatiodynamics within battery primary particles. *Science* **353,** 566–571 (2016).
52. Borkiewicz, O. J., Wiaderek, K. M., Chupas, P. J. & Chapman, K. W. Best Practices for Operando Battery Experiments: Influences of X-ray Experiment Design on Observed Electrochemical Reactivity. *The J. Phys. Chem. Lett.* **6,** 2081–2085 (2015).
53. Lin, C.-K., Ren, Y., Amine, K., Qin, Y. & Chen, Z. In Situ High-Energy X-ray Diffraction to Study Overcharge Abuse of 18650-size Lithium-Ion Battery. *J. Power Sources* **230,** 32–37 (2013).
54. Borkiewicz, O. J. *et al.* The AMPIX Electrochemical Cell: a Versatile Apparatus for In Situ X-ray Scattering and Spectroscopic Measurements. *J. Appl. Crystallogr.* **45,** 1261–1269 (2012).

55. Yu, Y.-S. *et al.* Three-dimensional localization of nanoscale battery reactions using soft X-ray tomography. *Nat. Commun.* **9,** 921 (2018).
56. Zhang, H. *et al.* Facet-Dependent Rock-Salt Reconstruction on the Surface of Layered Oxide Cathodes. *Chem. Mater.* **30,** 692–699 (2018).
57. May, B. M. *et al.* Nanoscale Detection of Intermediate Solid Solutions in Equilibrated Li_xFePO_4 Microcrystals. *Nano Lett.* **17,** 7364–7371 (2017).
58. Newman, J. Optimization of Porosity and Thickness of a Battery Electrode by Means of a Reaction-Zone Model. *J. Electrochem. Soc.* **142,** 97–101 (1995).
59. Wu, S.-L., Javier, A. E., Devaux, D., Balsara, N. P. & Srinivasan, V. Discharge Characteristics of Lithium Battery Electrodes with a Semiconducting Polymer Studied by Continuum Modeling and Experiment. *J. Electrochem. Soc.* **161,** A1836–A1843 (2014).
60. Sallis, S. *et al.* Surface degradation of $Li_{1-x}Ni_{0.80}Co_{0.15}Al_{0.05}O_2$ cathodes: Correlating charge transfer impedance with surface phase transformations. *Appl. Phys. Lett.* **108,** 263902 (2016).
61. De Groot, F. & Kotani, A. *Core Level Spectroscopy of Solids* (CRC Press, 2008).
62. Yoon, W.-S., Chung, K. Y., McBreen, J., Fischer, D. A. & Yang, X.-Q. Electronic structural changes of the electrochemically Li-ion deintercalated $LiNi_{0.8}Co_{0.15}Al_{0.05}O_2$ cathode material investigated by X-ray absorption spectroscopy. *J. Power Sources* **174,** 1015–1020 (2007).
63. Kleiner, K. *et al.* Unraveling the Degradation Process of $LiNi_{0.8}Co_{0.15}Al_{0.05}O_2$ Electrodes in Commercial Lithium Ion Batteries by Electronic Structure Investigations. *ACS Appl. Mater. Interfaces* **7,** 19589–19600 (2015).
64. Nonaka, T. *et al.* Surface-Sensitive X-Ray Absorption Study on $LiNi_{0.8}Co_{0.15}Al_{0.05}O_2$ Cathode Material for Lithium-Ion Batteries. *J. Electrochem. Soc.* **154,** A353–A358 (2007).
65. Hwang, S. *et al.* Investigating Local Degradation and Thermal Stability of Charged Nickel-Based Cathode Materials through Real-Time Electron Microscopy. *ACS Appl. Mater. Interfaces* **6,** 15140–15147 (2014).
66. Bak, S.-M. *et al.* Correlating Structural Changes and Gas Evolution during the Thermal Decomposition of Charged $Li_xNi_{0.8}Co_{0.15}Al_{0.05}O_2$ Cathode Materials. *Chem. Mater.* **25,** 337–351 (2013).
67. Jo, E., Hwang, S., Kim, S. M. & Chang, W. Investigating the Kinetic Effect on Structural Evolution of $Li_xNi_{0.8}Co_{0.15}Al_{0.05}O_2$ Cathode Materials during the Initial Charge/Discharge. *Chem. Mater.* **29,** 2708–2716 (2017).
68. Zhang, H. *et al.* Atomic Insight into the Layered/Spinel Phase Transformation in Charged $LiNi_{0.80}Co_{0.15}Al_{0.05}O_2$ Cathode Particles. *The J. Phys. Chem. C* **121,** 1421–1430 (2017).
69. Bang, H. J., Joachin, H., Yang, H., Amine, K. & Prakash, J. Contribution of the Structural Changes of $LiNi_{0.8}Co_{0.15}Al_{0.05}O_2$ Cathodes on the Exothermic Reactions in Li-Ion Cells. *J. Electrochem. Soc.* **153,** A731–A737 (2006).
70. Hwang, S. *et al.* Investigation of Changes in the Surface Structure of $Li_xNi_{0.8}Co_{0.15}Al_{0.05}O_2$ Cathode Materials Induced by the Initial Charge. *Chem. Mater.* **26,** 1084–1092 (2014).
71. Lin, F. *et al.* Surface reconstruction and chemical evolution of stoichiometric layered cathode materials for lithium-ion batteries. *Nat. Commun.* **5,** 3529 (Mar. 2014).

72. Nam, K.-W. *et al.* Combining In Situ Synchrotron X-Ray Diffraction and Absorption Techniques with Transmission Electron Microscopy to Study the Origin of Thermal Instability in Overcharged Cathode Materials for Lithium-Ion Batteries. *Adv. Funct. Mater.* **23,** 1047–1063 (2013).
73. Zheng, S. *et al.* Microstructural Changes in $LiNi_{0.8}Co_{0.15}Al_{0.05}O_2$ Positive Electrode Material during the First Cycle. *J. Electrochem. Soc.* **158,** A357–A362 (2011).
74. Sasaki, T. *et al.* Capacity-Fading Mechanisms of $LiNiO_2$-Based Lithium-Ion Batteries: I. Analysis by Electrochemical and Spectroscopic Examination. *J. Electrochem. Soc.* **156,** A289–A293 (2009).
75. Hwang, S. *et al.* Determination of the mechanism and extent of surface degradation in Ni-based cathode materials after repeated electrochemical cycling. *APL Mater.* **4,** 096105 (2016).
76. Hwang, S., Kim, D. H., Chung, K. Y. & Chang, W. Understanding local degradation of cycled Ni-rich cathode materials at high operating temperature for Li-ion batteries. *Appl. Phys. Lett.* **105,** 103901 (2014).
77. Wei, C. *et al.* Mesoscale Battery Science: The Behavior of Electrode Particles Caught on a Multispectral X-ray Camera. *Acc. Chem. Res.* **51,** 2484–2492 (2018).
78. May, B. M. *et al.* Effect of Synthetic Parameters on Defects, Structure, and Electrochemical Properties of Layered Oxide $LiNi_{0.80}Co_{0.15}Al_{0.05}O_2$. *J. Electrochem. Soc.* **165,** A3537–A3543 (2018).
79. Zhao, X., Zhou, F. & Dahn, J. R. Phases Formed in Al-Doped $Ni_{1/3}Mn_{1/3}Co_{1/3}(OH)_2$ Prepared by Coprecipitation: Formation of Layered Double Hydroxide. *J. Electrochem. Soc.* **155,** A642–A647 (2008).
80. Grenier, A. *et al.* Reaction heterogeneity in $LiNi_{0.8}Co_{0.15}Al_{0.05}O_2$ induced by surface layer. *Chem. Mater.* **29,** 7345–7352 (2017).
81. Wolfman, M. *Xanespy* `https://github.com/canismarko/xanespy`. 2019.
82. Van der Walt, S. *et al.* scikit-image: image processing in Python. *PeerJ* **2,** e453 (June 2014).
83. Malinowski, E. R. *Factor Analysis in Chemistry* 3rd ed. ISBN: 978-0-471-13479-4 (Wiley, New York, NY, Mar. 2002).
84. Arngren, M., Schmidt, M. N. & Larsen, J. Unmixing of Hyperspectral Images using Bayesian Non-negative Matrix Factorization with Volume Prior. *Journal of Signal Processing Systems* **65,** 479–496. ISSN: 1939-8115 (2010).
85. Kilcoyne, A. L. D. *et al.* Interferometer-controlled scanning transmission X-ray microscopes at the Advanced Light Source. *J. Synchrotron Radiat.* **10,** 125–136 (2004).
86. Freeland, J. W. *et al.* A unique polarized X-ray facility at the Advanced Photon Source. *Rev. Sci. Instrum.* **73,** 1408–1410 (2002).
87. Wang, K. *et al.* An easy-to-implement filter for separating photo-excited signals from topography in scanning tunneling microscopy. *Rev. Sci. Instrum.* **84,** 063704 (2013).
88. Shirato, N. *et al.* Elemental Fingerprinting of Materials with Sensitivity at the Atomic Limit. *Nano Lett.* **14,** 6499–6504 (2014).

89. De Groot, F. & Kotani, A. in *Core Level Spectroscopy of Solids* 225–285 (CRC Press, Boca Raton, FL, 2008).
90. Kobayashi, H., Emura, S., Arachi, Y. & Tatsumi, K. Investigation of inorganic compounds on the surface of cathode materials using Li and O K-edge XANES. *J. Power Sources* **174,** 774–778 (2007).
91. Zhuang, G. V. *et al.* Li_2CO_3 in $LiNi_{0.8}Co_{0.15}Al_{0.05}O_2$ cathodes and its effects on capacity and power. *J. Power Sources* **134,** 293–297 (2004).
92. Liu, X. *et al.* Distinct charge dynamics in battery electrodes revealed by in situ and operando soft X-ray spectroscopy. *Nat. Commun.* **4,** 2568 (Oct. 2013).
93. Xu, J., Lin, F., Doeff, M. M. & Tong, W. A review of Ni-based layered oxides for rechargeable Li-ion batteries. *J. Mater. Chem. A* **5,** 874–901 (3 2017).
94. Li, Q. *et al.* Quantitative probe of the transition metal redox in battery electrodes through soft x-ray absorption spectroscopy. *J. Phys. D: Appl. Phys.* **49,** 413003 (2016).
95. Lin, F. *et al.* Profiling the nanoscale gradient in stoichiometric layered cathode particles for lithium-ion batteries. *Energy Environ. Sci.* **7,** 3077–3085 (9 2014).
96. Deb, A. & Cairns, E. J. In Situ X-ray Absorption Spectroscopy – A Probe of Cathode Materials for Li-Ion Cells. *Fluid Phase Equilib.* **241,** 4–19 (2006).
97. Wang, H. *et al.* Integrated X-ray L Absorption Spectra. Counting Holes in Ni Complexes. *The J. Phys. Chem. B* **102,** 8343–8346 (1998).
98. Lu, M., Wang, J., Fang, H., Hu, Y. & Zhou, J. Unexpected phase separation in $Li_{1-x}Ni_{0.5}Mn_{1.5}O_4$ within a porous composite electrode. *Chem. Commun.* **54,** 4152–4155 (33 2018).
99. Farmand, M. *et al.* Near-Edge X-ray Refraction Fine Structure Microscopy. *Appl. Phys. Lett.* **110,** 063101 (2017).
100. Lebens-Higgins, Z. W. *et al.* Evolution of the Electrode–Electrolyte Interface of $LiNi_{0.8}Co_{0.15}Al_{0.05}O_2$ Electrodes Due to Electrochemical and Thermal Stress. *Chem. Mater.* **30,** 958–969 (2018).
101. Duarte, L. T., Moussaoui, S. & Jutten, C. Source Separation in Chemical Analysis : Recent achievements and perspectives. *IEEE Signal Processing Magazine* **31,** 135–146. ISSN: 1053-5888 (May 2014).
102. Knuth, K. H. *Informed Source Separation: A Bayesian Tutorial* `https://arxiv.org/abs/1311.3001`. Accessed: 2016-08-13.
103. Cummings, M. *et al.* Combining scanning tunneling microscopy and synchrotron radiation for high-resolution imaging and spectroscopy with chemical, electronic, and magnetic contrast. *Ultramicroscopy* **112,** 22–31 (2012).
104. Mom, R. V. *et al.* Simultaneous scanning tunneling microscopy and synchrotron X-ray measurements in a gas environment. *Ultramicroscopy* **182,** 233–242 (2017).
105. Rose, V., Freeland, J. W., Gray, K. E. & Streiffer, S. K. X-ray-excited photoelectron detection using a scanning tunneling microscope. *Appl. Phys. Lett.* **92,** 193510 (2008).
106. In Two Dimensions: Surfaces, C. *Gabor A. Somorjai* ISBN: 978-0-801-41179-3 (Cornell University Press, Ithica, NY, July 1981).
107. Rose, V. *et al.* Synchrotron X-Ray Scanning Tunneling Microscopy: Fingerprinting Near to Far Field Transitions on Cu(111) Induced by Synchrotron Radiation. *Adv. Funct. Mater.* **23,** 2646–2652 (2013).

108. Kersell, H. *et al.* Detecting element specific electrons from a single cobalt nanocluster with synchrotron x-ray scanning tunneling microscopy. *Appl. Phys. Lett.* **111,** 103102 (2017).
109. Kubin, M. *et al.* Probing the oxidation state of transition metal complexes: a case study on how charge and spin densities determine Mn L-edge X-ray absorption energies. *Chem. Sci.* **9,** 6813–6829 (33 2018).
110. Medarde, M. *et al.* $RNiO_3$ perovskites (R=Pr,Nd): Nickel valence and the metal-insulator transition investigated by x-ray-absorption spectroscopy. *Phys. Rev. B* **46,** 14975–14984 (23 Dec. 1992).
111. Piamonteze, C. *et al.* Spin-orbit-induced mixed-spin ground state in $RNiO_3$ perovskites probed by x-ray absorption spectroscopy: Insight into the metal-to-insulator transition. *Phys. Rev. B* **71,** 020406 (2 Jan. 2005).
112. Kojima, Y. *et al.* Degradation analysis of a Ni-based layered positive-electrode active material cycled at elevated temperatures studied by scanning transmission electron microscopy and electron energy-loss spectroscopy. *J. Power Sources* **196,** 7721–7727. ISSN: 0378-7753 (2011).
113. Muto, S. *et al.* Capacity-Fading Mechanisms of $LiNiO_2$-Based Lithium-Ion Batteries: II. Diagnostic Analysis by Electron Microscopy and Spectroscopy. *J. Electrochem. Soc.* **156,** A371–A377 (2009).
114. Karki, K. *et al.* Tuning the Activity of Oxygen in $LiNi_{0.8}Co_{0.15}Al_{0.05}O_2$ Battery Electrodes. *ACS Appl. Mater. Interfaces* **8,** 27762–27771 (2016).
115. Zhang, H., Omenya, F., Whittingham, M. S., Wang, C. & Zhou, G. Formation of an Anti-Core–Shell Structure in Layered Oxide Cathodes for Li-Ion Batteries. *ACS Energy Lett.* **2,** 2598–2606 (2017).
116. Mukherjee, P. *et al.* Surface Structural and Chemical Evolution of Layered $LiNi_{0.8}Co_{0.15}Al_{0.05}O_2$ (NCA) under High Voltage and Elevated Temperature Conditions. *Chem. Mater.* **30,** 8431–8445 (2018).
117. Xiao, P., Shi, T., Huang, W. & Ceder, G. Understanding Surface Densified Phases in Ni-Rich Layered Compounds. *ACS Energy Lett.* **4,** 811–818 (2019).
118. Wandt, J., Freiberg, A. T., Ogrodnik, A. & Gasteiger, H. A. Singlet oxygen evolution from layered transition metal oxide cathode materials and its implications for lithium-ion batteries. *Mater. Today* **21,** 825–833. ISSN: 1369-7021 (2018).
119. Jung, R., Metzger, M., Maglia, F., Stinner, C. & Gasteiger, H. A. Chemical versus Electrochemical Electrolyte Oxidation on NMC111, NMC622, NMC811, LNMO, and Conductive Carbon. *The J. Phys. Chem. Lett.* **8,** 4820–4825 (2017).
120. Jung, R., Metzger, M., Maglia, F., Stinner, C. & Gasteiger, H. A. Oxygen Release and Its Effect on the Cycling Stability of $LiNi_xMn_yCo_zO_2$ (NMC) Cathode Materials for Li-Ion Batteries. *J. Electrochem. Soc.* **164,** A1361–A1377 (2017).
121. Lee, J. *et al.* Unlocking the Potential of Cation-Disordered Oxides for Rechargeable Lithium Batteries. *Science* **343,** 519–522 (2014).
122. Gelb, J., Finegan, D. P., Brett, D. J. & Shearing, P. R. Multi-scale 3D investigations of a commercial 18650 Li-ion battery with correlative electron- and X-ray microscopy. *J. Power Sources* **357,** 77–86. ISSN: 0378-7753 (2017).

123. Yang, S. *et al.* Soft X-ray XANES studies of various phases related to $LiFePO_4$ based cathode materials. *Energy Environ. Sci.* **5,** 7007–7016 (5 2012).
124. Robert, R., Bünzli, C., Berg, E. J. & Novák, P. Activation Mechanism of $LiNi_{0.80}Co_{0.15}Al_{0.05}O_2$: Surface and Bulk Operando Electrochemical, Differential Electrochemical Mass Spectrometry, and X-ray Diffraction Analyses. *Chem. Mater.* **27,** 526–536 (2015).
125. Nowack, L., Grolimund, D., Samson, V., Marone, F. & Wood, V. Rapid Mapping of Lithiation Dynamics in Transition Metal Oxide Particles with Operando X-ray Absorption Spectroscopy. *Sci. Rep.* **6,** 21479 (2016).
126. Bobrikov, I. *et al.* Abnormal phase-separated state of $Li_xNi_{0.8}Co_{0.15}Al_{0.05}O_2$ in the first charge: Effect of electrode compaction. *Electrochim. Acta* **265,** 726–735. ISSN: 0013-4686 (2018).
127. Shizuka, K., Kiyohara, C., Shima, K. & Takeda, Y. Effect of CO_2 on layered $Li_{1+z}Ni_{1-x-y}Co_xM_yO_2$ (M=Al, Mn) cathode materials for lithium ion batteries. *J. Power Sources* **166,** 233–238. ISSN: 0378-7753 (2007).
128. Van Hulzen, M., Ooms, F. G. B., Wright, J. P. & Wagemaker, M. Revealing Operando Transformation Dynamics in Individual Li-ion Electrode Crystallites Using X-Ray Microbeam Diffraction. *Frontiers in Energy Research* **6.** doi:10.3389/fenrg.2018.00059. https://doi.org/10.3389%2Ffenrg.2018.00059 (July 2018).
129. Ahn, J. *et al.* Achieving high capacity and rate capability in layered lithium transition metal oxide cathodes for lithium-ion batteries. *J. Power Sources* **360,** 575–584 (Aug. 2017).
130. Zhou, Y.-N. *et al.* High-Rate Charging Induced Intermediate Phases and Structural Changes of Layer-Structured Cathode for Lithium-Ion Batteries. *Adv. Energy Mater.* **6,** 1600597 (Aug. 2016).
131. Yoon, W.-S., Chung, K. Y., McBreen, J. & Yang, X.-Q. A comparative study on structural changes of $LiCo_{1/3}Ni_{1/3}Mn_{1/3}O_2$ and $LiNi_{0.8}Co_{0.15}Al_{0.05}O_2$ during first charge using in situ XRD. *Electrochem. Commun.* **8,** 1257–1262 (2006).
132. Hua, W. *et al.* (De)Lithiation Mechanism of Hierarchically Layered LiNi1/3Co1/3Mn1/3O2 Cathodes during High-Voltage Cycling. *J. Electrochem. Soc.* **166,** A5025–A5032 (Nov. 2018).
133. Deb, A., Bergmann, U., Cramer, S. P. & Cairns, E. J. In situ X-ray absorption spectroscopic study of the $Li[Ni_{1/3}Co_{1/3}Mn_{1/3}]O_2$ cathode material. *J. Appl. Phys.* **97,** 113523 (2005).
134. Otsu, N. A Threshold Selection Method from Gray-Level Histograms. *IEEE Transactions on Systems, Man, and Cybernetics* **9,** 62–66 (Jan. 1979).
135. Jones, E., Oliphant, T., Peterson, P., *et al. SciPy: Open source scientific tools for Python* [Online; accessed 2019-06-21]. 2001. http://www.scipy.org/.
136. Hunter, J. D. Matplotlib: A 2D graphics environment. *Computing in Science & Engineering* **9,** 90–95 (2007).
137. Ohzuku, T. & Makimura, Y. Layered Lithium Insertion Material of $LiCo_{1/3}Ni_{1/3}Mn_{1/3}O_2$ for Lithium-Ion Batteries. *Chem. Lett.* **30,** 642–643 (2001).

138. Yabuuchi, N. & Ohzuku, T. Novel lithium insertion material of $LiCo_{1/3}Ni_{1/3}Mn_{1/3}O_2$ for advanced lithium-ion batteries. *J. Power Sources* **119-121.** Selected papers presented at the 11th International Meeting on Lithium Batteries, 171–174. ISSN: 0378-7753 (2003).
139. Hwang, B. J., Tsai, Y. W., Carlier, D. & Ceder, G. A Combined Computational/Experimental Study on $LiNi_{1/3}Co_{1/3}Mn_{1/3}O_2$. *Chem. Mater.* **15,** 3676–3682 (2003).
140. Patoux, S. & Doeff, M. M. Direct synthesis of $LiNi_{1/3}Co_{1/3}Mn_{1/3}O_2$ from nitrate precursors. *Electrochem. Commun.* **6,** 767–772. ISSN: 1388-2481 (2004).
141. Shaju, K. M., Subba Rao, G. V. & Chowdari, B. V. R. Influence of Li-Ion Kinetics in the Cathodic Performance of Layered $Li(Ni_{1/3}Co_{1/3}Mn_{1/3})O_2$. *J. Electrochem. Soc.* **151,** A1324–A1332 (2004).
142. Chen, C.-H., Wang, C.-J. & Hwang, B.-J. Electrochemical performance of layered $Li[Ni_xCo_{1-2x}Mn_x]O_2$ cathode materials synthesized by a sol–gel method. *J. Power Sources* **146.** Selected papers pressented at the 12th International Meeting on Lithium Batteries, 626–629. ISSN: 0378-7753 (2005).
143. Choi, J. & Manthiram, A. Role of Chemical and Structural Stabilities on the Electrochemical Properties of Layered $LiNi_{1/3}Mn_{1/3}Co_{1/3}O_2$ Cathodes. *J. Electrochem. Soc.* **152,** A1714–A1718 (2005).
144. Li, Z. *et al.* Comparative Study of the Capacity and Rate Capability of $LiNi_yMn_yCo_{1-2y}O_2$ (y=0.5, 0.45, 0.4, 0.33). *J. Electrochem. Soc.* **158,** A516–A522 (2011).
145. Kam, K. C., Mehta, A., Heron, J. T. & Doeff, M. M. Electrochemical and Physical Properties of Ti-Substituted Layered Nickel Manganese Cobalt Oxide (NMC) Cathode Materials. *J. Electrochem. Soc.* **159,** A1383–A1392 (2012).
146. Oh, P., Song, B., Li, W. & Manthiram, A. Overcoming the chemical instability on exposure to air of Ni-rich layered oxide cathodes by coating with spinel $LiMn_{1.9}Al_{0.1}O_4$. *J. Mater. Chem. A* **4,** 5839–5841 (16 2016).
147. Jung, R. *et al.* Effect of Ambient Storage on the Degradation of Ni-Rich Positive Electrode Materials (NMC811) for Li-Ion Batteries. *J. Electrochem. Soc.* **165,** A132–A141 (2018).
148. Xiong, X. *et al.* Washing effects on electrochemical performance and storage characteristics of $LiNi_{0.8}Co_{0.1}Mn_{0.1}O_2$ as cathode material for lithium-ion batteries. *J. Power Sources* **222,** 318–325. ISSN: 0378-7753 (2013).
149. Rohatgi, A. *WebPlotDigitizer* `https://automeris.io/WebPlotDigitizer`. Apr. 2019.
150. Nelson, J. *et al.* In Operando X-ray Diffraction and Transmission X-ray Microscopy of Lithium Sulfur Batteries. *J. Am. Chem. Soc.* **134,** 6337–6343 (2012).
151. Tsai, P.-C. *et al.* Single-particle measurements of electrochemical kinetics in NMC and NCA cathodes for Li-ion batteries. *Energy & Environmental Science* **11,** 860–871 (2018).
152. Tsai, E. H. *et al.* Correlated X-Ray 3D Ptychography and Diffraction Microscopy Visualize Links between Morphology and Crystal Structure of Lithium-Rich Cathode Materials. *iScience* **11,** 356–365 (2019).
153. Yang, Y. *et al.* Quantification of Heterogeneous Degradation in Li-Ion Batteries. *Adv. Energy Mater.* 1900674 (May 2019).
154. Liu, H., Yang, Y. & Zhang, J. Investigation and improvement on the storage property of $LiNi_{0.8}Co_{0.2}O_2$ as a cathode material for lithium-ion batteries. *J. Power Sources* **162,** 644–650. ISSN: 0378-7753 (2006).

155. Matsumoto, K., Kuzuo, R., Takeya, K. & Yamanaka, A. Effects of CO_2 in air on Li deintercalation from $LiNi_{1-x-y}Co_xAl_yO_2$. *J. Power Sources* **81-82,** 558–561 (1999).
156. Van der Ven, A., Bhattacharya, J. & Belak, A. A. Understanding Li Diffusion in Li-Intercalation Compounds. *Acc. Chem. Res.* **46,** 1216–1225 (2013).
157. Xia, S. *et al.* Chemomechanical interplay of layered cathode materials undergoing fast charging in lithium batteries. *Nano Energy* **53,** 753–762. ISSN: 2211-2855 (2018).
158. Yan, P. *et al.* Intragranular cracking as a critical barrier for high-voltage usage of layer-structured cathode for lithium-ion batteries. *Nat. Commun.* **8.** doi:10.1038/ncomms14101.
159. Padhi, A. K. Phospho-olivines as Positive-Electrode Materials for Rechargeable Lithium Batteries. *J. Electrochem. Soc.* **144,** 1188 (1997).
160. Andersson, A. Lithium extraction/insertion in $LiFePO_4$: an X-ray diffraction and Mössbauer spectroscopy study. *Solid State Ionics* **130,** 41–52 (May 2000).
161. Wang, J., Chen-Wiegart, Y.-c. K. & Wang, J. In Operando Tracking Phase Transformation Evolution of Lithium Iron Phosphate with Hard X-ray Microscopy. *Nat. Commun.* **5,** 4570 (2014).
162. Ariyoshi, K., Mizutani, S., Makino, T. & Yamada, Y. A Clue to High Rate Capability of Lithium-Ion Batteries Obtained by an Electrochemical Approach Using "Diluted" Electrode. *J. Electrochem. Soc.* **165,** A3965–A3970 (2018).
163. Liu, H. *et al.* Quantifying reaction and rate heterogeneity in battery electrodes in 3D through operando X-ray diffraction computed tomography. *ACS Appl. Mater. Interfaces* **0,** null (0).
164. Liu, J., Kunz, M., Chen, K., Tamura, N. & Richardson, T. Visualization of Charge Distribution in a Lithium Battery Electrode. *J. Phys. Chem. Lett.* **1,** 2120–2123 (2010).
165. Strobridge, F. C. *et al.* Mapping the Inhomogeneous Electrochemical Reaction Through Porous $LiFePO_4$-Electrodes in a Standard Coin Cell Battery. *Chem. Mater.* **27,** 2374–2386 (2015).
166. Robert, R. *et al.* Scanning X-ray Fluorescence Imaging Study of Lithium Insertion into Copper Based Oxysulfides for Li-Ion Batteries. *Chem. Mater.* **24,** 2684–2691 (2012).
167. Ohzuku, T., Kitagawa, M. & Hirai, T. Electrochemistry of Manganese Dioxide in Lithium Nonaqueous Cell. *J. Electrochem. Soc.* **137,** 769–775 (1990).
168. Kanamura, K., Naito, H., Yao, T. & Takehara, Z. Structural change of the $LiMn_2O_4$ spinel structure induced by extraction of lithium. *J. Mater. Chem.* **6,** 33–36 (Jan. 1996).
169. Bianchini, M., Suard, E., Croguennec, L. & Masquelier, C. Li-Rich $Li_{1+x}Mn_{2-x}O_4$ Spinel Electrode Materials: An Operando Neutron Diffraction Study during Li^+ Extraction/Insertion. *J. Phys. Chem. C* **118,** 25947–25955 (2014).
170. Xia, Y., Zhou, Y. & Yoshio, M. Capacity fading on cycling of 4 V Li/$LiMn_2O_4$ cells. *J. Electrochem. Soc.* **144,** 2593–2600 (1997).
171. Toby, B. H. & Von Dreele, R. B. GSAS-II: the genesis of a modern open-source all purpose crystallography software package. *J. Appl. Crystallogr.* **46,** 544–549 (2013).
172. *Scimap* `https://github.com/canismarko/scimap/`. Accessed: 2018-10-28.
173. Xia, Y. & Yoshio, M. An investigation of lithium ion insertion into spinel structure Li–Mn–O compounds. *J. Electrochem. Soc.* **143,** 825–833 (Mar. 1996).

174. Thackeray, M. M. Structural Considerations of Layered and Spinel Lithiated Oxides for Lithium Ion Batteries. *J. Electrochem. Soc.* **142,** 2558–2563 (1995).
175. David, W., Thackeray, M., Picciotto, L. D. & Goodenough, J. Structure refinement of the spinel-related phases $Li_2Mn_2O_4$ and $Li_{0.2}Mn_2O_4$. *J. Solid State Chem.* **67,** 316–323 (1987).
176. Thackeray, M. Manganese oxides for lithium batteries. *Prog. Solid State Chem.* **25,** 1–71 (1997).
177. Mukerjee, S. *et al.* Structural Evolution of $Li_xMn_2O_4$ in Lithium-Ion Battery Cells Measured In Situ Using Synchrotron X-Ray Diffraction Techniques. *J. Electrochem. Soc.* **145,** 466–472 (1994).
178. Swanson, H. E. & Tatge, E. in, 12 (National Bureau of Standards, Washington, D.C., 1953).
179. Kitada, K. *et al.* Factors determining the packing-limitation of active materials in the composite electrode of lithium-ion batteries. *J. Power Sources* **301,** 11–17 (2016).
180. Bard, A. J. & Faulkner, L. R. in *Electrochemical Methods* 137–140 (John Wiley & Sons, Inc., New York, 2001).
181. Liu, W., Lin, D., Pei, A. & Cui, Y. Stabilizing Lithium Metal Anodes by Uniform Li-Ion Flux Distribution in Nanochannel Confinement. *J. Am. Chem. Soc.* **138,** 15443–15450 (2016).
182. Malvadkar, S. B. & Kostin, M. D. Solutions of the Nernst-Planck Equations for Ionic Diffusion for Conditions near Equilibrium. *J. Chem. Phys.* **57,** 3263–3265 (1972).
183. Ciucci, F. & Lai, W. Derivation of Micro/Macro Lithium Battery Models from Homogenization. *Transp. Porous Media* **88,** 249–270 (June 2011).
184. Nyman, A., Zavalis, T. G., Elger, R., Behm, M. & Lindbergh, G. Analysis of the Polarization in a Li-Ion Battery Cell by Numerical Simulations. *J. Electrochem. Soc.* **157,** A1236–A1246 (2010).
185. Doyle, M., Fuller, T. F. & Newman, J. Modeling of Galvanostatic Charge and Discharge of the Lithium/Polymer/Insertion Cell. *J. Electrochem. Soc.* **140,** 1526–1533 (1993).
186. Zhang, X., Verhallen, T. W., Labohm, F. & Wagemaker, M. Direct observation of Li-ion transport in electrodes under nonequilibrium conditions using neutron depth profiling. *Adv. Energy Mater.* **5.** doi:10.1002/aenm.201500498 (2015).
191. Liu, H. *et al.* Intergranular Cracking as a Major Cause of Long-Term Capacity Fading of Layered Cathodes. *Nano Lett.* **17,** 3452–3457 (June 2017).

APPENDICES

Appendix A

RIGHTS AND PERMISSIONS

UIC

Mark Wolfman <mwolf22@uic.edu>

Regarding Incident 2811458 request to reuse article content for PhD thesis

support@services.acs.org <support@services.acs.org> Thu, Jun 13, 2019 at 6:49 PM
To: mwolf22@uic.edu

ACS Chemistry for Life®

Dear Dr. Mark Wolf,

Thank you for contacting ACS Publications Support.

Your permission request is granted and there is no fee for this reuse. In your planned reuse, you must cite the ACS article as the source, add this direct link <https://pubs.acs.org/doi/abs/10.1021/acs.chemmater.6b05114>, and include a notice to readers that further permissions related to the material excerpted should be directed to the ACS.

Should you need further assistance, please let us know.

Sincerely,

Noemi D. Cabalza

ACS Customer Services & Information

Website: https://help.acs.org/

Incident Information:

Incident #:	2811458
Date Created:	2019-06-14T01:22:41
Priority:	3
Customer:	Mark Wolf
Title:	request to reuse article content for PhD thesis
Description:	Hello, ACS. I would like to use a portion of this article[1] (on which I am the

lead author) in my PhD thesis. My thesis covers the topic of this paper and so the article represents my perspective and would fit nicely into the introduction of my thesis. My institution's guidelines require written permission from the publisher, or a statement from the journal's/publisher's website outlining their policies. Would you kindly provide me with a written statement or a link to the requested web page?

I would like to use the section starting with "Foreword: definition of resolution" on page 3348, up to (but not including) "Applications of X-ray imaging to problems in battery chemistry" on page 3354. I would also like to use Figure 3 on page 3348.

Thanks,
Mark

[1] https://pubs.acs.org/doi/abs/10.1021/acs.chemmater.6b05114

{CMI: MCID710999}

Copyright Clearance Center

Note: Copyright.com supplies permissions but not the copyrighted content itself.

1 PAYMENT 2 REVIEW 3 CONFIRMATION

Step 3: Order Confirmation

Thank you for your order! A confirmation for your order will be sent to your account email address. If you have questions about your order, you can call us 24 hrs/day, M-F at +1.855.239.3415 Toll Free, or write to us at info@copyright.com. This is not an invoice.

Confirmation Number: 11823854
Order Date: 06/14/2019

If you paid by credit card, your order will be finalized and your card will be charged within 24 hours. If you choose to be invoiced, you can change or cancel your order until the invoice is generated.

Payment Information

Mark Wolfman
canismarko@gmail.com
+1 (269) 767-8843
Payment Method: n/a

Order Details

Chemical Society reviews

Order detail ID:	71923873
Order License Id:	4607750665795
ISSN:	1460-4744
Publication Type:	e-Journal
Volume:	
Issue:	
Start page:	
Publisher:	ROYAL SOCIETY OF CHEMISTRY
Author/Editor:	Royal Society of Chemistry (Great Britain)

Permission Status: Granted

Permission type:	Republish or display content
Type of use:	Thesis/Dissertation
Requestor type	Academic institution
Format	Electronic
Portion	image/photo
Number of images/photos requested	1
The requesting person/organization	Mark Wolfman
Title or numeric reference of the portion(s)	Figure 4
Title of the article or chapter the portion is from	Recent advances in rechargeable battery materials: a chemist's perspective
Editor of portion(s)	N/A
Author of portion(s)	M. Rosa Palacín

Volume of serial or monograph	38
Issue, if republishing an article from a serial	9
Page range of portion	2565-2575
Publication date of portion	2009-06-23
Rights for	Main product
Duration of use	Current edition and up to 5 years
Creation of copies for the disabled	no
With minor editing privileges	no
For distribution to	United States
In the following language(s)	Original language of publication
With incidental promotional use	no
Lifetime unit quantity of new product	Up to 499
Title	Chemical and Structural Mapping of Li-Ion Cathodes From the Nano- to the Electrode-Scale
Institution name	University of Illinois Chicago
Expected presentation date	Jul 2019

Note: This item will be invoiced or charged separately through CCC's **RightsLink** service. More info **$ 0.00**

Total order items: 1

This is not an invoice.

Order Total: 0.00 USD

Confirmation Number: 11823854

Special Rightsholder Terms & Conditions

The following terms & conditions apply to the specific publication under which they are listed

Chemical Society reviews
Permission type: Republish or display content
Type of use: Thesis/Dissertation

TERMS AND CONDITIONS

The following terms are individual to this publisher:

None

Other Terms and Conditions:

STANDARD TERMS AND CONDITIONS

1. Description of Service; Defined Terms. This Republication License enables the User to obtain licenses for republication of one or more copyrighted works as described in detail on the relevant Order Confirmation (the "Work(s)"). Copyright Clearance Center, Inc. ("CCC") grants licenses through the Service on behalf of the rightsholder identified on the Order Confirmation (the "Rightsholder"). "Republication", as used herein, generally means the inclusion of a Work, in whole or in part, in a new work or works, also as described on the Order Confirmation. "User", as used herein, means the person or entity making such republication.

2. The terms set forth in the relevant Order Confirmation, and any terms set by the Rightsholder with respect to a particular Work, govern the terms of use of Works in connection with the Service. By using the Service, the person transacting for a republication license on behalf of the User represents and warrants that he/she/it (a) has been duly authorized by the User to accept, and hereby does accept, all such terms and conditions on behalf of User, and (b) shall inform User of all such terms and conditions. In the event such person is a "freelancer" or other third party independent of User and CCC, such party shall be deemed jointly a "User" for purposes of these terms and conditions. In any event, User shall be deemed to have accepted and agreed to all such terms and conditions if User republishes the Work in any fashion.

3. Scope of License; Limitations and Obligations.

3.1 All Works and all rights therein, including copyright rights, remain the sole and exclusive property of the Rightsholder. The license created by the exchange of an Order Confirmation (and/or any invoice) and payment by User of the full amount set forth on that document includes only those rights expressly set forth in the Order Confirmation and in these terms and conditions, and conveys no other rights in the Work(s) to User. All rights not expressly granted are hereby reserved.

3.2 General Payment Terms: You may pay by credit card or through an account with us payable at the end of the month. If you and we agree that you may establish a standing account with CCC, then the following terms apply: Remit Payment to: Copyright Clearance Center, 29118 Network Place, Chicago, IL 60673-1291. Payments Due: Invoices are payable upon their delivery to you (or upon our notice to you that they are available to you for downloading). After 30 days, outstanding amounts will be subject to a service charge of 1-1/2% per month or, if less, the maximum rate allowed by applicable law. Unless otherwise specifically set forth in the Order Confirmation or in a separate written agreement signed by CCC, invoices are due and payable on "net 30" terms. While User may exercise the rights licensed immediately upon issuance of the Order Confirmation, the license is automatically revoked and is null and void, as if it had never been issued, if complete payment for the license is not received on a timely basis either from User directly or through a payment agent, such as a credit card company.

3.3 Unless otherwise provided in the Order Confirmation, any grant of rights to User (i) is "one-time" (including the editions and product family specified in the license), (ii) is non-exclusive and non-transferable and (iii) is subject to any and all limitations and restrictions (such as, but not limited to, limitations on duration of use or circulation) included in the Order Confirmation or invoice and/or in these terms and conditions. Upon completion of the licensed use, User shall either secure a new permission for further use of the Work(s) or immediately cease any new use of the Work(s) and shall render inaccessible (such as by deleting or by removing or severing links or other locators) any further copies of the Work (except for copies printed on paper in accordance with this license and still in User's stock at the end of such period).

3.4 In the event that the material for which a republication license is sought includes third party materials (such as photographs, illustrations, graphs, inserts and similar materials) which are identified in such material as having been used by permission, User is responsible for identifying, and seeking separate licenses (under this Service or otherwise) for, any of such third party materials; without a separate license, such third party materials may not be used.

3.5 Use of proper copyright notice for a Work is required as a condition of any license granted under the Service. Unless otherwise provided in the Order Confirmation, a proper copyright notice will read substantially as follows: "Republished with permission of [Rightsholder's name], from [Work's title, author, volume, edition number and year of copyright]; permission conveyed through Copyright Clearance Center, Inc. " Such notice must be provided in a reasonably legible font size and must be placed either immediately adjacent to the Work as used (for example, as part of a by-line or footnote but not as a separate electronic link) or in the place where substantially all other credits or notices for the new work containing the republished Work are located. Failure to include the required notice results in loss to the Rightsholder and CCC, and the User shall be liable to pay liquidated damages for each such failure equal to twice the use fee specified in the Order Confirmation, in addition to the use fee itself and any other fees and charges specified.

3.6 User may only make alterations to the Work if and as expressly set forth in the Order Confirmation. No Work may be used in any way that is defamatory, violates the rights of third parties (including such third parties' rights of copyright, privacy, publicity, or other tangible or intangible property), or is otherwise illegal, sexually explicit or obscene. In addition, User may not conjoin a Work with any other material that may result in damage to the reputation of the Rightsholder. User agrees to inform CCC if it becomes aware of any infringement of any rights in a Work and to cooperate with any reasonable request of CCC or the Rightsholder in connection therewith.

4. Indemnity. User hereby indemnifies and agrees to defend the Rightsholder and CCC, and their respective employees and directors, against all claims, liability, damages, costs and expenses, including legal fees and expenses, arising out of any use of a Work beyond the scope of the rights granted herein, or any use of a Work which has been altered in any unauthorized way by User, including claims of defamation or infringement of rights of copyright, publicity, privacy or other tangible or intangible property.

5. Limitation of Liability. UNDER NO CIRCUMSTANCES WILL CCC OR THE RIGHTSHOLDER BE LIABLE FOR ANY DIRECT, INDIRECT, CONSEQUENTIAL OR INCIDENTAL DAMAGES (INCLUDING WITHOUT LIMITATION DAMAGES FOR LOSS OF BUSINESS PROFITS OR INFORMATION, OR FOR BUSINESS INTERRUPTION) ARISING OUT OF THE USE OR INABILITY TO USE A WORK, EVEN IF ONE OF THEM HAS BEEN ADVISED OF THE POSSIBILITY OF SUCH DAMAGES. In any event, the total liability of the Rightsholder and CCC (including their respective employees and directors) shall not exceed the total amount actually paid by User for this license. User assumes full liability for the actions and omissions of its principals, employees, agents, affiliates, successors and assigns.

6. Limited Warranties. THE WORK(S) AND RIGHT(S) ARE PROVIDED “AS IS”. CCC HAS THE RIGHT TO GRANT TO USER THE RIGHTS GRANTED IN THE ORDER CONFIRMATION DOCUMENT. CCC AND THE RIGHTSHOLDER DISCLAIM ALL OTHER WARRANTIES RELATING TO THE WORK(S) AND RIGHT(S), EITHER EXPRESS OR IMPLIED, INCLUDING WITHOUT LIMITATION IMPLIED WARRANTIES OF MERCHANTABILITY OR FITNESS FOR A PARTICULAR PURPOSE. ADDITIONAL RIGHTS MAY BE REQUIRED TO USE ILLUSTRATIONS, GRAPHS, PHOTOGRAPHS, ABSTRACTS, INSERTS OR OTHER PORTIONS OF THE WORK (AS OPPOSED TO THE ENTIRE WORK) IN A MANNER CONTEMPLATED BY USER; USER UNDERSTANDS AND AGREES THAT NEITHER CCC NOR THE RIGHTSHOLDER MAY HAVE SUCH ADDITIONAL RIGHTS TO GRANT.

7. Effect of Breach. Any failure by User to pay any amount when due, or any use by User of a Work beyond the scope of the license set forth in the Order Confirmation and/or these terms and conditions, shall be a material breach of the license created by the Order Confirmation and these terms and conditions. Any breach not cured within 30 days of written notice thereof shall result in immediate termination of such license without further notice. Any unauthorized (but licensable) use of a Work that is terminated immediately upon notice thereof may be liquidated by payment of the Rightsholder's ordinary license price therefor; any unauthorized (and unlicensable) use that is not terminated immediately for any reason (including, for example, because materials containing the Work cannot reasonably be recalled) will be subject to all remedies available at law or in equity, but in no event to a payment of less than three times the Rightsholder's ordinary license price for the most closely analogous licensable use plus Rightsholder's and/or CCC's costs and expenses incurred in collecting such payment.

8. **Miscellaneous.**

8.1 User acknowledges that CCC may, from time to time, make changes or additions to the Service or to these terms and conditions, and CCC reserves the right to send notice to the User by electronic mail or otherwise for the purposes of notifying User of such changes or additions; provided that any such changes or additions shall not apply to permissions already secured and paid for.

8.2 Use of User-related information collected through the Service is governed by CCC’s privacy policy, available online here: http://www.copyright.com/content/cc3/en/tools/footer/privacypolicy.html.

8.3 The licensing transaction described in the Order Confirmation is personal to User. Therefore, User may not assign or transfer to any other person (whether a natural person or an organization of any kind) the license created by the Order Confirmation and these terms and conditions or any rights granted hereunder; provided, however, that User may assign such license in its entirety on written notice to CCC in the event of a transfer of all or substantially all of User’s rights in the new material which includes the Work(s) licensed under this Service.

8.4 No amendment or waiver of any terms is binding unless set forth in writing and signed by the parties. The Rightsholder and CCC hereby object to any terms contained in any writing prepared by the User or its principals, employees, agents or affiliates and purporting to govern or otherwise relate to the licensing transaction described in the Order Confirmation, which terms are in any way inconsistent with any terms set forth in the Order Confirmation and/or in these terms and conditions or CCC's standard operating procedures, whether such writing is prepared prior to, simultaneously with or subsequent to the Order Confirmation, and whether such writing appears on a copy of the Order Confirmation or in a separate instrument.

8.5 The licensing transaction described in the Order Confirmation document shall be governed by and construed under the law of the State of New York, USA, without regard to the principles thereof of conflicts of law. Any case, controversy, suit, action, or proceeding arising out of, in connection with, or related to such licensing transaction shall be brought, at CCC's sole discretion, in any federal or state court located in the County of New York, State of New York, USA, or in any federal or state court whose geographical jurisdiction covers the location of the Rightsholder set forth in the Order Confirmation. The parties expressly submit to the personal jurisdiction and venue of each such federal or state court.If you have any comments or questions about the Service or Copyright Clearance Center, please contact us at 978-750-8400 or send an e-mail to info@copyright.com.

v 1.1

Close

Confirmation Number: 11823854

Citation Information

Order Detail ID: 71923873

Chemical Society reviews by Royal Society of Chemistry (Great Britain) Reproduced with permission of ROYAL SOCIETY OF CHEMISTRY in the format Thesis/Dissertation via Copyright Clearance Center.

Close

JOHN WILEY AND SONS LICENSE TERMS AND CONDITIONS

Jun 14, 2019

This Agreement between Mark Wolfman ("You") and John Wiley and Sons ("John Wiley and Sons") consists of your license details and the terms and conditions provided by John Wiley and Sons and Copyright Clearance Center.

License Number	4607760448722
License date	Jun 14, 2019
Licensed Content Publisher	John Wiley and Sons
Licensed Content Publication	Advanced Energy Materials
Licensed Content Title	Nonequilibrium Pathways during Electrochemical Phase Transformations in Single Crystals Revealed by Dynamic Chemical Imaging at Nanoscale Resolution
Licensed Content Author	Young-Sang Yu, Chunjoong Kim, Yijin Liu, et al
Licensed Content Date	Dec 22, 2014
Licensed Content Volume	5
Licensed Content Issue	7
Licensed Content Pages	8
Type of use	Dissertation/Thesis
Requestor type	University/Academic
Format	Electronic
Portion	Figure/table
Number of figures/tables	1
Original Wiley figure/table number(s)	Figure 1
Will you be translating?	No
Title of your thesis / dissertation	Chemical and Structural Mapping of Li-Ion Cathodes From the Nano- to the Electrode-Scale
Expected completion date	Jul 2019
Expected size (number of pages)	1
Requestor Location	Mark Wolfman 4701 N Campbell Ave Apt 3 CHICAGO, IL 60625 United States Attn: Mark Wolfman
Publisher Tax ID	EU826007151
Total	0.00 USD
Terms and Conditions	

TERMS AND CONDITIONS

This copyrighted material is owned by or exclusively licensed to John Wiley & Sons, Inc. or one of its group companies (each a"Wiley Company") or handled on behalf of a society with which a Wiley Company has exclusive publishing rights in relation to a particular work (collectively "WILEY"). By clicking "accept" in connection with completing this licensing

transaction, you agree that the following terms and conditions apply to this transaction (along with the billing and payment terms and conditions established by the Copyright Clearance Center Inc., ("CCC's Billing and Payment terms and conditions"), at the time that you opened your RightsLink account (these are available at any time at http://myaccount.copyright.com).

Terms and Conditions

- The materials you have requested permission to reproduce or reuse (the "Wiley Materials") are protected by copyright.

- You are hereby granted a personal, non-exclusive, non-sub licensable (on a stand-alone basis), non-transferable, worldwide, limited license to reproduce the Wiley Materials for the purpose specified in the licensing process. This license, **and any CONTENT (PDF or image file) purchased as part of your order,** is for a one-time use only and limited to any maximum distribution number specified in the license. The first instance of republication or reuse granted by this license must be completed within two years of the date of the grant of this license (although copies prepared before the end date may be distributed thereafter). The Wiley Materials shall not be used in any other manner or for any other purpose, beyond what is granted in the license. Permission is granted subject to an appropriate acknowledgement given to the author, title of the material/book/journal and the publisher. You shall also duplicate the copyright notice that appears in the Wiley publication in your use of the Wiley Material. Permission is also granted on the understanding that nowhere in the text is a previously published source acknowledged for all or part of this Wiley Material. Any third party content is expressly excluded from this permission.

- With respect to the Wiley Materials, all rights are reserved. Except as expressly granted by the terms of the license, no part of the Wiley Materials may be copied, modified, adapted (except for minor reformatting required by the new Publication), translated, reproduced, transferred or distributed, in any form or by any means, and no derivative works may be made based on the Wiley Materials without the prior permission of the respective copyright owner.**For STM Signatory Publishers clearing permission under the terms of the STM Permissions Guidelines only, the terms of the license are extended to include subsequent editions and for editions in other languages, provided such editions are for the work as a whole in situ and does not involve the separate exploitation of the permitted figures or extracts,** You may not alter, remove or suppress in any manner any copyright, trademark or other notices displayed by the Wiley Materials. You may not license, rent, sell, loan, lease, pledge, offer as security, transfer or assign the Wiley Materials on a stand-alone basis, or any of the rights granted to you hereunder to any other person.

- The Wiley Materials and all of the intellectual property rights therein shall at all times remain the exclusive property of John Wiley & Sons Inc, the Wiley Companies, or their respective licensors, and your interest therein is only that of having possession of and the right to reproduce the Wiley Materials pursuant to Section 2 herein during the continuance of this Agreement. You agree that you own no right, title or interest in or to the Wiley Materials or any of the intellectual property rights therein. You shall have no rights hereunder other than the license as provided for above in Section 2. No right, license or interest to any trademark, trade name, service mark or other branding ("Marks") of WILEY or its licensors is granted hereunder, and you agree that you shall not assert any such right, license or interest with respect thereto

- NEITHER WILEY NOR ITS LICENSORS MAKES ANY WARRANTY OR REPRESENTATION OF ANY KIND TO YOU OR ANY THIRD PARTY, EXPRESS, IMPLIED OR STATUTORY, WITH RESPECT TO THE MATERIALS OR THE ACCURACY OF ANY INFORMATION CONTAINED IN THE MATERIALS, INCLUDING, WITHOUT LIMITATION, ANY IMPLIED WARRANTY OF MERCHANTABILITY, ACCURACY, SATISFACTORY QUALITY, FITNESS FOR A PARTICULAR PURPOSE, USABILITY, INTEGRATION OR NON-INFRINGEMENT AND ALL SUCH WARRANTIES ARE HEREBY EXCLUDED BY WILEY AND ITS LICENSORS AND WAIVED BY YOU.

- WILEY shall have the right to terminate this Agreement immediately upon breach of this Agreement by you.

- You shall indemnify, defend and hold harmless WILEY, its Licensors and their respective directors, officers, agents and employees, from and against any actual or threatened claims, demands, causes of action or proceedings arising from any breach of this Agreement by you.

- IN NO EVENT SHALL WILEY OR ITS LICENSORS BE LIABLE TO YOU OR ANY OTHER PARTY OR ANY OTHER PERSON OR ENTITY FOR ANY SPECIAL, CONSEQUENTIAL, INCIDENTAL, INDIRECT, EXEMPLARY OR PUNITIVE DAMAGES, HOWEVER CAUSED, ARISING OUT OF OR IN CONNECTION WITH THE DOWNLOADING, PROVISIONING, VIEWING OR USE OF THE MATERIALS REGARDLESS OF THE FORM OF ACTION, WHETHER FOR BREACH OF CONTRACT, BREACH OF WARRANTY, TORT, NEGLIGENCE, INFRINGEMENT OR OTHERWISE (INCLUDING, WITHOUT LIMITATION, DAMAGES BASED ON LOSS OF PROFITS, DATA, FILES, USE, BUSINESS OPPORTUNITY OR CLAIMS OF THIRD PARTIES), AND WHETHER OR NOT THE PARTY HAS BEEN ADVISED OF THE POSSIBILITY OF SUCH DAMAGES. THIS LIMITATION SHALL APPLY NOTWITHSTANDING ANY FAILURE OF ESSENTIAL PURPOSE OF ANY LIMITED REMEDY PROVIDED HEREIN.

- Should any provision of this Agreement be held by a court of competent jurisdiction to be illegal, invalid, or unenforceable, that provision shall be deemed amended to achieve as nearly as possible the same economic effect as the original provision, and the legality, validity and enforceability of the remaining provisions of this Agreement shall not be affected or impaired thereby.

- The failure of either party to enforce any term or condition of this Agreement shall not constitute a waiver of either party's right to enforce each and every term and condition of this Agreement. No breach under this agreement shall be deemed waived or excused by either party unless such waiver or consent is in writing signed by the party granting such waiver or consent. The waiver by or consent of a party to a breach of any provision of this Agreement shall not operate or be construed as a waiver of or consent to any other or subsequent breach by such other party.

- This Agreement may not be assigned (including by operation of law or otherwise) by you without WILEY's prior written consent.

- Any fee required for this permission shall be non-refundable after thirty (30) days from receipt by the CCC.

- These terms and conditions together with CCC's Billing and Payment terms and conditions (which are incorporated herein) form the entire agreement between you and WILEY concerning this licensing transaction and (in the absence of fraud) supersedes all prior agreements and representations of the parties, oral or written. This Agreement may not be amended except in writing signed by both parties. This Agreement shall be binding upon and inure to the benefit of the parties' successors, legal representatives, and authorized assigns.

- In the event of any conflict between your obligations established by these terms and conditions and those established by CCC's Billing and Payment terms and conditions, these terms and conditions shall prevail.

- WILEY expressly reserves all rights not specifically granted in the combination of (i) the license details provided by you and accepted in the course of this licensing transaction, (ii) these terms and conditions and (iii) CCC's Billing and Payment terms and conditions.

- This Agreement will be void if the Type of Use, Format, Circulation, or Requestor Type was misrepresented during the licensing process.

- This Agreement shall be governed by and construed in accordance with the laws of the State of New York, USA, without regards to such state's conflict of law rules. Any legal action, suit or proceeding arising out of or relating to these Terms and Conditions or the breach thereof shall be instituted in a court of competent jurisdiction in New York County in the State of New York in the United States of America and each party hereby consents and submits to the personal jurisdiction of such court, waives any objection to venue in such court and consents to service of process by registered or certified mail, return receipt requested, at the last known address of such party.

WILEY OPEN ACCESS TERMS AND CONDITIONS

Wiley Publishes Open Access Articles in fully Open Access Journals and in Subscription journals offering Online Open. Although most of the fully Open Access journals publish open access articles under the terms of the Creative Commons Attribution (CC BY) License only, the subscription journals and a few of the Open Access Journals offer a choice of Creative Commons Licenses. The license type is clearly identified on the article.

The Creative Commons Attribution License

The Creative Commons Attribution License (CC-BY) allows users to copy, distribute and transmit an article, adapt the article and make commercial use of the article. The CC-BY license permits commercial and non-

Creative Commons Attribution Non-Commercial License

The Creative Commons Attribution Non-Commercial (CC-BY-NC)License permits use, distribution and reproduction in any medium, provided the original work is properly cited and is not used for commercial purposes.(see below)

Creative Commons Attribution-Non-Commercial-NoDerivs License

The Creative Commons Attribution Non-Commercial-NoDerivs License (CC-BY-NC-ND) permits use, distribution and reproduction in any medium, provided the original work is properly cited, is not used for commercial purposes and no modifications or adaptations are made. (see below)

Use by commercial "for-profit" organizations

Use of Wiley Open Access articles for commercial, promotional, or marketing purposes requires further explicit permission from Wiley and will be subject to a fee.

Further details can be found on Wiley Online Library
http://olabout.wiley.com/WileyCDA/Section/id-410895.html

Other Terms and Conditions:

v1.10 Last updated September 2015

Questions? customercare@copyright.com or +1-855-239-3415 (toll free in the US) or +1-978-646-2777.

SPRINGER NATURE LICENSE TERMS AND CONDITIONS

Jun 14, 2019

This Agreement between Mark Wolfman ("You") and Springer Nature ("Springer Nature") consists of your license details and the terms and conditions provided by Springer Nature and Copyright Clearance Center.

License Number	4607760067848
License date	Jun 14, 2019
Licensed Content Publisher	Springer Nature
Licensed Content Publication	Nature Photonics
Licensed Content Title	Chemical composition mapping with nanometre resolution by soft X-ray microscopy
Licensed Content Author	David A. Shapiro, Young-Sang Yu, Tolek Tyliszczak, Jordi Cabana, Rich Celestre et al.
Licensed Content Date	Sep 7, 2014
Licensed Content Volume	8
Licensed Content Issue	10
Type of Use	Thesis/Dissertation
Requestor type	academic/university or research institute
Format	electronic
Portion	figures/tables/illustrations
Number of figures/tables/illustrations	1
High-res required	no
Will you be translating?	no
Circulation/distribution	<501
Author of this Springer Nature content	no
Title	Chemical and Structural Mapping of Li-Ion Cathodes From the Nano- to the Electrode-Scale
Institution name	University of Illinois Chicago
Expected presentation date	Jul 2019
Portions	Figure 1
Requestor Location	Mark Wolfman 4701 N Campbell Ave Apt 3 CHICAGO, IL 60625 United States Attn: Mark Wolfman
Total	0.00 USD
Terms and Conditions	

Springer Nature Terms and Conditions for RightsLink Permissions

Springer Nature Customer Service Centre GmbH (the Licensor) hereby grants you a non-exclusive, world-wide licence to reproduce the material and for the purpose and

requirements specified in the attached copy of your order form, and for no other use, subject to the conditions below:

1. The Licensor warrants that it has, to the best of its knowledge, the rights to license reuse of this material. However, you should ensure that the material you are requesting is original to the Licensor and does not carry the copyright of another entity (as credited in the published version).

   If the credit line on any part of the material you have requested indicates that it was reprinted or adapted with permission from another source, then you should also seek permission from that source to reuse the material.

2. Where **print only** permission has been granted for a fee, separate permission must be obtained for any additional electronic re-use.

3. Permission granted **free of charge** for material in print is also usually granted for any electronic version of that work, provided that the material is incidental to your work as a whole and that the electronic version is essentially equivalent to, or substitutes for, the print version.

4. A licence for 'post on a website' is valid for 12 months from the licence date. This licence does not cover use of full text articles on websites.

5. Where **'reuse in a dissertation/thesis'** has been selected the following terms apply: Print rights of the final author's accepted manuscript (for clarity, NOT the published version) for up to 100 copies, electronic rights for use only on a personal website or institutional repository as defined by the Sherpa guideline (www.sherpa.ac.uk/romeo/).

6. Permission granted for books and journals is granted for the lifetime of the first edition and does not apply to second and subsequent editions (except where the first edition permission was granted free of charge or for signatories to the STM Permissions Guidelines http://www.stm-assoc.org/copyright-legal-affairs/permissions/permissions-guidelines/), and does not apply for editions in other languages unless additional translation rights have been granted separately in the licence.

7. Rights for additional components such as custom editions and derivatives require additional permission and may be subject to an additional fee. Please apply to Journalpermissions@springernature.com/bookpermissions@springernature.com for these rights.

8. The Licensor's permission must be acknowledged next to the licensed material in print. In electronic form, this acknowledgement must be visible at the same time as the figures/tables/illustrations or abstract, and must be hyperlinked to the journal/book's homepage. Our required acknowledgement format is in the Appendix below.

9. Use of the material for incidental promotional use, minor editing privileges (this does not include cropping, adapting, omitting material or any other changes that affect the meaning, intention or moral rights of the author) and copies for the disabled are permitted under this licence.

10. Minor adaptations of single figures (changes of format, colour and style) do not require the Licensor's approval. However, the adaptation should be credited as shown in Appendix below.

Appendix — Acknowledgements:

For Journal Content:
Reprinted by permission from [**the Licensor**]: [**Journal Publisher** (e.g. Nature/Springer/Palgrave)] [**JOURNAL NAME**] [**REFERENCE CITATION** (Article name, Author(s) Name), [**COPYRIGHT**] (year of publication)

For **Advance Online Publication papers:**
Reprinted by permission from [**the Licensor**]: [**Journal Publisher** (e.g. Nature/Springer/Palgrave)] [**JOURNAL NAME**] [**REFERENCE CITATION** (Article name, Author(s) Name), [**COPYRIGHT**] (year of publication), advance online publication, day month year (doi: 10.1038/sj.[JOURNAL ACRONYM].)

For Adaptations/Translations:
Adapted/Translated by permission from [**the Licensor**]: [**Journal Publisher** (e.g.

Nature/Springer/Palgrave)] [**JOURNAL NAME**] [**REFERENCE CITATION** (Article name, Author(s) Name), [**COPYRIGHT**] (year of publication)

Note: For any republication from the British Journal of Cancer, the following credit line style applies:

Reprinted/adapted/translated by permission from [**the Licensor**]: on behalf of Cancer Research UK: : [**Journal Publisher** (e.g. Nature/Springer/Palgrave)] [**JOURNAL NAME**] [**REFERENCE CITATION** (Article name, Author(s) Name), [**COPYRIGHT]** (year of publication)

For **Advance Online Publication** papers:
Reprinted by permission from The [**the Licensor**]: on behalf of Cancer Research UK: [**Journal Publisher** (e.g. Nature/Springer/Palgrave)] [**JOURNAL NAME**] [**REFERENCE CITATION** (Article name, Author(s) Name), [**COPYRIGHT**] (year of publication), advance online publication, day month year (doi: 10.1038/sj. [JOURNAL ACRONYM])

For Book content:
Reprinted/adapted by permission from [**the Licensor**]: [**Book Publisher** (e.g. Palgrave Macmillan, Springer etc) [**Book Title**] by [**Book author**(s)] [**COPYRIGHT**] (year of publication)

Other Conditions:

Version 1.1

CAMBRIDGE UNIVERSITY PRESS LICENSE TERMS AND CONDITIONS

Jun 14, 2019

This Agreement between Mark Wolfman ("You") and Cambridge University Press ("Cambridge University Press") consists of your license details and the terms and conditions provided by Cambridge University Press and Copyright Clearance Center.

License Number	4607760876975
License date	Jun 14, 2019
Licensed Content Publisher	Cambridge University Press
Licensed Content Publication	Microscopy and Microanalysis
Licensed Content Title	Development of a Hard X–ray Nanoprobe Beamline at the Advanced Photon Source
Licensed Content Author	J Maser, B Stephenson, R Winarski, C Benson, D Shu, B Lai, S Vogt, M Holt
Licensed Content Date	Aug 1, 2005
Licensed Content Volume	11
Licensed Content Issue	S02
Start page	680
End page	681
Type of Use	Dissertation/Thesis
Requestor type	Author
Portion	Text extract
Number of pages requested	1
Author of this Cambridge University Press article	No
Author / editor of the new work	Yes
Order reference number	
Territory for reuse	North America Only
Title of your thesis / dissertation	Chemical and Structural Mapping of Li-Ion Cathodes From the Nano- to the Electrode-Scale
Expected completion date	Jul 2019
Estimated size(pages)	1
Requestor Location	Mark Wolfman 4701 N Campbell Ave Apt 3 CHICAGO, IL 60625 United States Attn: Mark Wolfman
Publisher Tax ID	GB823847609
Total	0.00 USD
Terms and Conditions	

TERMS & CONDITIONS

Cambridge University Press grants the Licensee permission on a non-exclusive non-transferable basis to reproduce, make available or otherwise use the Licensed content

'Content' in the named territory 'Territory' for the purpose listed 'the Use' on Page 1 of this Agreement subject to the following terms and conditions.

1. The License is limited to the permission granted and the Content detailed herein and does not extend to any other permission or content.
2. Cambridge gives no warranty or indemnity in respect of any third-party copyright material included in the Content, for which the Licensee should seek separate permission clearance.
3. The integrity of the Content must be ensured.
4. The License does extend to any edition published specifically for the use of handicapped or reading-impaired individuals.
5. The Licensee shall provide a prominent acknowledgement in the following format:
author/s, title of article, name of journal, volume number, issue number, page references, , reproduced with permission.

Other terms and conditions:
v1.0

Questions? customercare@copyright.com or +1-855-239-3415 (toll free in the US) or +1-978-646-2777.

ELSEVIER LICENSE
TERMS AND CONDITIONS

Jun 14, 2019

This Agreement between Mark Wolfman ("You") and Elsevier ("Elsevier") consists of your license details and the terms and conditions provided by Elsevier and Copyright Clearance Center.

License Number	4607770387268
License date	Jun 14, 2019
Licensed Content Publisher	Elsevier
Licensed Content Publication	Journal of Power Sources
Licensed Content Title	Improved high-temperature performance of lithium-ion batteries through use of a thermally stable co-polyimide-based cathode binder
Licensed Content Author	Jaecheol Choi,Myung-Hyun Ryou,Bongki Son,Jongchan Song,Jung-Ki Park,Kuk Young Cho,Yong Min Lee
Licensed Content Date	Apr 15, 2014
Licensed Content Volume	252
Licensed Content Issue	n/a
Licensed Content Pages	6
Start Page	138
End Page	143
Type of Use	reuse in a thesis/dissertation
Intended publisher of new work	other
Portion	figures/tables/illustrations
Number of figures/tables/illustrations	1
Format	electronic
Are you the author of this Elsevier article?	No
Will you be translating?	No
Original figure numbers	Figure 6
Title of your thesis/dissertation	Chemical and Structural Mapping of Li-Ion Cathodes From the Nano- to the Electrode-Scale
Publisher of new work	University of Illinois Chicago
Expected completion date	Jul 2019
Estimated size (number of pages)	1
Requestor Location	Mark Wolfman 4701 N Campbell Ave Apt 3 CHICAGO, IL 60625 United States Attn: Mark Wolfman
Publisher Tax ID	98-0397604
Total	0.00 USD

Terms and Conditions

INTRODUCTION

1. The publisher for this copyrighted material is Elsevier. By clicking "accept" in connection with completing this licensing transaction, you agree that the following terms and conditions apply to this transaction (along with the Billing and Payment terms and conditions established by Copyright Clearance Center, Inc. ("CCC"), at the time that you opened your Rightslink account and that are available at any time at http://myaccount.copyright.com).

GENERAL TERMS

2. Elsevier hereby grants you permission to reproduce the aforementioned material subject to the terms and conditions indicated.
3. Acknowledgement: If any part of the material to be used (for example, figures) has appeared in our publication with credit or acknowledgement to another source, permission must also be sought from that source. If such permission is not obtained then that material may not be included in your publication/copies. Suitable acknowledgement to the source must be made, either as a footnote or in a reference list at the end of your publication, as follows:
"Reprinted from Publication title, Vol /edition number, Author(s), Title of article / title of chapter, Pages No., Copyright (Year), with permission from Elsevier [OR APPLICABLE SOCIETY COPYRIGHT OWNER]." Also Lancet special credit - "Reprinted from The Lancet, Vol. number, Author(s), Title of article, Pages No., Copyright (Year), with permission from Elsevier."
4. Reproduction of this material is confined to the purpose and/or media for which permission is hereby given.
5. Altering/Modifying Material: Not Permitted. However figures and illustrations may be altered/adapted minimally to serve your work. Any other abbreviations, additions, deletions and/or any other alterations shall be made only with prior written authorization of Elsevier Ltd. (Please contact Elsevier at permissions@elsevier.com). No modifications can be made to any Lancet figures/tables and they must be reproduced in full.
6. If the permission fee for the requested use of our material is waived in this instance, please be advised that your future requests for Elsevier materials may attract a fee.
7. Reservation of Rights: Publisher reserves all rights not specifically granted in the combination of (i) the license details provided by you and accepted in the course of this licensing transaction, (ii) these terms and conditions and (iii) CCC's Billing and Payment terms and conditions.
8. License Contingent Upon Payment: While you may exercise the rights licensed immediately upon issuance of the license at the end of the licensing process for the transaction, provided that you have disclosed complete and accurate details of your proposed use, no license is finally effective unless and until full payment is received from you (either by publisher or by CCC) as provided in CCC's Billing and Payment terms and conditions. If full payment is not received on a timely basis, then any license preliminarily granted shall be deemed automatically revoked and shall be void as if never granted. Further, in the event that you breach any of these terms and conditions or any of CCC's Billing and Payment terms and conditions, the license is automatically revoked and shall be void as if never granted. Use of materials as described in a revoked license, as well as any use of the materials beyond the scope of an unrevoked license, may constitute copyright infringement and publisher reserves the right to take any and all action to protect its copyright in the materials.
9. Warranties: Publisher makes no representations or warranties with respect to the licensed material.
10. Indemnity: You hereby indemnify and agree to hold harmless publisher and CCC, and their respective officers, directors, employees and agents, from and against any and all claims arising out of your use of the licensed material other than as specifically authorized pursuant to this license.

11. No Transfer of License: This license is personal to you and may not be sublicensed, assigned, or transferred by you to any other person without publisher's written permission.
12. No Amendment Except in Writing: This license may not be amended except in a writing signed by both parties (or, in the case of publisher, by CCC on publisher's behalf).
13. Objection to Contrary Terms: Publisher hereby objects to any terms contained in any purchase order, acknowledgment, check endorsement or other writing prepared by you, which terms are inconsistent with these terms and conditions or CCC's Billing and Payment terms and conditions. These terms and conditions, together with CCC's Billing and Payment terms and conditions (which are incorporated herein), comprise the entire agreement between you and publisher (and CCC) concerning this licensing transaction. In the event of any conflict between your obligations established by these terms and conditions and those established by CCC's Billing and Payment terms and conditions, these terms and conditions shall control.
14. Revocation: Elsevier or Copyright Clearance Center may deny the permissions described in this License at their sole discretion, for any reason or no reason, with a full refund payable to you. Notice of such denial will be made using the contact information provided by you. Failure to receive such notice will not alter or invalidate the denial. In no event will Elsevier or Copyright Clearance Center be responsible or liable for any costs, expenses or damage incurred by you as a result of a denial of your permission request, other than a refund of the amount(s) paid by you to Elsevier and/or Copyright Clearance Center for denied permissions.

LIMITED LICENSE

The following terms and conditions apply only to specific license types:
15. **Translation**: This permission is granted for non-exclusive world **English** rights only unless your license was granted for translation rights. If you licensed translation rights you may only translate this content into the languages you requested. A professional translator must perform all translations and reproduce the content word for word preserving the integrity of the article.
16. **Posting licensed content on any Website**: The following terms and conditions apply as follows: Licensing material from an Elsevier journal: All content posted to the web site must maintain the copyright information line on the bottom of each image; A hyper-text must be included to the Homepage of the journal from which you are licensing at http://www.sciencedirect.com/science/journal/xxxxx or the Elsevier homepage for books at http://www.elsevier.com; Central Storage: This license does not include permission for a scanned version of the material to be stored in a central repository such as that provided by Heron/XanEdu.
Licensing material from an Elsevier book: A hyper-text link must be included to the Elsevier homepage at http://www.elsevier.com . All content posted to the web site must maintain the copyright information line on the bottom of each image.

Posting licensed content on Electronic reserve: In addition to the above the following clauses are applicable: The web site must be password-protected and made available only to bona fide students registered on a relevant course. This permission is granted for 1 year only. You may obtain a new license for future website posting.
17. **For journal authors:** the following clauses are applicable in addition to the above:
Preprints:
A preprint is an author's own write-up of research results and analysis, it has not been peer-reviewed, nor has it had any other value added to it by a publisher (such as formatting, copyright, technical enhancement etc.).
Authors can share their preprints anywhere at any time. Preprints should not be added to or enhanced in any way in order to appear more like, or to substitute for, the final versions of articles however authors can update their preprints on arXiv or RePEc with their Accepted Author Manuscript (see below).

If accepted for publication, we encourage authors to link from the preprint to their formal publication via its DOI. Millions of researchers have access to the formal publications on ScienceDirect, and so links will help users to find, access, cite and use the best available version. Please note that Cell Press, The Lancet and some society-owned have different preprint policies. Information on these policies is available on the journal homepage.
Accepted Author Manuscripts: An accepted author manuscript is the manuscript of an article that has been accepted for publication and which typically includes author-incorporated changes suggested during submission, peer review and editor-author communications.
Authors can share their accepted author manuscript:

- immediately
  - via their non-commercial person homepage or blog
  - by updating a preprint in arXiv or RePEc with the accepted manuscript
  - via their research institute or institutional repository for internal institutional uses or as part of an invitation-only research collaboration work-group
  - directly by providing copies to their students or to research collaborators for their personal use
  - for private scholarly sharing as part of an invitation-only work group on commercial sites with which Elsevier has an agreement
- After the embargo period
  - via non-commercial hosting platforms such as their institutional repository
  - via commercial sites with which Elsevier has an agreement

In all cases accepted manuscripts should:

- link to the formal publication via its DOI
- bear a CC-BY-NC-ND license - this is easy to do
- if aggregated with other manuscripts, for example in a repository or other site, be shared in alignment with our hosting policy not be added to or enhanced in any way to appear more like, or to substitute for, the published journal article.

Published journal article (JPA): A published journal article (PJA) is the definitive final record of published research that appears or will appear in the journal and embodies all value-adding publishing activities including peer review co-ordination, copy-editing, formatting, (if relevant) pagination and online enrichment.
Policies for sharing publishing journal articles differ for subscription and gold open access articles:
Subscription Articles: If you are an author, please share a link to your article rather than the full-text. Millions of researchers have access to the formal publications on ScienceDirect, and so links will help your users to find, access, cite, and use the best available version.
Theses and dissertations which contain embedded PJAs as part of the formal submission can be posted publicly by the awarding institution with DOI links back to the formal publications on ScienceDirect.
If you are affiliated with a library that subscribes to ScienceDirect you have additional private sharing rights for others' research accessed under that agreement. This includes use for classroom teaching and internal training at the institution (including use in course packs and courseware programs), and inclusion of the article for grant funding purposes.
Gold Open Access Articles: May be shared according to the author-selected end-user license and should contain a CrossMark logo, the end user license, and a DOI link to the formal publication on ScienceDirect.
Please refer to Elsevier's posting policy for further information.
18. **For book authors** the following clauses are applicable in addition to the above:
Authors are permitted to place a brief summary of their work online only. You are not

allowed to download and post the published electronic version of your chapter, nor may you scan the printed edition to create an electronic version. **Posting to a repository:** Authors are permitted to post a summary of their chapter only in their institution's repository.
19. **Thesis/Dissertation**: If your license is for use in a thesis/dissertation your thesis may be submitted to your institution in either print or electronic form. Should your thesis be published commercially, please reapply for permission. These requirements include permission for the Library and Archives of Canada to supply single copies, on demand, of the complete thesis and include permission for Proquest/UMI to supply single copies, on demand, of the complete thesis. Should your thesis be published commercially, please reapply for permission. Theses and dissertations which contain embedded PJAs as part of the formal submission can be posted publicly by the awarding institution with DOI links back to the formal publications on ScienceDirect.

Elsevier Open Access Terms and Conditions
You can publish open access with Elsevier in hundreds of open access journals or in nearly 2000 established subscription journals that support open access publishing. Permitted third party re-use of these open access articles is defined by the author's choice of Creative Commons user license. See our open access license policy for more information.
Terms & Conditions applicable to all Open Access articles published with Elsevier:
Any reuse of the article must not represent the author as endorsing the adaptation of the article nor should the article be modified in such a way as to damage the author's honour or reputation. If any changes have been made, such changes must be clearly indicated.
The author(s) must be appropriately credited and we ask that you include the end user license and a DOI link to the formal publication on ScienceDirect.
If any part of the material to be used (for example, figures) has appeared in our publication with credit or acknowledgement to another source it is the responsibility of the user to ensure their reuse complies with the terms and conditions determined by the rights holder.
Additional Terms & Conditions applicable to each Creative Commons user license:
CC BY: The CC-BY license allows users to copy, to create extracts, abstracts and new works from the Article, to alter and revise the Article and to make commercial use of the Article (including reuse and/or resale of the Article by commercial entities), provided the user gives appropriate credit (with a link to the formal publication through the relevant DOI), provides a link to the license, indicates if changes were made and the licensor is not represented as endorsing the use made of the work. The full details of the license are available at http://creativecommons.org/licenses/by/4.0.
CC BY NC SA: The CC BY-NC-SA license allows users to copy, to create extracts, abstracts and new works from the Article, to alter and revise the Article, provided this is not done for commercial purposes, and that the user gives appropriate credit (with a link to the formal publication through the relevant DOI), provides a link to the license, indicates if changes were made and the licensor is not represented as endorsing the use made of the work. Further, any new works must be made available on the same conditions. The full details of the license are available at http://creativecommons.org/licenses/by-nc-sa/4.0.
CC BY NC ND: The CC BY-NC-ND license allows users to copy and distribute the Article, provided this is not done for commercial purposes and further does not permit distribution of the Article if it is changed or edited in any way, and provided the user gives appropriate credit (with a link to the formal publication through the relevant DOI), provides a link to the license, and that the licensor is not represented as endorsing the use made of the work. The full details of the license are available at http://creativecommons.org/licenses/by-nc-nd/4.0.
Any commercial reuse of Open Access articles published with a CC BY NC SA or CC BY NC ND license requires permission from Elsevier and will be subject to a fee.
Commercial reuse includes:

- Associating advertising with the full text of the Article
- Charging fees for document delivery or access

- Article aggregation
- Systematic distribution via e-mail lists or share buttons

Posting or linking by commercial companies for use by customers of those companies.

20. **Other Conditions**:

v1.9

Questions? customercare@copyright.com or +1-855-239-3415 (toll free in the US) or +1-978-646-2777.

Title: Reaction Heterogeneity in LiNi0.8Co0.15Al0.05O2 Induced by Surface Layer

Author: Antonin Grenier, Hao Liu, Kamila M. Wiaderek, et al

Publication: Chemistry of Materials

Publisher: American Chemical Society

Date: Sep 1, 2017

PERMISSION/LICENSE IS GRANTED FOR YOUR ORDER AT NO CHARGE

This type of permission/license, instead of the standard Terms & Conditions, is sent to you because no fee is being charged for your order. Please note the following:

- Permission is granted for your request in both print and electronic formats, and translations.
- If figures and/or tables were requested, they may be adapted or used in part.
- Please print this page for your records and send a copy of it to your publisher/graduate school.
- Appropriate credit for the requested material should be given as follows: "Reprinted (adapted) with permission from (COMPLETE REFERENCE CITATION). Copyright (YEAR) American Chemical Society." Insert appropriate information in place of the capitalized words.
- One-time permission is granted only for the use specified in your request. No additional uses are granted (such as derivative works or other editions). For any other uses, please submit a new request.

If credit is given to another source for the material you requested, permission must be obtained from that source.

BACK CLOSE WINDOW

VITA

Education

- B.S., Chemistry, Western Michigan University, Kalamazoo, Michigan, 2008.
- Ph.D., Physical Chemistry, University of Illinois Chicago, Chicago, Illinois, 2019.

Employment

- Scientist, Kalsec Inc., Kalamazoo, MI, 2008–2014.
- Teaching Assistant, Department of Chemistry, University of Illinois Chicago, Chicago, IL, 2014-2015.
- Research Assistant, Department of Chemistry, University of Illinois Chicago, Chicago, IL, 2016-2019.

Awards

- Creative Activities and Research Award, Western Michigan University College of Arts and Sciences, 2007.
- Local Section Service Award, Kalamazoo Section of the American Chemical Society, 2017.
- Science Graduate Research Program Fellowship, Office of Science, U.S. Department of Energy, 2017.
- Paaren Fellowship, Department of Chemistry, University of Illinois Chicago, 2018.

VITA (Continued)

Publications

1. Wolfman, M. *et al.* Operando Microstructural Effects in Layered Battery Cathode Particles. *[In preparation]*
2. Wolfman, M. *et al.* Multi-Scale Chemical Imaging of Reaction Inhomogeneities in $LiNi_{0.8}Co_{0.15}Al_{0.05}O_2$ Primary Particles. *[In preparation]*
3. Wolfman, M. *et al.* Mapping of Chemical Heterogeneity in $LiMn_2O_4$ Battery Electrodes with High Energy Density. *[In preparation]*
4. Yoo, S. *et al.* Sinogram Image Completion for Limited Angle Tomography with Generative Adversarial Networks. *IEEE International Conference on Image Processing 2019 [Accepted]*
5. Tsai, P.-C. *et al.* Single-particle measurements of electrochemical kinetics in NMC and NCA cathodes for Li-ion batteries. *Energy & Environmental Science* **11,** 860–871 (2018)
6. Liu, H. *et al.* Intergranular Cracking as a Major Cause of Long-Term Capacity Fading of Layered Cathodes. *Nano Lett.* **17,** 3452–3457 (June 2017)
7. Wolf, M. *et al.* Visualization of Electrochemical Reactions in Battery Materials with X-ray Microscopy and Mapping. *Chem. Mater.* **29,** 3347–3362 (2017)

Presentations

1. Wolfman, M. *et al. Multi-scale chemical microscopy of reaction inhomogeneities in* $LiNi_{0.8}Co_{0.15}Al_{0.05}O_2$ *cathode primary particles* Oral presentation and selected for SciMix presentation at 256^{th} ACS National Meeting & Exposition. Aug. 2018

VITA (Continued)

2. Wolfman, M. *et al. Nanoscale Chemical Imaging of Lihtium Ion Battery Cathodes* Poster presentation at University of Illinois Chicago Student Research Forum. Nov. 2017
3. Wolfman, M. *et al. Operando Chemical Imaging of Ni-Based Layered Cathodes for Lithium-Ion Batteries* Presentation at Materials Research Society Fall Meeting and Exhibit, Boston MA. Nov. 2017
4. Wolf, M. *et al. Mapping of Spatial Inhomogeneities with Laboratory X-ray Diffraction* Presentation at 65$^{\text{th}}$ Annual Conference on Applications of X-Ray Analysis, Rosemont IL. Aug. 2016
5. Wolf, M. *et al. Operando Microdiffraction Mapping of Single Particle Cathode Materials* Presentation at 65$^{\text{th}}$ Annual Conference on Applications of X-Ray Analysis, Rosemont IL. Aug. 2016
6. Wolf, M. *et al. Mapping of Spatial Inhomogeneities with Laboratory X-Ray Diffraction* Poster presentation at 18$^{\text{th}}$ International Meeting on Lithium Batteries, Chicago IL. June 2016
7. Wolf, M. *et al. Natural Antioxidants and Addition Methods for Oxidative Stability of Noodles* Presentation at 105$^{\text{th}}$ AOCS Annual Meeting & Expo, San Antonio TX. May 2014

Professional Memberships

- American Chemical Society
- Electrochemical Society

VITA (Continued)

Service

- Vice-president, secretary and treasurer, Chemistry Graduate Student Association, Department of Chemistry, University of Illinois Chicago, Chicago, IL, 2015–2019.
- Webmaster, Kalamazoo Section of the American Chemical Society, Kalamazoo, MI, 2013–Present.
- Organizing Committee, Joint Great Lakes/Central Regional Meeting of the American Chemical Society, Grand Rapids, MI, 2015.
- Science Coach, American Chemical Society, 2011–2014.